TECHNISCHE UNIVERSITÄT MÜNCHEN

Lehrstuhl für Nanoelektronik

A Hybrid CMOS-Imager with Integrated Solution-Processable Organic Photodiodes

Daniela Baierl

Vollständiger Abdruck der von der Fakultät für Elektrotechnik und Informationstechnik der Technischen Universität München zur Erlangung des akademischen Grades eines

Doktors der Naturwissenschaften

genehmigten Dissertation.

Vorsitzender:

Univ.-Prof. Dr.-Ing. Sandra Hirche

Prüfer der Dissertation:

1. Univ.-Prof. Paolo Lugli, Ph.D.

2. Univ.-Prof. Jonathan J. Finley, Ph.D.

Die Dissertation wurde am 20. Juni 2012 bei der Technischen Universität München eingereicht und durch die Fakultät für Elektrotechnik und Informationstechnik am 26. November 2012 angenommen.

Abstract

The aim of this work was to create a novel imaging sensor with a photoactive layer consisting of solution-processable organic semiconductors. The base of this sensor is a chip for signal processing and read-out, fabricated with state-of-the-art complementary metal oxide semiconductor (CMOS) technology. Combining this technology, deployed for imagers in most digital cameras, with organic materials, allows the creation of a hybrid imager with new and enhanced features. In this thesis, the solution-processability of certain organic materials, as conjugated polymers, was exploited since they allow a straightforward deposition on different substrates, as also the CMOS-chips, without increasing cost and process complexity significantly compared with conventional crystalline semiconductors. A spray-deposition process for the bulk-heterojunction of the blend PCBM:P3HT (poly(3-hexylthiophene): [6,6]-phenyl C61 butyric acid methylester) on top of the CMOS-chip was developed, resulting in the formation of homogeneous organic layers with good electro-optical performance. Furthermore, to allow the integration of organic materials onto the chip, a new kind of organic photodetector layout with an inverted stack of the different layers, introducing a sensitive oxygen plasma treatment of PCBM:P3HT, was invented. To increase the external quantum efficiency of this device over 70 %, a PEDOT:PSS (Poly(3,4-ethylenedioxythiophene) poly(styrenesulfonate)) formulation was optimized towards high conductivity and transparency and was integrated as top electrode onto the inverted organic photodetector. With the spray-coating process this inverted organic architecture was then deposited on top of the CMOS-chips. The final hybrid prototype imagers were fully opto-electronically characterized. The results proved the suitability of the device for imaging application and generated new knowledge about noise types in organic photodetectors. The external quantum efficiency of up to 50 % is remarkable higher as for standard active pixel CMOS-imagers because the pixel (geometrical) fill factor of the hybrid device is about three times higher. Additionally, by integrating different organic materials, as a squaraine dye, on the chip, the cost-effective portability of the hybrid concept to different wavelength regions, also beside the visible range of the spectrum, was demonstrated.

Table of Contents

Chapter 1

Introduction

During the last years, a new industry dealing with the large field of organic electronics has started to emerge. According to a recent study in april 2012 [Res12], the global organic electronic market is expected to be worth 8.2 billion US$ in 2012, currently mostly driven by display technologies like AMOLED (active-matrix organic light-emitting diode) for mobile phones, and will demonstrate high growth at an annual rate of 33 % from 2012 to 2018 [Res12]. Although the emerging technologies are complementary to conventional crystalline (silicon) electronic devices, most applications will be of a new kind rather than a replacement. This is due to the fact that the organic materials do not outmatch the electrical performance of their inorganic counterparts, but offer some major advantages like flexibility and low-cost processing which will create a market over the next few years mainly for flexible displays, bio-sensors and RFID (Radio-frequency identification) labels.
One of the major strengths of organic electronics is their solution-processability, referring to the ability of organic materials to be processed in a liquid state. The deposition of the dissolved organic materials is a low-cost fabrication process since no vacuum or high temperature processing steps are required. Additionally, the availability of cheap and renewable materials decreases the overall cost of organic electronics.
The organic layers can be deposited with different solution-processing techniques, such as spin-coating, and allow a cost effective mass production with a continuous fabrication line, a so called roll-to-roll processing like slot-die-coating [Bla09, Kre09], ink-jet printing [Hot07] and spray-coating [Gir11, Na10, Ted09], as also explored for this work. These low-cost processing techniques can unfold their full potential when efficient multilayer engineering is feasible [Zho11] and when in addition to the organics, also the electrode materials can be replaced with solution-processable materials. Especially a replacement of the brittle ITO (indium tin oxide) containing expensive indium, much in demand for LCD (liquid crystal display) production, is a major task which was also investigated in this work. ITO is commonly deployed in organic optoelectronic devices as transparent electrode material as in OLED (organic light emitting diode) displays, solar cells and photodetectors.

The liquid state of the organic semiconductors allows not only a deposition on flexible substrates, but on any kind of substrates, including inorganic electronic circuitry like amorphous silicon thin-film transistor circuitry [Ted07, Rau09] and combination with inorganic materials, for example colloidal quantum dots as infrared absorber [Rau09]. Hence, the solution-processability is the key to develop low-cost hybrid technologies which combine certain advantages of organic materials with additional benefits of the inorganic material. Such a hybrid combination was investigated in this work.

The main focus of this thesis is the development of a hybrid imaging device based on inorganic complementary metal oxide semiconductor (CMOS) technology. Here, the well-established processing of silicon circuitry and the state-of-the art imaging performance are exploited at the CMOS-side. The benefits of the integration of organic materials can be understood taking a closer look on a state-of-the-art CMOS-imager as used for consumer or industrial applications. It consists of APSs (active pixel sensors) in which read-out amplifiers are incorporated to each pixel in addition to the photoactive silicon photodiodes to obtain a similar good noise performance as with the competitive CCD (charge coupling device) technology [Big06]. The APS imager is a more cost-effective imaging system as a CCD-imager since the CMOS-technology offers the possibility to integrate monolithically the required electronic circuits on one single chip [Big06].
The disadvantage of an APS is the reduced area for photodetection in each pixel due to the integrated electronics. The ratio between the photoactive to the non-photoactive area of a pixel is defined as pixel fill factor. This value is usually below 30 % [Fos97, Big06], decreasing the light sensitivity of the pixel, which can be expressed as quantum efficiency, by the same amount and hence also the signal-to-noise-ratio respective the quality of signal detection. To overcome this limitation, focusing microlens-arrays can be implemented [Iid97, Hur97], a multilayer of amorphous silicon (thin film on ASIC) can be deposited [Lul99, Sch98] or the sensor can be transformed into a back-illuminated imager [Pai05]. The disadvantage of these methods is that they all require significant additional processing and therefore increasing cost. At this point, low-cost solution-processable organic materials, like conjugated polymers, offer a significant improvement since they can be deposited with a low-cost process on top of the CMOS-chip to cover it as continuous film. Hence, the vertical integration results in a 100 % fill factor and the light sensitivity of each pixel can be increased significantly depending on the organic photoactive material. For the commonly used bulk-heterojunction of PCBM:P3HT (poly(3-hexylthiophene): [6,6]-phenyl C61 butyric acid methylester), employed for photodetection in the visible range of the spectrum up to 650 nm, EQE values of about 75 % [Ted09, Bai11a] are reported.
To demonstrate the improvement of CMOS-sensitivity with organic photoactive layers was one of the major challenges of this thesis.

Another benefit which arises due to the use of organic layers for photodetection is the ease of switching the process to different organic materials without increasing pro-

cess complexity and cost. Most interesting are soluble polymers exhibiting different absorption characteristics, especially with wave length ranges which can not be addressed with conventional CMOS-imagers. Since the silicon absorption edge is situated at about 1.1 µm, near-infrared light (NIR) (780 nm - 3 µm) is only partly detectable. This wave length region is interesting for a number of applications, including security and military applications as security cameras, automotive night vision systems [Luo10] and optical fiber communication due to fiber attenuation minima at 1.3 µm and 1.55 µm. Regarding imaging, especially the wave length region between 1200 and 1800 nm is interesting due to a phenomenon called 'night-glow' which refers to a natural, stable night sky light source due to interaction of the atmosphere with solar winds. With a radiant sterance of about $1 \cdot 10^{-10}$ W cm^{-2} sr^{-1} [Vit72], it is bright enough for the use as illumination for security cameras. So far, only expensive solutions like compound semiconductor cameras, as InGaAs and MCdTl, are available for this wave length region. Instead, a hybrid NIR CMOS-detector, e.g. containing a NIR sensitive polymer as reported in [Gon09] would not increase cost compared to the imager version sensitive in the visible range of the spectrum.

Within this thesis, the way towards a hybrid CMOS-imager is illustrated, demonstrating the development of an organic photodiode suitable for integration to the CMOS-chip.
Chapter 2 informs the reader about organic semiconductors, especially about solution-processable conjugated polymers, and passes information for a basic understanding of CMOS image sensors. Chapter 3 focuses on the experimental background, containing descriptions of the used materials and the OPD fabrication steps. Additionally, important photodiode performance and material characteristics will be addressed as well as the ways to measure them. In chapter 4 and 5 the results of the development of an OPD suitable for CMOS-chip integration are presented. With spin-coating, an efficient OPD is developed in chapter 4 which features top-absorption with a highly transparent polymer top anode. In chapter 5, spray-deposition is investigated for the deposition of organic materials. This vertical deposition method turned out to be suitable for the organic material integration on top of the textured CMOS-substrates. The results of these two chapters are then combined to finally create a hybrid CMOS-imager in chapter 6. The performance of this imager is explored to test the suitability for imaging application.

Chapter 2

Physical and technological background of the hybrid imager

This chapter provides a physical and technical background about the organic and inorganic materials used in this work. State-of-the-art CMOS-technology is addressed and compared to CCD-technology to understand the present limits of imaging.

2.1 Organic semiconductors

Semiconductivity can be found in numerous carbon based materials. Two main classes are the so-called small molecules [Mis12], which contain polycyclic aromatic compounds like pentacene and anthracene, and the polymeric semiconductors like regioregular poly(3-hexylthiophene) and [6,6]-phenyl-C_{61}-butyric acid methyl ester (see section 3.2.2.1, 3.8). Both are employed in various electronic devices like OLEDs (organic light emitting diodes), OSC (organic solar cells), OTFTs (organic thin film transistors) and OPDs (organic photodiodes) [Sch04]. The main difference is their type of processing, either evaporation or solution processing techniques are used. Evaporation and sublimation are thin film depositions with a low degree of contamination since no solvents are involved and the vacuum applied reduces contaminants like oxygen and water. Long-chained polymers decompose under excessive heat and exhibit a too large molar mass for evaporation. They are chemically designed to be soluble in common aromatic solvents and can be deposited with various techniques like spin-coating (see section 3.3.2), spray-coating (see section 3.3.3), doctor-blading and ink-jet printing [Hot07]. The processing of a liquid phase is the major strength of organic polymers since it reduces cost due to application of low temperature, the expandability of vacuum and the ease of large scale deposition.

The main elements of an organic semiconductor are carbon and hydrogen which usually

form only electrical insulating materials. To understand the origin of the semiconducting property of some organic molecules and polymers, it is necessary to take a closer look on the formation of molecular orbitals which are a mathematical concept to describe the wave-like behavior of electrons inside the molecule. They are formed by combining atomic orbitals from each atom of the molecule. The valence shell of carbon has a $2s$ and three $2p$ orbitals, filled with four valence electrons building a $2s^2 2p_x 2p_y$ configuration. Whereas the orbital shape $|\Phi|^2$ with the wavefunction Φ is spherical for the $2s$ orbital, the p orbital is dumbbell shaped.
One way to describe the formation of a molecule is the hybridization concept. Here, the atomic orbitals are mixed to form so-called hybrid orbitals before the actual bonding of two atoms occur. It is not valid for free atoms since the transformation of the orbitals is related to an energy release. Depending on the number of atomic orbitals which contribute to the hybridization, there are different types. Two interfering orbitals lead to sp hybridization, three to sp^2 hybridization and four to sp^3 hybridization. For instance, sp^3 hybridization leads to the formation of diamond, the sp^2 hybridization occurs in graphite and most conjugated polymers and is described in detail in the following section.

2.1.1 Conjugated polymers

The sp^2 hybridization involves the formation of three hybrid orbitals which are arranged in a plane with angles of 120° and a remaining orthogonal p orbital, as indicated in Fig.2.1. In the basic sp^2 hybridized molecule, the ethylene (C_2H_4), the sp^2 orbitals of the carbon overlap with the s orbitals of two hydrogen atoms as well as with the sp^2 orbital of the other carbon atom. The resulting bonds are called σ-bonds. The orthogonal p orbitals interaction leads to the formation of π-bonds which lie above and below the plane spanned by the sp^2 orbitals. Since the degree of overlap of the p orbitals is low, the π-bonds are weak [Mor11] and the electrons do not belong to a certain orbital respective atom. This strong electron delocalization is the origin of the semiconducting property of organic semiconductors. In conjugated systems, the p orbitals with their delocalized electrons are connected via each other through alternating single (σ) and double (σ plus π) bonds. In conjugated polymers, consisting of a chain of repeating organic monomers, the delocalization occurs along the whole chain and hence one dimensional conduction arises.
The fundamental origin of the bandgap of the conjugated polymers is related to the Pauli principle. Due to orbital overlapping the atomic energy levels split and a bonding respective antibonding state is created to prevent that electrons are in the same quantum state. The corresponding energy levels are the LUMO (lowest unoccupied molecular orbital) and the HOMO (highest occupied molecular orbital) in analogy to the valence and conduction band of an inorganic semiconductor. Compared to the structural unit of the polymer, the bandgap E_g decreases with increasing number n of the unit molecule, as illustrated in Fig.2.3 for n thiophene rings [Sal98, Mul01].

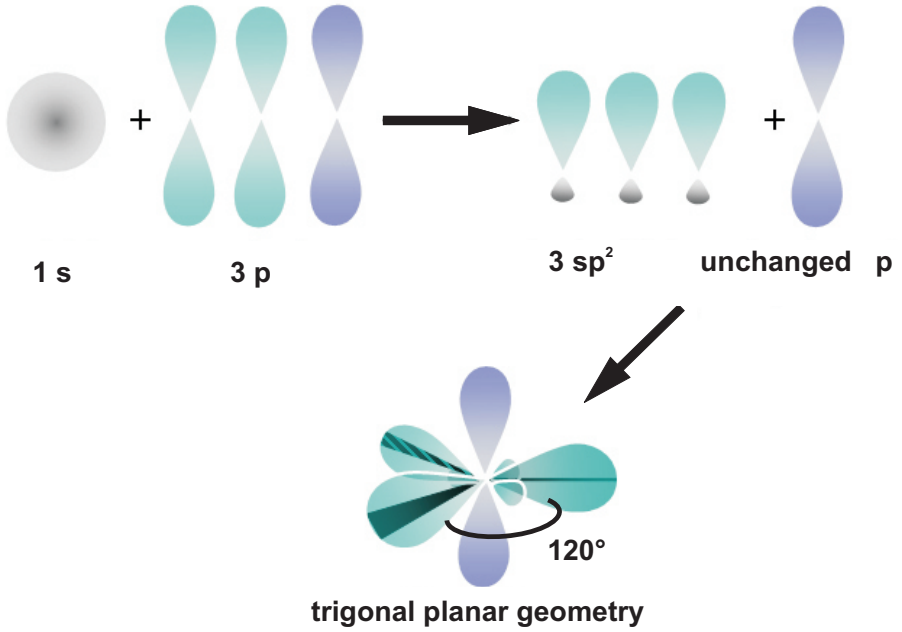

Figure 2.1: The sp^2 hybridization of a carbon atom with the hybrid sp^2 orbitals in a trigonal planar geometry with a separating angle of 120°.

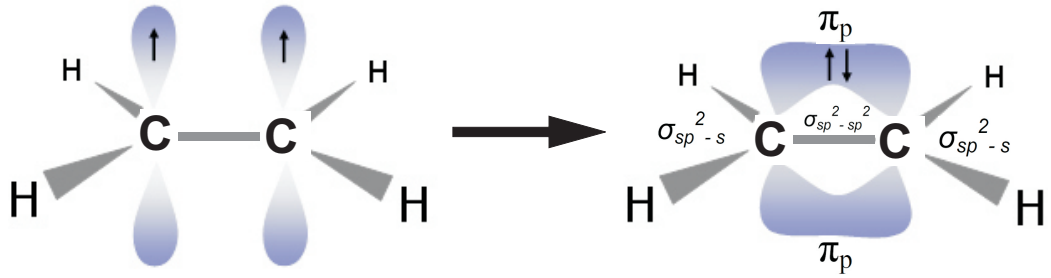

Figure 2.2: The formation of an ethylene molecule gives rise to σ and π-bonds.

Addition of thiophene rings leads to a splitting of the energy levels until a band structure is created containing all discrete energy levels of the polymer monomers. Fig.2.3 indicates that E_g gets infinitely small for increasing n and therefore the conjugated polymers would lose their semiconducting property and would become metallic. This is not observed experimentally and can be explained by the Peierl distortion theory [Pei55]. Due to the introduction of a periodic distortion of the molecules along the

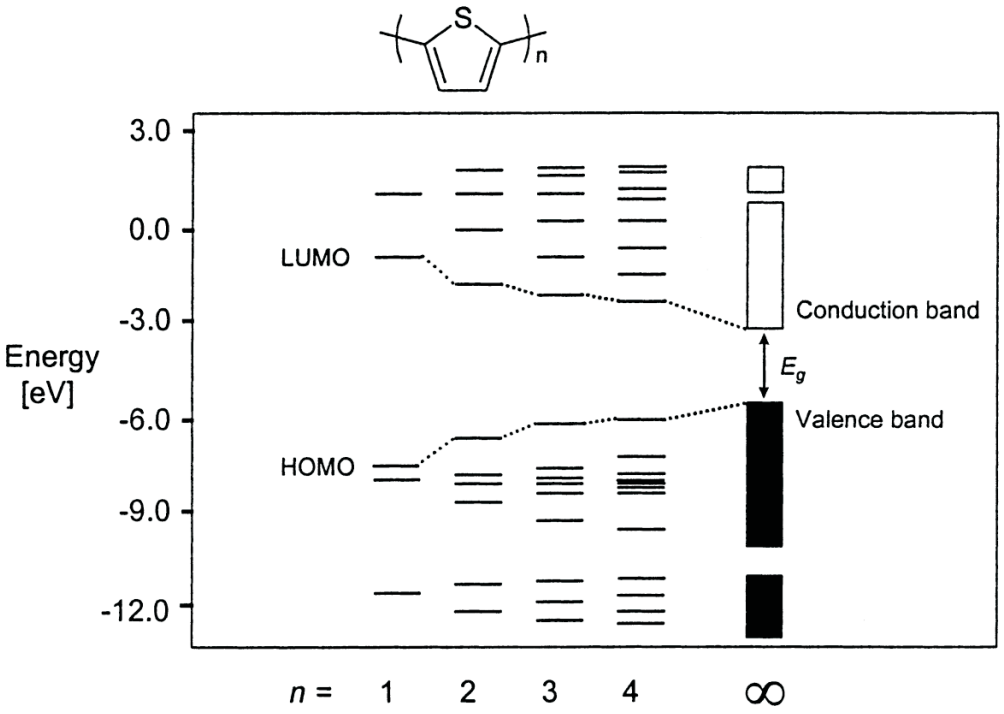

Figure 2.3: Splitting of the energy levels due to the Pauli principle with increasing number n of the thiophene monomer. Picture taken from [Mul01].

polymer chain, an elastic energy is added to the total energy of the system. This problem can be solved in analogy to the basic free electron gas model with a periodic potential, the Kronig-Penney model [Gro12]. In this model, the periodicity of the crystal creates energy band gaps in the E-k diagram at multiples of the value $k = \pi/a$, with a the period length of the system and k the wave vector related to the crystal momentum. A distortion of every second molecule just increases the period length to $2a$. Hence, the displacement, or phonon, leads to the formation of new energy gaps in the Brillouin zone at multiples of $k = \pi/2a$ which lowers the electron energy compared to a undistorted chain. These new bandgaps are indicated in Fig.2.4. In conjugated polymers, these energy savings outweigh the additional cost of elastic energy and lead to the formation of a finite bandgap E_{gap} which is proportional to the amplitude of the periodic potential respective the difference between long and short bonds Δr [Ker95]:

$$E_{gap} \propto \Delta r \tag{2.1}$$

2.1.2 Charge transport

Due to a predominant amorphous character, the charge transport in organic materials is quite different compared to an inorganic semiconductor with a crystalline structure.

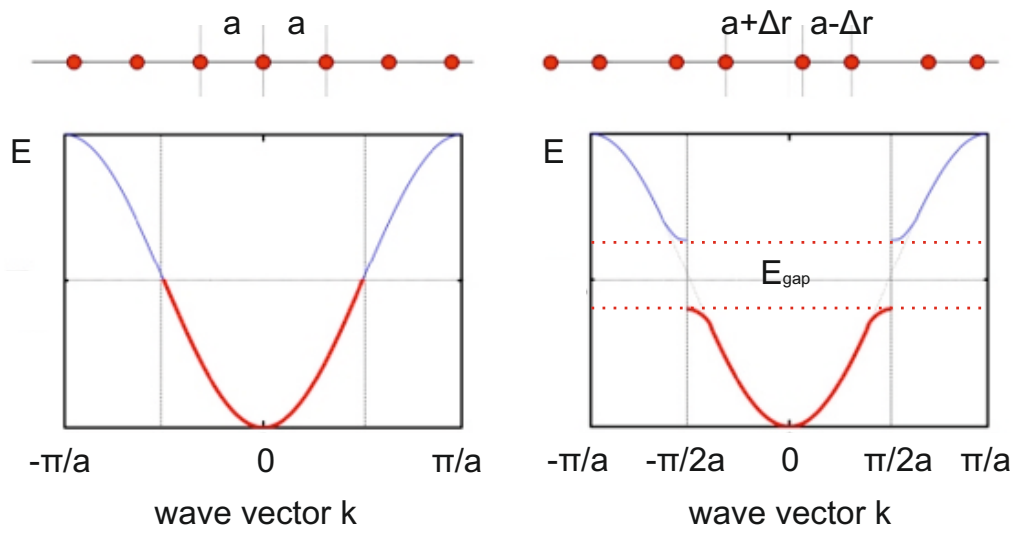

Figure 2.4: The formation of a bandgap due to a periodic distortion Δr after Peierl in the E-k-diagram.

In the inorganic material, the carriers are described by Bloch waves and considered to be quasi-free, disturbed by a periodic potential which gives rise to their bandstructure. In comparison, the polymer represents a 1-dimensional system, but disrupted by structural defects like chain twists and kinks which change the nature of charge carrier transport. The degree of order among the single polymer chains is generally low. An organic material can be therefore considered as amorphous material where the disorder gives rise to a localization of the wave functions. The charge carriers which are involved in the transport along the polymer chain are located in the monomer levels in the HOMO respective LUMO band as shown in Fig.2.3. A sufficiently large number of the single states justifies a statistical model as suggested by Bässler et al. [Bae93]. Here, the density of states $D(E)$ for electrons in the LUMO and holes in the HOMO is expressed as Gaussian distribution:

$$D(E) = \frac{N}{\sqrt{2\pi\sigma^2}} \cdot exp\left(-\frac{(E-E_0)^2}{2\sigma^2}\right) \tag{2.2}$$

N is the density of the monomer states, $E - E_0$ is the energy measured relative to the center of $D(E)$ and σ is the width of the Gaussian density of states.
With this Gaussian shaped $D(E)$, a transport model for the movement of charges between the localized states was developed by Miller and Abrahams [Mil60]. In this model, the transport takes place via tunneling between an initial state E_i to a target state E_j. Because of the quantum mechanical tunneling nature of the charge transport and the dependence on a probability function, this transport process is commonly

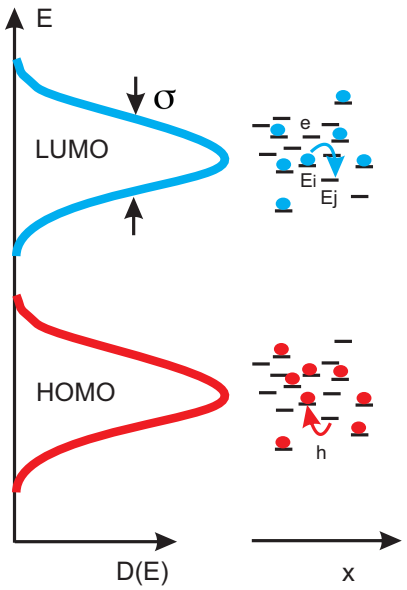

Figure 2.5: The Gaussian density of states for the HOMO and the LUMO level. The electron respective hole hopping from one energy state to another is indicated.

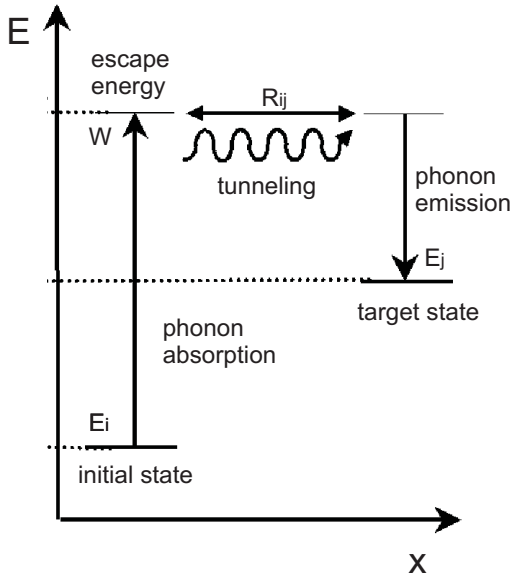

Figure 2.6: The hopping process of the carrier from the initial to a target state involving phonon absorption and emission.

referred to as hopping transport. Generally, the hopping rate is given by [Mil60, Sch02]:

$$\nu = \nu_0 \cdot e^{-2\alpha R} \tag{2.3}$$

Here, ν_0 is the maximum hopping rate, sometimes called attempt-to-escape frequency, α is the inverse localization radius, stating how well charge carriers can tunnel across the distance, and R is the spatial distance between both states.
Since tunneling occurs only for $E_i = E_j$ phonons have to contribute to the process to provide the missing energy. This is indicated in Fig.2.6. For an upward jump to the higher state E_j, an escape energy $W > E_j - E_i$ has to be expended to reach the target state. The phonon absorption probability is approximated by Boltzmann statistics whereas the emission is usually set to 1 [Sch02]. With Eq.2.2, a total transfer rate can be given by an integral over the differential escape rate for all W. In case of a downward jump, Eq.2.3 is valid, whereas for an upward jump only phonon energies $W > E_j - E_i$ are relevant:

$$\nu = \nu_0 \cdot exp\left(-2\alpha R - \frac{E_j - E_i}{k_B T}\right) \tag{2.4}$$

In case of an applied electric field, the site energies include also the electrical energy. Bässler et al. [Bae93] found with Monte-Carlo simulations a dependence of the charge

carrier mobility μ on temperature T and the applied electric field F which was also validated experimentally [Gil72]:

$$ln(\mu) \propto \sqrt{F}, \quad ln(\mu) \propto \frac{1}{T^2} \tag{2.5}$$

The model of Miller and Abraham does not take into account the presence of trap states, in which carriers are trapped and released with certain time constants. Arkhipov et al. [Ark01] reduced the charge transport to a trap-controlled transport with an effective transport level and a distribution of trap states keeping hold of the mobile charges. This model was extended [Mon11, Ram06, Man07] by introducing an exponential density of traps. In [Mon11], Montero et al. take the influence of SCLC (space charge limited current, see section 3.4.1) into account. Here, the trapped population is the charge carrier density n_t in the exponential distributed trap states along the bandgap:

$$n_t(E_f) = \int_{E_c - E_{gap}}^{E_c} D(E_t) f(E_t, E_f) dE_t \qquad D(E_t) = \frac{N_t}{k_b T_t} e^{\frac{E_t - E_c}{k_b T_t}} \tag{2.6}$$

with N_t the effective density of traps, T_t the characteristic trap temperature, $f(E_t, E_f)$ the fermi function, E_t a trap energy level and E_c the transport level.

In organic semiconductors, the transport of charge can involve various quasiparticles in contrast to an inorganic semiconductor. In a crystal, the weak interaction of electrons with the lattice gives rise to an electron quasiparticle which is still considered as an electron but with a different effective mass.
Depending on the arrangement of the σ and π bonds within the disordered conjugated polymer, different electronic ground state configurations are possible. The excited states are then generated by forming of quasiparticles due to the interaction of σ and π bonds. Among the various different quasiparticles, the most important ones are the so called polaron and the more familiar exciton. A polaron is a fermionic quasiparticle carrying charge e, deforming the local atomic geometry, e.g. by changing the nearby bond alternation lengths respective the difference in bond-lengths of two adjacent bonds. In other words, it is a charged particle surrounded by a cloud of phonons. This kind of quasi-particle can not be created in inorganic semiconductors since the crystal lattice is quite rigid.
Another important excitation is the chargeless exciton which is generated by photon absorption or interaction between two opposite charged polarons [Sun11]. It couples strongly to phonons, giving rise to structural deformations. The spin of the exciton is an integer value, for generation by light absorption it is zero (Singlet exciton) due to the spin conservation during the optical transition. Since the photoexcitation brings the electron in a higher state, also spatially, leaving back an equally, but positive charged localized hole, this two particle system can be described using the model of an hydrogen atom. In inorganic semiconductors, the binding energy of an exciton is small due to the coulombic screening by other electrons (high dielectric constant) and the small

effective electron and hole mass. These kind of exciton is also called Mott-Wannier exciton, exhibiting typical binding energies of several meV [Gro12]. The Frenkel-exciton can be found in materials with small dielectric constant ϵ, as conjugated polymers with $\epsilon \approx 3-4$ [Dei10a], and comprises therefore a high binding energy which can be in the range of about 0.5 to 1 eV [Dei10a]. In organic materials, the excitons usually reside on a single polymer chain segment and are called intrachain excitons.
To reach an excited state in the polymer, a pulse of light can be employed. How a typical photoexcitation process in a conjugated polymer looks like, is shown in Fig.2.7 [Dei10b]. After photon absorption, a singlet exciton is generated with an optical gap

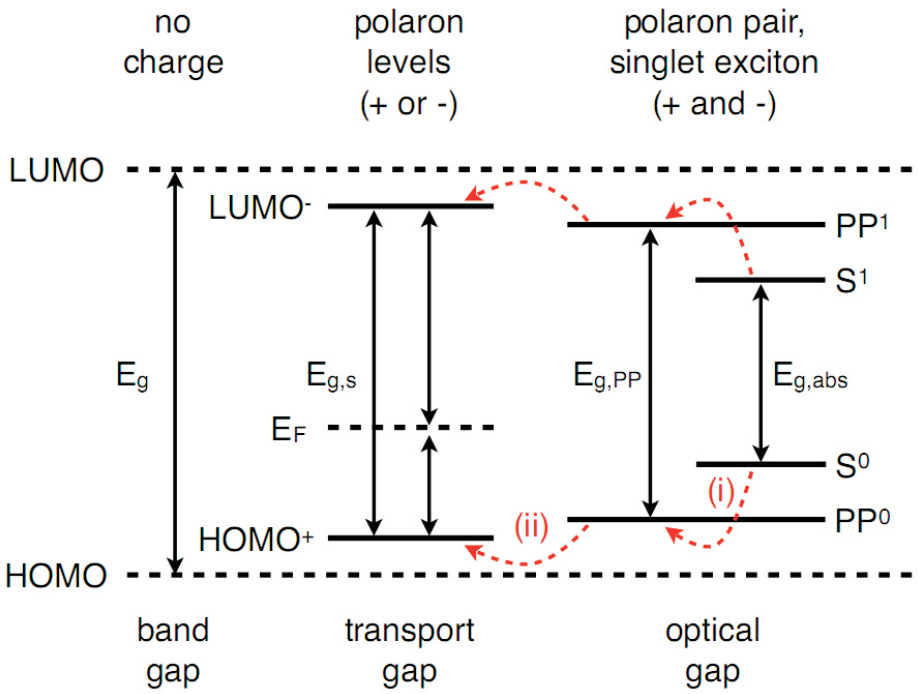

Figure 2.7: Polymer energy levels in the ground state, during charge transport and after photoexcitation. Picture taken from [Dei10b].

$E_{g,abs}$ between the excitonic levels far away from the HOMO and LUMO levels due to the high binding energy. The exciton can either recombine or the charges get separated (see section 2.1.3). In case of dissociation of the exciton (i), a strongly coulombic bound polaron pair of a negative and positive polaron is formed with levels PP^0 and PP^1. For charge transport this polaron pair has to be separated. The dissociation can be described by the Onsager model [Ons38] which gives a probability to separate a Coulomb-bound pair of ions of opposite charge with a given initial distance under the influence of an external electric field. But the model does not take into account the energetic and spatial disorder of a conjugated polymer neither the high local charge

carrier mobilities of a polymer chain [Dei09]. The polaron pair dissociation process is so far not conclusively understood which constrains the finding of a trade-off between photocurrent and open circuit voltage in an organic solar cell [Dei10a].
For charge transportation, after overcoming of the polaron pair binding energy (ii), the single charged polarons are conducted on the polaronic levels separated by a so called single particle gap $E_{g,s}$. The transport takes place by the described hopping transport from one localized state to the next, under influence of an internal or external electric field, until they reach the electrodes. The final step is a charge extraction from the organic material which is influenced by surface recombination and hence carrier concentration at the electrode-organic interface.
Whereas the optical band gap can be measured by absorption, the polaronic transport levels and the transport gap can be accessed by photoelectron spectroscopy [Dei10b].

2.1.3 Bulk-heterojunction

In the previous section the charge transport in an organic material was described, but not the driving force of exciton dissociation. Since the exciton binding energy is in the 1 eV range, thermal energy k_BT is not sufficient. By introducing a second organic material with different HOMO and LUMO levels in a bilayer architecture, the energy can be provided for exciton separation. This is shown in Fig.2.8. The material with a higher LUMO and higher HOMO level is working as electron donor material. A photon which is absorbed in the donor, creates an exciton which diffuses until is recombines or reaches the second material, the electron acceptor. At the interface, the energy is provided for the exciton to be separated since the electron reaches a state with much lower energy. The same accounts for the hole in the HOMO level.
The dissociation process occurs on a very fast time scale of tens of femtoseconds [Hwa08] and is much faster than any competing loss processes like photoluminesence or a transition from a singlet to a triplet exciton. The dissociation occurs only if the energy gain is larger than the exciton binding energy. The energy gain is not the energy offset between the HOMO respective LUMO levels since these levels describe uncharged polymer chains. The relevant energy levels are the PP^0 and PP^1 levels of the polaron pair, see Fig.2.7.

Although the organic active layer can be fabricated quite thin (minimum layer thickness about 100 nm) due to the high photon absorption coefficients of up to 10^7 m^{-1} [Gun07], most excitons recombine in bilayer devices. The reason is the very small exciton diffusion length due to the high exciton binding energy in conjugated polymers, which is usually in the range of 10 nm. For the electron donor P3HT (see section 3.2.2.1) it is only 4 nm [Lue04]. Thus, the donator and acceptor material phases should be chosen with the same dimensions to minimize recombination losses. This concept can be realized with a bulk-heterojunction architecture. Here, the solution processable

donator and acceptor materials are mixed together in their liquid phase to fabricate films with a random nanoscale network of the two phases. This is indicated in Fig.2.9. The interface between both phases is not planar, but spatially distributed over the whole layer. This allows the generation and extraction of excitons in the whole film. The random forming of the network has also certain disadvantages. A percolation path to the respective electrode might not be given. If percolation occurs between both electrodes, ohmic paths in parallel to the diode increase the dark current of a photodiode (see section 3.4.1). In addition, the random forming make the control about the internal structure difficult, but it can be influenced by the choice of the solvents and an annealing step. That the choice of the solvent has indeed an huge impact on device

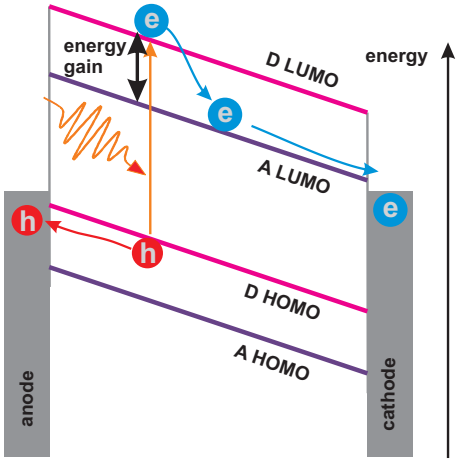

Figure 2.8: Simplified energy diagram of a photon absorption process. A singlet exciton is generated by the photon in the donor phase and dissociated at the acceptor interface. Electron hopping occurs towards the cathode due to an electrical field. The process is concluded by carrier extraction to the cathode.

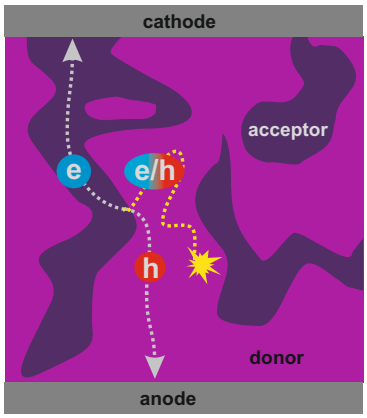

Figure 2.9: Light absorption in a bulk heterojunction. An exciton diffuses until it dissociates at the donator acceptor interface.

characteristics will be shown in section 4.1. Additives to the donator-acceptor blend can also enhance the nanomorphology [Yao08]. Also different fabrication methods result in different device characteristics due to different polymer orientation in the blend [Kre03]. The influence of annealing, which is usually performed at temperatures between 100°C - 150°C, is manifold. Annealing improves the crystallinity of the polymer, by e.g. a more parallel orientation of P3HT chains to each other, and results in a higher carrier mobility [Van06]. The random networking tends to form films with a vertical donor-acceptor phase gradient. This can be disadvantageous in case the concentration of the acceptor is higher at the anode compared to the donor concentration because the electron extraction probability at the wrong electrode increases, resulting in a carrier loss mechanism. Annealing of the organic films reduces the gradient remarkably and can enhance therefore the extraction selectivity [CQ08, Zen10].

The before mentioned term ‘wrong‘ electrode becomes clearer considering the origin

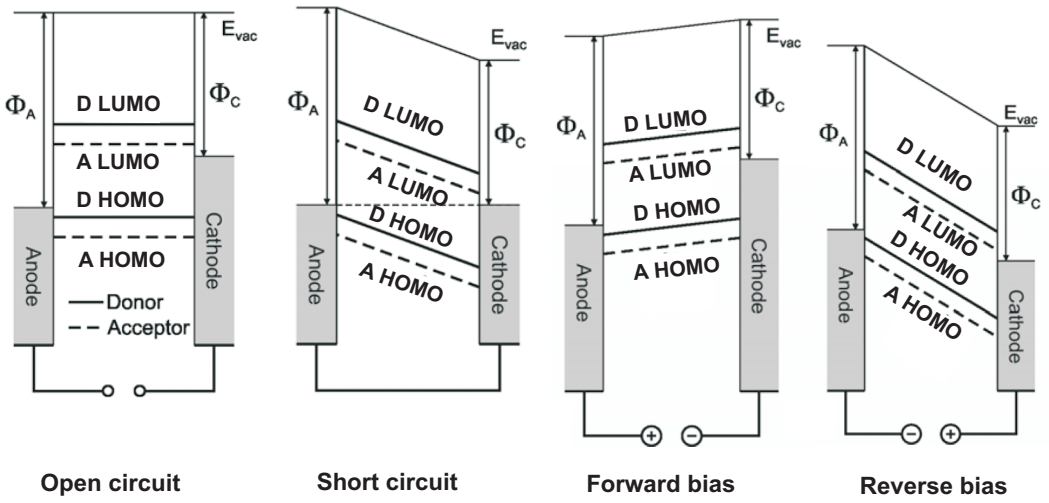

Figure 2.10: Operating modes of an organic bulk heterojunction device with a high work function anode and a low work function cathode.

of the rectification of an organic device, including photodiodes, solar cells and light-emitting diodes. The simplest device architecture is a bulk-heterojunction sandwiched between two metallic electrodes. If the two electrodes are symmetrical, also the IV-characteristic (see section 3.4.1) for forward and reverse bias voltages would show only a weak asymmetry (due to the offsets of HOMO and LUMO levels) which is critical for photodetectors since a high current (without illumination) in reverse bias is related to a bad detectivity (see section 3.4.4). The choice of electrode materials with a similar work function like the acceptor LUMO level (cathode) and the donator HOMO level (anode) increases the device asymmetry for applied bias as shown in Fig.2.10. The first case, the open circuit condition, accounts for applying an external forward bias which is equal to the open circuit voltage V_{oc}. As estimation, V_{oc} is related to the work function difference $\phi_A - \phi_C$ of the electrodes, but the physical origin is more complicated (see section 3.4.1). Since the HOMO and LUMO levels are in a flat band condition, there is no electrical driving force present and hence the current is almost zero.
The short-circuit mode accounts for the absence of an external electrical field. Since Fermi levels adjust themselves to their equilibrium state, a net built-in electric field remains inside the device. Hence, photogenerated carriers can drift under influence of this field to the respective contacts, electrons to the cathode and holes to the anode. Organic solar cells work in this operating mode.
If a forward bias larger then V_{oc} is applied, the charges can be efficiently injected into the blend. Here the asymmetry favors a very high forward current due to the small injection barriers. If the injected charges recombine radiatively, the device is working

as a light emitting diode.
For reverse bias, the injection barrier is very high, and can only be overcome by a small amount of carriers ('dark current') by thermal excitation or tunneling. For photogenerated carriers the situation is different, they are drifted like under short-circuit condition to the respective electrodes. The difference between this two modes arises due to different strengths of the electric field. A high electric field enhance the polaron pair dissociation [Mih04] which increases the photocurrent, and in addition the transit time is increased and hence the photodiode speed (see section 3.4.3).

2.2 CMOS image sensors

This section provides a basic overview about present silicon imaging to motivate the need for hybrid solutions involving organic materials as photoactive layer.
The most important silicon imager technologies, the complementary metal oxide semiconductor (CMOS) and charge-coupling-device (CCD) sensors, are used for various imaging applications ranging from low-cost consumer products like phone cameras to high-end products such as the Hubble space telescope.
Both type of imagers are manufactured in silicon foundries with the same basic materials (silicon, polysilicon, silicon oxide/nitride), but their architecture is fundamentally different. CCD imagers comprise MOS-structures which confine the photogenerated carriers in potential wells. These charge packages are transported sequentially from pixel to pixel. This is a fundamental difference to CMOS-imagers which have a pn or pin junction as photosensitive element. CMOS-imagers which will be addressed in detail in section 2.2.2 and 2.2.3 since they present the base of the development of hybrid sensors.
CMOS-imagers were originally developed in the 1960s [Fos97], but not used commercially because of large pixel size compared to CCD. Not until middle of the 1990s, CMOS reemerged as alternative to CCD due to the following advantages:

- **Low power consumption**: The power consumption of a CMOS-imager is up to factor 100 less than that of a CCD-imager [Big06]. The reason is that CMOS-imagers need only one low voltage supply while a CCD requires multiple voltages for efficient photocarrier shifting between the MOS-potential wells.

- **Lower cost**: The lower costs compared to CCD arise because of the potential of on-chip-integration. Required processing electronics like functions for timing or analog-to-digital conversion (ADC) can be monolithically integrated in CMOS-technology on a single chip. This decreases system size and complexity. CCDs for comparison, require 3-8 supporting chips [Sto02].

- **High speed imaging**: The CCDs are fundamentally limited to the serial read out of the charge packages. With CMOS-technology, an ultrahigh-speed imager

design that increases the frame rate over one million fps (frames/s) [ED09] is feasible.

- **Less blooming**: Blooming is an effect arising due to high illumination which saturates the pixel so that charges are injected also to adjacent pixels. In CMOS-imagers, a so called anti-blooming transistor can be introduced which drains excess photocurrent.

The first generation of CMOS-imagers were so called Passive Pixel Sensors (PPS), referring to the fact that the pixel mainly consists of the photoactive silicon area. By implementing a read-out transistor (source follower amplifier) on the pixel level, a part of the photoactive area got lost but the imager performance could be remarkably increased regarding noise performance [Big06]. This architecture is called Active Pixel Sensor (APS) (see 2.2.3).
Today, the main difference between CMOS and CCD sensors is that the later ones are still the more mature technology, used for high-quality imaging whereas CMOS-imagers are still one their way to be equally competitive in terms of mainly light sensitivity (reduced fill factor, see section 2.2.3) and noise (under a low illumination level) [Big06].

2.2.1 Silicon photodiode

The core of a CMOS-imager is the photosensitive element, a silicon photodiode with a pn-junction. Silicon is the preferred material in CMOS-technology since it is abundant on earth and the fabrication of the crystalline form is cheaper compared to other semiconductors like gallium arsenide (GaAs). In addition, the existence of a native oxide allows an easy incorporation of it as insulator on silicon circuits. GaAs does not provide a stable insulating layer.
Regarding the use as photoactive material, silicon is not an optimal choice due to its indirect bandgap $E_g = 1.12$ eV [Sze69] which decreases the photon absorption coefficient α due the additional phonons involved for conservation of momentum. Starting at the band gap edge at 1.1 µm, α increases to about 10^4 cm^{-1} at about 500 nm wave length (P3HT as comparison, at 500 nm: 10^5 cm^{-1} [Kim06]) and reaches its maximum of 10^6 cm^{-1} at 400 nm wave length due to transition over the zero-momentum gap at 3.4 eV [Sze94]. Since up to this energy, α remains small, and since the light power $I(x)$ of an incident beam decreases in depth x inside the silicon with $I(x) = I_0 \cdot e^{-\alpha x}$, typical absorption lengths $1/\alpha$ are in the range of 1 µm for green wave lengths and 10-100 µm for the higher wave length part (800-1100 nm).

A typical photodiode architecture as shown in Fig.2.11, fabricated with CMOS-technology, exhibits a depletion zone up to a depth of about 2 µm [Cho11] due to limitations of the ion implantation for creating the doped layer. As a result of this non-optimal layout of the pn-diode, most photocarriers are generated deeply in the substrate region and diffuse in all directions. If the exciton diffusion length is not sufficient to reach the

depletion layer where the electric field accelerates holes towards the p-layer respective electrons to the n-doped layer, the carriers recombine and hence the charge collection efficiency is decreased. Especially the long wave length part which can penetrate deeply into the substrate leads to a decreased spatial resolution [Sto02] correlated with cross talk to adjacent pixels. Another drawback arising due to the design is a slow photoresponse because of the slow diffusion movement [Cho11, Sto02].

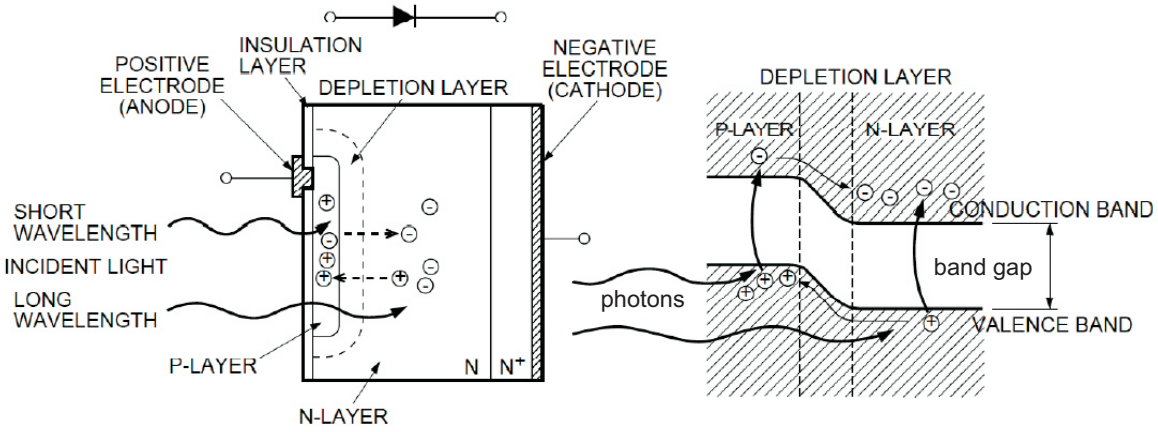

Figure 2.11: On the left side a silicon photodiode is shown with a pn junction created by doping the surface region oppositely compared to the silicon substrate. The on the right side positioned energy diagram shows the pn-junction with the depletion zone. Incident light generates excitons inside the neutral p an n regions as well the depletion zone. In the depletion zone, the electric field accelerates the electrons to the n and holes to the p layer. Carriers in the neutral region can reach the depletion zone within their diffusion length. Picture taken from [ham].

Due to the small pixel size necessary for large pixel arrays, typical illumination levels result in photocurrents in the range of pico- to femtoampere. These very low signals are difficult to detect due to the additional generated noise floor. To ease the readout, the photodiodes are operated in storage mode [Sto02]. The photodiode is biased at a known voltage V_0, and the incident photons cause a voltage variation across the diode for a certain time, called integration time. The longer this time, the more charges are collected and the higher is the voltage change:

$$I_{ph} = \frac{dQ}{dt} = -C(V) \cdot \frac{dV}{dt} \tag{2.7}$$

$C(V)$ is the diode capacitance that is dependent on the applied voltage since for the depletion layer width W account: $W \propto (\Phi_B - V)^m$ [Sze69] with Φ_B the built-in potential and m a coefficient accounting for the junction geometry ($m = 1/2$ for a step junction).

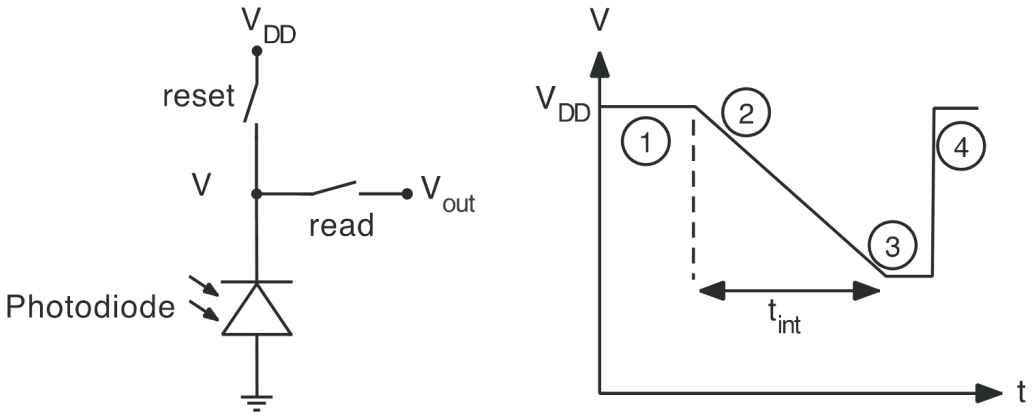

Figure 2.12: The general concept of integrated signal read-out of a CMOS imager.

The integration concept is illustrated schematically in Fig.2.12. The circuit contains a photodiode that should provide after a time $t = t_{int}$ an output voltage V_{out} proportional to the number of accumulated photogenerated carriers. At the beginning (1), the reset switch is closed and a reset voltage $V = V_{DD}$ is applied to the photodiode. The reset switch opens (2) and the photocurrent causes a voltage drop of ΔV during $t = t_{int}$. At (3), the read switch closes and the charge, integrated on the photodiode capacitance and related to the voltage drop, is then output as $V_{out} = \Delta V$ [YP04]. At (4), the read switch is closed again and the reset switch opens. At this point, the circuit returns to the initial state (1).

2.2.2 CMOS-chip architecture

A typical CMOS-imager, as shown in Fig.2.13 consists of:

- **Pixel array**: Mordern CMOS imagers exceed the 1000 x 1000 pixels per array since the pixel size is continuous reduced, currently to about 1 µm [Lee11].
- **Analog Signal Processors (ASP)**: These electronic circuits perform functions such as charge integration over a certain (light) exposure time, noise filtering by correlated-double-sampling, and fixed-pattern-noise (see chapter 6) suppression. Correlated double-sampling refers to a high-pass filter operation to reduce reset noise (see chapter 6).
- **Analog-to-Digital Converters (ADC)**: In Fig.2.13 column-parallel ADCs are shown, connected to every pixel column. An ADC converts the analog voltage signal of the photodiodes to a digital number to allow further signal processing.

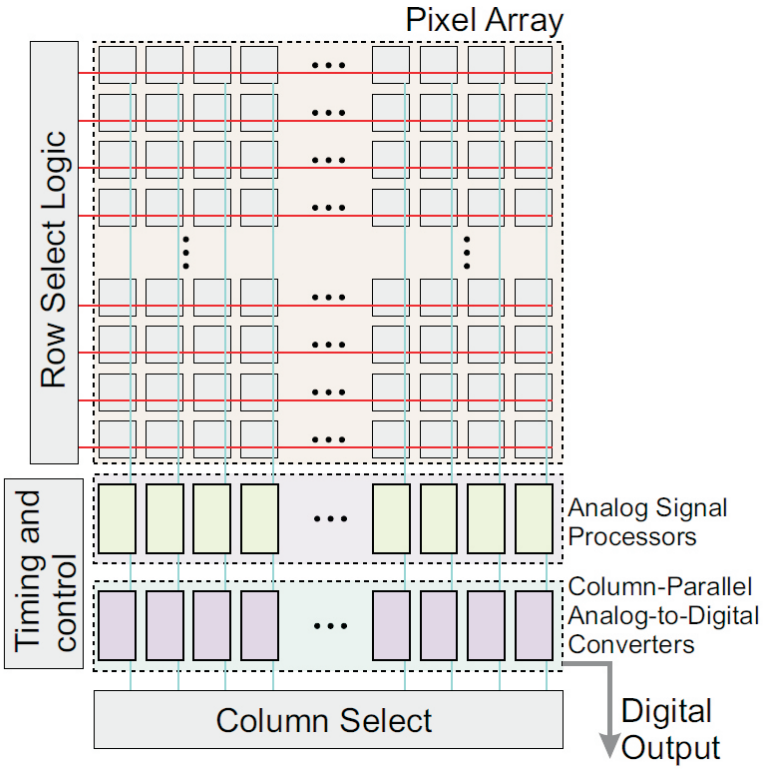

Figure 2.13: A typical CMOS-imager architecture on a silicon chip. Picture taken from [Sto02].

- **Row and column selector**: This logic consists of switches that connect a row of pixels via vertical busses to the ASPs.
- **Timing and control**: The pixel read out and re-initializing requires a precise time-dependent control about the logic operations. In section 2.2.3 this will be further addressed.

Independent on the pixel type (APS, PPS) the most common read-out method is the progressive-scan read out [Sto02]. The row selectors are sequentially activated which initialize the transfer of the pixel signal to the column outputs. A readout register serially shifts the column output values towards the ACDs.

2.2.3 CMOS-pixel concepts

The pixel does not only contain the photoactive area, but provides also some circuitry for the read out. The main sensor types, the passive pixel sensor (PPS) and the active pixel sensor (APS) differ regarding their complexity.
The PPS is a simple circuit as already depicted in Fig.2.12 in the previous section. The read-out is achieved by connecting the photodiode to the column bus, which resets the photodiode voltage and allows the photogenerated charge to flow to a charge

integrating amplifier, which converts the charge to a voltage signal, at the end of the column bus.
An advantage of this approach is, that the PPS exhibits a large ratio of the photoactive area compared to the overall pixel area. This ratio is referred to as (pixel) 'fill factor'. Although the pixel area of a PPS-imager is about 100 % photoactive, the overall photoactive area (including not only the sum of all pixels but also the space in between) can not reach 100 % due to the space needed for the read-out circuitry and additional pixel spacing to avoid cross talk effects (see chapter 6). Hence, for a PPS imager, the overall fill factor is typically in the order of 80 % [Fuj00].
The high fill factor of the PPS leads to a high sensitivity and a high signal-to-noise ratio (for definition of SNR, see section 3.4.2). Nevertheless, several disadvantages limit the performance remarkably. The high capacitance of the metallic bus lines which connect the pixel to the amplifier leads to a readout noise scaling with $\sqrt{C}$ (for reset noise see section 3.4.4) which is about factor 10 higher than in CCD-imagers [Fos97]. The long bus lines also deteriorate the scalability of the pixel area. Since the readout of a pixel column is of serial nature (e.g. one amplifier for one column), the readout speed is decreased resulting in decreasing image capture times for increasing the pixel array. To overcome this problem, the APS was developed. Here, a read out amplifier

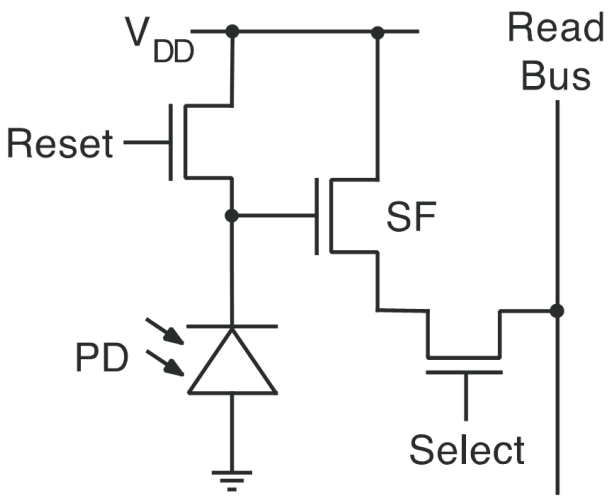

Figure 2.14: A T3-APS architecture

is incorporated in addition to the photodiode to each pixel. Hence, since the amplification is performed inside the pixel, this sensor type is less affected by reset noise. The simplest architecture, a T3-APS, is shown in Fig.2.14. It contains a MOSFET as reset transistor to initialize and reverse bias the photodiode with V_{DD}. The charge integration in the photodiode occurs during an integration time. The process is continued by switching on the row-select transistor which connects the amplifier transistor in the selected pixel to its load to form a source follower (SF). The photodiode charge is thus converted into a voltage by the source follower operation and can be read out via the

column bus. This amplification allows to observe the pixel voltage without removing the accumulated charge.
Although the APS-sensor provides a better performance compared to a PPS, it has a major drawback due to the reduced fill factor. Since the electronic circuits are laterally implemented in CMOS-technology (e.g. doping via ion implantation of the substrate) and shadow the light incidenting on the silicon, the photoactive pixel area is reduced by the number and lateral dimensions of the electric components inside the pixel. For a typical APS, the pixel fill factor is only in the range of 30 % instead of up to 100 % in PPS- and CCD-imagers [Big06].
The reduced photoactive area has an impact on sensitivity as well as the signal-to-noise ratio. Since the sensitivity of a pixel can be expressed as product of fill factor and its quantum efficiency it is decreased linearly by the fill factor. Besides, a low fill factor limits the scaling perspective of the pixel. A smaller pixel exhibits a smaller capacitance which can store less carriers. Since the shot noise (see section 3.4.4) increases by $\sqrt{N}$ with the number of photogenerated carriers N, the signal-to-noise ratio $N/\sqrt{N}$ (see section 3.4.2) is reduced for small N.
Hence, one of the main research topics of CMOS-imagers concerns the improvement of the fill factor. A common method for increasing the fill factor is to employ microlens-arrays on top of the pixel to focus the incident light on the photoactive area [YTF00, Iid97]. With this processing step, the fill factor can be increased up to 90 % [Big06]. A fill factor of almost 100 % can be reached by a vertical deposition of photoactive amorphous silicon on top of an ASIC-readout circuit [Lul99, Lul00, Sch98]. An alternative is also to transform the CMOS-imager from a front-side to a back-side illuminated imager. By thinning the substrate to a thickness in the range of the absorbance length of the photons, the opaque circuitry on the front side can be avoided [Pai05]. All these methods have in common that they are expensive due to the additional amount of processing. In addition, the down-scaling perspective might be limited.

Chapter 3

Solution-processed organic photodetectors

This chapter will give the reader information about the build-up of OPDs as well as about the methods involved in fabrication and organic layer treatment of the devices. The most important photodetector performance characteristics are defined and a description about the setups used for measuring them is included.

3.1 The organic photodetector build-up

3.1.1 Layer stack

The most simple build-up of an OPD consists of the photoactive material sandwiched between two electrodes, as also described in section 2.1.3. To improve the performance of the OPD, usually interlayers are additionally introduced to improve carrier injection into or extraction out of the photoactive layer. In this thesis, an interlayer of Poly(3,4-ethylenedioxythiophene):poly(styrenesulfonate) (PEDOT:PSS), described in chapter 3.2.3, is used to suppress electron conduction to the anode and with it also the dark current flowing in the device. On this impact is also reported in section 4.1.5.
The different materials are enclosed by electrodes with a low and a high work function, see section 3.2.4 and 3.2.3. In this thesis, either indium tin oxide (ITO), gold or conductive PEDOT:PSS was used as high work function material and aluminum as the low work function cathode.
Different build-ups are possible depending on the particular application. The most common layer stack starts with a transparent substrate, either glass or a flexible foil, and ITO as bottom electrode. The low work function cathode completes the stack, as depicted in Fig.3.1. This build-up was deployed in this thesis mainly in section 5.3.1.

Another concept which can be found in literature concerns inverted photovoltaic devices in which the roles of the electrodes are exchanged by introducing an electron selective contact on top of the ITO electrode. For this concept, an improved photocurrent generation can be observed due to a favorable vertical material phase segregation [Wal06].
A different inversion can be achieved by flipping the whole layer stack, starting with the low work function cathode and concluding with the high work function anode, as depicted in Fig.3.2. This inversion of the fabrication steps is appealing mainly for flexible organic solar cells [Lun07, Na08] since the brittle and expensive ITO conventionally used as bottom electrode can be replaced by a metal deposited with a cost-efficient roll-to-roll process [Kre09, Ahn08, SR00].
In this thesis, the main focus was on this inverted layer-stack since it can be integrated onto a CMOS-chip. With an inverted layer stack the aluminum layer of the CMOS top metalization acts also as bottom electrode of the OPD. An additional advantage is that transparent and conductive high work function materials, as PEDOT:PSS (see section 3.2.3 and 4.3) can be used as top contact, changing the device henceforth from a bottom to a top absorbing photodetector as it is necessary when using opaque substrates like silicon.
The build-up of the OPD, regardless which layer stacking concept is used, is concluded by an encapsulation to protect the organic layers from reacting with oxygen and water which leads to a degradation of the device performance, see section 4.5.

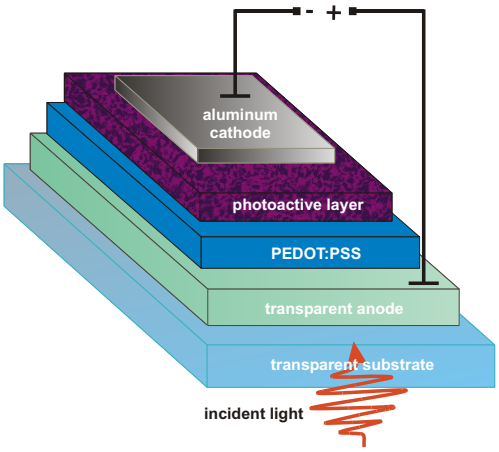

Figure 3.1: Conventional build-up starting with a transparent substrate, followed by an ITO anode, the hole conductor PEDOT:PSS, the photoactive layer and the top cathode material.

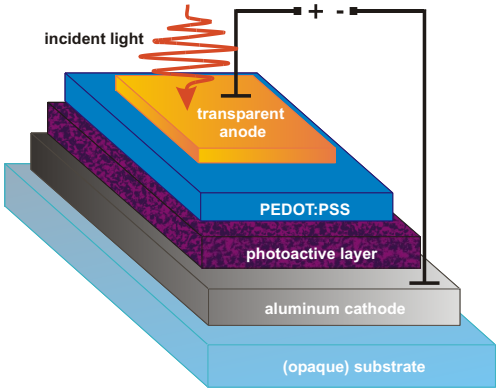

Figure 3.2: The inverted layer-stack forming a top-absorbing photodetector.

3.1.2 Diode layout

The photoactive area of the diode is laterally defined as the overlapping area between both electrodes since the diffusion length of photogenerated carriers parallel to the organic layers is in the range of only a few micrometers which will be discussed in section 6.2.3, addressing pixel-to-pixel crosstalk.
In this work, most organic photodetectors were fabricated as large scale devices on glass substrates with a dimension of 2.5 x 2.5 cm^2. In Fig.3.3 two typical layouts with the inverted as well the non-inverted layer stack are shown. Through a metallic shadow mask eight metallic electrodes with a lateral size of 7 mm^2 are thermally evaporated onto the substrate. The other large scale electrode, only sparing the part of the substrate on which the eight counterelectrodes are electrically contacted, is either evaporated (aluminum or gold) or spin-coated (conductive PEDOT:PSS).

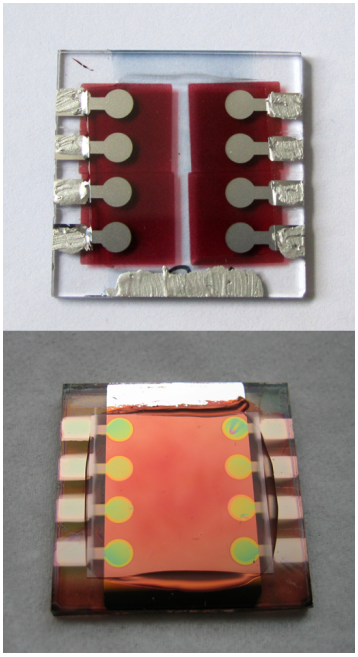

Figure 3.3: Large scale photodetectors:
bottom: an inverted spincoated detector with eight gold top electrodes (anodes)
top: a non-inverted sprayed detector with eight aluminum top electrodes (cathodes).

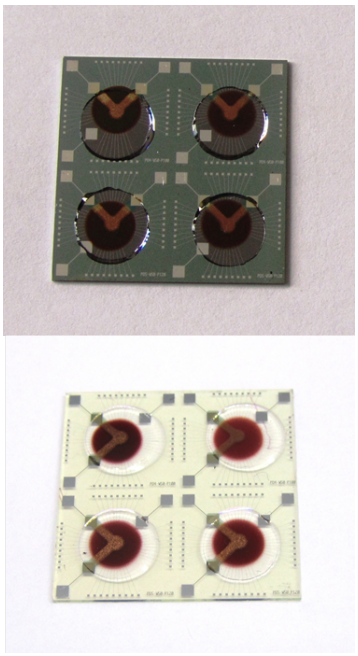

Figure 3.4: Four sprayed arrays of photodetectors on either glass or silicon substrates. Each array, consisting of 36 pixels, is covered by a sprayed organic spot and a thermally evaporated gold electrode.

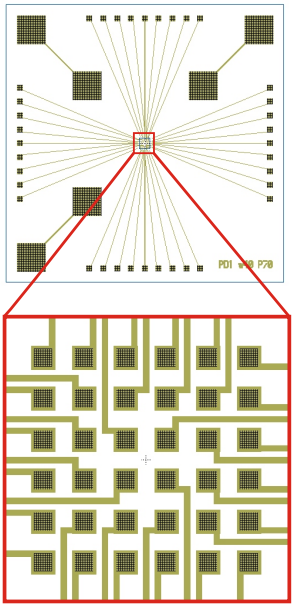

Figure 3.5: Layout of the CMOS test structure:
top: the whole, 1 cm^2 big structure, consisting of the array, the wires and contacting pads for the aluminum cathode and the gold top electrode.
bottom: the enlargement of the array in the middle of the structure, consisting of 36 photolithographically defined pixels.

To validate the organic deposition processes before implementing them on top of CMOS-chips, test structures (see Fig.3.4) with similar active area sizes were fabricated using CMOS compatible methods and materials. As substrate either glass or silicon was used. The layout of the test structure, defining the geometry of the aluminum cathode, is depicted in Fig.3.5. The structure, with an overall dimension of 1 cm^2, consists of an array of 36 square shaped pixels with pad sizes varying from 40 to 70 µm and gaps in between varying from 30 to 100 µm.
The pixel dimension on the test structure is too small to allow a metal deposition through an aluminum mask as used for large scale detectors. This is due to the fact that shadowing effects of the metal mask with a thickness of about 500 µm would prevent a homogeneous deposition on the substrate. Instead, a photolithographical definition of the structures with a photoresist was necessary. The contacting lines, connecting the array to the outside contacting pads (200 µm pad size), are passivated with a thin layer of SiN to guarantee that only the pixel themselves overlap with the large scale top gold electrode to allow a precise definition of the photoactive area.

3.2 Materials for organic photodetectors

3.2.1 Solvents

The choice of the solvent to dissolve the conjugated polymers is critical to the device performance since the solvent influences the film formation during the drying process. In general, conjugated polymers are soluble in aromatic hydrocarbons like toluene, dichlorobenzene (DCB) and xylene which were mainly used in this thesis. High boiling point solvents like (di)chlorobenzene are known to lead to improved mobility and henceforth device efficiency due to a better crystallisation of the photoactive polymers achieved by the slow drying of the films. A review is given in [Li07].
Also in this thesis better results of spin-coated OPDs (EQE and dark currents), see section 4.1.4 were achieved by the use of 1,2-DCB, but this is believed to originate from the higher photoactive layer thickness. Due to the slower evaporation of the solvent during spincoating, also lower spin speeds which result in increased layer thickness lead to the formation of homogeneous films. A thick photoactive film increases the amount of absorbed photons as well as the shunt resistance which decreases the dark current due to the reduction of leakage paths through the bulk heterojunction. The choice of the solvent influences the nano-scale distribution of donator and acceptor materials as reported in [Aud10, Yao08]. In section 4.1.4 it will be shown that this can have a huge impact on device interface properties.
For different organic deposition methods, different organic solvents can be favorable, as will be shown in section 5.2.1, since also solvent properties like viscosity and surface tension influence the layer formation. An overview of important solvent properties is given in Tab.3.1. The surface tension values are taken from [Jas72], the other properties

are information given by the manufacturers.

Table 3.1: Parameters of typical solvents

Solvent	Toluene	1,2-Dichlorobenzene	Xylene
Boiling point (° C)	111	180	140
Density (g·cm^{-3})	0.87	1.32	0.87
Surface tension (mN/m @ 20° C)	27.9	35.4	28-29.8
Viscosity (mPas @ 20° C)	0.56	1.32	0.6

3.2.2 Photoactive materials

3.2.2.1 P3HT (Regioregular poly(3-hexylthiophene))

Polythiophenes emerge from the polymerization of a sulfur heterocycle, called thiophene, and can be functionalized with a huge variety of substituents. The conjugated polymer P3HT is generated by adding a hexyl group as the side chain of the thiophene ring, see Fig.3.6.

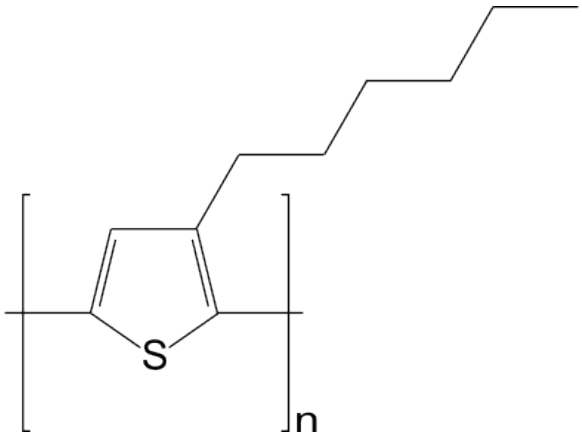

Figure 3.6: Molecular structure of the polythiophene P3HT.

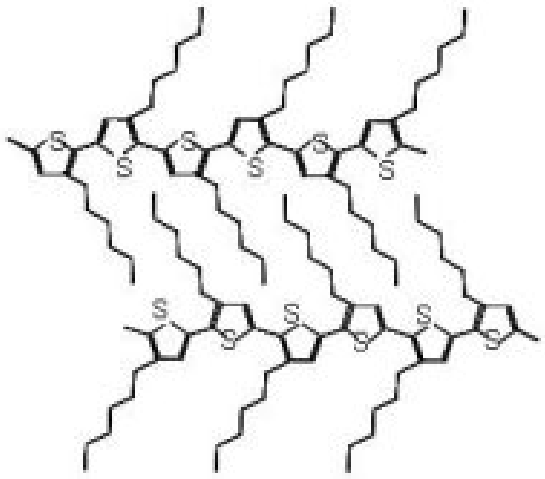

Figure 3.7: Interdigit structure of regioregular P3HT.

Depending on the position of this side chain, when single monomers are attached to each other two basic configurations are possible, the so-called regioregular P3HT (rr-P3HT), depicted in Fig.3.7 and the regiorandom P3HT (rra-P3HT). For device applications, the rr-P3HT is preferred since its flat structure and the chain orientation enable the formation of an interdigitated network of the P3HT polymers, as shown in Fig.3.7,

which increases the degree of crystallinization. As a result, the charge carrier mobility is increases compared to rra-P3HT [Pan00]. The monomer coupling regularity of the rr-P3HT used in this thesis is 95 %. A further increase of the amount of regioregularity would increase the charge carrier mobility, but this effect is not observed when blending the P3HT together with a electron acceptor like PCBM forming a bulk-heterojunction [Mau10].
The HOMO and LUMO levels of P3HT are at 3.0 eV respective 4.9 eV [Shr06] which turns the P3HT to a electron donator and hole acceptor material in a P3HT:PCBM bulk-heterojunction. Here, typical hole mobilities are in the order of $1 \cdot 10^{-6}$ cm^2/Vs [Cai07].

3.2.2.2 PCBM ([6,6]-phenyl-C_{61}-butyric acid methyl ester)

PCBM is a derivative of the fullerene C60, consisting of 60 carbon atoms ordered in a shape similar to a football. Although evaporated C60 films show high electron mobilities up to $8 \cdot 10^{-2}$ cm^2/Vs [Had95], the material cannot not be used in solution-processable electronics due to low soluability in common aromatic solvents. To overcome this problem, the C60 is functionalized with a methyl-ester-group, as indicated in Fig.3.8. The LUMO level of PCBM is 3.7 eV and the HOMO level 6.1 eV [Shr06]. Blended with P3HT, PCBM acts as electron acceptor material with electron mobilities around $1 \cdot 10^{-7}$ cm^2/Vs [Cai07].

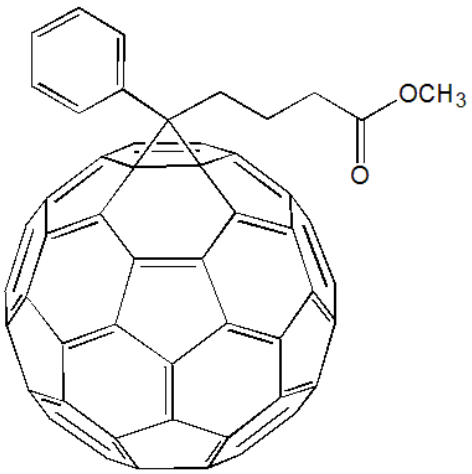

Figure 3.8: Molecular structure of the fullerene derivative PCBM.

3.2.2.3 Squaraine

The standard bulk-heterojunction of PCBM:P3HT exhibits photon absorption up to a wavelength of about 650 nm, respective 900 nm, taking the low absorption of PCBM

up to this wave length into account which can be only exploited for devices when applying high external bias [Che10]. In chapter 4, Fig.4.21, showing a typical spectral PCBM:P3HT photodetector quantum efficiency, the low PCBM absorption is visible around 700 nm wave length.
For organic solar cells, a sensitivity in the near-infrared (NIR) part of the sun spectrum would enhance the power conversion efficiency. Also for organic photodetectors sensitivity beyond the visible part of the spectrum (390 nm - 750 nm) would enable a range of applications. Among these is the active night vision, which refers to the active illumination of objects with NIR light. It is interesting for security and military applications and is also applied by the automotive industry [Luo10].
As also motivated in the introduction, the phenomenon called 'night-glow' between 1200-1800 nm in the earth atmosphere, is also an interesting option for NIR imaging with security cameras.
The NIR wave length range is also interesting for optical fiber communication since the attenuation in the fibers due to Rayleigh scattering is strongly decreased with increasing wave length. At about 600 nm wave length the attenuation is about 10 dB/km and is decreased to about 1 dB/km at 1000 nm with attenuation minima at 1.3 µm and 1.55 µm.
In contrast to the demand of NIR-devices, there exist only a few families of low-band gap polymers since a synthetization of large scale quantities that are sufficiently pure for incorporation in devices is as challenging as providing sufficient solubility for processing and a long term stability. Reviews of the synthetization of different conjugated polymers are given in [Kre07, Ron07].
Furthermore, only a few materials are sensitive beyond the absorption edge of silicon which is especially interesting since this would enable the realization of cost effective NIR detectors as alternative to expensive detectors based on III/V-semiconductors, as reported in [Gon09].
In this thesis the NIR sensitive organic dye squaraine was valuated regarding the suitability of integration into the hybrid imager. Squaraine [Bev10, Bin09, Bin11, Wei10], a condensation product of electron rich molecules with squaric acid, is know for an efficient NIR absorption from the red up to about 1000 nm and good stability against oxygen and water [Sil08]. Amongst various possible substituents around the squarylium core, in this thesis hydrazone end-capped symmetric squaraines with a glycolic functionalization chain was chosen [Bin09, Bin11], see Fig.3.9. The glycolic chain, indicated in Fig.3.9 as R, is necessary to guarantee a good soluability in aromatic solvents. Furthermore the glycolic chain enables a proper mixing capability with PCBM [Bin09] which acts as electron acceptor when blended with squaraine (HOMO: -3.3 eV, LUMO -5.0 eV). This enables the fabrication of efficient bulk-heterojunction detectors with electron mobilities of about $6 \cdot 10^{-6}$ cm^2/Vs and hole mobilities of about $2 \cdot 10^{-6}$ cm^2/Vs [Bin11].

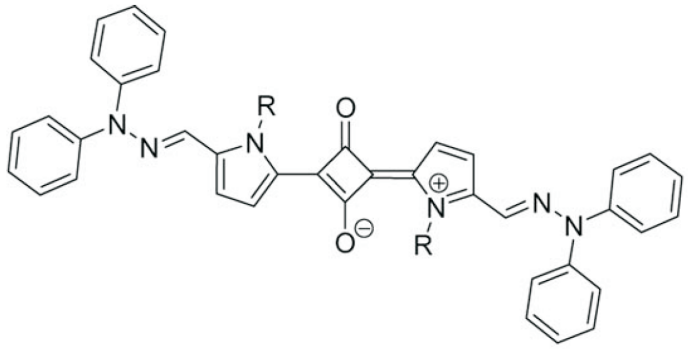

Figure 3.9: Molecular structure of a hydrazone end-capped squaraine dye.

3.2.3 PEDOT:PSS (Poly(3,4-ethylenedioxythiophene) poly(styrenesulfonate))

Poly(3,4-ethylenedioxythiophene):poly(styrenesulfonate) or PEDOT:PSS is a polymer which is widely used in organic photovoltaics. It contains the conjugated polymer PEDOT which is based on polythiophene. In its pure form, PEDOT is not soluble in common solvents. This problem has been solved by polymerization of PEDOT in the presence of the water-soluble poly(styrenesulfonic acid) (PSS) to produce the aqueous dispersion PEDOT:PSS. The chemical structure of PEDOT:PSS is represented in Fig.3.10.
PEDOT itself is not intrinsically conductive since the p-conjugated carbon chain does not conduct. But doped with PSS it becomes a p-type semiconductor with a conductivity which is controlled by the excess amount of PSS in the solution [Kir05, Cri03]. Depending on the bulk resistivity, ranging from about $1 \cdot 10^5$ Ohm·cm down to values comparable to a metal, different applications of PEDOT:PSS are feasible.

3.2.3.1 PEDOT:PSS as interlayer

PEDOT:PSS is widely used in organic solar cells, light emitting diodes and photodetectors as interlayer between the electrode and the photoactive respective emitting layer of the device. An advantage of the PEDOT:PSS-interlayer is that hole extraction and injection properties to and from the active layer are improved which leads also to a higher quantum efficiency. For the improved device performance of an organic photodetector with a PEDOT:PSS interlayer different reasons can be found in literature although many are related to conventional devices with an ITO bottom electrode. The high work function (5.2 eV) of PEDOT:PSS allows the formation of an ohmic contact with most common donor polymers and with the ITO anode by reducing energy barriers [Bro99] to allow effective charge injection and extraction. Secondly, it is reported

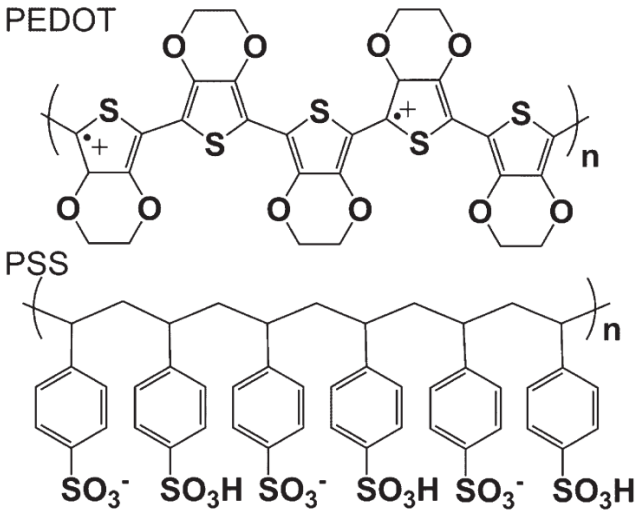

Figure 3.10: Molecular structure of PEDOT and PSS.

that PEDOT:PSS can be used to planarize the ITO anode which can exhibit superficial spikes [Lim11, Fri09]. This planarization also explains the lower dark current for photodiodes with an ITO anode observed when inserting a PEDOT:PSS interlayer [Fri09]. For an inverted diode with the PEDOT:PSS on top of the photoactive layer, this explanation does not account. The author supposes that in this case the PEDOT:PSS covers the low-resistance pathways (like pure phases of either donator or acceptor material) through the photoactive film, suppressing therefore electron transport between the two electrodes since the PEDOT:PSS is an electron blocking layer. This assumption is confirmed by the fact that only the use of high resistive PEDOT:PSS formulations lead to a significant reduction of the dark current. In section 4.1.5 the impact of the insertion respective the abstinence of a PEDOT:PSS interlayer will be investigated.
In this work, for the PEDOT:PSS interlayer the formulation Clevios P VP CH 8000 by H.C. Starck was used. It exhibits a bulk resistivity of about $1 \cdot 10^5$ to $3 \cdot 10^5$ Ohm·cm.

3.2.3.2 PEDOT:PSS as electrode

By decreasing the amount of PSS the conductivity of PEDOT:PSS formulations could be significantly increased during the last years, currently culminating with the formulation Clevios PH 1000 by H.C. Starck in the year 2010. Conductivities up to 1400 S/cm are reported [Kim11]. This increase of conductance is not an intrinsic feature of the formulations but has to be activated by adding high boiling solvents like ethylene glycol (EG), glycerol, dimethyl sulfoxide (DMSO), N-methylpyrrolidone and sorbitol [Ouy05, Cri06, Wan05, Na09, Kim11] which increase the conductivity of dried PEDOT:PSS films by several orders of magnitude. The origin of the enhancement of conductivity in the treated PEDOT:PSS films is believed to arise from both

the morphological changes and the more uniform distributions of PEDOT-rich regions throughout the PEDOT:PSS films. The high boiling point solvents remove the insulating PSS partly and increase therefore the contact areas between the conductive PEDOT grains to form highly conductive pathways [Na08, Na09, Kim11].
In section 4.3 the fabrication of highly conductive PEDOT:PSS films by adding ethylene glycol is investigated.

3.2.4 Electrical contacts

Materials have to fulfill certain requirements to be suitable as electrode materials for organic photodetectors:

- low sheet resistance for low serial resistance of the device
- transparency of at least one electrode
- low roughness of the bottom electrode
- high work function for the anode, low work function for the cathode
- stability against chemical reactions with other device layers and against oxidation
- low cost and unlimited availability

There exist a range of metals available suitable as anode and cathode materials, but a drawback is their low transmittance which decreases also the external quantum efficiency of the device. Additionally their processing is costly, since high temperature and vacuum involving thermal evaporation (see section 3.3.1) is used.
In this work, aluminum with a work function of 4.3 eV [Mic77] was used as cathode material for the inverted as well the non-inverted photodetector. Since it is a low work function material, surface oxidation can occur and alter the device characteristics (see section 4.2).
Due to the free moving of electrons in a metal, the electrons screen the electric field of the incident light effectively, thus even very thin layers suppress light effectively. A 20 nm thin film of gold (work function 5.1 eV [Mic77]), used as anode material, transmits only about 50 % of green light, see section 4.3.
A common used anode material with high transmittance (90 % for the visible spectrum) and low resistance (down to 5 Ω/sq.) is indium-tin-oxide (ITO). The drawback of this material is the limited availability of the indium which increases the cost of ITO. A low cost and solution-processable alternative, a conductive version of the PEDOT:PSS, was investigated in this work as reported in section 4.3 and 3.2.3.
The work function of electrode materials has to be chosen similar to the HOMO respective LUMO level of the organic polymers. For an organic solar cell this is important since the difference of the work function has an impact on the open-circuit voltage. For an organic photodetector this has almost no relevance since a photodiode is driven in

reverse bias much larger than the internal field generated by the difference of the work functions.
For a photodetector, the mismatch of work functions to polymer energy levels has a big impact on the device performance. It can enhance electron injection from the anode into the organic layer which increases the dark current [Xue04]. Applying a reverse external voltage, the polymer LUMO level bends downwards and enables Fowler-Nordheim-tunneling of electrons from the anode trough the triangular shaped energy barrier to the polymer. The lower the anode work function, the higher is the tunneling probability.

3.3 Fabrication of organic photodetectors

The major strength of solution-processable organic electronics is the availability of cheap and renewable materials and the low-cost fabrication since no vacuum or high temperature processing steps are required. The organic materials can be deposited with spin-coating, see section 3.3.2, and spray-coating, see section 3.3.3 which is also suitable for implementation on large-scale substrates. Furthermore, the solution-processability allows a continuous fabrication line, a so called roll-to-roll processing [Bla09, Kre09], which can be implemented with deposition methods like spray-coating, ink-jet-printing [Hot07] and slot-die-coating [Bla09, Kre09]. Only the electrodes are critical regarding cost-efficient deposition and can be in addition resource-limited, like ITO. In a polymer solar cell the ITO anode is accounted for 30 % of the overall module cost [Kre09].
Also the deposition of the metal cathode can be implemented witout the use of a vacuum coating step, e.g. with solution-processable silver nanoparticles [Kre09].
A processing step which can increase the overall cost is the packaging which has to encapsulate the organic materials carefully to avoid the segregation of oxygen and water which react with the organics and cause a device performance degradation, see section 4.5. Related to that, for long term stability an entire processing in an inert atmosphere might be necessary to avoid the contamination with oxygen and water during the fabrication. In this work, the spin-coated devices were fabricated in a nitrogen filled glovebox system of the company MBraun.

3.3.1 Electrode deposition by thermal evaporation

For the deposition of metallic electrodes for organic devices resistive thermal evaporation is commonly used since it allows a thickness control in the range of a few nanometers as well as a precise evaporation rate adjustment below one angstrom per second. The basic working principle of the thermal evaporation is the resistive heating of the material inside a container, a so called ‘boat‘.
A schematic drawing of the setup is shown in Fig.3.11. By applying a sufficiently high

electrical current through the boat, usually consisting of tungsten, the solid metal starts to evaporate inside the evaporation chamber which is evacuated down to a pressure of about $5 \cdot 10^{-7}$ mbar. The low pressure guarantees a long mean free path of the atoms so that they can reach the substrate. In addition, the low amount of residual gases enables the fabrication of metal films with low contamination.
The evaporation rate of the metal atoms is determined by the current flowing through the boats and monitored by the change of the eigenfrequency of an oscillating quartz crystal. Since this quartz and the substrate are located at different places inside the evaporation chamber, the spatial ratio of the rate differences, the so-called tooling factor, has to be precisely measured (e.g. with an AFM, see section 3.4.5.2) for the different metals used for evaporation. To reach a stable evaporation rate, the material is heated in several steps with pauses in between to enable a homogeneous heat distribution inside the material. After reaching a stable evaporation rate, the shutter protecting the substrate during the heating phases is removed and kept open until the quartz crystal measures the desired layer thickness. For a homogeneous material deposition on the substrate, a rotating substrate holder is used.
The optimal evaporation rate depends on several factors, including the geometry of the whole setup, and a general recommendation cannot be given. In [Lee04] it is reported that an increase of the evaporation rate of aluminum from 0.3 A/s to 1.5 A/s leads to a better device performance of an OLED due to a decreasing amount of nitrogen incorporated into the metallic films and a less rough morphology. Also in this work, a significant change of the aluminum roughness was observed when increasing the rate from 1 A/s (about 7 nm RMS-roughness) to 10 A/s (about 2.5 nm RMS-roughness). However, a high deposition rate is also related to a high temperature generated at the boat which can be radiated to the substrate and can decompose the organic materials. A clear dependence of theses factors was not observed regarding the organic photodetector device performance. For the deposition of the aluminum cathode for the inverted devices on the glass substrates, a high deposition rate of 10 A/s was chosen to keep the electrode roughness low to decrease the amount of leakage paths through the organic layers. For the deposition on top of the organic layers in a non-inverted device, 1 A/s was used to keep the thermal budget on the organic layers as low as possible.

To define the electrode area, two different methods were used, depending on the structure size. For a structure size down to about half a millimeter, a metallic shadow mask was used to shield the substrate where no material should be deposited. Since a typical mask is about 500 to 700 µm thick, a certain area inside the structure is ‘shadowed‘ by this barrier. Therefore, a thinner mask has to be used which allows also the lateral definition of structures down to 10 µm as necessary for the CMOS test structures in section 3.1.2. For the generation of such a mask, a photoresist was spincoated on top of the substrate and structured by means of photolithography.

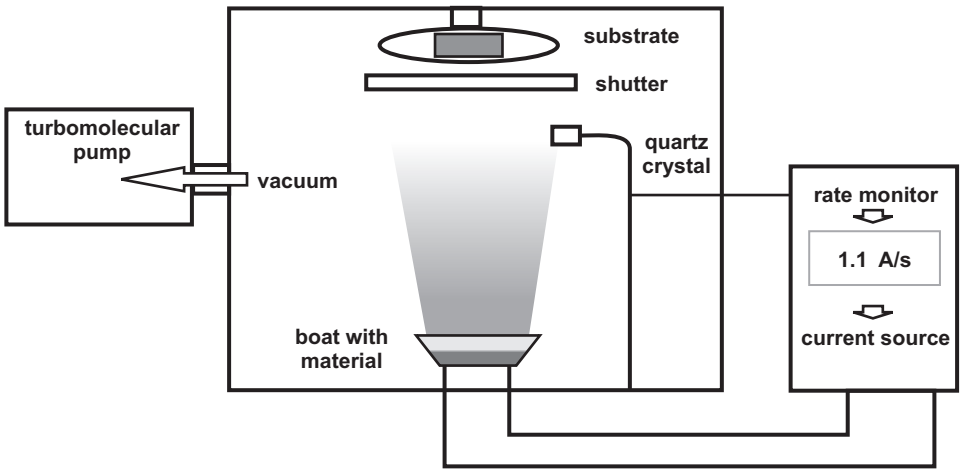

Figure 3.11: Schematic build-up of an evaporation machine.

3.3.2 Organic layer deposition with spin-coating

Spin-coating is a lateral deposition method since the only relevant force involved is the centrifugal force which spreads the liquid material over a rotating substrate. It is a common method to deposit photoresist with high layer thickness uniformity and reproducibility for photolithography, but is also wide spread for the organic layer deposition. An advantage is that it is a quite simple method since along with materials parameters like viscosity and boiling point, there are only a few spin parameters influencing the resulting film thickness and quality. After applying the material on the substrate, the acceleration of the rotating substrate is the first relevant spin parameter. Since many commonly used solvents like toluene or chloroform exhibit a low boiling point and evaporate therefore quickly, the choice of a too low acceleration could lead to non-uniform films. The final spin-speed, usually expressed as number of rotations per minute, is the most relevant parameter since the related radial force, quadratically dependent of the angular speed, determines the layer thickness. During spin-coating, the film becomes more viscous due to solvent evaporation and reaches a final layer thickness.
Typical layer thicknesses relevant in this work are between 100 and 300 nm. Thick photoactive layer thicknesses (> 200 nm) turned out to be favorable for low dark current and high EQE, but by decreasing the spin speed and the related radial force, also the layer homogeneity suffers and even a de-wetting of the substrate can occur. Another drawback of spin-coating is that it can not be applied for large scale deposition and that it is limited to flat substrates. High surface textures lead to high layer inhomogeneities [Gu95] and film cracks.

3.3.3 Organic layer deposition with spray-coating

Spraycoating is widely used for lacquer deposition in large scale industry production. During the last years there were also several attempts to establish this technique for fabrication of organic solar cells [Na10, Gir09, Gir11, Hot09] and photodetectors [Ted09]. In this work, first a simple hand-held commercial airbrush gun, usually used for artistic purposes, was tested. Since this simple system provides no control of the resulting film thickness, drop size and layer roughness, the experiments were continued with a commercial automatic air atomizing spray gun, containing a dual fluid nozzle with external mixing (Krautzberger M10). Fig.3.12 shows a schematic drawing and Fig.3.13 a picture of this setup. The term 'dual fluid nozzle' refers to the separate control of the liquid medium, the organic polymer, and the atomizing gas, which allows the adjustment of the material flow independently of the gas pressure. Furthermore, the external mixing of the two media, outside of the nozzle, provides a better protection against obstruction of the nozzle and allow therefore also the spraying of quite viscous fluids. The spray gun is pneumatically controlled by an electromechanical 3/2-way valve which has two purposes. Starting the spraying process, it opens the atomizer air valve and moves shortly afterwards the needle towards an upper position (see Fig.3.12) to open the nozzle. Stopping the deposition, the nozzle is closed first. This procedure bears an important advantage compared to simpler spraying guns since a homogeneous spray pattern can be achieved and dripping is prevented.
The spray pattern is influenced strongly by the geometry of the spray setup as well by solvent properties and by a set of spray parameters that were varied in this work to obtain organic films with suitable morphological and electrical characteristics for device application, see section 5.1.

Among the solvent properties, mainly boiling point, surface tension and viscosity influence the spray pattern and the drop formation. A low boiling point leads to an enhanced evaporation of the solvent until the drops reach the substrate. As will be shown in section 5.1, this leads to an increased material consumption and hence a more expensive deposition process. Viscosity and surface tension are related to each other, but whereas viscosity is a dynamic property defined as the ability of a liquid to resist a change in the shape or arrangement of its molecules during flow, the surface tension is a static cohesive force which tries to arrange the liquid in a shape with minimum energy. Surface tension can be determined by measuring the contacting angle of a liquid drop and a substrate. Both properties have an influence on the drop size since they represent the force resisting the formation of new drop surfaces. The surface tension plays also a major role on the substrate where the impinging drops form an interconnected network. During this work it was shown that this networking has a major influence on the opto-electronical OPD performance, see section 5.2.1.

Regarding the spraying parameters, the choice of the **distance between nozzle and substrate** is critical since only a certain range guarantees the formation of uni-

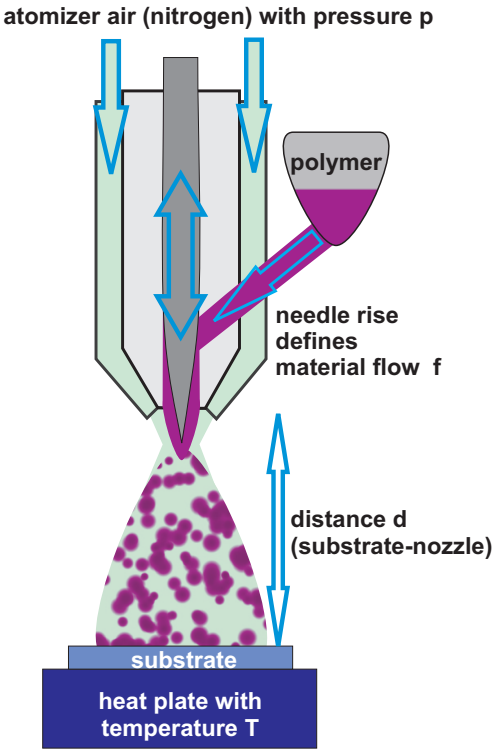

Figure 3.12: Schematic build-up of the spraying setup.

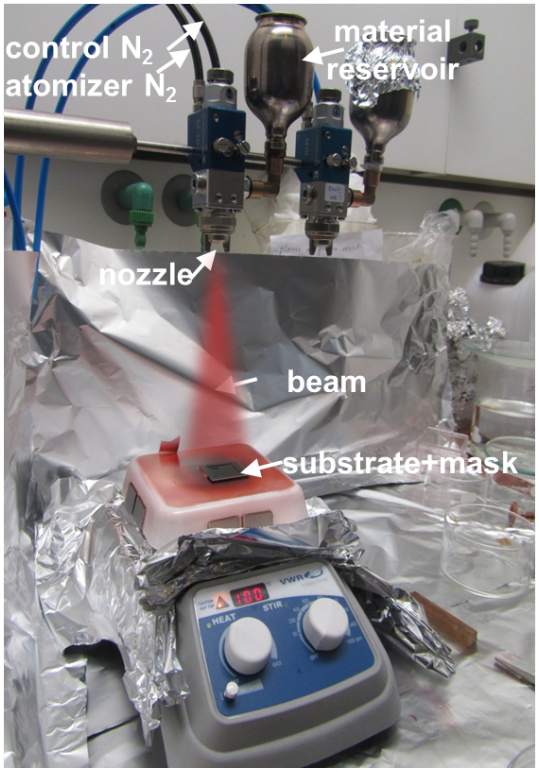

Figure 3.13: Picture of the spraying setup used in this work.

form films. In the wet regime, corresponding to a position of the nozzle close to the substrate, the sprayed drops do not lose a sufficient amount of the solvent during their flight and hence the on the substrate impinging drops form a wet film with uncontrollable thickness and uniformity. The upper extremity, a distance far away from the substrate, causes a complete evaporation of the solvent until the drops reach the substrate, thus only powder is deposited. The intermediate regime allows the drops to lose a sufficient amount of solvent during their flight and therefore a quick drying when they reach the substrate, forming a homogeneous network of drops with a thickness depending on the **spraying time**. The spraying time can be precisely adjusted with a timer connected to the pneumatic control. It influences the layer thickness linearly as will be shown in chapter 5. The substrate can be heated during the spraying process which enhances the drying of the drops and influences the resulting morphology. The heating **temperature** is critical since it influences the drop-networking, e.g. it controls the roughness of PEDOT:PSS, see section 5.2.2. The **pressure of the atomizing air** influences the velocity of the atomizing gas and of the drops. An increased pressure leads also to a finer atomization of the polymer since the amount of kinetic energy is in-

creased to overcome the material surface tension at the nozzle. A smaller influence has the **material flow** which is the amount of material flowing towards the nozzle, driven only by gravitational force. It turned out that it is also the most critical parameter regarding the reproducibility of the layer thicknesses, using the same set of spraying parameters. A readjustment of the needle rise of some 10 micrometers changes the layer thickness in the order of several hundred nanometers, see section 5.1. Due to this effect, a careful control of the layer thickness was necessary, which can be done by comparing the color of sprayed film with a set of films with known thicknesses or measuring the thicknesses directly with a profilometer, see section 3.4.5.2.
Another important factor influencing the reproducibility of results is a careful cleaning of the spraying gun after each spraying step since only one gun was used for spraying the blend as well the water-containing PEDOT:PSS formulation.
The whole spraying process was performed in air. To minimize the impact of this ambient condition on the sprayed layers, inert nitrogen was used as atomizing gas.

3.3.4 Low pressure plasma treatment

Along with the different physical states of matter, solid - liquid - gas, neutral ionized gas known as plasma, is the fourth state.
For many technical processes a so called low pressure plasma is generated by the supply of electrical energy. The term ‘low pressure plasma‘ refers to the low pressures of the reactive gas, which are typically in the range of 1 mbar. At such low pressures, the temperature of free electrons is much higher than the temperature of heavy particles such as atoms, molecules and ions inside the plasma since in two-body collisions, the lighter particle is favored. Typically, the electron kinetic energy can be as high as some 10 000 K [Spa78]. Due to the low density and heat capacity of the electrons the amount of heat transferred to the gas, the walls and the sample is very small. Therefore a low pressure plasma is also called ‘cold‘ plasma. This feature is crucial for an usage on temperature sensitive materials like polymers.
Typical process gas pressures applied during this work are in the range of 0.3 Torr, which is well below the critical pressure at about 10-100 Torr [Bel67] at which the electron and gas temperature reach a thermal equilibrium.
The interaction of the plasma with the sample surface induce various chemical and physical reactions which involve modifications of the surface and also a removal of material. The most common applications are:

- Cleaning and etching
- Cross-linking of surface molecules to increase surface-hardness
- Chemical change of the surface through incorporation of plasma particles.

Almost any kind of gas can be used to generate a plasma, even ambient air. Reactive gases like oxygen are usually preferred, since the atomic species in the plasma easily

break surface bonds to be incorporated or to form volatile gases like carbon dioxide or water. In this work, it is exploited that oxygen radicals adsorb at the uppermost atomic surface layer of the polymer which results in the formation of a considerable amount of functional polar regions which increase the surface energy and also the hydrophility. This will be reported in detail in section 4.1.

To ionize the gas, a sufficient amount of electrical energy has to be supplied. This can be implemented by several methods, including glow discharge plasma generated by the application of a low frequency (< 100 kHz) electric field between two metal electrodes and capacitive plasmas generated with high frequency electric fields (13.6 MHz). In this work, a microwave plasma asher was used in which a magnetron generates a microwave with a frequency of 2.45 GHz respective 12 cm wave length. The advantage of microwave generated plasmas over RF plasmas is that due to the higher frequency oscillations of the electric field in microwave plasmas, electrons travel shorter distances compared to RF plasmas before they switch direction. Subsequently, fewer electrons reach the sample surface per switching cycle thus minimizing the charging of the surface. With a minimum surface charge, the acceleration of positive ions towards the sample surface is only weak, decreasing the undesirable surface ion bombardment to a minimum.
In this work, it turned out that the organic materials can be easily damaged during plasma treatment. A careful adjustment of plasma parameters, like treatment time and power had to be performed to prevent a morphological and electrical damage. In the used model 'Femto' by 'Diener Electronics' morphological changes of the organic polymer layers were observed even for very short oxygen treatment times and low microwave powers.

In Fig.3.14 to Fig.3.16 the morphology change of a spin-coated P3HT layer, measured with an AFM (see section 3.4.5.2), is shown. An untreated and two treated films are shown, one of them with a minimum treatment power for hydrophilization of the layer and one exposed to a plasma generated by a microwave with doubled power. There are clear changes, apparent as cracks and craters, visible at the treated samples compared with the untreated film. The RMS-roughness changed from 2 nm (untreated) to 10 nm (180 W microwave power). Deep cracks evolved during the treatment, the depth of these craters increases for different long treatment times and different plasma powers. Typical values are about 10 nm for an applied power of 90 W and 50-100 nm for 180 W power, respectively. No general change of the layer thickness was observed.
A similar result shows the treatment of PCBM:P3HT blends (Fig.3.17 to Fig.3.19). Here the effect is not as pronounced which is attributed to the influence of PCBM, but on a different lateral scale also here cracks, with similar depths and roughnesses compared to P3HT, become visible. Since these changes do not appear when only microwaves are coupled into the chamber without a reactive gas, they are attributed to the ion bombardment. The layers turned out to be not suitable for device integration

since the cracks cause a considerable increase of the electric leakage current.

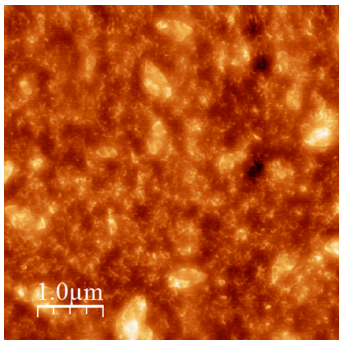

Figure 3.14: Untreated P3HT-film. RMS-roughness: 2 nm

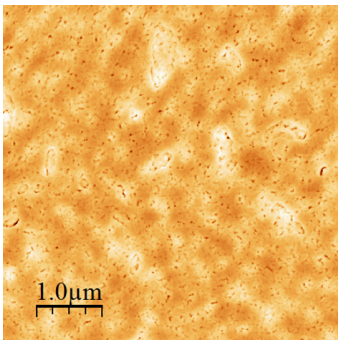

Figure 3.15: Treated P3HT-film (90 W, 18 s): RMS-roughness: 2 nm, cracks

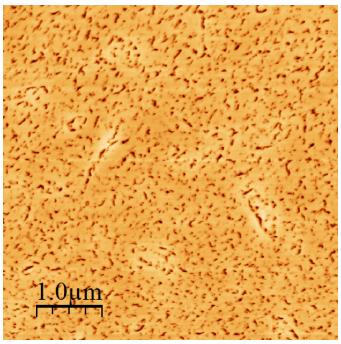

Figure 3.16: Treated P3HT-film (180 W, 18 s): RMS-roughness: 10 nm, deep cracks

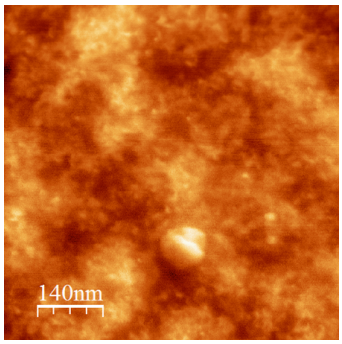

Figure 3.17: Untreated PCBM:P3HT-film. RMS-roughness: 1.6 nm

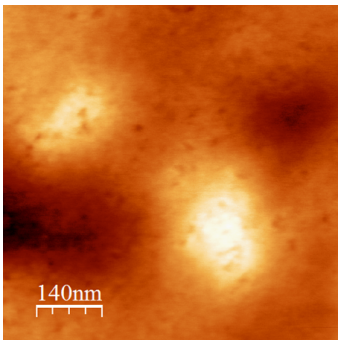

Figure 3.18: Treated PCBM:P3HT-film (90 W, 18 s): RMS-roughness: 5 nm, small craters

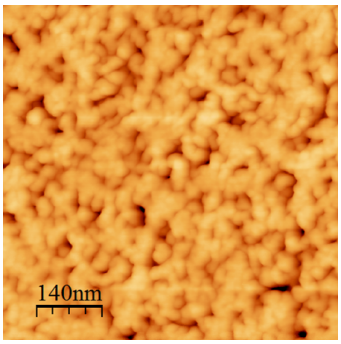

Figure 3.19: Treated PCBM:P3HT-film (180 W, 18 s): RMS-roughness: 5 nm, deep cracks

Finally, only a setup geometry with a ‘down-stream‘ chamber, see Fig.3.20 turned out to be sufficient sensitive for the organic processing needs. In the asher model ‘TePla 100-E‘ the plasma is generated at a different location, about 20-30 cm over the sample position and then transported towards the sample using a vacuum pump. During this transport, the plasma state actually breaks down and primarily neutral species, including reactive radicals and metastable molecules, remain which react with the sample surface, but without the otherwise inevitable ion bombardement. Interestingly, no morphological chances were sensed also after long treatment times when parts of the materials were already etched away.

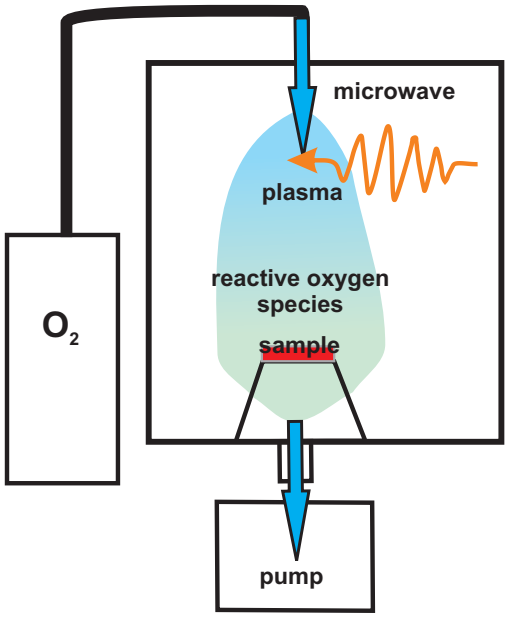

Figure 3.20: Schematic build-up of a down stream plasma asher.

3.3.5 Encapsulation

A careful shielding of organic devices to ambient conditions is necessary due to the sensitivity of organic materials to oxygen and water. These molecules can react directly with the polymers or also with the low work function electrodes like aluminum to form insulating oxides which alter the photocurrent-voltage characteristic [Kre07]. The degradation process is further enhanced since PEDOT:PSS is hygroscopic. A review about different degradation effects is given in [Jor08].
To shield the organic device, a simple encapsulation was used consisting of a thin glass plate and an UV-curing epoxy glue. Since the encapsulation is fabricated on top of the device, it is only a one-dimensional effective barrier for oxygen and water because there can be still a side segregation of the polymer layers towards the active diode area. Still, very good long term stability can be reached by this simple encapsulation which will be shown in section 4.5.

3.4 Characterization of organic photodetectors

The following chapter is a survey on the most important photodetector characteristics and the methods to measure them. To convert light into a voltage signal, low and

high light levels have to be detected by the device and timely variant signals have to be processed. In addition, also material parameters like electrical resistance and layer thickness have a huge influence on the device performance and will be addressed here too.

3.4.1 Current-voltage (IV) characteristics

In Fig.3.21 a typical organic photodetector current-voltage curve is shown for a measurement under dark and illuminated condition. Typically, the current is scaled logarithmically to accentuate the light on/off-ratio. Whereas the reverse dark current should be kept as low as possible to ease the detection of low level light signals, the current under illumination should be ideally as high as the amount of the incident photons (see section 3.4.2).
The shape of the IV-curve is determined by a number of different parameters and physical processes inside the organic photodetector. To describe them, an equivalent circuit diagram as shown in Fig.3.22 can be used, even when the details of these processes are not known. The main components are also indicated in Fig.3.21 and described in the following paragraph.

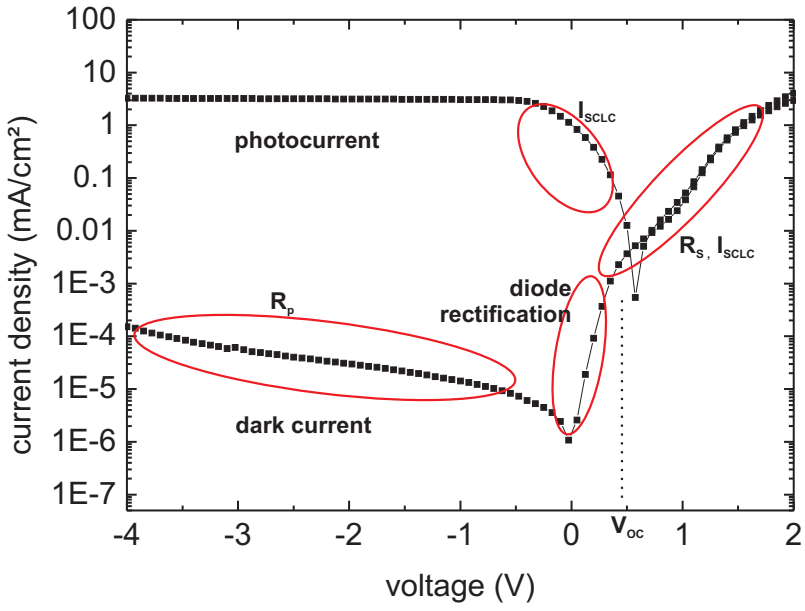

Figure 3.21: A typical IV-curve in a semilogarithmic plot of an inverted photodiode under dark and illuminated conditions (100 mW/cm^2).

Current source I_L: This parameter presents the number of dissociated excitons, generated by the incident light, before any recombinations processes can take place.

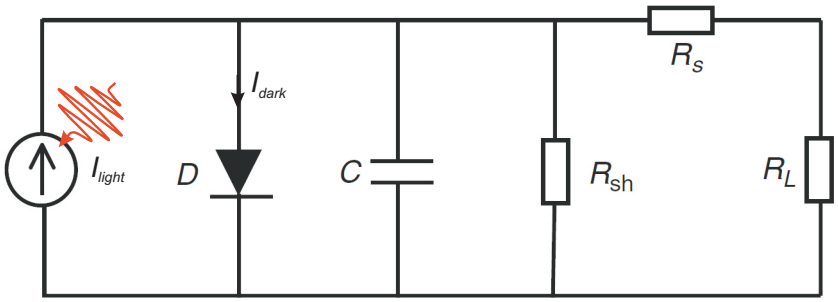

Figure 3.22: The equivalent circuit diagram of an organic photodiode. It consists of a (photo) current source I_L, a diode D, a serial resistance R_s, a shunt resistance R_{sh} and a capacitance C.

Ideal diode D: The diode is a voltage dependent resistor with a rectifying behavior due to the asymmetry of the electrode work functions. An ideal diode IV-characteristic is only present with the serial resistance R_s=0 and the parallel resistance $R_{sh} = \infty$.

Serial resistance R_s: It can be divided into a contribution of the electrical contacts (wiring, electrode sheet resistance) and of the organic materials themselves. The carrier transport through the organic layers is affected by the mobility and the layer thickness. Additionally, the carrier mobility can be affected by traps and space charge effects. The general low charge carrier mobility in most organic semiconductors favors the build up of excesses charges which create an electric counter field that reduces the current throughput. This current, the so called 'space charge limited current' (SCLC) can be expressed by the Mott and Gurney equation [Mon09]:

$$I_{sclc} = \frac{9}{8}\epsilon\mu_0\frac{V^2}{d^3} \tag{3.1}$$

with μ_0 the mobility, ϵ the dielectric constant and d the organic layer thickness. The expression is only valid if no traps are present or for shallow traps with a trapping time shorter than the charge carrier transit time. For deep traps, with a trapping time longer than the transit time, the SCLC depends on the density of traps and their energetic distribution. Trapped charges can play a major role in the IV-characteristics. At low reverse bias, most carriers are trapped, creating a counter electric field which hinders the photocarrier transport. In forward direction, the SCLC is visible as abrupt increase of the current slope V^m with $m \geq 2$ [Mon09]. For high forward bias, the trapping states are completely filled and the injected carriers are transported like in the trap free condition which is visible as transition from a $V^{m\geq 2}$ to a V^2 regime.
In this work, the deep trap SCLC was observed for the inverted OPDs and will be reported in detail in section 4.1.
R_s can be estimated from the slope at a positive voltage where the IV-curves become

linear since the diode D becomes very conductive. In case of a dominant space charge including deep traps, a direct extraction is not possible.

Shunt resistance R_{sh}: This parallel resistance R_p is related to leakage paths through the bulk heterojunction, mainly the pure phases of either n- or p-type semiconductor connecting the two electrodes. In reverse bias, R_{sh} limits the dark current and must therefore kept as high as possible, ideally $R_{sh} = \infty$, to decrease the dark current to a minimum.

Capacitance C: Time dependent effects like charging-discharging are taken into account. Since the ratio A/d of the photoactive area A to the layer thickness d is generally large for OPDs due to $d \propto 100$ nm, C is not negligible. It influences the speed of a photodiode via the RC-time constant.

Open-circuit voltage V_{oc}: It is influenced by the difference of the electrode work functions which causes a built-in electrical field, but the impact is lower as expected due to the influence of Fermi level pinning of the cathode and the reduction potential of the fullerene [Bra01, Den05]. V_{oc} is also related to the energy difference between the the HOMO level of the donor and the LUMO level of the acceptor material [Bra01]. The relevance of the open circuit voltage for an OPD is marginal since an OPD is driven in reverse bias.

An organic bulk heterojunction can be described in analogy to an inorganic diode since it consists of numerous pn-junctions at the donator-acceptor interfaces in the random network. For an ideal diode in the dark follows with the Shockley-equation and an ideality factor n which describes the organic bulk material:

$$I = I_0 \cdot (e^{\frac{eV}{nk_BT}} - 1) \tag{3.2}$$

Under illumination, the light generates the photocurrent I_L which adds to the Shockley-equation. In addition, R_s and R_{sh} can be introduced in a simple model [Rau04]:

$$I = I_0 \cdot (e^{\frac{e(V-IR_s)}{nk_BT}} - 1) + \frac{V - IR_s}{R_{sh}} - I_L \tag{3.3}$$

The measurement of the IV-curve of an OPD is performed with a Keithley 2602 controlled by a Labview interface. A special sample holder eases the selection of the different diodes of each substrate. Illumination occurs with a wide spectrum halogen source which is calibrated to a light intensity to 100 mW/cm^2 before each measurement run.

3.4.2 Sensitivity and external quantum efficiency (EQE)

Quantum efficiency is a quantity to describe the light sensitivity of a photosensitive device. The most common term is the external quantum efficiency (EQE) which is defined as:

$$EQE = \frac{\text{number of electrons in the external circuit}}{\text{incident photons on the device}} \tag{3.4}$$

It expresses the efficiency of the photon to electron conversion in the device. A related term is the internal quantum efficiency (IQE) which considers only the amount of photons which actually reach the photoactive layer, see Eq.3.5. The IQE is determined mainly by the mobility of the photogenerated charge carriers and strongly influenced by the photoactive layer thickness and the related serial resistance (see section 5.2.1). The IQE can be almost 100 % which was demonstrated in [Par09]. The EQE, in contrast, is reduced mainly by transmission T and reflectivity R losses at the transparent electrode, the encapsulation and the PEDOT:PSS layer.

$$IQE = \frac{\text{number of electrons in the external circuit}}{\text{incident photons on the photoactive layer}} = \frac{EQE}{1 - R - T} \tag{3.5}$$

Another common quantity to describe the photodiode sensitivity is the spectral response (SR). It is the electric current in the external circuit per Watt of incident light (A/W). It gives lower values for shorter wave lengths compared to the EQE since the SR is related to the energy $E = hc/\lambda$ of photons (with h the Planck constant, c the speed of light, λ the wave length and e the elementary charge) and not the number. It can be calculated with the EQE:

$$SR = EQE \cdot \frac{e\lambda}{hc} \tag{3.6}$$

A high sensitivity is especially important for imagers since the photoactive pixel area is very small which also reduces the amount of light which can be transformed into an electrical signal.

For imagers, a common quantity which is related to the EQE is the signal-to-noise ratio (SNR). The SNR can be regarded as a measure of the sensitivity of an imager and is defined as the ratio of the average light signal and the standard deviation of the signal representing the amount of noise (see section 3.4.4 for details about noise):

$$SNR = \frac{\text{average number of photogenerated electrons}}{\text{RMS-noise of photogenerated electrons}} \tag{3.7}$$

n_{ph}, the number of photogenerated electrons, is expressed as: $n_{ph} = EQE \cdot \frac{\Phi\lambda}{hc} \cdot t \cdot A$

with Φ the light intensity (W/m^2), A the pixel area and t the exposure time. The number of noise electrons is dependent on different fundamental noise sources which are described in section 3.4.4.

The measurement setup used in this work to determine the EQE and also trans-

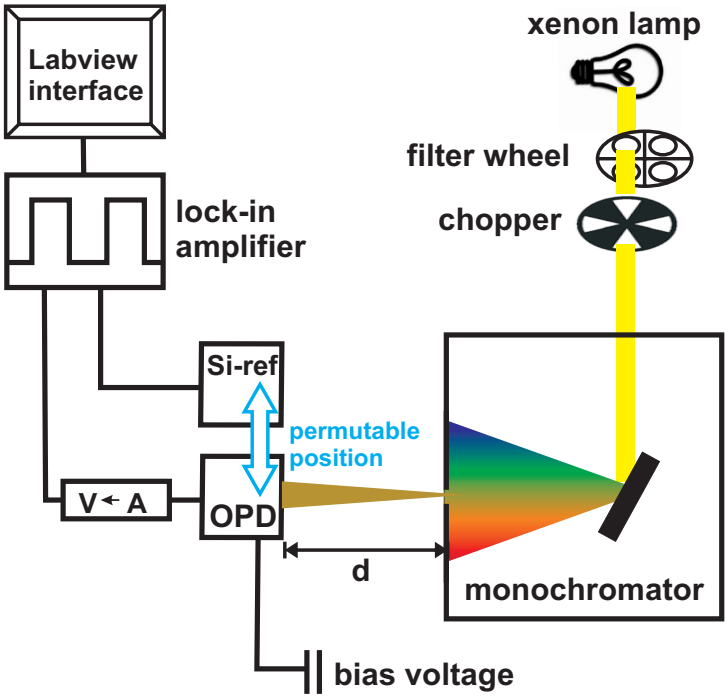

Figure 3.23: The schematic built-up of an EQE setup.

mission and absorption of the different diode layers is shown in Fig.3.23. As wide spectrum light source, a 300 W xenon-lamp, is used which covers a wave length region from 300 to about 2500 nm. The light is transmitted through filters which cut off the wave length range in which higher orders of the constructive interference at the grating would appear. After passing a chopper wheel which modulates the light at a frequency of 210 Hz, the beam hits the grating inside the monochromator(Oriel Cornerstone 260) and is spectrally dispersed. Two gratings with different blaze wave lengths (350 nm, 1000 nm) are installed to cover a wave length region from 300 nm to 2.0 µm. The monochromatic light illuminates first the calibrated reference silicon diode with known spectral response to determine the amount of photons arriving at a certain distance from the monochromator. Afterwards, the device under test is moved to the same position. An external bias can be applied to the diode. The photocurrent signal is amplified, converted to a voltage and displayed by a lock-in amplifier which sends the

signal to a labview interface where it is displayed as EQE with Eq.3.4. The lock-in amplifier (Merlin Digital Lock-in Radiometry System) substracts the background signal of the chopped signal which makes the measurement less sensitive to background illumination.
A reliable EQE measurement requires an accurate positioning of the sample as well as careful reference measurements. Since two different amplifiers are used for the reference silicon diode and the device under test, a mismatch of the signals occurs which had to be corrected by multiplying the corresponding device EQE by a factor of 0.9.
Regarding the positioning of the sample, the variance of the distance d from monochromator slit to the device has a big impact on the EQE due to the beam broadening. For Δd=2 mm, the error is 5 % of the EQE value. Due to a specially designed sample holder, the distance variation was kept to a minimum (±1 mm).

3.4.3 Photodiode speed

Depending on the intended use, the organic photodetector speed is more or less relevant. For an application as low cost optical interconnect in data transmission [Pun07] much higher demands have to be met than for imaging [Bai12].
The speed is usually characterized as rise and fall time or cut-off frequency. The rise time is defined as the time which is required to increase the output signal from 10 % to 90 % of the final output level. This is illustrated in Fig.3.24 with a square wave excitation signal (light pulse) and the corresponding response signal (as voltage signal).
A different way to describe the photodetector speed is the 3 dB cut-off frequency f_c. It

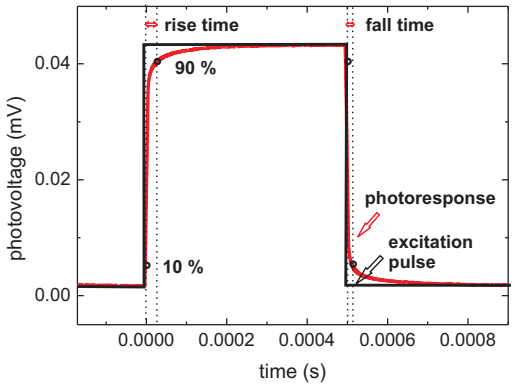

Figure 3.24: The photodiode response on a square wave excitation light pulse.

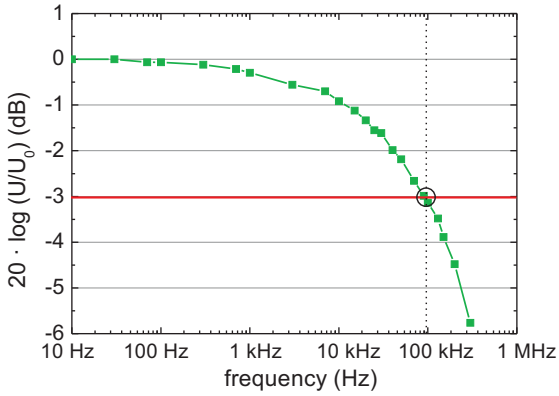

Figure 3.25: A typical cut-off frequency measurement result of an OPD.

is defined as the frequency at which the maximum signal response of the photodiode decreases to $\sqrt{1/2}$ of the DC value. The measurement of the 3 dB cut-off frequency is performed by illuminating the photodiode with light pulses of constant height but varied

frequency. The maximum height of the output signal of the photodiode is determined for the different excitation frequencies and plotted with respect to the DC value. The DC value can be determined by applying very low frequencies where the signal height does not vary for increasing the excitation frequency slightly. A typical measurement is indicated in Fig.3.25. Since the logarithmic unit decibel (with base 10) is defined for power quantities P but the signal height is displayed as voltage V, a factor of 20 has to be included for the voltage ratio: $10 \cdot log(P/P_0) = 10 \cdot log(V^2/V_0^2) = 20 \cdot log(V/V_0)$.

The photodetector response time respective frequency is influenced mainly by two components, the transit time t_{tr} and the RC time constant t_{rc}. The transit time is the time which is required by the photogenerated carriers to cross the photoactive layer to reach the electrodes. It is given by $t_{tr} = d^2/\mu V$ with the layer thicknesses d, the carrier mobility μ and the voltage drop V. In the RC time constant $t_{rc} = RC$, R sums up the serial resistance of the electrodes and the load resistances and C is the photodiode capacitance plus all additional capacitances of the external circuit. In case the photodetector is limited by t_{rc}, the signal shape in Fig.3.24 at the fall time side can be described with:

$$V(t) = V_0 \cdot \left[1 - e^{\frac{-t}{RC}}\right] \tag{3.8}$$

With this equation and the definition of the rise time t, the rise time is calculated to $t = RC \cdot ln(9)$. The RC limitation allows also a direct relation between t respective f_c: [Shi09]

$$t = RC \cdot ln(9) = \frac{ln(9)}{2\pi f_c} = \frac{0.35}{f_c} \tag{3.9}$$

Since the photodiode speed can be strongly influenced by various physical processes, this relation is only an approximation, but a similar relation was found in [Bai11a].
The precise way of performing the cut-off or rise time measurement influences strongly the result. This is illustrated on the basis of two parameters in Fig.3.26 and 3.27. The organic layer mobility can be affected by trap filling which can introduce a dependence on the applied light intensity [Arc13]. This effect is illustrated in Fig.3.26. In this work, all cut-off measurements, if not otherwise mentioned, were performed at a light intensity of 800 μW/cm^2.
The duty cycle is related to the repetition rate of the excitation pulses. A duty cycle of 50 % means that the time between two pulses is equal to the pulse length. A duty cycle of 1 % means that in one period, only 1 % of the time is occupied by the pulse and 99 % is idle time. The dependence between f_c and the duty cycle is shown in Fig.3.27. For about 20 % duty cylce, f_c is saturating which means that by extending the idle time to 80 % of the period the neighbouring pulses do not influence each other, e.g. by overlapping. In this work, all measurements were performed at a duty cylce of 50 % since this is a common way of measuring silicon diodes. It has to be noted that this method decreases the measured cut-off frequencies about 10 % compared to

a single puls measurement.

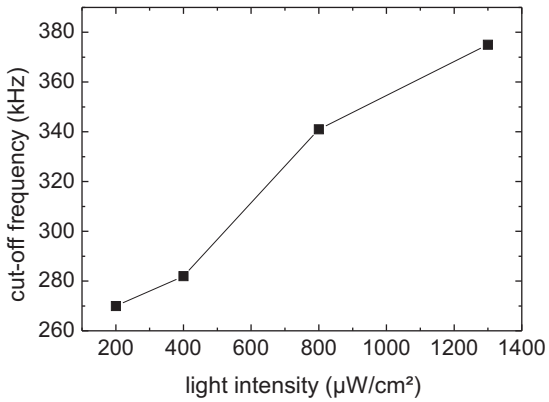

Figure 3.26: The influence of different light intensities on the cut-off frequency of an OPD.

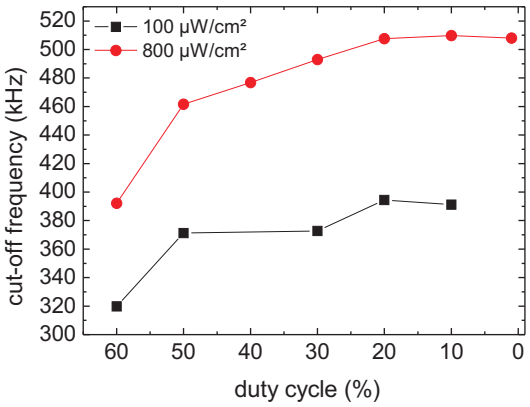

Figure 3.27: The influence of a varying duty cycle on the cut-off frequency for two different light intensities.

The instrumentation for performing the dynamic measurements consists of a wave-form generator (Keithley2602) which generates voltage pulses applied to a light source, a transimpedance amplifier (FEMTO Current Amplifier DHPCA-100) and a 1.5 GHz digital sampling oscilloscope (LeCroy Wavepro 715zi). The light source is a fast green LED (525 nm, rise time: 15 ns, fall time 45 ns) which outputs the square wave pulses illuminating the OPD. The photocurrent of the OPD is amplified and converted to a voltage signal with the FEMTO and displayed at the oscilloscope. The cables used to wire the OPD to the amplifier and the LED to the wave form generator should exhibit low capacitance to suppress related artifacts in the response signal to a minimum.

3.4.4 Temporal noise

Temporal noise, referring to the time-dependent fluctuations in the signal value, is the fundamental limitation of the acquisition of small light signals in a photodiode. Around the actual signal, these instantaneous noise voltage amplitudes form a random pattern which is specified by a probability density function. Commonly, noise follows a Gaussian distribution. Then the noise can be expressed as RMS-noise voltage V_{noise} which corresponds to the standard deviation of the Gaussian distribution.
For a small number of occurrences, e.g. a low photon count relevant for photon shot noise, the Poisson distribution is valid:

$$f(s) = \frac{N^s e^{-N}}{s!} \tag{3.10}$$

Here, N is the mean number of occurrences and s the number of occurrences. The standard deviation and the RMS-noise voltage is then $V_{noise} \propto \sqrt{N}$.

The three main types of temporal noise in (inorganic) photodiodes are shot noise, thermal noise and flicker noise. The **shot noise** is the most relevant noise source known for CMOS-imagers [Big06]. It is associated with the random fluctuations of moving carriers in a conductor (dark shot noise) or with the random arrival of photons on the detector (photon shot noise), both obeying the poisson distribution. The fundamental origin is the discrete nature of the charge flow in units of the elementary charge and the presence of potential barriers, like a pn-junction of a photodiode. When encountering a potential step, potential energy of the carrier is abruptly transferred to kinetic energy which leads to inhomogeneous current flow.
Shot noise has an uniform power density in the time domain and is independent on temperature. Since the standard deviation of the electron distribution is $\sqrt{N}$, for the RMS-noise voltage follows:

$$V_{noise} = \sqrt{N}\frac{e}{C} = \sqrt{\frac{Signal(V) \cdot e}{C}} \tag{3.11}$$

$Signal(V)$ is the measured mean voltage signal and C is the photodiode capacitance.
Thermal noise or Johnson noise arises due to the thermal (Brownian) motion of the carriers in any kind of conductors and follows a gaussian distribution with an uniform power density like shot noise. It is described by the Nyquist relation (valid for frequencies < 100 MHz) and is expressed in units of $A/\sqrt{Hz}$: [Car09]

$$V_{noise} = \sqrt{4kTR\Delta f} \tag{3.12}$$

with T as temperature, R as resistance and Δf as noise bandwidth. A noise type related to the thermal noise is the so called **reset noise** which is not a fundamental noise source but a repacking of thermal noise in presence of a capacitor. Reset noise can be found in CMOS-imager electronics during the conversion from the charge to the voltage domain involving a thermal affected reset voltage [Big06]. The noise bandwidth of a circuit with a capacitor and a resistor is $\Delta f = 1/4RC$ [Rob75]. With Eq. 3.12, the thermal noise can be rewritten as:

$$V_{noise} = \sqrt{\frac{kT}{C}} \tag{3.13}$$

This reset noise is the result of the low-pass filtering of the noise from a resistor, using a capacitor.
Flicker noise is also called 1/f noise. It is the least understood noise source, but can be observed in various passive (carbon resistors) and active (MOSFETs) devices [Hun90]. It is related to a carrier number or mobility fluctuation due to trapping of carriers (e.g. the gate oxide of a MOSFET) or bulk scattering. A high impurity level increases the flicker noise. The noise spectral density S_f has a time dependence and is

proportional to [Mar00]:

$$S_f \propto \frac{I^\alpha}{f^\beta} \tag{3.14}$$

α is a factor related to the trapping nature (surface or volume) and β hints to the distribution of trap energies inside the semiconductor band gap. Usually, $\beta = 1$ is valid which accounts for an uniform trap distribution over space and energy [Lin10].

Important photodiode parameters related to the temporal noise is the noise-equivalent power NEP and the detectivity D. The NEP is related to the responsivity SR of a detector, but it takes into account the ability to detect small light signals. It is the radiant light intensity Φ in W/cm^2 on the area A that produces a signal voltage V_{signal} equal to the total noise voltage V_{noise} from the detector:

$$NEP = \frac{\Phi A}{V_{signal}/V_{noise}} \tag{3.15}$$

The detectivity D is defined as the inverse of the NEP. A higher D indicates the ability of the OPD to detect lower light levels. D increases with shrinking the photoactive area A. The specific detectivity $D*$ eliminates this dependence:

$$D* = \frac{\sqrt{A \cdot B}}{NEP} \tag{3.16}$$

$D*$ is the signal-to-noise ratio in case 1 W of radiation is incident on a detector with a sensitive area A of 1 cm^2 and the noise is measured with an electrical bandwidth B of 1 Hz, expressed in cm$\sqrt{\text{Hz}}$/W. Hence it is a normalized detectivity that is practical for comparing the performance of detectors with different areas and different bandwidths.

Noise voltage measurements of photodetectors are very sensitive to influences of the measurement setup itself. A main problem arises with the photodetector area. Large areas are related to large capacitances. The noise gain of an amplifier is proportional to the input capacitance and hence measurement of large scale organic photodiodes is not reliable. Instead of the large OPDs fabricated in this thesis, their down-scaled counterparts on the CMOS chips were investigated to quantify the amount of noise present in organic materials, see section 6.2.2.

3.4.5 Material characterization

Beside the opto-electronical characterization of a whole device, also the single materials have to be addressed to improve the organic layers of the device independent of each other. The most important characteristics investigated in this work are the sheet resistance of the polymer electrode as well the thicknesses and morphologies of the

individual organic layers.

3.4.5.1 Sheet resistance determination

The sheet resistance ρ_{sheet} is a measure of resistance of a two-dimensional thin film with uniform thickness. It is the result of a four-point measurement. The term refers to the use of four co-linear and equidistant (distance s) electrical probes on the sample instead of two. Current injection and voltage measurement are separated. The voltage is sensed with the inner needles while a current is applied to the two outer probes. Using a high impedance voltmeter, no current is flowing through the inner needles and contact and spreading resistances are eliminated in the measurement. Fig.3.28 shows a schematic drawing of a four point measurement setup. A reliable measurement presumes an infinite size of the sample ($r \to \infty$) and that the film thickness d is much smaller than the probe spacing s ($d << s$). With known current I and sensed voltage V, for the sheet resistance follows:

$$\rho_{sheet} = \frac{\pi}{ln2} \cdot \frac{V}{I} = \frac{\rho}{d} \tag{3.17}$$

By multiplying the sheet resistance with the layer thickness d, the bulk resistivity ρ can be calculated. The unit of ρ_{sheet} is $\Omega/sq.$ which refers to the lateral measurement method. Practically, to account for the non-infinite size r and the shape (e.g. circular

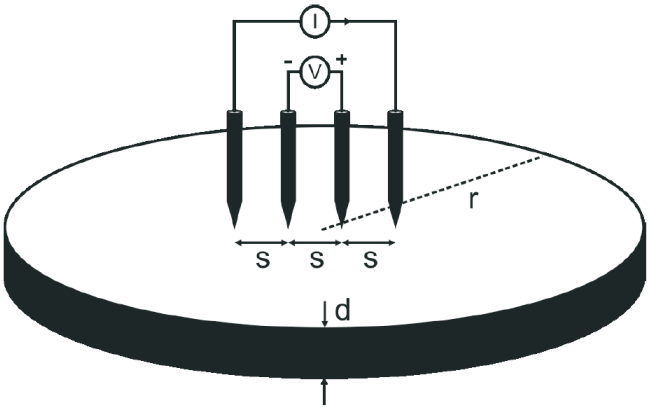

Figure 3.28: The schematic built-up of a four-point measurement setup.

or rectangular) of the sample, a correction factor has to be multiplied to the measured ρ_{sheet}. Depending on r/s, correction tables can be found in [Smi58].
The fourpoint measurements were performed with a setup designed for polymer sheet resistance measurements. Common probe station needles with small curvature radius (micrometers) turned out to be not suitable for the characterization. The local high

current densities in the measured polymer, related to the small tip radius, lead to creation of high resistive channels or contact areas in the polymer which distort the measurement. Reliable characterization was performed with spring mounted gold tips with round tops for a bigger contact area to the sample surface.

3.4.5.2 Thickness and morphology

For thickness and morphology characterization, an atomic force microscope (AFM) (JEOL JSPM 5200) as well a mechanical profilometer (Dektak 8) was used.

The **AFM** provides a sub-nanometer vertical resolution for a precise measurements of layer thicknesses and roughnesses due to the exploitations of surface forces in the range of 10^{-10} N. Among theses forces, the attractive van-der-Waals force and the repulsive force due to overlapping of electron orbitals (Pauli exclusion principle) are the most important ones, commonly described as Lennard-Jones potential [Bai08]. The forces act on a tip of a silicon cantilever which is scanned over a sample to obtain a two-dimensional image of the surface topography. The scan modus is typically the tapping-mode. In this modus, the cantilever is vertically oscillating (driven by a piezo element) at a frequency near the resonant frequency (in the range of about 100 kHz). Since the tip is only in direct contact with the sample for a short time within the oscillation period, this modus minimizes sample damages compared to the non-oscillating contact modus.
The change of the cantilever oscillation due to the surface forces is detected with a laser beam which is reflected by the cantilever backside and hits a silicon photodiode, as indicated in Fig.3.29. The deviations of the laser beam are converted to height information. Commonly, a feedback loop is employed to maintain a constant force between tip and sample. This is realized by the piezoelectric tube which moves the sample in vertical direction.

The quality of an AFM picture is limited by various factors. The fundamental horizontal resolution is limited by the tip radius (about 7 nm). The geometry of the tip strongly influences the topography result. An electrostatic discharge or a collision with dust particles can damage the tip and hence worse the lateral resolution. For high aspect topographies (long vertical dimension plus thin lateral size) special tips have to be used. The gain of the feedback loop, which is related to the time delay of the re-adjustment of the piezo to maintain constant force between sample and tip, has to be adjusted for each scan to avoid a blurred depiction of sharp edges. A high measurement speed can also lead to a similar blurring effect. Hysteresis of the piezo elements, visible as concave image curvature, can not be avoided but can be corrected with a software post-processing. In this work, the program ‘WSxM‘ by ‘Nanotec‘ was used for these corrections.
A general drawback of the AFM is the limitation of scanning large (vertical) structures as well as large (lateral) images. The maximum lateral image size of the JEOL is 25

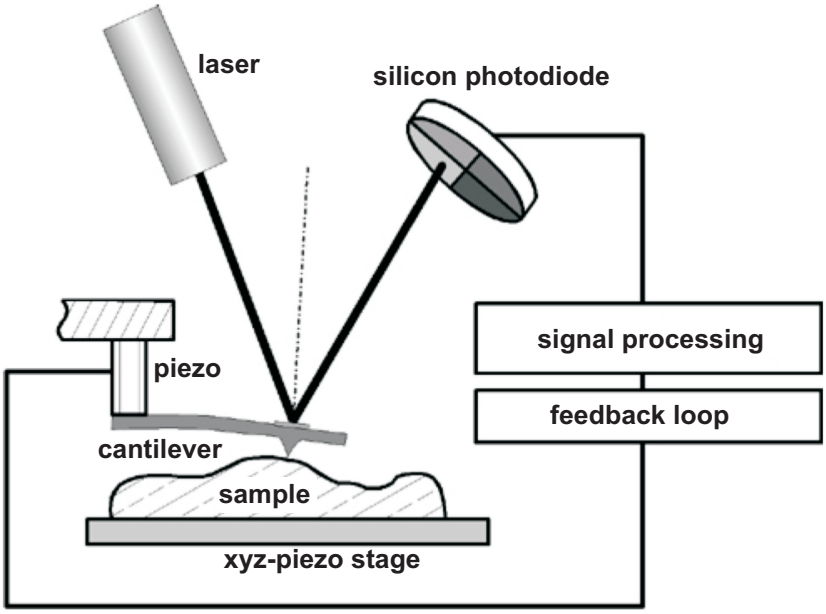

Figure 3.29: The schematic built-up of an AFM.

µm. Henceforth, big structures like sprayed polymer drops with typical lateral dimensions of 5-50 µm can not be investigated regarding the layer roughness.

Consequently, for investigation of the sprayed samples a 'Dektak' **profilometer** was used. Here, a diamond stylus is moved with a specified pressure (5 mg) laterally across a sample which is in vertical contact. In comparison with the AFM, the profilometer is an electromechanical instrumentation in which the vertical change of the stylus is capacitively detected. Nevertheless, it provides an excellent vertical resolution < 5 nm. The horizontal resolution is limited by the tip radius which is 12.5 µm for all measurements performed in this work.
The RMS-roughness is defined, with N the number of measurement points, $\langle y \rangle$ the average height level, as:

$$RMS = \sqrt{\frac{1}{N} \sum_{n=1}^{N} \left(y_{xn} - \langle y \rangle \right)^2} \tag{3.18}$$

It was determined by performing a line scan of 1.5 mm across the sample, correcting the sample tilt with substracting the linear fit of the data and finally calculated using Eq.3.18.

Chapter 4

Towards an efficient top-absorbing photodetector fabricated with spin-coating

The first step towards the hybrid CMOS-imager is to develop an organic photodetector stack which can be integrated to the CMOS chip. The main challenge concerns the opacity of the chip. As mentioned in section 3.1.1, the commonly used OPD layout is a bottom-absorbing detector. Hence, the OPD has to be transformed to a top-absorbing device. The easiest way for this transformation is to reduce the layer thickness of the metallic top electrode (usually a low-work function material like aluminum or silver) to obtain a semi-transparency. But since metals shield efficiently electro-magnetic waves, their transparency stays low, therefore limiting also the OPD quantum efficiency.
A second issue arises due to the interface between the chip and the OPD. Since the uppermost layer of the chip has to act as bottom electrode for the OPD, it must exhibit a suitable work function for the rectifying behavior of the OPD. In the state-of-the-art bottom absorbing detector, the bottom electrode is a high work function material, usually ITO (as described in section 3.1.1). Since the bottom electrode can be opaque like the chip itself, an alternative high-work function material would be gold with a work function of 5.1 eV [Mic77]. Generally, metals can be well deposited in CMOS-technology, either by thermal (see section 3.3.1) and electron beam deposition or sputtering. But only a small number of metals are actually deployed in CMOS-technology due to unwanted contaminations by diffusion into silicon. Gold is CMOS incompatible due to its tendency to form deep energy traps inside the silicon bandgap. Aluminum is a preferred contacting material, but it is a low work function material with 4.3 eV [Mic77]. Using aluminum as bottom electrode for the OPD means that the whole layer structure of the OPD has to be inverted, with a high work function electrode as uppermost layer.
The easiest way to inverted the layer sequence would be to flip-chip the state-of-the-art

detector and connect it via bumps to the CMOS-substrate, e.g. via the low melting point (157 °C) Indium [Air05] which can be processed at temperatures not damaging the organic layers. But this technique is costly due to the processing itself and the use of indium.
A cost-efficient way is to develop a new kind of an organic photodetector with inverted layer structure. How the basic structure of this CMOS-compatible OPD looks like, is depicted in Fig.4.1.

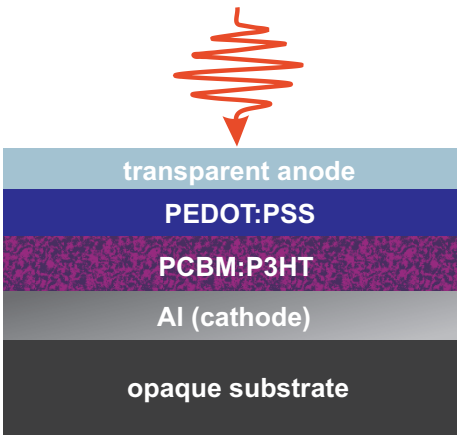

Figure 4.1: Basic layer sequence of an inverted, top-absorbing photodetector.

Inverting the layer sequence is related to several main challenges and questions:

1. How does the inverted material interfaces influence the device characteristics?
2. What top electrode material provides best device performance?
3. Is it possible to deposit the water based PEDOT:PSS solution on top of a hydrophobic blend layer?

These challenges are addressed, investigated and overcome in the following chapters.

4.1 PEDOT:PSS deposition on the hydrophobic blend

The electron-blocking layer PEDOT:PSS is commonly inserted between the photoactive blend and the anode since it considerably decreases the dark current due to suppressed leakage current to the anode (see section 3.2.3) and since it leads also to improved quantum efficiency (as shown in section 4.1.5) due to the improved photogenerated hole extraction from the photoactive blend. There are only few reports about equivalent methods to improve the device performance. Arca et al. insert self-assembling

monolayers [Arc13] and Ramuz et al. tried to omit the PEDOT:PSS by simply increasing the blend layer thickness, showing low dark currents but no EQE values for the PEDOT:PSS free OPD.
In an inverted OPD structure, the water based PEDOT:PSS solution has to be deposited on top of the photoactive blend instead on top of the ITO anode in the common non-inverted structure. This fabrication step is a challenging task since the conjugated polymers exhibit a high hydrophobicity due to the non-polarity of their bonds. Spin-coating of the PEDOT:PSS solution Clevios P VP CH 8000 directly on top of the blend resulted in no adhesion of the PEDOT:PSS at all.
In literature, different inverted layouts containing a PEDOT:PSS layer were already proposed, but focusing on organic solar cells (OSCs). A difference to photodetectors arises due to the choice of the PEDOT:PSS formulation. For organic solar cells, usually high conductive formulations like Clevios TM P VP Al 4083 (bulk resistivity $500-5000$ Ωcm) and Clevios F CPP105D (bulk resistivity $1 \cdot 10^{-2}$ Ωcm [Gla05]) are used which exhibit a higher conductance than the OPD formulation Clevios P VP CH 8000 (bulk resistivity $1-3 \cdot 10^{5}$ Ωcm). The use of the OSC PEDOT:PSS formulations increases the dark current which is not important for an OSC but critical for an OPD. Reports about sufficient wetting properties of Clevios TM P VP Al 4083 mixed with isopropanol can be found [Hau08] and also using Clevios F CPP105D was successful [Gla05, Zim07]. In this work, these chemical modifications of the PEDOT:PSS proved to be not suitable for the inverted layer structure. Mixing Clevios P VP CH 8000 with isopropanol (up to 50 %) and the wetting agent Dynol 604 (0.3 %) contained in Clevios F CPP105D turned out to properly wet the blend, but IV-measurements showed an one order of magnitude increased dark current compared to non-inverted reference samples.
Other alternatives for PEDOT:PSS deposition concern a soft contact lamination of the PEDOT:PSS onto the blend [Kim08a] and the chemical or physical change of the blend layer itself. This can be performed by silanization [Tob04] or oxidation [Hsi09] of the blend surface to introduce polar species necessary for wetting with PEDOT:PSS. In this work, a mild oxygen microwave plasma process turned out to be suitable for a proper PEDOT:PSS deposition without deteriorating the OPD performance [Bai10, Bai11a]. As already reported in detail in section 3.3.4, a sensitive plasma has to be created to avoid a damage of the blend layer surface. For typical plasma parameters used in this work, no blend damage was detected by AFM measurements.
In the next sections, the impact of the plasma treatment on the organic blend itself and on the electro-optical characteristics is reported.

4.1.1 Blend layer surface wetting

To determine the best plasma process for maximum wetting of the blend surface, different parameter sets were tested on glass substrates covered with thermal evaporated aluminum and spin-coated PCBM:P3HT blend. The aluminum layer underneath has to be included (like in the device) because of an additional heating effect arising in the

metal due to electrical currents induced by the micro-wave.
Plasma parameters which can be changed are the electrical power applied at the magnetron to generate the micro-wave (abbreviated as 'micro-wave power'), the pressure of the oxygen atmosphere and the treatment time. For a sensitive plasma treatment either the microwave power as well as the treatment time should be kept low. The minimum power which could be applied to generate a stable oxygen plasma is about 100 W. The treatment times can be varied from about 5 s (corresponding to the timescale for ignition of the plasma) to hours. After about 5 min treatment time at 100 W, a visible etching of the blend layer occurs starting at the edges of the samples while the blend distant from the edges remains unaffected. For all tested treatment times the roughness of the layers, investigated by AFM, does not change (RMS-roughness: 1.3 nm ±0.1 nm). No physical damages are observed.

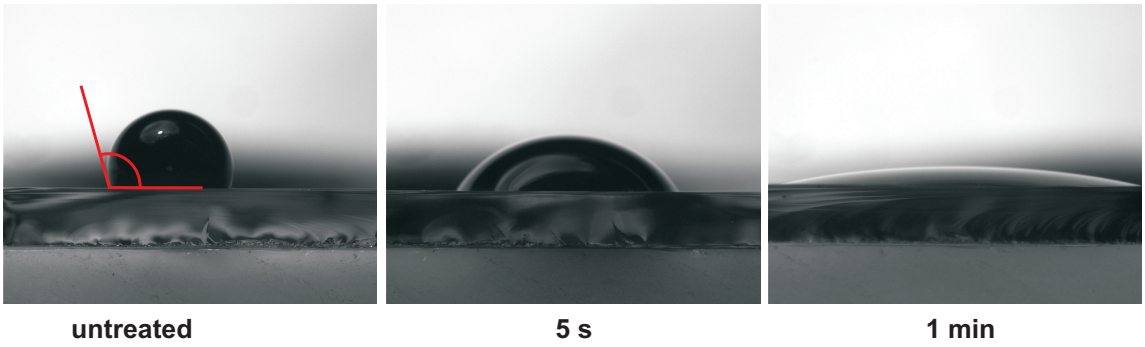

Figure 4.2: PEDOT:PSS drops on top of glass substrates covered with a blend layer. Different oxygen treatment times are employed. The contact angle is indicated in the left picture.

A quantitative parameter to measure the adhesiveness of PEDOT:PSS on top of the treated samples is the so called contact angle. It is defined as the angle between the surface of the solid blend layer and the tangent of a liquid drop of the test substance, as indicated in Fig.4.2. The contact angle is a result of the interface and surface tensions (surface free energies) between the liquid and solid material surround by air and is related to the surface energies by the Young equation, with γ_s the solid surface free energy, γ_l the liquid surface free energy and γ_{sl} the interface energy between solid and liquid:

$$\gamma_s = \gamma_l \cdot cos(\theta) + \gamma_{sl} \tag{4.1}$$

A contact angle $\theta > 90$ř indicates a hydrophobic surface with a low surface free energy and a very poor wetting ability while $\theta \to 0$ accounts for highly hydrophilic surfaces. The contact angle was determined by applying drops of PEDOT:PSS (with equivalent volumina) on the horizontal leveled substrates with the treated blend layer which were

photographed directly after PEDOT:PSS deposition (to avoid unwanted evaporation of the liquid). The contact angle between drop and surface was evaluated assuming that the drop shape is spherical. The accuracy of the measurement is limited by the manual procedure and it is estimated to be $< 2°$.
Fig.4.3 shows the the impact of the different plasma treatment times on the wetting ability of the blend layer. The untreated blend surface has a very hydrophobic contact angle of about 106°. Even very short plasma treatment times result in a strong decrease of the contact angle which is saturating for treatments longer than 15 s. The very small contact angles in the order of 10° reached by the plasma treatment indicate highly hydrophilic surfaces. Spin-coating on these samples resulted in the formation of homogeneous PEDOT:PSS layers.

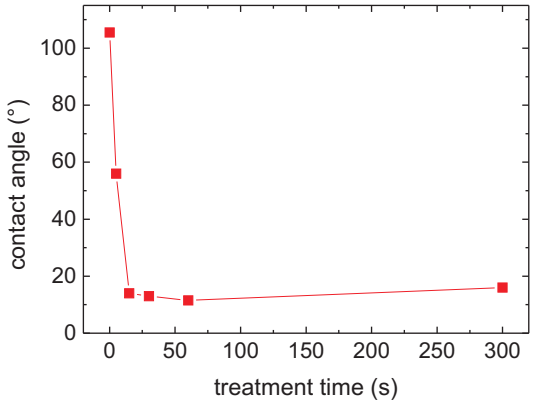

Figure 4.3: The contact angle of PEDOT:PSS drops on blend layer samples treated with oxygen plasma with different treatment times.

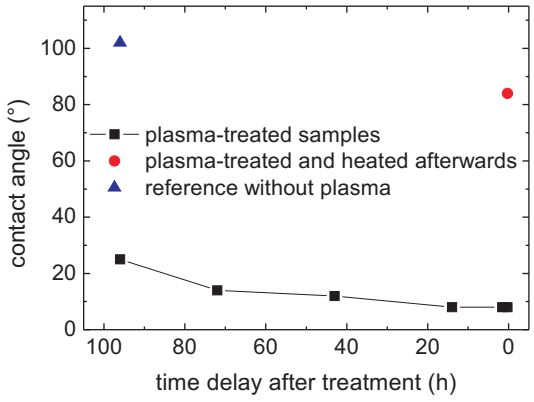

Figure 4.4: Change of the contact angle for samples stored for different times in nitrogen atmosphere after plasma treatment (1 min, 100 W). As comparison,an untreated sample and one exposed to heat after the treatment are shown.

Another issue related to the plasma treatment is the stability of the treated surface due to time delays or temperature changes before further processing. In Fig.4.4 samples are shown which were plasma treated and then stored for different time scales (up to 4 days) inside a nitrogen atmosphere. The plasma effect occurs to be quite stable during this time scale due to the small change of the contact angle. Heat applied after the treatment leads to strong change of the contact angle. A typical annealing condition for the blend (140°C for 7 min) turns the blend almost hydrophobic again. This conclusion is important for spray-deposition of PEDOT:PSS as reported in section 5.2.2.

4.1.2 Composition of the plasma-induced oxidized interface layer

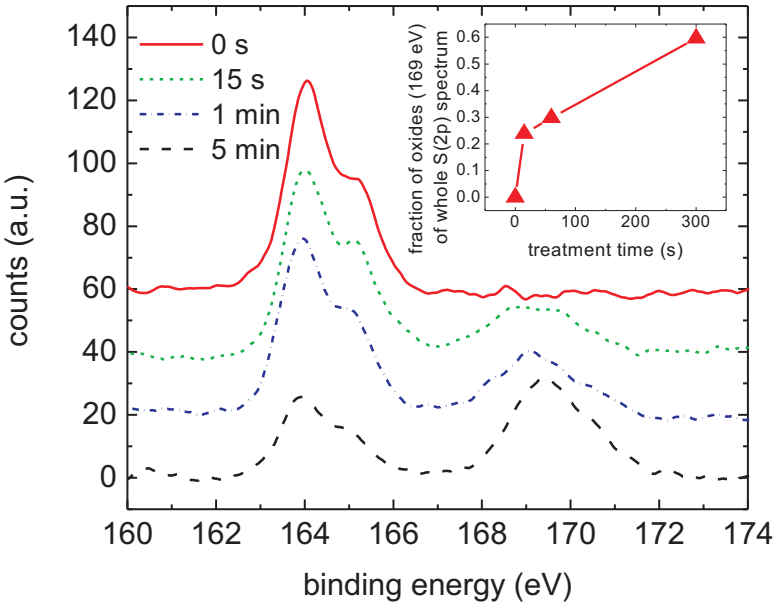

Figure 4.5: Decomposition of the S(2p) peak (164 eV) of P3HT due to different long plasma treatments. The inset shows the increase of the integrated area of the sulfur oxides (around 169 eV) with respect to the integrated area of the whole spectrum. At 165 eV the S($2p\frac{3}{2}$) signal is visible. The setup used for XPS is a SPECS MCD5 XPS instrument. The base pressure in the XPS analysis chamber was about $5 \cdot 10^{-10}$ mbar. The samples were excited with X-rays with a monochromatic MgKa radiation at 1253.6 eV. The photoelectrons were detected with a hemispherical analyzer positioned normal to the sample surface. The energy resolution was about 0.3 eV. The high resolution spectra were taken at a pass energy of 15 eV and with a 0.025 eV energy step.

To understand the chemical reactions of the oxygen plasma with the blend surface and in order to extract qualitative and quantitative information about the generated oxygen species, X-ray photoelectron spectroscopy (XPS) measurements were performed. This method (experimental details see in Fig.4.5) gives information about the electronic state of an element. The electron binding energy, corresponding to the electronic configuration of the electrons within the atom (e.g. 1s, 2s, etc.), is changed due to molecule formation like oxidation processes. The number of detected electrons in the characteristic peaks is related to the amount of the material within the area which is irradiated by the x-rays. To extract percentage values, the raw signal must be corrected by a sensitivity factor unique for each material. Still, it has to be noted, that only the photo-emitted electrons are counted. Re-capturing of electrons appears in a material depth of about 5 nm and less. Therefore the XPS measurement is only a surface sensitive measurement without giving information of the actual thickness or profile of

the modified surface, but tells about the average composition within a depth related to a distance where the electron kinetic energy is high enough to escape the material. The samples which were investigated consist as for the contact angle measurements, of a glass substrate with 100 nm thermal evaporated aluminum and a PCBM:P3HT layer (dissolved in toluene). The plasma treatment was performed at 100 W microwave power and for treatment times of 15 s, 1 min and 5 min.
Fig.4.5 shows different S(2p) spectra of the blend for the different plasma treatment times of the blend. Sulfur is present due to the thiophene ring of P3HT. Without plasma treatment, only a signal at 164 eV is present which is related to the sulfur bonded to carbon in the thiophene ring of P3HT. Beside the main peak, a second feature appears after plasma treatment at about 169 eV, which can be assigned to polar sulfur oxides. The amount of these oxides increases with longer treatment times. After an abrupt rise to an oxide content (corresponding to the fraction of oxides of the overall S(2p) spectrum) of about 25% at 15 s, it increases to 60% at 5 min treatment as shown in the inset of Fig.4.5. This result indicates that for gaining a sufficient wetting ability, the blend surface has to be significantly changed. For 1 min, a typical treatment time, already about one third of the P3HT molecules (P3HT concentration in the blend is 50 %), exhibits a oxidized thiophene ring. This effect is also pronounced

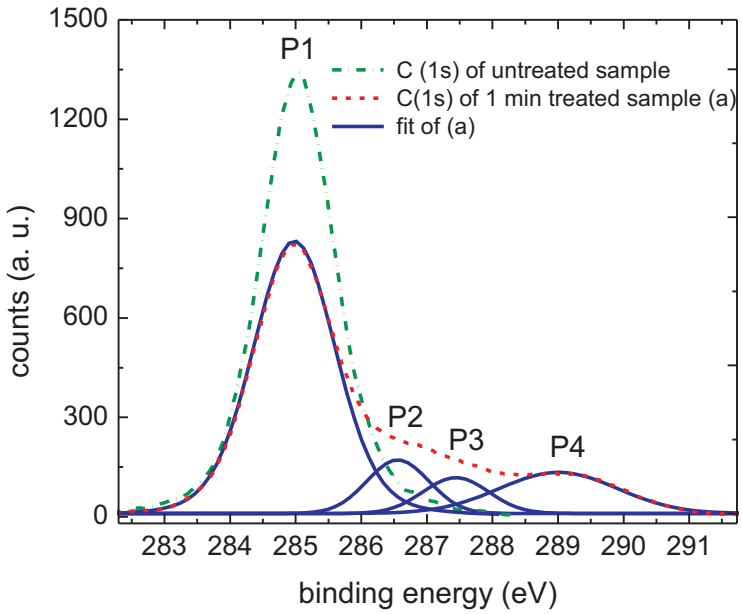

Figure 4.6: Decomposition of the C(1s) peak of the PCBM:P3HT blend after a 1 min long plasma treatment. The envelope curve represents the measured spectrum of the 1 min treated sample. Using Lorentz-Gauss shapes, different peaks (P1-P4) were fitted.

in the C(1s) spectrum. Since carbon is the main element contained in both PCBM and P3HT, the change of it gives a hint on the overall oxidation of the blend. In Fig.4.6 two samples are compared, the untreated with a 1 min treated sample. Both exhibit a

main peak at 285.0 eV (P1) due to the C-C and C-H bonds of the conjugated polymers. With the plasma treatment a higher energy shoulder besides the main peak at 285.0 eV becomes apparent. According to typical chemical species found on plasma treated polymers [Lop91, Lis93], three different components (P2, P3, P4) to the spectrum shoulder on the right side of the main peak (see Fig.4.6) can be qualitatively identified. The P2 peak at 286.5 eV corresponds to C-O bonds (hydroxyl, ether), P3 at 287.9 eV to carbonyl (C=0) or double ether (O-C-O) bonds, and P4 at 289.0 eV is due to ester (O=O-OH) and carboxyl (O=C-O) groups. All these species are polar functional groups enhancing the hydrophility of the blend surface.

4.1.3 Impact of plasma treatment on device performance

The blend layer hydrophilization with plasma treatment was demonstrated in the previous sections. The impact of the modified blend layer surface on the electro-optical performance of inverted organic photodetectors will be investigated within this and the next section.
Since the hybrid CMOS concept requires aluminum as bottom electrode, this material was also chosen for the large scale spin-coated reference samples with a lateral diode size of 7 mm^2. The general architecture was already described in section 3.1.2 and 3.1.1. As top electrode the high work function material gold was chosen due to the possibility of thermal evaporation and since it exhibits a semi-transparency for thin layer thicknesses.
The blend layer was prepared and spin-coated as described in the *experimental details*. The use of toluene as solvent results in a blend layer thickness of 110 nm after spin-coating. The PEDOT:PSS solution was spin-coated on top of the plasma-treated blend, resulting in a thickness of 170 nm. Along with the inverted OPDs, also non-inverted reference samples were fabricated with ITO as bottom and aluminum as top electrode. All fabrication steps were performed under nitrogen atmosphere.

In Fig.4.7 the IV-curves of the inverted together with non-inverted reference samples are shown. The plasma treatment on the blend layer was performed for 1 min and at 100 W. The non-inverted reference with ITO shows typical light and dark current characteristics. Compared to that, also the inverted OPD exhibits an equally good light-on/off-ratio for external bias larger than -1 V which indicates that the plasma treatment does not severely alter the carrier injection and extraction properties of the photoactive layer.
Obvious differences with respect to the non-inverted reference are the decreased forward current of the inverted diode (factor 100 @ + 2 V) and a photocurrent decrease for low reverse bias between -1 V and the open circuit voltage V_{oc} which is smaller than for the non-inverted reference. This deviation from the expected exponential behavior is observable as a kink respective s-shape in the linear scale which is shown in Fig.4.9. The forward photocurrent density of an inverted diode measured up to 3 V is shown

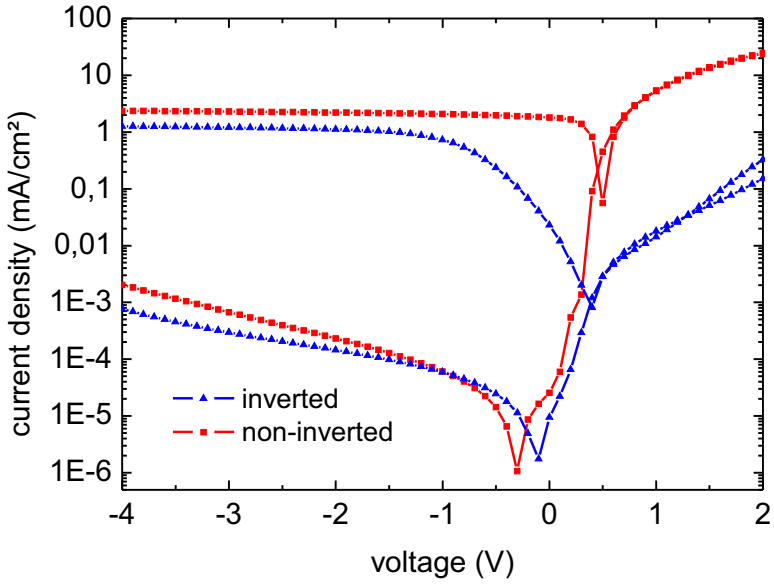

Figure 4.7: Typical IV-curves of an inverted diode and a non-inverted reference diode (with an ITO-anode) for dark and illuminated conditions. The applied light intensity was 100 mW/cm^2.

in Fig.4.8. For bias voltage starting at V_{oc} up to V < 0.5 V the current can be well fitted with an exponential increase $e^{qV/nkT}$ (with q=elementary charge, n=ideality factor, k=Boltzmann constant, T=temperature) according to the Shockley equation for inorganic diodes. For increasing voltage the current slope begins bending downwards (which might be related to a serial resistance) before it increases stronger again for bias voltages higher than +2.2 V best fitted with a V^4 voltage dependence. This voltage dependence V^m with $m \geq 2$ is typical for space charge limited current (SCLC) [Mon09, Jai01, Kum09] (see section 3.4.1). Generally, SCLC describes the charge transport in a material with low conductivity, where the concentration of the injected charge (into an organic layer) may exceed the intrinsic charge concentration which is followed by the build-up of space charge. Without traps or shallow traps involved in SCLC and without an effect of the electrical field on the mobility $m = 2$ holds, but if deep traps or a field dependent mobility are present $m > 2$ accounts, which is characteristic of the filling of exponential distributed traps [Mon09]. The fact that also at high forward bias of +3 V the exponent m is equal to 4, hints to a high number of trap states which still captures charges. Otherwise the IV-curve would bend downwards to change to a square law dependence.

Since the plasma treatment introduces a big amount of interface states by generating oxides on the blend, the origin of the SCLC in the inverted devices can be understood as follows. The oxides act as traps which accumulate charges which in turn reduce the electric field inside the device. That oxides can indeed lead to SCLC, is observed during

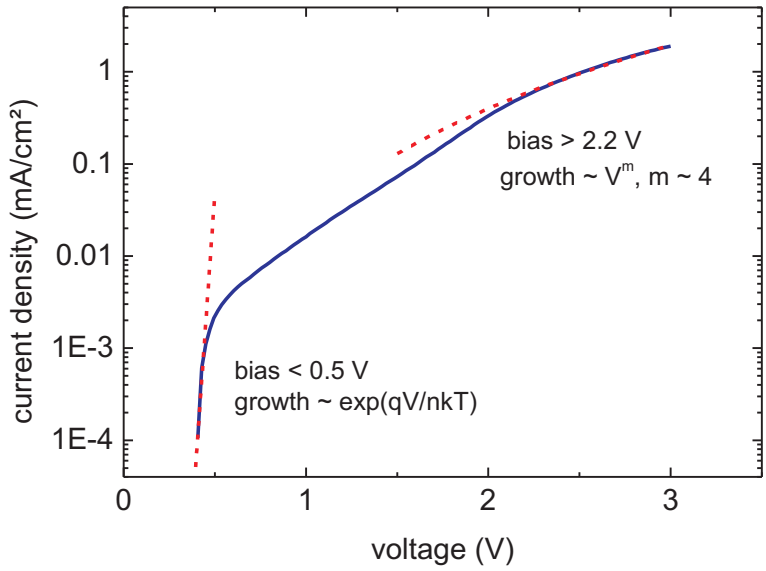

Figure 4.8: Semilogarithmic plot of the forward photocurrent density of an inverted device. The dashed curves represent fitted curves.

lifetime measurements [Jor08, Kre07] of solar cells and is related to oxygen diffusion into the device forming insulating interfaces, especially between the low work function electrode and the polymer layers.

A qualitative explanation of the s-shaped photocurrent in Fig.4.9 can be given by discussing the influence of the electric field E_{sc} generated by the space charge. For point A in Fig.4.9, the external electric field E_{ext} (reverse bias) is high which is equivalent to $E_i + E_{ext} >> E_{sc}$, with E_i the internal electric field respective built-in field of the device. At A, the photocurrent is high and starts to reach a plateau value for large reverse bias. For decreasing the external field at B, the photocurrent decreases too since E_{sc} becomes the dominant electric field in the device. E_{sc} is a counter electric field to the reverse bias since the photogenerated holes which are transported towards the anode by the external field charge the oxide traps positively, building up a space-charge region. Hence, the hole transportation through the positively charged interface is slowed down. At C, there is no drift component of the charge transport and $E_i + E_{ext} = E_{sc}$ is valid. Compared to the non-inverted reference with ITO, V_{oc} is decreased for the inverted OPD (from $V_{oc} = 0.5$ to 0.4 V) due to the space charge field. Also in forward direction, at D, E_{sc} decreases the current since hole injection creates an additional barrier for the holes traveling through the plasma-treated interface.

The electric field E_{sc} generated by the accumulation of the holes is also visible in the dynamic light response of the OPD since it has a characteristic time constant to reach

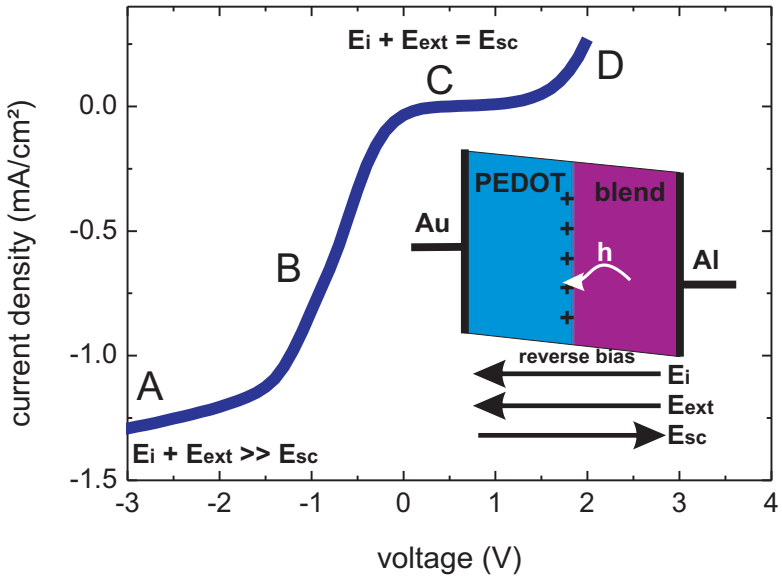

Figure 4.9: The photocurrent of the inverted device shown in Fig.4.7 on a linear scale. The different regimes A-D are explained in the text.

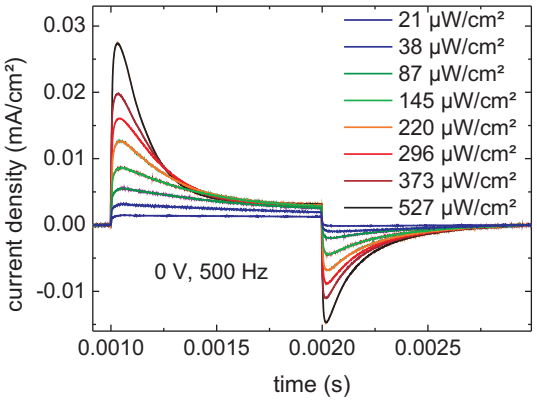

Figure 4.10: Photocurrent density shape versus time of various light intensities (1 ms long square pulse) without applied bias voltage.

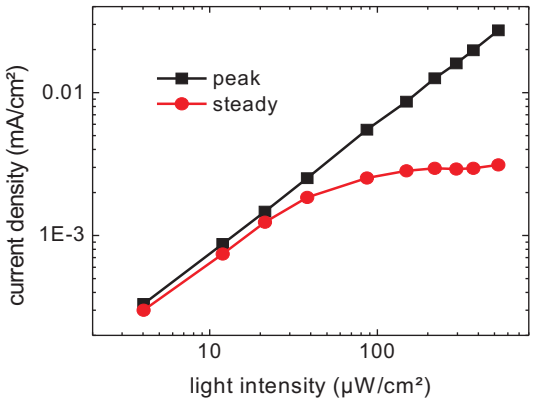

Figure 4.11: Increase of the photocurrent peak and the steady state value as function of the light intensity on a double-logarithmic scale.

the saturation value. In Fig.4.10 the photocurrent of an inverted device after illumination with a 1 ms long square light pulse with different light intensities for $E_{ext} = 0$ is shown. Illumination of the device with the pulse leads to the formation of a signal peak at the beginning of the light pulse response which starts to decrease within a time range of about 0.5 ms to a steady state value. A similar transient shape was observed

before by Zaus et al. [Zau07] when inserting a hole conductor layer with low hole mobility in a non-inverted PCBM:P3HT photodetector. The observed characteristic peak (at the beginning of the photoresponse) which increases within several microseconds, is due to a normal transient response with a typical rise time as described in section 3.4.3, dominated by the carrier transient time and the RC-time constant. During the carrier transport, holes are trapped at the oxides which leads to a continuous increase of the counter field E_{sc} which results in an exponential decrease of the photocurrent on a time scale of about 1 ms. After the light pulse, there is a negative signal of the photoresponse observed which is due to the decay of the accumulated charge. At 500 µW/cm^2, the accumulated charge, calculated as the integral of the negative signal, reaches a value of $3 \cdot 10^{-9}$ C/cm^2.
While the peak value of the photoresponse increases linearly with increasing light intensity, as shown in Fig.4.11, as for normal organic photodiodes [Bra01], for the steady state value a saturation effect occurs at about 50 µW/cm^2 which indicates the efficient trapping of the increasing amount of photogenerated charges. Below this value, the amount of photogenerated charges is not sufficient to build up a E_{sc} with significant strength.

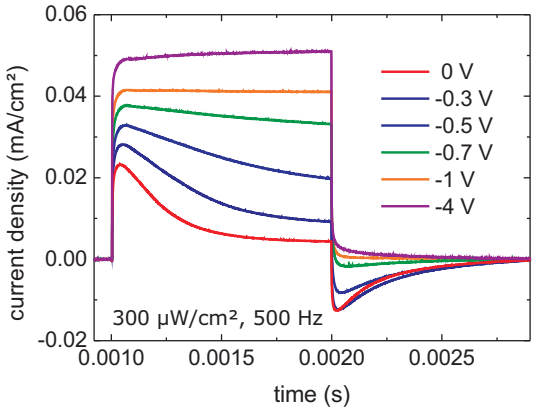

Figure 4.12: Dependence of the dynamic photocurrent density shape of various bias voltages. The light intensity is 0.3 mW/cm^2.

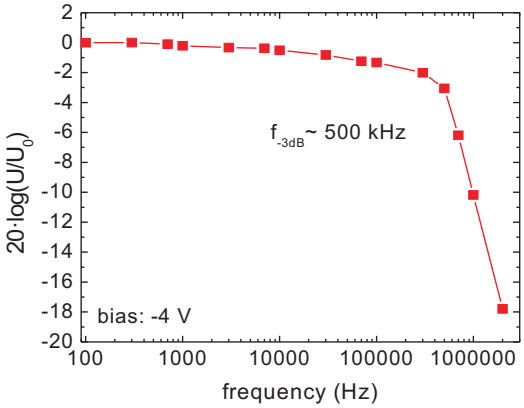

Figure 4.13: Frequency response of the inverted diode for an applied voltage of -4 V.

For applying an additional external bias voltage, the shape of the photoresponse changes, which is illustrated in Fig.4.12. For bias voltages larger than -1 V, a value at which the kink of the IV-curves disappears and $E_i + E_{ext} >> E_{sc}$ accounts, a behavior is observed which is typical for organic photodetectors and not dependent on the light intensity. Within typical rise times of about 5 µs @ -1V the photocurrent reaches a plateau, see Fig.4.12. The corresponding cut-off frequency measurement, measured at -4 V, is shown in Fig.4.13, measured by applying 300 µW/cm^2 at 530 nm wave length.

A further understanding of the impact of the oxide traps can be gained by determining the influence of an increasing oxidation of the blend layer on the electronic performance. Inverted OPDs were fabricated with different treatment times and different microwave powers. The on/off ratio between light and dark current was similar for different samples, but a change of the forward current density and of the photocurrents (Fig.4.14 and Fig.4.15), could be observed. For either increasing treatment time or plasma power the forward current density increases too. In addition, also the kink at reverse bias is influenced. For the smallest applied power (respective times $\leq$ 15 s, not shown here) the kink is more pronounced. This observation is a contradiction of the SCLC

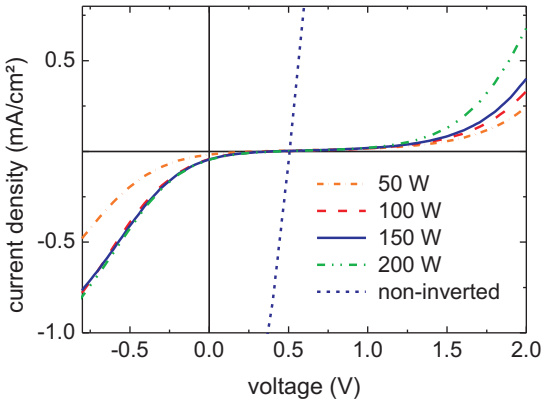

Figure 4.14: IV-curves (linear scale) under illuminated conditions (100 mW/cm^2) for plasma treatment performed with different power settings. A non-inverted device is shown as reference.

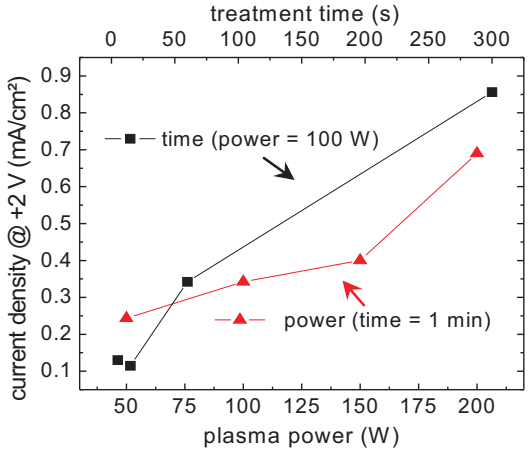

Figure 4.15: Increase of the forward photocurrent density @ +2 V with increasing plasma treatment time and microwave power.

model. Since, as shown in Fig.4.5, the amount of sulfur oxides on P3HT increases on the blend surface with time, also the number of trapping states increases. This should result in an increased space charge field due to the increased number of accumulated holes. An additional effect that could explain the observation is suggested by the author [Bai10]. Since also traps located well below the intrinsic DOS distribution (deep traps) can take part considerably at the transport when sufficiently states are available [Ark02], an increased number of oxides can enhance the current transport by trap-assisted hopping. This additional contribution can decrease the built-up of space charges at the plasma-treated interface. This assumption is further investigated in the following section.

4.1.4 Impact of different solvents on device performance

In order to investigate the assumption that trap-assisted hopping transport can alter the SCLC characteristic, a possibility is to alter the nano-morphology of the blend and

with it the number of transport paths.
The use of different solvents influences the random-networking of the PCBM and P3HT phases as reported in [Aud10, Yao08]. Audinot et al. [Aud10] report on a P3HT enriched surface of a blend layer dissolved in 1,2-dichlorobenzene (DCB). This effect should have a positive influence on the inverted devices since a high amount of P3HT, which is responsible for the photogenerated hole transport towards the anode, would also result in a high number of trap states after plasma treatment.
To compare the P3HT amount in layers fabricated with two different solvents, namely toluene (as so far used) and DCB, XPS measurements of the S2p spectrum were performed. In Fig.4.16 two plasma-treated (1 min) blend layers, fabricated with toluene and DCB, are shown. Both show a very similar shape, the peaks correspond to the created sulfur oxides at about 169-170 eV and to the sulfur in the thiophene at 164 eV (as already shown in Fig.4.5). For both solvents, the amount of oxides compared to the overall S2p spectrum is about 40 %. The signal height of the blend layer prepared with DCB is much larger than compared to toluene. The ratio of the integrals of the two spectra reveals a factor 5 higher signal for DCB. This result confirms the P3HT enrichment on top of the DCB-blend layer surface. This finding is finally proofed by the

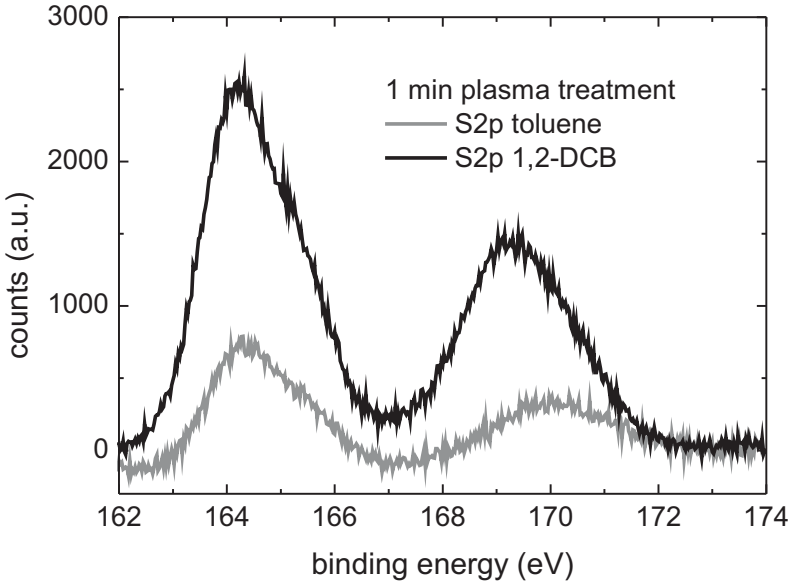

Figure 4.16: Decomposition of the S(2p) peak (164 eV) of P3HT due to plasma treatment for two different blend layers. One is prepared with DCB, the other with toluene.

IV-characteristic of the inverted OPD prepared with DCB, as shown in Fig.4.17. Two inverted devices are identical except for the blend layer, one fabricated with toluene and a thickness of 110 nm and the other spin-coated to 300 nm by using the high-boiling point solvent DCB. Due to the slow evaporation of the DCB, spin-coating results in

much higher layer thicknesses for the same polymer concentration compared to toluene.

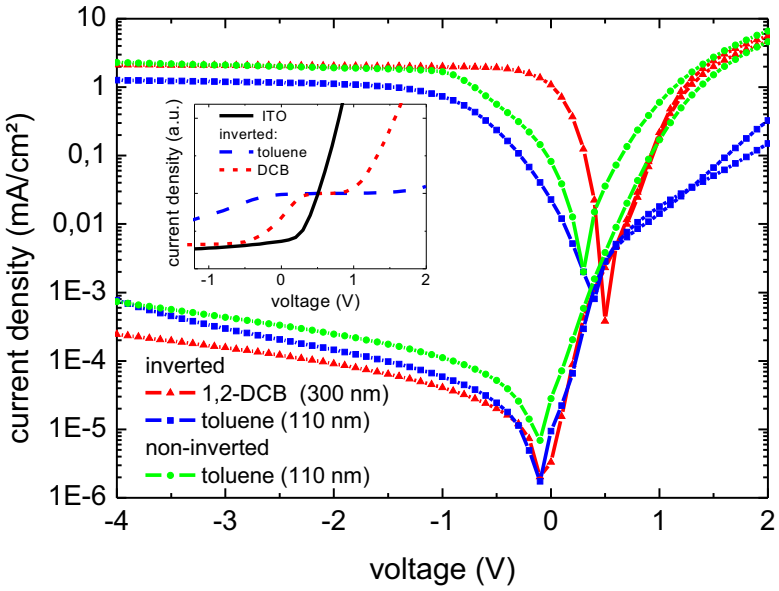

Figure 4.17: Typical IV-curves of inverted and non-inverted diodes (with ITO) prepared with toluene and with DCB for dark and illuminated conditions. The applied light intensity was 100 mW/cm^2.

The SCLC is much less pronounced for DCB since the s-shape is reduced as well the forward current increased. This is even better visible on a linear scale, shown in the inset of Fig.4.17, including a non-inverted reference without plasma treatment as comparison. Going from forward to reverse bias, the photocurrent plateau value is reached at about -0.5 V for using DCB, compared to -1 V for using toluene as solvent. This result supports the assumption that indeed the number of trap hopping paths influences the impact of the built-up of space charge within the device.
In Fig.4.17, V_{oc} is slightly increased (by 0.1 eV) which can be due to the reduced space charge field or also related to the different blend composition. The dark current could be almost improved by one order of magnitude by using DCB. This effect is not due to the different nano-morphology but simply related to the higher blend layer thickness which decreases the probability of ohmic leakage paths (e.g. pure PCBM or P3HT phases) from one electrode to the other. OPDs made with DCB with the same layer thickness as the toluene devices exhibit an equal dark current compared to toluene.

Fig.4.17 shows in addition an IV-curve of a non-inverted device with a blend layer, fabricated with toluene, and exposed to an oxygen plasma (100 W, 1 min) prior to aluminum evaporation. The difference to the inverted diode (fabricated with toluene)

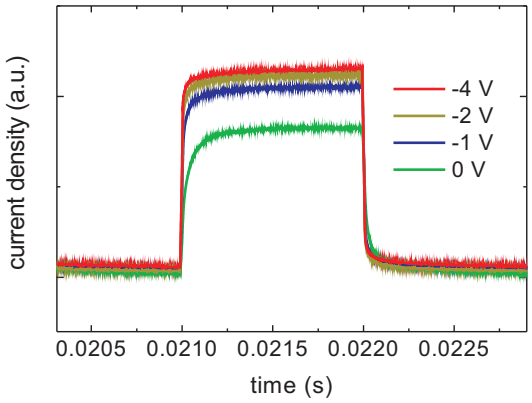

Figure 4.18: The bias voltage dependence of an inverted OPD prepared with DCB for a light intensity of 800 µW/cm^2.

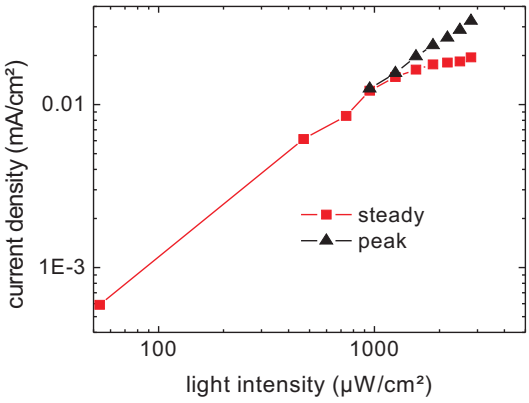

Figure 4.19: Increase of the photocurrent peak and the steady state value of the photoresponse as function of the light intensity on a double-logarithmic scale.

is that at the blend (PCBM)-Al interface of the non-inverted device electron injection and extraction occurs and the blend (P3HT)-PEDOT:PSS interface of the inverted device enables hole transport. A different device performance of the two diodes would therefore further confirm the impact of a P3HT respective PCBM gradient within the blend layer. The plasma-treatment of the blend in the non-inverted device before cathode evaporation leads to the formation of a kink resembling to that of the inverted device. A pronounced difference between the plasma-treated non-inverted and the inverted OPD is the increased forward current density (factor 25 @ +2 V).
The increased forward current density resembles more that one of the inverted device fabricated with DCB. According to the assumption that trap states are involved in the current transport, this behavior can be explained with the different plasma layer interface. Whereas the inverted device fabricated with DCB exhibits a P3HT enriched blend surface for efficient hole transport from the gold anode, the non-inverted device fabricated with toluene can efficiently transport electrons through the plasma-treated blend interface from the aluminum cathode since it is enriched with PCBM (and depleted of P3HT).

The reduction of the space charge field of devices fabricated with DCB is also strongly visible in the dynamic photoresponse which is illustrated in Fig.4.18 and Fig.4.19. In Fig.4.18, although a high intensity is applied to the photodiode, there is no overshoot visible in the beginning of the photoresponse for small applied external bias. Typical response times are slightly higher compared to the thinner toluene blend due to the higher transit time through the blend. The rise time is 5-10 µs for external bias applied and about 100 µs for 0 V. Typical cut-off frequencies measured are around 300-350 kHz. In Fig.4.19 the light dependence of the photoresponse without applied

external field is showed in analogy to Fig.4.11. There is a strong difference between toluene and DCB devices regarding the amount of light which is necessary to create an overshoot at the beginning of the photoresponse as shown for toluene in Fig.4.10. For toluene, the onset light intensity is only about 50 µW/cm^2 whereas for DCB this value increases to about 1000 µW/cm^2. This improvement is quite important for an application as imaging device since highly linear responses are required for signal processing.

Another important electro-optical device characteristic not discussed until now, is the external quantum efficiency (EQE). This performance value is limited by the transmission of the top electrode. As already mentioned, gold was chosen as top electrode due to the suitable work function and the possibility of thermal evaporation. A 20 nm thick layer of gold, exhibiting a roughness of about 2 nm, was deposited on top of the hole conductor. The transmission of this layer, compared to the standard material ITO used in non-inverted photodetectors, is shown in Fig.4.20.
Compared to ITO, the gold layer exhibits a remarkably decreased transmission due to the efficient screening of light by the free electrons. Fortunately, the maximum transmission of the gold layer corresponds to the absorption maximum of the blend layer. Still, the maximum transmission of 55 % limits the EQE to the same value in case

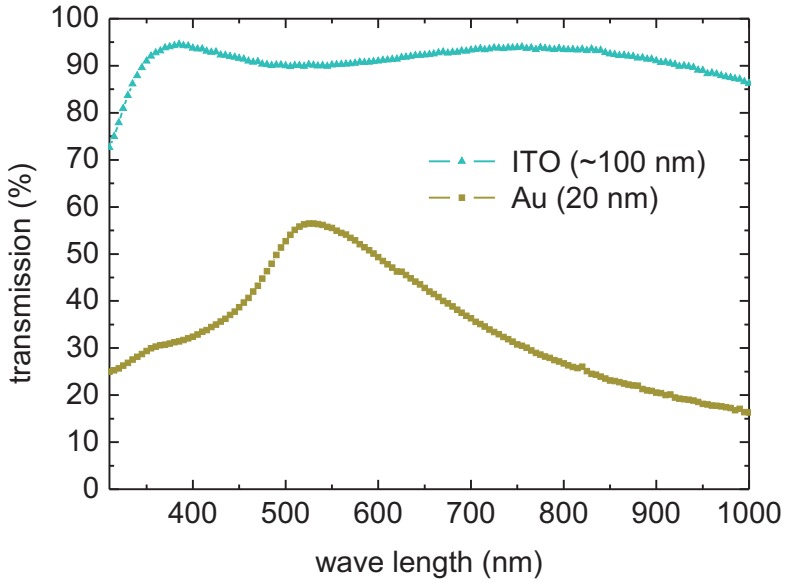

Figure 4.20: Transmission of a 20 nm thick gold layer and of an about 100 nm thick ITO-anode.

no further losses appear. The other losses, which have to be taken into account for a device, are due to the light transmission through the hole conductor PEDOT:PSS and the encapsulation layer (for the inverted OPD) respective glass substrate (for the non-inverted diode). These losses were measured at a complete stack of relevant materials.

At 500 nm, for a non-inverted device, about 80% of the incoming light is transmitted to the blend layer (through the glass-substrate, the ITO-anode and a 170 nm thick PEDOT:PSS-layer). In an inverted device, a maximum of 50% of the photons at 500 nm reach the blend layer after passing the encapsulation, the gold and the PEDOT:PSS layer.
Theses limits can be compared with the spectral EQE, measured at -4 V, shown in Fig.4.21. Comparing the EQE @ 500 nm with the amount of light reaching the active layer after transmission, about 75 % of the photons are converted into current for both the non-inverted and the inverted diode. Thus the reduced EQE of inverted devices can be completely explained by the loss of light due to the reduced transmission of gold. There is no indication that the plasma treatment has a negative impact on the EQE.
For the two different solvents toluene and DCB, there is no remarkable difference visible in the EQE. OPDs prepared with DCB exhibit slightly higher EQE due to the increased absorption length in the thicker blend for the incident photons.
The space charge field due to the plasma treatment is only visible in the EQE measurements for low reverse bias since then the condition $E_i + E_{ext} \rightarrow E_{sc}$ is valid. This leads to a strong non-linear dependence of the EQE on bias voltage instead of a linear dependence usually observed [Pun07]. As can be seen in Fig.4.22 for an inverted OPD prepared with toluene, from -1 V to 0 V bias, at which also the s-shape of the IV-curve is present, the EQE decreases as much as between -4 V to -1 V. A similar observation was made for devices prepared with DCB. For both, a saturation of the efficiency is reached for bias voltages larger than -5 V.

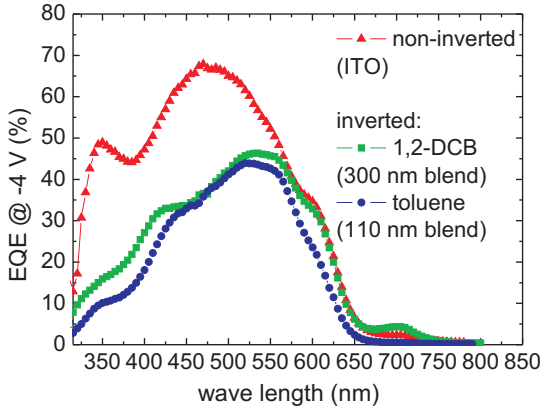

Figure 4.21: External quantum efficiency (EQE) of a non-inverted and two inverted diodes (prepared with toluene respective DCB) for an external bias voltage of -4 V.

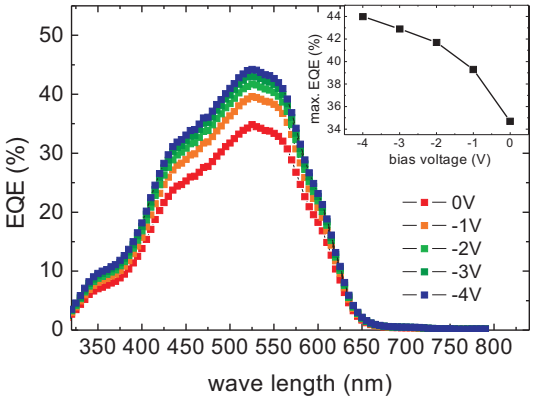

Figure 4.22: The bias dependence of the EQE of the inverted OPD prepared with toluene.

4.1.5 OPDs without the hole-conductor PEDOT:PSS

The plasma-treatment is necessary to deposit the water based PEDOT:PSS. Since it leads to the formation of an additional interfacial layer, the impact on the device characteristics without the PEDOT:PSS layer could be of interest. Devices were fabricated as reported so far, with 1,2-DCB as solvent, and with the plasma treatment, without inserting the PEDOT:PSS layer but directly evaporating the gold electrode on top. Additional OPDs without plasma treatment and without PEDOT:PSS were fabricated as reference diodes.
In Fig.4.23 the results are illustrated. Compared to the standard inverted OPD, the OPD with just a blend layer exhibits the expected high dark current. This is due to the low-resistive, ohmic pathways through the photoactive film which consists of only one phase of donator or acceptor material which result in a decreased shunt resistance of the device. By inserting the PEDOT:PSS layer, dark electron injection from the anode to the blend is blocked and, regarding the high resistance of the PEDOT:PSS layer, also the transport of the thermally generated holes towards the anode is hindered. These effects lead to the about two orders of magnitude decrease of the dark current by inserting the high resistive formulation Clevios P VP CH 8000.
The sample without PEDOT:PSS, with the oxide layer, shows an even better device

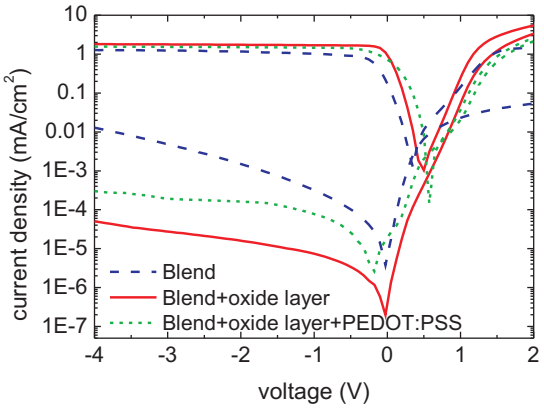

Figure 4.23: IV-curves of the OPDs with untreated blend, treated blend and treated blend with included PEDOT:PSS layer.

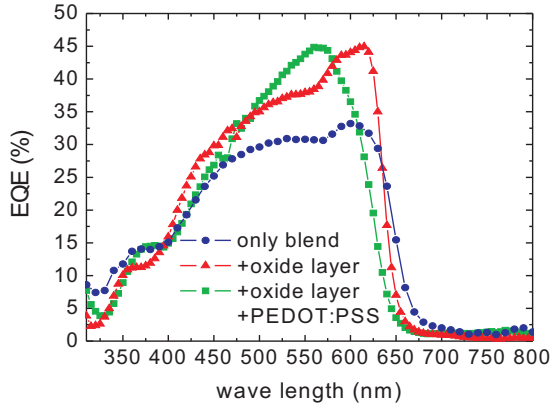

Figure 4.24: External quantum efficiency (EQE) of the different structured inverted OPDs at an external bias voltage of -4 V.

performance. The dark current is further reduced to about $5 \cdot 10^{-5}$ mA/cm^2 at -4 V. Also the EQE is remarkably improved compared to the pristine blend layer. As showed in Fig.4.24, the EQE is increased from 33 % (untreated blend) to 45 % for the treated blend without PEDOT:PSS. The origin of these improvements is not clear. It can be related to a similar working principle as with PEDOT:PSS, but an effiecient suppressing of carrier injection might be difficult due to the very thin thickness of the oxide layer, which is in the range of some nanometers, since tunneling can occur. That

the oxide interfacial layer is indeed very thin and sensitive is supported by the fact that about 50 % of the fabricated samples exhibit a behavior as the untreated sample showed in Fig.4.23. It seems that the layer can be easily damaged, e.g. by the thermal evaporation of the gold layer. This high scrap rate hampers the application of this concept for a hybrid imager.

4.2 Aluminum as cathode material

Aluminum is a commonly used cathode material due to its low work function of 4.3 eV [Mic77] which is similar to the LUMO level of PCBM at 3.7 eV (see section 3.2.2.2). A characteristic of aluminum is an excellent corrosion resistance due to the forming of a native oxide (Al_2O_3) when exposed to air or water. This thin layer effectively prevents further oxidation. The thickness of this native layer is quite thin, in the range of 2 nm [Lu08] and it forms instantly after air exposure. Since the native oxide is an insulator, the presence of it on top of the aluminum cathode can alter the interface properties to the organic materials. The inverted OPD can be fabricated in nitrogen atmosphere, but the fabrication of the CMOS chip is performed in air. A typical time scale between aluminum deposition on the chip and further organic fabrication can be in the order of weeks.

4.2.1 Oxidation of the aluminum cathode

In order to investigate the influence of the native oxide on the electric behavior of the inverted OPDs, 100 nm thick aluminum layers were thermally evaporated and oxidized under different conditions. Two substrates were stored under ambient air conditions and two under nitrogen atmosphere, for two respective six days. The oxygen contamination inside the glove box with nitrogen atmosphere was around 1 ppm.
Together with a fresh evaporated aluminum layer, the substrates were used for OPD fabrication. In Fig.4.25 the measured IV-characteristic is shown.

Whereas the dark current in reverse direction is not affected by the changed organic-aluminum interface, the method of storing as well as the time scale of oxidation lead to different forward and photocurrent behavior. The IV-curve of the device stored six days in the glove box shows slightly decreased forward current and photocurrent around 0 V bias. The oxidized samples exhibit strongly changed characteristics. The sample stored six days in air shows strong disturbances of the photocurrent around 0 V. The open-circuit voltage point is shifted to lower values. The strong decrease of the photocurrent around 0 V hints to a space charge limited current similar to the space charge region at the plasma treated blend surface. Similar observations at the aluminum-organic interface were made by Glatthaar et al. [Gla07] who reported about slow charge transfer at the aluminum-organic interface of an organic solar cell due to a corrosion of the

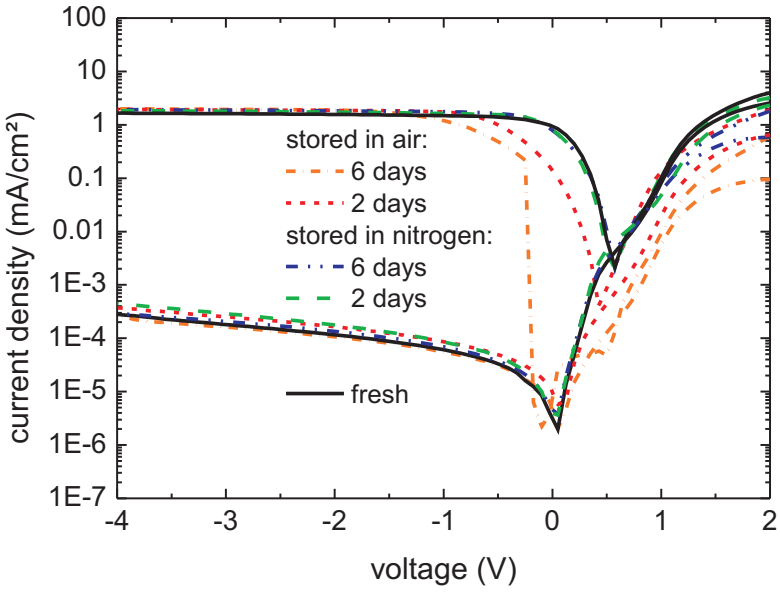

Figure 4.25: IV-curves of inverted OPDs with oxidized aluminum bottom electrodes.

aluminum electrode. Interestingly, for other organic materials in non-inverted layouts contradicting reports can be found. Vogel et al. [Vog06] reported about reduced solar cell performance due to recombination centers at the C60-aluminum interface because of aluminum diffusion during thermal evaporation of aluminum without involving oxides. Li et al. [Li97], faced a similar problem, showed that these unwanted aluminum gap states can be eliminated in an OLED by introduction of a thin layer of Al_2O_3 between the organic emission layer Alq_3 and the aluminum layer.
The EQEs of all devices in Fig.4.25, not shown here, are hardly influenced in reverse bias. At -4 V, only the device stored 6 days in ambient air showed an EQE reduction of about 5 %.
According to literature [Bar12], the saturation thickness of the native oxide, in the range of a few nanometers, is reached within hours. But the results in Fig.4.25 suggest, that the oxidation occurs on a larger time scale. To investigate this, also a 5 months old aluminum substrate (exposed to ambient air) was used for OPD fabrication. The IV-curve, shown in Fig.4.26, is strongly influenced compared to the reference diode. This final result hints to either a time-dependent thickness growth of the oxide or the occurrence of additional chemical reactions. Although the aluminum covered substrates were carefully cleaned with acetone and 2-propanol before further fabrication, still water might be attached to the surface reacting with the organic layers.
As conclusion, regarding the time delayed fabrication of the OPDs on top of CMOS-substrates, a treatment of the aluminum surface is necessary for good electrical performance.

4.2.2 Removal of the native aluminum oxide

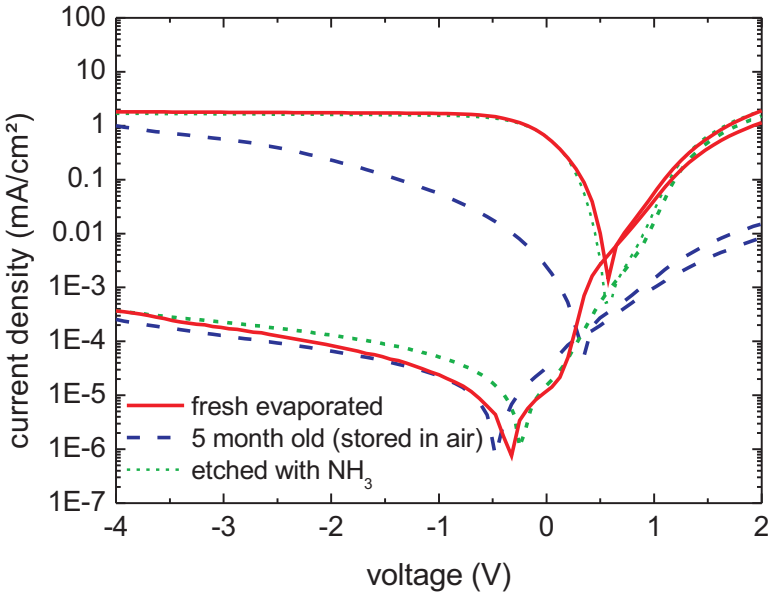

Figure 4.26: IV-curves of inverted OPDs with and without wet-chemical etching of the aluminum bottom electrode.

The native oxide on top of the aluminum layer can be either removed by physical methods (e.g. reactive ion etching) or wet chemical etching. Taking into account that the whole CMOS-chip, maybe already bonded and mounted inside a chip carrier, has to withstand the treatment, a physical method is not practicable since the electromagnetic fields involved could cause a damage to the chip (see also section 6.1.2). A more convenient way is wet-chemical etching with suitable etchants comprising low-etching rates and a high selectivity since the aluminum itself should not be considerable removed. Since Al_2O_3 is harder than aluminum itself, it turned out that only an etchant with an extremely low etching rate leads to satisfying results. Ammonium hydroxide NH_4OH, with a concentration of 30 % in water, was identified as suitable candidate since it comprises a low etching rate of about 30 nm/min (of both aluminum and the oxide) and does not react with the silicon or the passivations layers like SiN of the CMOS chip. The echting rate was determined with AFM which also proofed that there is not any surface roughness increase due to the etching.
Etched aluminum layers were used for inverted OPD fabrication to prove the suitability of the method. In Fig.4.26 three different devices are shown: an OPD fabricated with fresh aluminum and two with aluminum bottom electrodes exposed 5 months to ambient air. One of them was directly etched for 30 s with NH_4OH in ambient air before further processing in nitrogen atmosphere. The unetched sample shows a strong

degradation due to the native oxide layer as discussed before, whereas the etched sample does not differ from the reference sample.
In addition, further tests demonstrated that ammonium hydroxide does not damage (for a typical etching time of 30 s) electronics nor bonding wires on the CMOS-chip. Only for long exposure to the etchant (> some minutes) a damage could be observed with the microscope on the aluminum pads respective bottom electrodes for the organic photodiodes.

4.3 Inverted OPDs with a solution-processable polymer electrode

So far it was shown that the inverted OPDs exhibit comparable device performance to the non-inverted OPDs with an ITO anode. The only drawback concerns the low transmission of the semi-transparent gold top electrode which reduces the EQE as reported in section 4.1.4. To improve the EQE, the gold layer thickness can be decreased to enhance the transmission. In Fig.4.27 the spectral resolved transmissions of three different gold layers evaporated on glass substrates are shown. The 20 nm thick gold

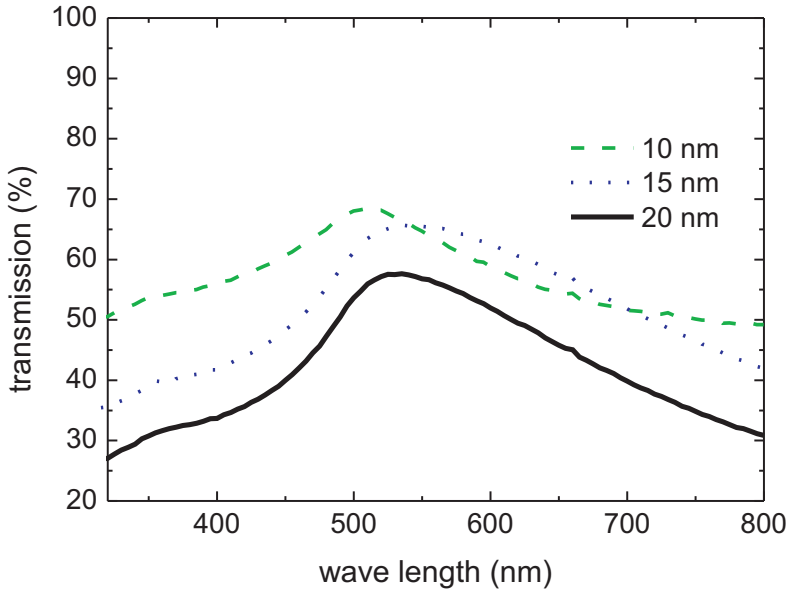

Figure 4.27: Transmission of thermal evaporated gold films with different thicknesses.

film was so far used for device fabrication. By decreasing the thickness by factor 2, the maximum transmission is improved from 55 % to about 70 %. Also the spectral shape is more flattened for the 10 nm thick gold film. This result indicates that also

the EQE could be positively influenced. But the fabricated devices with a 10 nm and also a 15 nm thick gold anode exhibit a strong device degradation (not shown here) during subsequent IV-curve measurements visible as decrease of the photcurrent and the forward current. Although the overall RMS-roughness of gold is < 5 nm, a probable strong local decrease of the already shrinked layer thickness, resulting in the formation of highly resistive spots, could explain the degradation since these resistive spots can heat up during the current flow and damage the heat sensitive organic layers underneath.
Hence, to improve the EQE, the gold layer has to be replaced by a material with similar high work function, but enhanced transmission. Since the deposition of transparent conductive oxides like ITO involve high temperatures and kinetic energies which can damage the organic layers [Sch09], they are not suitable electrode materials for the inverted OPD.
An alternative is the conductive version of the polymer poly(3,4-ethylenedioxythiophene) : poly(styrenesulfonate) (PEDOT:PSS). As described in section 3.2.3, it is solution-processable, highly transparent and it is a suitable anode material due to the high work-function of 4.8-5.2 eV. It is well known that by adding high boiling point polar solvents as ethylene glycol, N-methylpyrrolidone and dimethylsulfoxide, PEDOT:PSS undergoes a conductivity increase of several orders of magnitude [Cri06, Ouy05]. The origin of the enhanced conductivity is not completely understood, however, it is related to a morphological change of the PEDOT:PSS film as investigated by Na et al. [Na08, Na09]. Na et al. reported about the decrease of the thickness of the insulating and hydrophilic PSS shell around the PEDOT-rich core of a PEDOT:PSS grain. The decrease of this electrical barrier leads to the formation of superior charge transport paths between the single grains.
In recent years, the sheet resistance of PEDOT:PSS films could be decreased to around 100 Ω/sq. and even less and consequently also grid free organic solar cells with a transparent polymer electrode [Na08, Na09, Kim11, Hau09, Zho08, Na10, Lim08] were fabricated, including large scale deposition techniques like spray-coating [Na10, Lim08]. Since the sheet resistance of the polymer electrode is increased compared to ITO (5-30 Ω/sq.), which leads also to an increase of the device serial resistance, the solar cell fill factor is reduced. Hence, these kind of devices are usually less efficient than ITO reference samples.
The impact of a polymer electrode on the OPD performance, significant at reverse bias voltage, was investigated during this work, published in [Bai11a] and is summarized in the following section.

4.3.1 PEDOT:PSS as highly transparent and conductive electrode

Before device integration, the conductive PEDOT:PSS film was optimized towards low sheet resistance R_{sheet} combined with a high transmittance T. There is a trade-off

between R_{sheet} and T since increasing the layer thickness d is related to a decrease of $R_{sheet} \propto 1/d$ but also to a decrease of $T \propto e^{-\alpha d}$, with α as absorption coefficient.
The high boiling point solvent which was chosen as conductivity enhancer is ethylene glycol (EG). Together with dimethylsulfoxide, the highest conductivities are reported, but EG additionally provides the possibility of applying it as post treatment for dried PEDOT:PSS films as reported by Kim et al. [Kim11].
At first, the sheet resistance of spin-coated films consisting of the PEDOT:PSS formulation Clevios PH 1000 by H.C. Starck, which is currently the formulation which provides the highest achievable polymer conductivities, and EG was investigated. The two substances were mixed together with different mixing ratios and stirred for several hours at room temperature before the spin-coating deposition. An optimal mixing

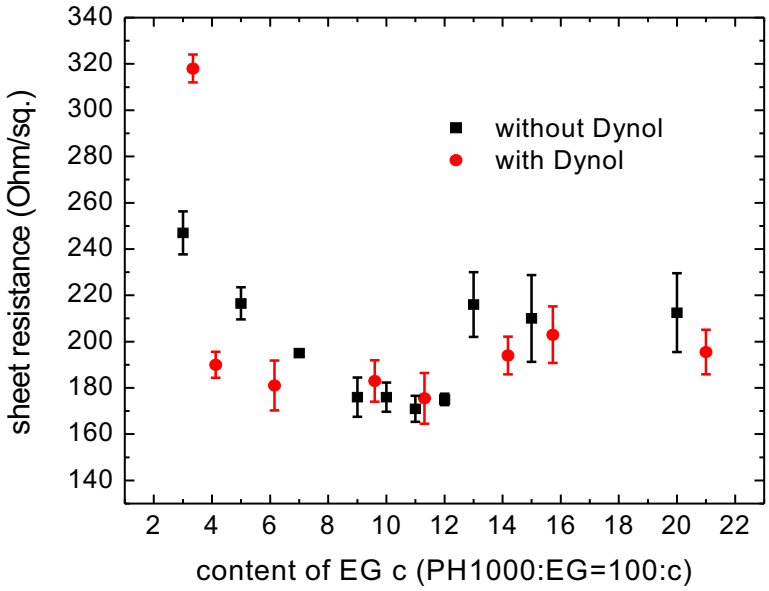

Figure 4.28: The median of the measured sheet resistance of polymer layers with varying amount (by weight) of EG inside the PEDOT:PSS formulation PH1000, with and without containing 0.3 % of the wetting agent Dynol. The errors bars indicate the standard deviation of about 5 subsequent measurements.

ratio can be extracted with Fig.4.28, which shows the sheet resistance of the material mix, spin-coated with 2000 rpm which corresponds to a film thickness of about 120 nm which was quite comparable for the different mixing ratios. Without adding EG, for the PH1000 formulation $R_{sheet} \approx 200$ kΩ/sq. accounts. The mix, after drying at 140 °C for 10 min on a hot plate, shows a strong decrease of R_{sheet} after adding only small amounts of EG. An optimum can be found around 100:10=PH1000:EG at about 180 Ω/sq. For higher amounts, R_{sheet} increases slightly again.
For comparison, also layers of other electrode materials were characterized. The 20 nm thick gold layer exhibits $R_{sheet} \approx 5$ Ω/sq. and ITO about $R_{sheet} \approx 15$ Ω/sq.

The wetting of the mix on top of the glass substrates turned out to be insufficient since the film tends to tear-off. To improve adhesion, about 0.3 % of the wetting agent Dynol^{TM} 604 was added to the mix before stirring. In Fig.4.28 it can be seen that this additional component does not worsen the conductivity of the layers. The optimal mixing ratio for high conductive polymer films, which was determined and chosen for device fabrication, is EG:PH1000=10:100 (by weight).

Consequently, the influence of the layer thickness on R_{sheet} and transmission T was investigated. The spin-speed was varied between 3000 rpm and 500 rpm, which is the lowest spin-speed to obtain homogeneous films, resulting in layer thicknesses between about 75 nm and 265 nm. In Fig.4.29 the transmission spectra of conductive PEDOT:PSS layers with different layer thicknesses are shown. For comparison, two alternative anode materials, commercially available indium-tin-oxide (ITO) and a 20 nm thick gold layer, are added to Fig.4.29. Compared to these standard materials, the modified PEDOT:PSS exhibits a very high transmission even for thick layers. Thin layers up to about 150 nm layer thickness are even more transparent than the ITO layer for a wave length region up to the absorption edge of the PCBM:P3HT heterojunction at about 650 nm. In Fig.4.30, the transmission change for two different wave lengths is indicated. The change of T within this thickness range is almost linear. At around 500 nm wave length, where the T is next to its maximum, the thinnest layer of 75 nm exhibit $T = 98$ % which decreases only about 10 % for increasing the thickness to 265 nm. At 800 nm, the transmission is for all thicknesses above 75 %.

Combining these results with the measured R_{sheet}, which is related to the layer thick-

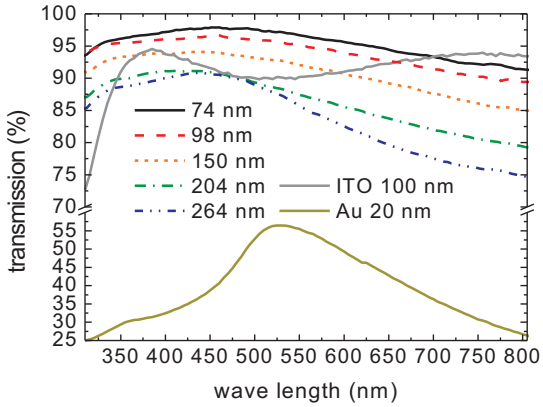

Figure 4.29: Transmission spectra of PEDOT:PSS layers (with different thicknesses), commercially available ITO and a 20 nm thick gold layer electrode.

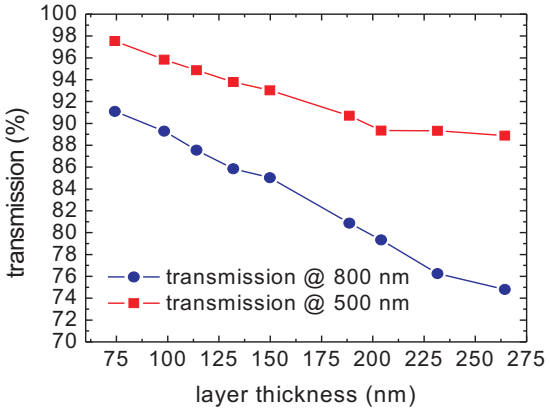

Figure 4.30: Transmission change at different wave lengths as a function of the PEDOT:PSS layer thickness.

ness d by $R_{sheet} \propto \frac{1}{d}$, gives rise to the curve plotted in Fig.4.31. The thickest layer with 265 nm exhibits a very good sheet resistance of $R_{sheet} = 80\ \Omega$/sq. and a still high

transmittance. Generally, the conductive PEDOT:PSS layer exhibit a conductivity σ of $\sigma = 1/(d \cdot R_{sheet}) \approx 500$ Scm^{-1}.

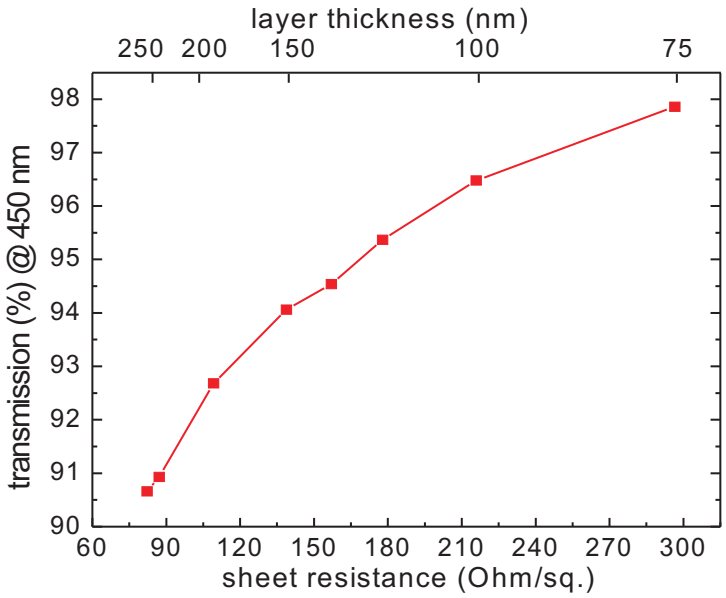

Figure 4.31: Transmission change at 450 nm (max. transmission) of PEDOT:PSS layers as a function of their sheet resistance and layer thickness.

Ethylene glycol can not be only mixed to the PEDOT:PSS solution, but it can also be used for a post-treatment of dried PEDOT:PSS films. The whole dried layer is 'dipped' for a certain time, usually minutes, in pure EG and dried afterwards again. This can be also performed with layers that are already fabricated with a mix of PEDOT:PSS and EG, as reported by Kim et al. [Kim11]. They report about conductivities up to 1400 Scm^{-1} compared to pristine films fabricated with only a PEDOT:PSS:EG mix exhibiting about 700 Scm^{-1}.
To investigate the impact of the dipping on R_{sheet}, different samples were fabricated with different layer thicknesses which were determined precisely (< 5 nm uncertainty) with the AFM. The reference samples (A) were fabricated as reported so far, with a mixing ratio of 100:10=PEDOT:PSS:EG. Two other samples (B) were additionally dipped afterwards for 5 min respective 20 min in EG and dried afterwards for 10 min at 140°C. They are referred as 'mix + dip' samples. The last one (C) is a spin-coated pure PEDOT:PSS film, dipped for 5 min in EG ('dip').
As also observed in [Kim11], the post-treatment causes a strong change of the layer morphology. In Fig.4.32, the change of the layer thickness for the post-treated films is shown, for the different treatment times (5 respective 20 min) of the B samples no difference was observable. As initial layer thickness the thickness before the post-treatment is meant. For the thicker layers a significant change of about 1/3 of the layer thickness occurred. For sample C the effect is similar, but less pronounced.
The origin of the thickness reduction is related to the morphological changes reported

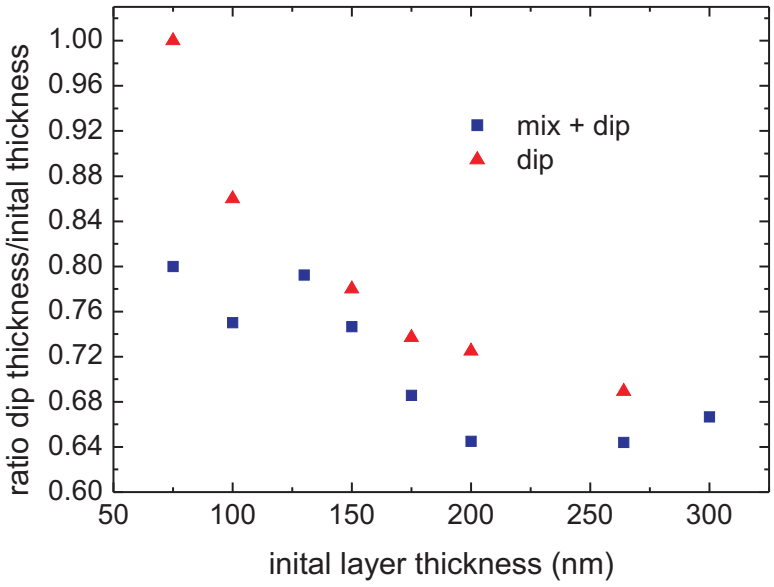

Figure 4.32: The change of the initial film thicknesses of the samples B (mix + dip) and C (dip) after the post-treatment with EG.

in [Kim11]. With the post-treatment the reduction of the insulating PSS regions is much stronger than with only mixing EG to the PEDOT:PSS for which no thickness change was observed. This 'washing-out' leads to the formation of a compact, PEDOT rich layer. The information about thickness change is important since the improvement of conductivity reported by Kim et al. in [Kim11] could be simply related to the reduction of film thickness. Actually, the important quantity for the electrical transport in the device is R_{sheet}, independent on the physical dimensions, and not the bulk resistivity $1/\sigma$ since there is no difference in the electrical transport in case σ is doubled but d is reduced by half compared to the initial state.
In Fig.4.33 the dependence of the sheet resistance on the layer thickness is shown. The difference of R_{sheet} for the same d between the reference samples A and the treated samples (B+C) is significant. But taking the results of Fig.4.32 into account, R_{sheet} of the treated samples is almost the same as before the treatment, only a thickness change occurs. The best results for R_{sheet} could be obtained with the 20 min treated sample, $R_{sheet} = 50\ \Omega$/sq., but this result is only slightly better as the best reference sample A with $R_{sheet} = 65\ \Omega$/sq.
A similar result can be obtained by characterizing the transmission T in Fig.4.34. Here, for the same layer thickness, the treated samples exhibit lower transmission. This effect can be attributed to the morphological changes of the PEDOT:PSS. As for R_{sheet}, the transmission curve is shifted to the left side by a value corresponding to the change of thickness. Only the amount of PSS is different between the samples, but not the

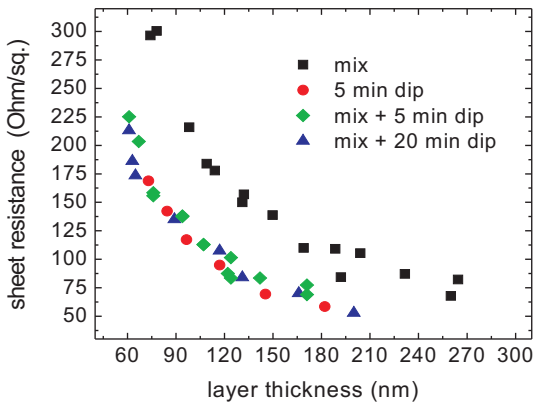

Figure 4.33: The sheet resistance dependent on the layer thickness for all samples.

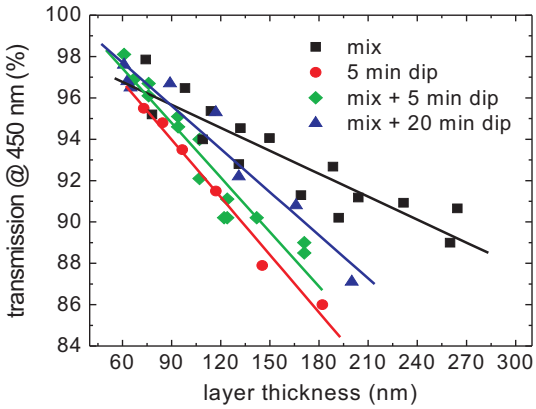

Figure 4.34: The transmittance dependent on the layer thickness for all samples.

PEDOT which leads to the similar transmission compared with the reference samples A. The different treated samples show a slightly different behavior, as indicated with linear fits, which can be partly influenced by the measurement inaccuracy related by the T measurements (± 1.5 %).

A final comparison between the different samples, shown in Fig.4.35, illustrates the

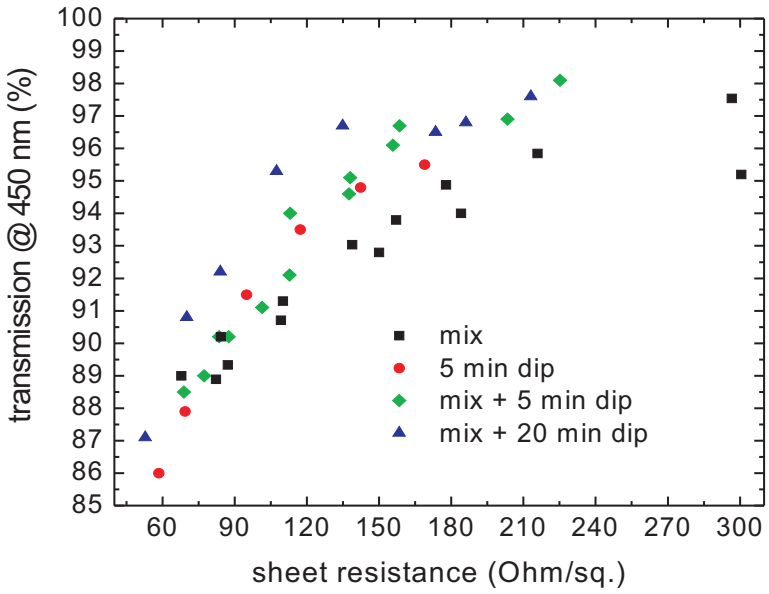

Figure 4.35: Transmission over sheet resistance for the various treated films.

dependence of T on R_{sheet}. All samples show a quite similar behavior, with a slight

worse T/R ratio for the reference samples. This result proves that the post-treatment concept does not bring an improvement regarding R_{sheet} nor T, although the conductivities could be increased from 500 to 900 Scm^{-1} (Kim et al.: 1400 Scm^{-1}). Hence, the simple mix of PEDOT:PSS with EG was chosen for device integration.

4.3.2 Electro-optical performance of inverted OPDs with polymer electrode

To test the impact of the very different R_{sheet} and T of the conductive PEDOT:PSS on devices and to compare with the gold layer, devices with different thick polymer electrode were fabricated. The processing of the new anode was equally performed as with the dummies on glass substrates and the photoactive diode area was defined with a heat-resistant adhesive tape to shield the material during spin-coating. The other device parts were fabricated as in section 4.1.4.

In Fig.4.36 the IV-characteristics of two inverted photodetectors, one with the so far

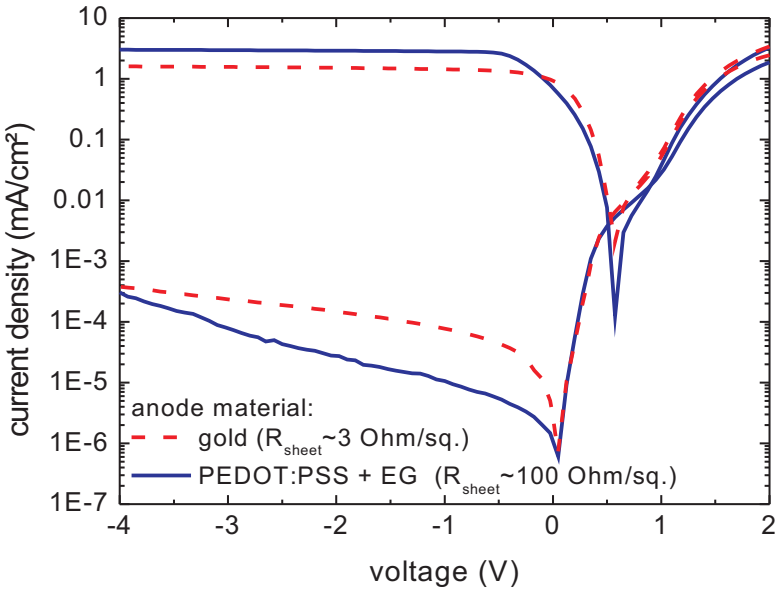

Figure 4.36: Typical IV-curves of inverted diodes with a gold respective polymer electrode under dark and illuminated conditions. The applied light intensity was 100 mW/cm^2.

used gold electrode and the other with the new solution-processable polymer electrode, comprising a sheet resistance of 100 Ω/sq., is shown. The new device sustains a similar low dark current for high reverse bias ($2 \cdot 10^{-4}$ mA/cm^2 @ -4 V), but even one order of magnitude lower current for smaller reverse bias ($1 \cdot 10^{-5}$ mA/cm^2 @ -1 V). The current density under illumination increases about 50 % due to the enhanced trans-

parency of the polymer layer thus improving the photocurrent on/off-ratio at -4 V to four orders of magnitude. The forward current density is slightly reduced due to the higher resistance of the polymer electrode (100 Ω/sq.) compared to the gold electrode (3 Ω/sq.).
Comparing the impact of different layer thicknesses and according sheet resistances of the anode on the IV-characteristics, by increasing R_{sheet} from 100 Ω/sq. to 300 Ω/sq., neither the for a photodetector relevant dark nor light backward current are influenced within accuracy of fabrication and characterization, whereas the forward current density slightly decreases. Since a photodetector is operated in reverse bias, the increased serial resistance introduced by the polymer electrode, even if deposited as a thin layer with lower conductance, does not limit the electrical detector performance.
The improved light transmittance of the PEDOT:PSS anode compared to the semi-

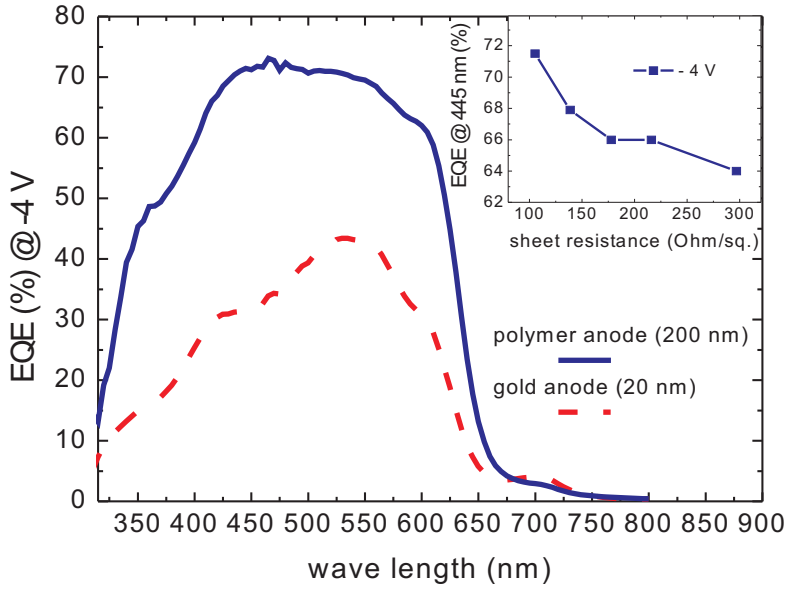

Figure 4.37: External quantum efficiency (EQE) of devices with gold respective polymer electrodes. The inset shows the EQE decrease with increasing anode sheet resistance.

transparent gold layer manifests itself by remarkable values of the external quantum efficiency (EQE). In Fig.4.37 the EQEs of inverted photodetectors with gold (20 nm thick) respective polymer anode (200 nm thick, 100 Ω/sq.) are shown. Whereas the narrow transmission spectrum of a 20 nm thick gold layer with a transmission maximum of about 55 % showed in Fig.4.29 is responsible for an EQE exhibiting a maximum of only about 45 % @ 530 nm (-4 V) and efficiency losses at the short wave length range, the replacement with PEDOT:PSS increases the short wave length part of the EQE and shifts the maximum over 70 % (-4 V). This value is comparable to the EQE of state-of-the-art non-inverted ITO photodetectors [Ted09, Ram08].

The dependence of the EQE on the electrode sheet resistance is shown in the inset of Fig.4.37. With increasing R_{sheet} (decreasing layer thickness) from 100 Ω/sq. to 300 Ω/sq. the EQE decreases by about 7.5 %. This is interesting since the transmission at the same wavelength (see Fig.4.31) increases by 6.5 % when increasing R_{sheet} from 100 Ω/sq. to 300 Ω/sq. Consequently, decreasing the sheet resistance has bigger impact on device performance than increasing the transmission.
An optimal layer thickness for the inverted photodetector could not be determined since lowering of the spin-coating speed results in the formation of inhomogenous PEDOT:PSS films. All devices fabricated with polymer electrodes thicker than about 200 nm exhibit large EQE variations and were not exploited for further investigations.

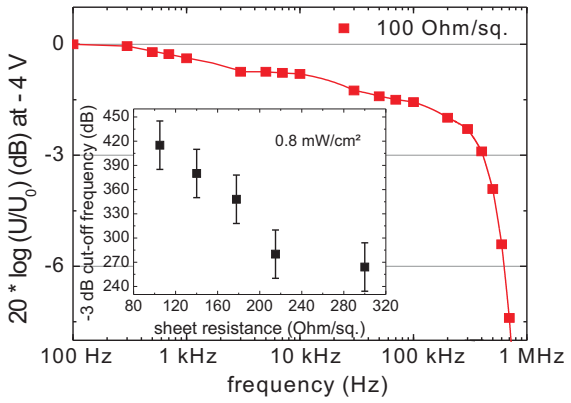

Figure 4.38: Frequency response of an photodiode with electrode sheet resistance of 100 Ω/sq. at -4 V. The inset shows the dependence of the -3 dB cut-off frequency on the electrode sheet resistance. The error bars represent the standard deviation of subsequent measurements of the same diodes.

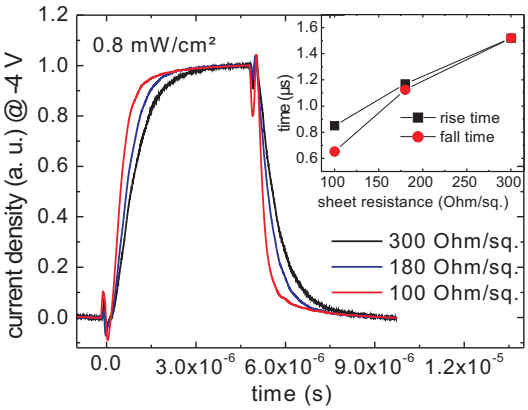

Figure 4.39: Dynamic photocurrent response for diodes with different sheet resistances. The applied light pulse length was 5 µs and the frequency 100 kHz. The inset shows the decrease of rise and fall time with decreasing sheet resistance. Overshoots are dedicated to capacitive effects arising from cables.

A further performance parameter which is influenced by R_{sheet} is the dynamic behavior respective the -3db cut-off frequency f_c. The serial resistance of the electrodes, proportional to the R_{sheet}, plus additional load resistances sum up to a total resistance R. The time constant $t_{rc} = RC$ takes this resistance into account, together with the photodiode capacitance $C \propto A/d$ (with diode area A). f_c is also influenced by the transit time t_{tr} of the light generated carriers traveling through blend and PEDOT:PSS to the electrodes. The transit time is given by $t_{tr} = \frac{d^2}{\mu V}$ with layer thicknesses d, carrier mobility μ and voltage drop V. For inverted photodetectors with different conductive electrodes but with the same layer structure in between, the transit time towards the electrodes is constant.

The overall device time constant t is the root-sum-square value of the individual time

constants [Wal48] and is related to the cut-off frequency $f_c \propto 1/2\pi t$:

$$t = \sqrt{t_{tr}^2 + t_{rc}^2} \tag{4.2}$$

Since the sheet resistance of a polymer electrode can be about two orders of magnitude higher than that of a metal electrode, also t_{rc} can increase remarkably. To investigate the impact of the sheet resistance on the dynamic behavior of photodiodes with a polymer top electrode, the cut-off frequencies were measured.
In Fig.4.38 the frequency response of an inverted diode with a polymer electrode (100 Ω/sq.) on illuminating it with square light pulses (light intensity 0.8 mW/cm^2, duty cycle 50%) is shown. At about 420 kHz the -3dB attenuation is reached. This is a state-of-the art -3db cut-off frequency for organic photodiodes [Bai10, Pun07, Ram08]. Increasing R_{sheet} from 100 Ω/sq. to 300 Ω/sq. results in a cut-off frequency decrease to about 260 kHz.
Considering this experimentally determined dependence between sheet resistance and cut-off frequency in the inset of Fig.4.38 and assuming that C is equal for each diode, it is possible to determine a proportional factor $x = t_{tr}/t_{rc}$ for different t_{rc} respective R_{sheet} with Eq.4.2. Assuming $R \propto R_{sheet}$, a change of R_{sheet} also causes a proportional change of t_{rc}. For the device with the lowest sheet resistance, $R_{sheet} = 100$ Ω/sq., $x = 2$ follows, which means that t_{tr} contributes about 4 times more (see Eq.4.2) to the overall time constant than t_{rc}. In addition, also an upper limit of the cut-off frequency of the photodetectors with polymer electrodes can be estimated with Eq.4.2 and the data of the inset of Fig.4.38. With $RC = 0$ only the transit time determines the overall time constant t, resulting in an upper cut-off frequency limit of about 470 kHz which is barely higher as the highest cut-off frequency measured in Fig.4.38. The conclusion of these dynamic measurements is, that although R_{sheet} of the polymer electrode is two orders of magnitude higher than that of a metal electrode, it is not the dominant contribution to the time constant. Still the transit time, governed by the layer thicknesses in the devices and the mobility, determines the speed of a detector.
Interestingly, the best obtained cut-off frequencies of devices fabricated with the polymer electrode are significant higher than of devices with a gold electrode as reported in section 4.1.4 (300-350 kHz). This result can be influenced by the different interface to the electrode which might enhance the carrier extraction for the polymer electrode due to the supposed almost equal work function of both conductive PEDOT:PSS and the hole-conductor PEDOT:PSS.
In Fig.4.39 typical light pulse responses of the photodetectors with different anode sheet resistances are shown for a light pulse frequency of 100 kHz. The shape of the response changes for the different resistances, meaning that also rise and fall time (the fall time is defined as time required for a pulse to decrease from 90% to 10% percent of the peak value) change accordingly. This is shown in the inset of Fig.4.39 where the response times double for increasing R_{sheet}=100 Ω/sq. to 300 Ω/sq. The behavior is consistent with the trend shown before in Fig.4.38 where the cut-off frequency is reduced approximately by half.

4.4 A panchromatic photodetector with squaraine

So far, all inverted OPDs were fabricated with the common mix of the donator P3HT and the acceptor material PCBM. For sensing, especially for the hybrid concept, also the wave length region beyond the absorption edge of PCBM:P3HT (650 nm) is interesting since currently, there are no cheap night vision systems available. InGaAs cameras are employed for the NIR-region (up to 1700 nm), but they are expensive, among other factors due the rare resource of indium. Possible applications for NIR-enhanced imagers are given in section 3.2.2.3.
In this thesis, to enhance the absorption range of the organic bulk-heterojunction towards the NIR-region, the organic dye squaraine was valuated and a panchromatic detector, sensitive over a broad wave length range between 300-900 nm, was fabricated. For details about squaraine, see section 3.2.2.3 and [Bev10, Bin09, Bin11, Wei10].
To obtain the broad wave length sensitivity, squaraine (SQ) can be mixed together with PCBM and P3HT. In Fig.4.40 the absorption spectra of different organic layers containing SQ are shown. The mix with 1:3=SQ:PCBM by weight was chosen since it is an optimized mixing ratio for SQ:PCBM for high quantum efficiency since it balances the electron and hole mobilities ($\mu_n = 6 \cdot 10^{-6}$ cm^2/V s, $\mu_p = 2 \cdot 10^{-6}$ cm^2/V s) [Wei10, Bin11]. The mix exhibits almost no absorption in the green wave length region. To increase this part, P3HT was gradually added. For a mixing ratio of 1:1.5:3=SQ:P3HT:PCBM, the absorption at 500 nm is almost as high as at the SQ maximum at 760 nm.

To validate the broad wave length sensitivity, non-inverted OPDs with an ITO an-

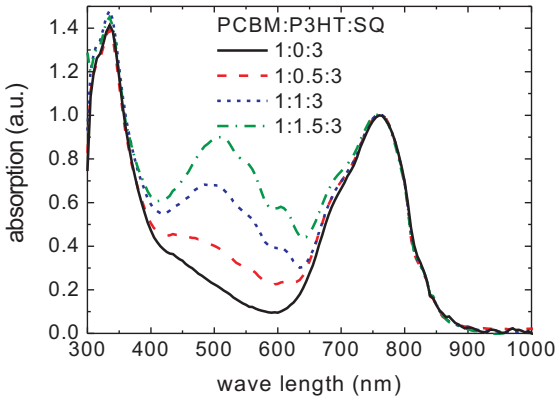

Figure 4.40: The absorbance spectra of various mixed organic layers. The spectra are normalized on the SQ peak at about 760 nm.

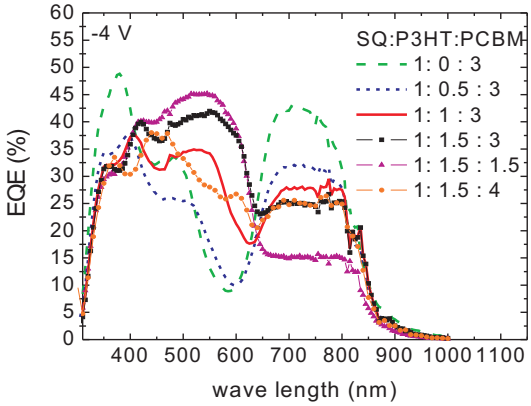

Figure 4.41: The EQEs of non-inverted OPDs, measured at -4 V, with various mixed blend layers.

ode (which exhibits at 1000 nm a transmission of > 80 %) and PEDOT:PSS as hole conductor were fabricated. In Fig.4.41, the corresponding EQEs are shown. As with the absorption, the EQE in the green wave length region increases by increasing the

amount of P3HT, but this occurs at the expense of an EQE decrease of squaraine. Both materials are electron donator materials. Since the SQ exhibits a slightly lower LUMO level (3.3 eV) compared to the P3HT (3.0 eV), a possible explaination for the EQE trade off between P3HT and SQ is that the P3HT LUMO acts as a barrier for the photogenerated electrons inside the SQ dye which hinders the electron transfer to the PCBM when not directly transferred from SQ to PCBM. The optimum mixing ratio is around 1:1.5:3 since for this ratio the spectral EQE up to 850 nm is at least 25 % for the applied -4 V external bias voltage. Either increasing or decreasing the amount of PCBM worsens the EQE, as indicated in Fig.4.41 since either the green or NIR EQE suffers.

In Fig.4.42 the IV-curves of the OPD which the optimized mixing ratio is shown to-

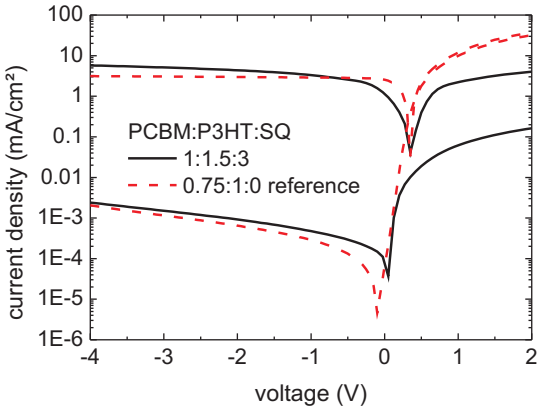

Figure 4.42: IV-curves of non-inverted OPDs with and without SQ.

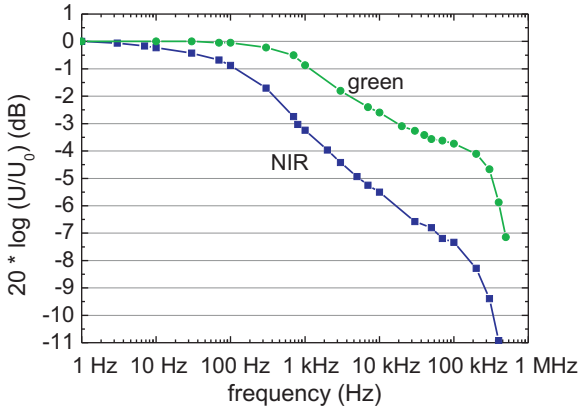

Figure 4.43: The dynamic behavior of a OPD with mixing ratio 1:1.5:3=SQ:P3HT:PCBM, measured at -4 V. Two different light LEDs were used: 800 µW/cm^2 at 525 nm and 5.4 mW/cm^2 at 905 nm.

gether with a reference sample with contains only the common P3HT:PCBM bulk heterojunction. Both show very similar dark currents. The photocurrent for the SQ-containing detector exhibits a slope also for high reverse bias compared to the reference. This increase is also manifested in the EQE-measurements which were performed for reverse bias up to -10 V, as shown in Fig.4.44 for the OPD without P3HT (1:3=SQ:PCBM) and with P3HT (1:1.5:3=SQ:P3HT:PCBM). In difference to the standard and inverted OPD EQE which saturates at about -5 V, the EQE does not even saturate for an applied voltage of -10 V. EQEs above 50 % are feasible for the panchromatic photodiode.

The dynamic performance of the optimized panchromatic detector, determined as cut-off frequency, is showed in Fig.4.43. It was measured at two different wave lengths, green (525 nm) and NIR (905 nm). The -3-dB-cut-off frequency is significantly lower (15 kHz at 525 nm) than for the standard OPDs, especially for the the NIR part (800 Hz), but still sufficient for an imaging application [Bai12].

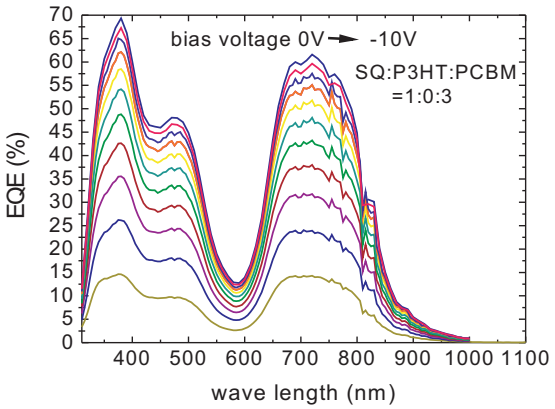

Figure 4.44: The voltage dependence of the EQE for an OPD with mixing ratio 1:3=SQ:PCBM

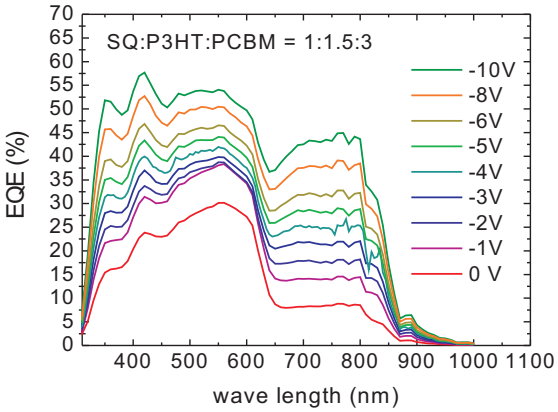

Figure 4.45: The voltage dependence of the EQE for an OPD with mixing ratio 1:1.5:3=SQ:P3HT:PCBM

4.5 Degradation of spin-coated OPDs

A drawback of organic electronics in general is the tendency of the organic materials to react with ambient air, e.g. with oxygen and water. These chemical reactions lead to a degrading performance of the organic devices within hours or days. To protect the layers, an encapsulation is indispensable. In this work, a simple encapsulation was used, consisting of an epoxy glue and a thin glass sheet which was positioned over the active diode area and fixed with the glue. This simple encapsulation does prevent vertical diffusion of oxygen (trough the top electrode), but still a lateral diffusion through the spin-coated layers and the epoxy glue towards the active diode area, which is usually positioned at a distance of about 2 mm to the encapsulation glass edge, can occur. Short diode lifetimes (days) with this encapsulation were experienced at the beginning of this work. To improve diode lifetimes, the first step was to exchange the type of epoxy glue while still maintaining the lateral encapsulation type. The new epoxy resin Dymax OP-4-20632, an UV-hardening acrylate, was chosen due to previous positive reports about the application in organic solar cells [Zim08]. Together with the glue used in the beginning, the urethane Dymax 9001-E-v3.1, both glues were tested in spin-coated OPDs with a gold anode. The fabrication process was completely performed in nitrogen atmosphere, including the encapsulation which was performed equally for all test OPDs except for the epoxy type. Altogether, several samples were fabricated for each type of glue, with each 6-8 diodes to gain statistics. IV-curves and EQE measurements were performed regularly over a time period of 3 respective 9 months.
In Fig.4.46 the dark current at -4 V of the OPDs with different epoxy resins are compared. Each data set corresponds to one substrate, containing 8 diodes, averaged, and the standard deviations are included as error bars. The tendency is clear, with Dymax 9001-E-v3.1, the dark currents are continuously increasing. After 9 months, they

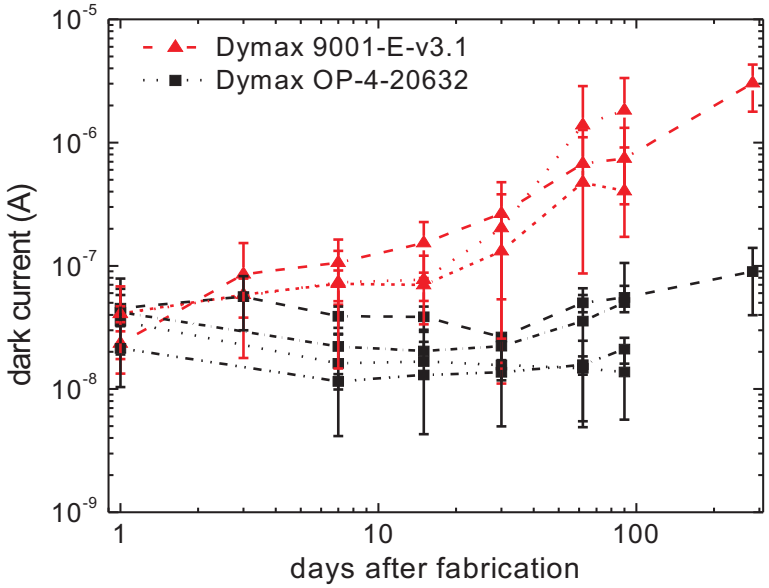

Figure 4.46: The evolution of the dark current for seven different samples with 8 diodes fabricated with the two different epoxy glues. The applied bias voltage is -4 V.

are increased by about two orders of magnitude due to a decrease of the diode shunt resistance related to the chemical reactions. For the Dymax OP-4-20632, over a time period of 3 months no degradation is observed, even after 9 months there is no clear indication. This long-term stability is a surprising result, since the encapsulation does not block lateral diffusion through the organic and glue layer.
For the photocurrents, shown in Fig.4.47, the results are similar. For a time period of 9 months, the photocurrents at -4 V of the samples with Dymax OP-4-20632 do not decrease at all whereas the other glue leads to about factor 10 worse photocurrents.

Along with the stable photocurrents, also the EQE does not suffer, as indicated in Fig.4.48. With Dymax 9001-E-v3.1, the OPDs lose about one third of their EQEs after three months.
The only changes observed by using Dymax OP-4-20632 affect the forward current of the OPDs. The slight decrease of the forward current after nine months hints to an increase of the serial resistance of the photodiode of a space-charge limited current because of oxygen diffusion as reported in [Kre07].
The big difference of the performance obtained by the use of two different glues has to be related to a different lateral diffusion rate through the glues. This can be due to different material properties or different layer thicknesses of the glues. SEM (scanning-electron-microscope)-measurements of the glues revealed an equal layer thickness but a different morphology which hints to a very different structure of the two epoxy glues.
As conclusion, the life time of the inverted OPDs could be significantly improved, to

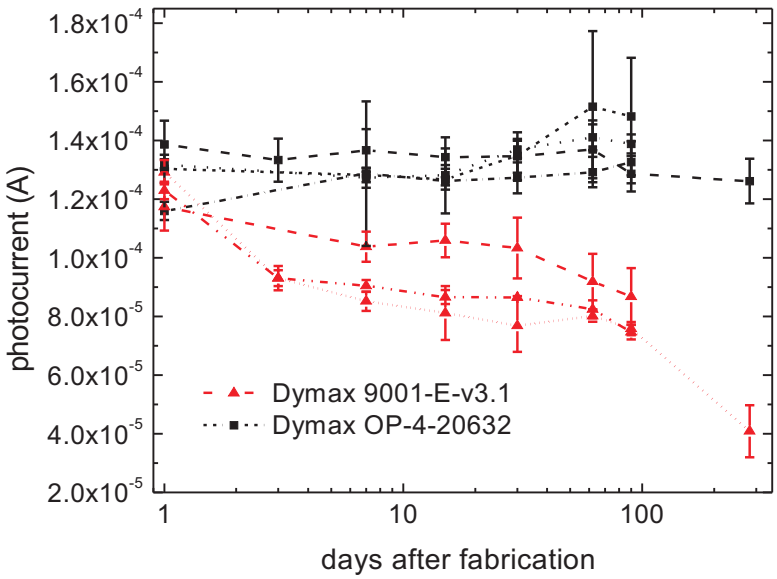

Figure 4.47: The evolution of the photocurrent for seven different samples with 8 diodes fabricated with the two different epoxy glues. The applied bias voltage is -4 V.

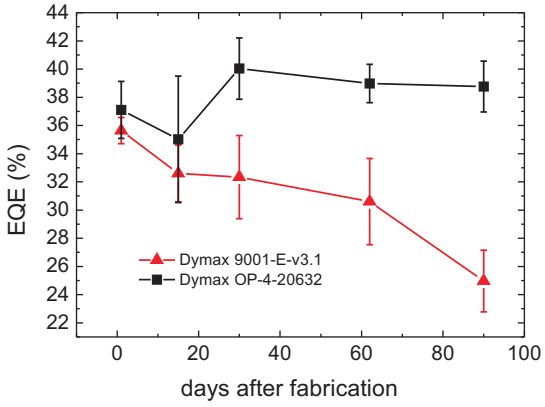

Figure 4.48: The change of the EQE for two substrates covered by the two different glues, measured at -4 V.

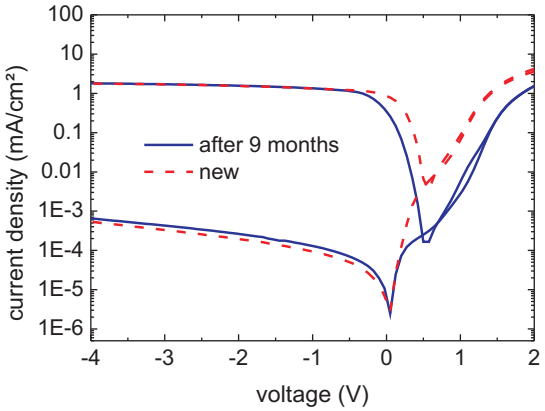

Figure 4.49: IV-curves of a typical OPD fabricated with Dymax OP-4-20632 directly measured after fabrication and after 9 months.

about at least 9 months, which is important for the integration into imager prototypes due to the high cost of prototype production. A further improvement of the encapsulation should be possible by introducing a complete encapsulation, e.g. by removing the residual polymer layers before applying the epoxy glue, thus suppressing lateral diffusion.

Chapter 5

Spray-deposition of organic photodiodes

In the previous chapter two major challenges for the hybrid imager development were overcome. The inverted OPD is now fully compatible with the CMOS top-metalization and is an efficient top-absorbing device.
Another challenge for the integration of organics arises due to the high texture of the chip. In Fig.5.1 the three dimensional profile of a pixel with 15 µm pad size (of a CMOS-chip used for hybrid imager fabrication in chapter 6) is illustrated as measured with an AFM. The inside is sputtered aluminum with a RMS-roughness of about 10 nm. The bulge which surrounds the metalization is a silicon nitride (SiN) passivation layer. It is used for electrical isolation between the silicon substrate and organic layers. The openings in this passivation layer, created by an etching process, define precisely the lateral aluminum pad size (15 µm) of the pixel, as shown in the height profile in Fig.5.1. The profile reveals also the very high texture of the SiN-layer, of about 2 µm, which is a typical value arising due to the CVD (chemical vapor deposition) process.
So far, all OPDs were fabricated with spin-coating. Since this method is driven by the lateral centrifugal force, the deposition on rough substrates can lead to very inhomogeneous layers or film tear-offs. Actually, spin-coating on test CMOS-dummies (see section 3.1.2 with a 200 nm high passivation layer led already to the formation of an inhomogeneous layer and high diode dark currents.
Hence, a different deposition method had to be chosen for the CMOS-chips. In this work, spray-coating was chosen since it is a vertical deposition method independent on surface roughness. An additional advantage is also the possibility to generate layers with different thicknesses, only limited to a minimum thickness determined by the roughness of the spraydrop-network.
Spray-deposition of organic devices, like solar-cells [Gir11, Na10, Sus11] and photodiodes [Ted09] was employed before, mainly to demonstrate the possibility of large-scale fabrication.
The setup used for spray-deposition in this work, as well the various spray parameters,

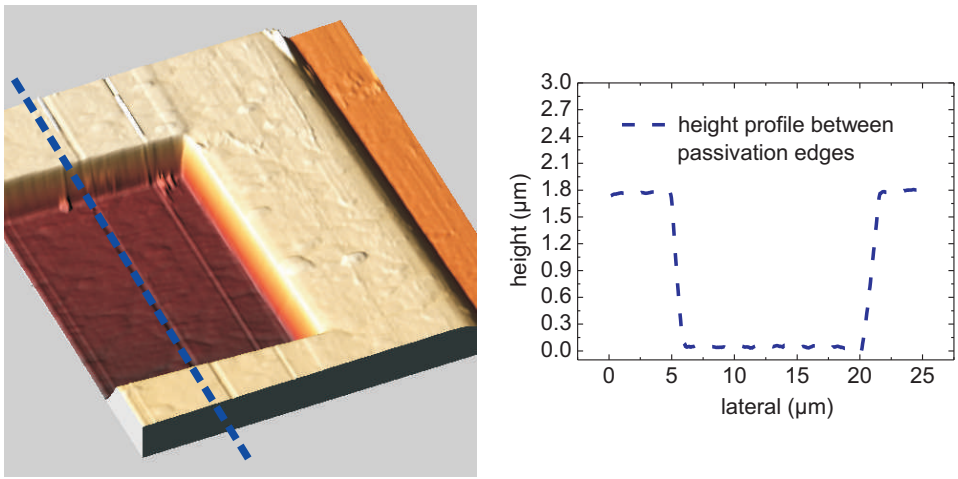

Figure 5.1: An AFM image of the surface of a pixel of the CMOS chip used for hybrid imager fabrication. The inside is the aluminum cathode, its lateral dimensions and the SiN-passivation height are indicated in the height profile.

are described in section 3.3.3.
Since, compared to spin-coating, the spraying of organic layers can be influenced by various setup changes, the most important parameters will be briefly discussed in the first section. The second section deals with the optimization of the single sprayed layers of the OPD to improve device performance, followed by the results of completely sprayed devices.

5.1 Impact of spray-deposition parameters on organic layer quality

The most important spraying parameters (nozzle-substrate distance, spraying time, pressure, heating and material flow) were already addressed in section 3.3.3. Here, their impact on the organic layers regarding thickness and roughness is described. Prior to fabrication of devices, a suitable set of spraying parameters has to be identified for each individual layer. Following criteria are most important:

- Uniform film thickness: prior to the formation of a film on the substrate, a part of the solvent has to evaporate thus the impinging drops do not form a wet layer with high thickness variations. On the other side, if too much solvent evaporates, only polymer powder will reach the substrate. A suitable regime between wet and dry condition has to be found, mainly by varying the nozzle-substrate distance and substrate heating temperature.
- Low material consumption: as with spin coating, a big part of the solution does not reach the substrate due to polymer 'powder' generation in the spray beam and due to the bigger diameter of the spray beam compared to the substrate size.
- Minimized layer roughness: Since a sprayed film consists of a network of single drops, the layer roughness can be much higher than with spin-coating. This must not be a severe issue for device performance [Ted09], but since the hybrid imager consists of numerous small pixels, the layer inhomoginity can also increase the fixed pattern noise, see section 6.2.

5.1.1 Distance nozzle-substrate

The spray distance for the intermediate regime, in which the drops lose a sufficient amount of solvent during their way to form uniform films, was determined for the PCBM:P3HT blend for different solvents, including toluene (Tol), 1,2-dichlorobenzene (DCB) and xylene. For the optimized solvent, a mixture of DCB:Tol (as discussed in section 5.2.1) was chosen with a corresponding spray pattern shown in Fig.5.2 for three different nozzle-substrate distances. Here it can be seen that a variation of only ± 10 mm vertical distance, starting at 15 cm, changes the maximum layer height by about ± 20 % of the layer thickness. This high value implicates that a careful adjustment of the distance is critical for reproducible results. The distance of 14 cm would be the optimum for low material consumption, but since here the intermediate regime starts to change already to the wet regime for the substrate temperature of 100 °C, for all spraying processes of the blend in section 5.3 the distance of 15 cm was chosen.
Increasing the substrate temperature could also prevent blend spraying in the wet regime, but this is directly opposed to the intention of minimizing the material consumption since a decrease of the layer thickness for the PCBM:P3HT blend was observed.
The lateral profile of the spray pattern corresponds to a gaussian beam profile. The height change related to a lateral shift of 5 mm from the middle point (maximum) is about 15 % of the layer thickness. For a typical blend layer thickness of 500 nm this value corrsponds to about 75 nm which is much regarding the impact on the EQE (see section 5.3). Hence, a careful positioning is not enough but has to be supported by the use of spraying masks. For large scale OPDs, an aluminum mask with 1 cm opening was used. Two diodes (see Fig.3.3 in section 3.1.2) were sprayed at once, with the maximum of the gaussian beam positioned between the two diodes to guarantee that

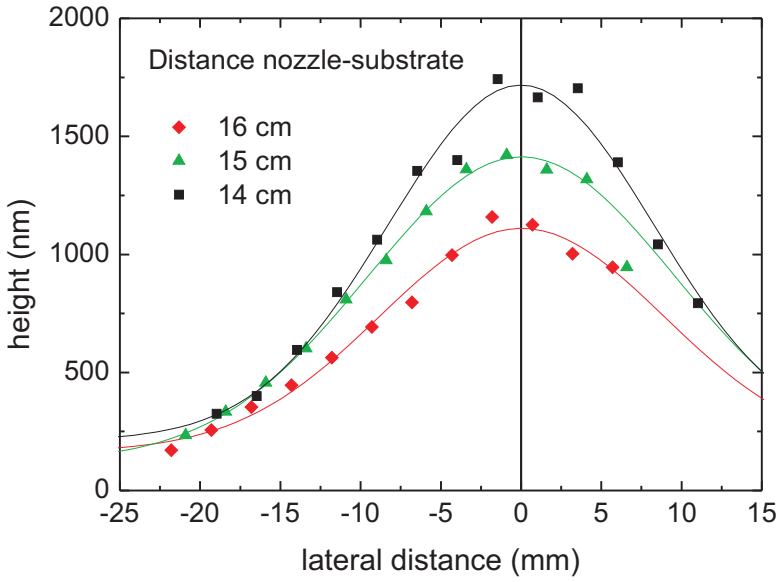

Figure 5.2: The lateral height profile of sprayed layers with DCB:Tol as solvent and an applied temperature of 100°C. The single measurement points, which were determined with a Dektak profilometer, were overlaid with a gaussian fit.

both diodes are covered with an equal amount of blend. Still, since the diameter of the active OPD area is 3 mm, the spraying of these large OPDs is always prone to thickness non-uniformities, especially, since also the lateral middle point determination of the gaussian beam, supported by a pendulum and sprayed test patterns, is error-prone. One reason why a mixture of DCB:Tol was chosen as solvent is the increased boiling point compared to the low-boiling point solvent toluene (111°C). Blend layers sprayed with toluene (with an interim regime distance of 14 cm), exhibit a much lower thickness than compared to layers with DCB:Tol for the same spraying time. The material consumption of the toluene blends is about factor 3 higher, which could be due to a loss of blend because of the generation of polymer powder in the spray beam.

5.1.2 Substrate heating

During the spraying process, the substrate can be heated via a hot plate. A main reason for applying temperature is the enhancement of solvent evaporation for a given nozzle-substrate distance to avoid the wet regime. Heating influences also the roughness of the sprayed layers. For the blend, no significant changes of the roughness occurred for changing the temperature, but a strong temperature impact on PEDOT:PSS films (for the preparation of the solution see the *experimental details* in 7.2) was observable.
In Fig.5.3 four images of different PEDOT:PSS layer are shown which were fabricated

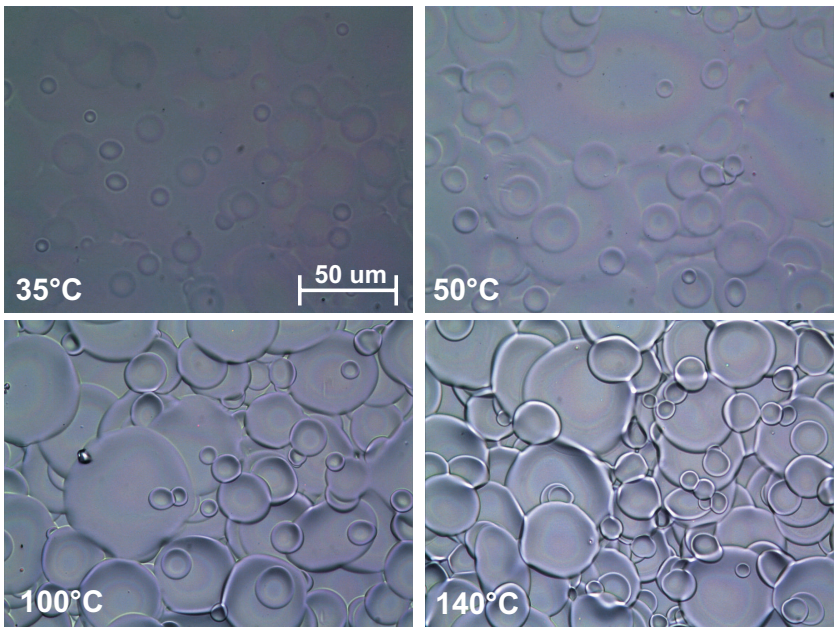

Figure 5.3: Microscopic pictures of PEDOT:PSS layers sprayed at different temperatures. The scale is the same for all images.

identically apart from the glass substrate heating. Increasing the temperature leads to a strong three-dimensional shaping of the layers, the single drops appear much more distinguishable for a spraying temperature of 140°C although the lateral drop size does not change. It can be seen that the edges of the drops are getting more distinct, indicating a material redistribution. This phenomenon is also known as coffee drop or coffee ring effect [Dee97]. The pattern is due to an induced material flow from the inner part of the drop towards the edge to replace the evaporated solvent. This temperature dependence was already observed by Soltman et al. [Sol08] for PEDOT:PSS deposition with ink-jet printers. They investigated that increasing the temperature results also in an increase of the PEDOT:PSS transfer rate towards the edges by measuring the profile of drying drops.
The significance for PEDOT:PSS deposition is also shown in Fig.5.4. For increasing the temperature from 35°C to 140°C, the layer thickness increases by less than factor two whereas the RMS-roughness increases by about factor 6, from about 100 nm to 600 nm. This very strong increase cannot be due to the related increase of layer thickness, as shown in Fig.5.5. Here, as also valid for the photoactive layer, the roughness increases only slightly for increasing the layer thickness by changing the valve opening time. While the thickness changes by about factor 4, the roughness almost doubles. Hence, the weak dependence of the layer roughness on the layer thickness respective

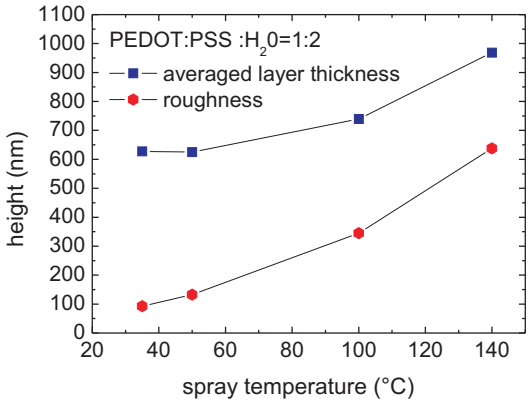

Figure 5.4: The layer thickness and roughness of PEDOT:PSS layers, measured with a profilometer, sprayed for 90 s at different temperatures.

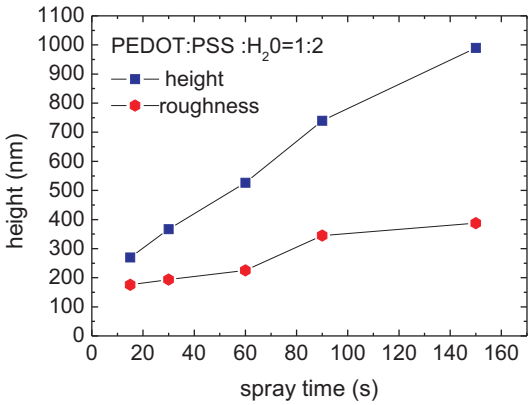

Figure 5.5: The layer thickness and roughness of PEDOT:PSS layers sprayed at 100°C and different spraying times.

spraying time can not explain the strong effect in Fig.5.4. Rather, the before mentioned temperature dependent increase of the PEDOT:PSS transfer rate towards the drop edges seems responsible for the observed behavior.
As conclusion, the spraying temperature for PEDOT:PSS was set to 50°C for all devices fabricated in section 5.3 to decrease the layer non-uniformities as well the avoid current leakage paths through the hole conductor. A lower temperature does not significantly decrease layer roughness and can unintentionally favor spraying in the wet regime.

5.1.3 Spraying pressure

The spraying pressure of the nitrogen gas which is used as transportation medium and for polymer atomization (abbreviated in the following just as pressure) is a further crucial parameter since it influences the drop size in the beam. High pressure is related to high kinetic energy which acts against the surface tension of the polymer solution, resulting in a finer drop size distribution.
For the photoactive blend, this spray parameter turned out to be crucial for layer uniformity whereas PEDOT:PSS was not significantly affected. In Fig.5.6 single blend drops are shown which were sprayed for 1 s with different pressures. For the lowest pressure applied, 0.5 bar (above the ambient pressure) large drops are formed which can exhibit diameters larger than 50 µm. Increasing the pressure leads to a significant change. For 2 bar, most drops are distributed in a diameter range of about 5-20 µm. The highest pressure which could be applied to the nozzle, is 2.8 bar due to the limitations of the magnetic valves used in the setup.

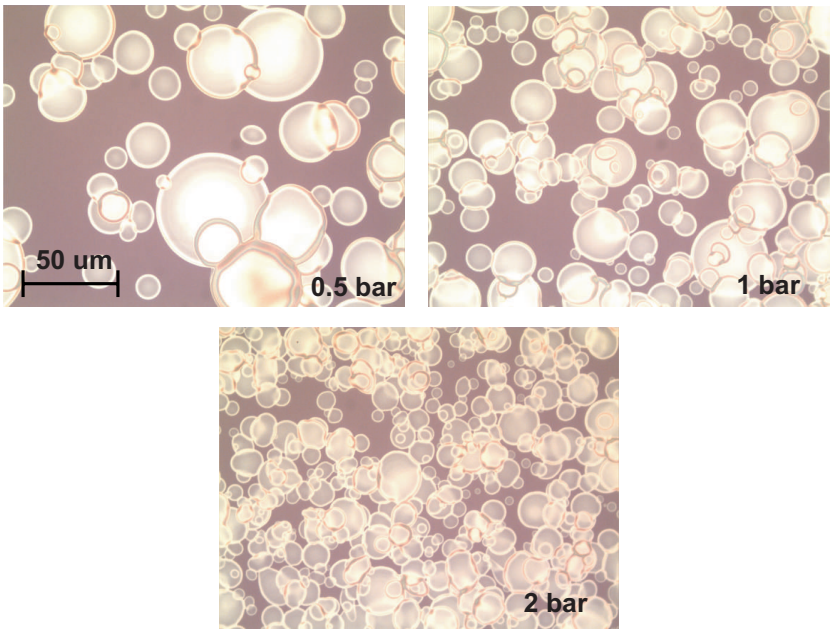

Figure 5.6: Microscopic pictures of blend drops sprayed at different pressures for 1 s. The blend solution and the parameter set are the optimized ones described in section 5.2.1. The scale is the same for all images.

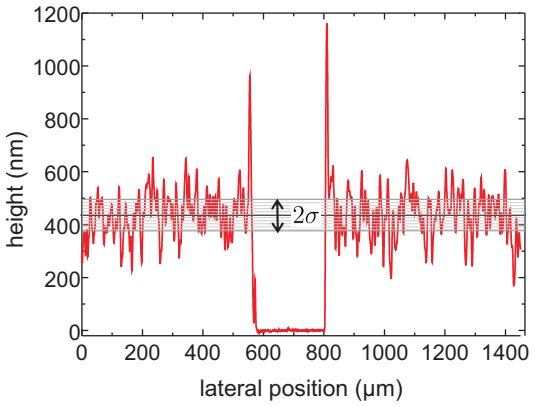

Figure 5.7: The height profile of a blend layer sprayed with 2.8 bar, including a scratch which is used to determine the layer thickness. The RMS-roughness σ is indicated.

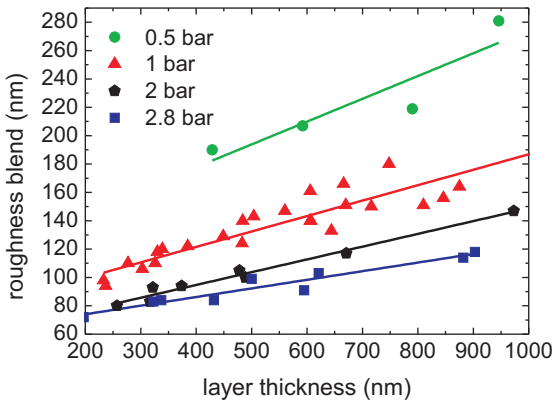

Figure 5.8: The layer roughness dependent on the blend layer thickness for different pressures, fitted linearly.

In Fig.5.7 the height profile of a layer sprayed at this maximum pressure is shown.

The gap is due to an intentional scratch to measure the averaged layer thickness. The layer, with a typical thickness as used for devices, does not exhibit any holes nor a locally very thin layer thickness which is important for a maximized device shunt resistance. Although the layer is quite rough (σ represents the RMS-value, see Eq.3.18, respective standard deviation) compared to a spin-coated layer (RMS-roughness < 5 nm), it represents the result of an optimized spraying process used also for the hybrid imager. This can be seen in Fig.5.8. Here the layer roughness is shown dependent on the measured average layer thickness of blend layers sprayed on glass substrates, fitted linearly. Starting with the lowest pressure, the RMS-roughness is almost about 200 nm at 500 nm layer thickness. Increasing the pressure to 2.8 bar, the roughness decreases to about 90 nm.
In the previous section the temperature turned out to be the critical parameter for uniform PEDOT:PSS layers, here, for the blend, the spraying pressure can be identified as tool to increase uniformity.

5.2 Optimization of the individual sprayed organic layers

Not only the spraying parameters influence massively the layer formation, but also the mixing (ratio) of the organic materials with different solvents. It turned out that the optimizations explored for spin-coating deposition in chapter 4 (regarding e.g. high EQE) were in most cases not valid for spray deposition.
Especially the conductive PEDOT:PSS solution had to be optimized for spray-coating towards high conductivity, since the mixing ratio with the conductivity enhancer ethylene glycol determined for spin-coating did not lead to satisfying results.
In the following, each organic layer will be addressed separately, including opto-electronical characteristics of OPDs with sprayed blend layers.

5.2.1 Photoactive blend

Three solvents, namely 1,2-DCB (DCB), toluene (Tol) and xylene (Xyl), with different characteristics concerning boiling point and surface energy were tested. A detailed comparison can be found in section 3.2.1. Since their different boiling points have a huge impact regarding the spraying regime (wet, intermediate or dry), the spraying parameters, mainly the heating temperature and spraying distance had to be adjusted for each solution. Firstly, the PCBM:P3HT solutions (with a concentration of P3HT:PCBM:solvent=1:0.75:100) were compared regarding the layer uniformity respective roughness, as showed in Fig.5.9. For xylene, the highest roughness values were measured. For thickness values suitable for device fabrication, the rms-roughness is bigger than 200 nm. During the spraying process, a strong flocculation of the polymer

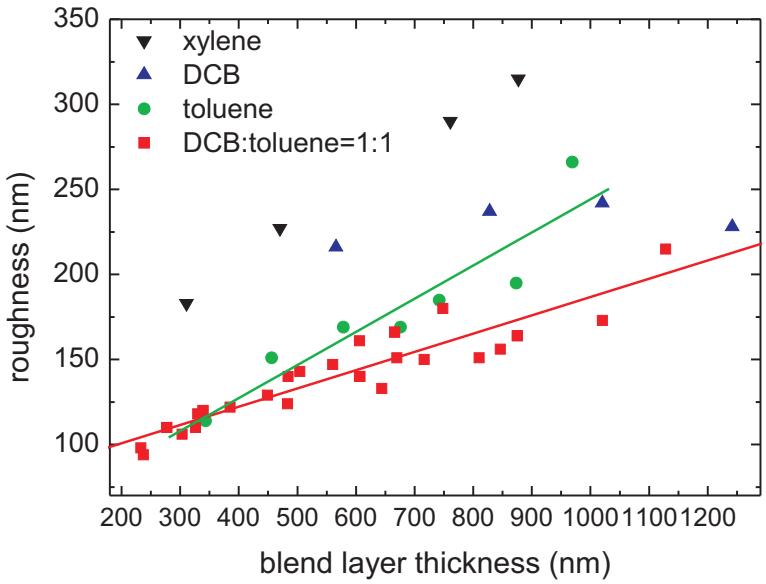

Figure 5.9: Comparison of the layer roughness for different solution with equal PCBM:P3HT concentrations. Spraying temperatures: 150 °C (DCB), 100 °C (Tol, Xyl), nozzle-substrate distance: 14 cm (Tol), 15 cm (Xyl, DCB), spray pressure: 1 bar. Two data sets were fitted linearly to point out the different slope.

was observed (unsolved grains in the spray beam) which could eventually lead also to a blocking of the spray nozzle. Since it is known that the solubility of PCBM in xylene is low [Cho11], this could also explain the high roughness of the sprayed layers. This assumption is supported by the fact that xylene and toluene exhibit approximately the same surface tension which determines the drop interconnection at comparable spraying parameters and should therefore result in similar RMS-roughnesses. Due to the high roughness and the handling problems, xylene blends were not further investigated. Also DCB exhibits a very high roughness, but due to the high boiling point (180 °C) the material consumption was significant lower, about factor 3, compared to toluene (111 °C), as mentioned already in section 5.1.1. Regarding a minimized layer roughness, toluene would be the optimal choice for device fabrication.

Toluene and DCB were also tested in inverted OPDs, fabricated with gold-anode, aluminum cathode and spin-coated PEDOT:PSS layers, in order to investigate the electro-optical differences to complete spin-coated reference samples. The blend layers were sprayed using parameters as described in Fig.5.9 and in section 3.1.2.
In Fig.5.10 the IV-curves of OPDs prepared with DCB are shown for different blend layer thicknesses. Compared to a spin-coated reference diode, as shown in section 4.1.4, the dark currents are very low for high layer thickness (>500 nm) due to the decreased probability of leakage paths and the increase of the serial resistance. Furthermore,

the photocurrent kink is much more pronounced. Regarding the EQE, there is a huge difference to the reference samples. As shown here in Fig.5.11 for a typical example, the maximum EQE, reached for the thinnest layer, is at -4 V only about 20 %. The spin coated references in section 4.1.4 exhibit maxima around 45 % with a gold anode. Increasing the layer thickness to values around 2 µm leads to a significant change, not only of the maximum which decreases due to increased serial resistance respective low charge carrier mobility [Mou06], but also of the spectral shape. For increasing layer

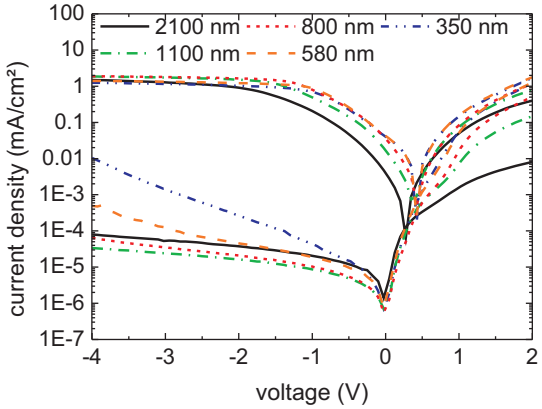

Figure 5.10: The IV-curves of inverted OPDs with a spraycoated blend prepared with DCB, a spin-coated PEDOT:PSS layer and a gold anode.

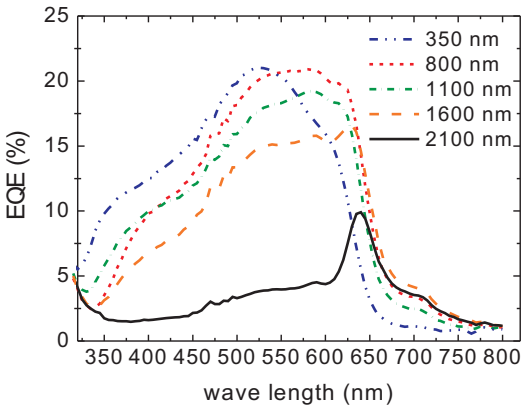

Figure 5.11: The corresponding EQE-curves of the diodes shown in Fig.5.10, measured at -4 V.

thickness, the maximum EQE shifts towards longer wavelengths. For a thickness of about 2 µm the maximum is around the absorption edge of the P3HT at about 650 nm and the efficiency 'hill' due to PCBM absorption is more pronounced than for thin layers. The reason for this behavior is related to the low charge carrier mobility in the blend combined with different absorption length for photons with different wave lengths [Che10]. Red and infrared photons exhibit a longer penetration depth and can be hence absorbed near the aluminum cathode after passing a thick blend layer. Green photons are likely absorbed near the PEDOT:PSS blend interface. Thus, the resulting electrons of the dissociated excitons likely recombine on the way through the blend layer towards the collecting cathode. The 'red' carriers, since generated in the whole layer, have a higher probability to reach the respective electrodes. Therefore the red region of the EQE is more pronounced compared to the green part, although the general low carrier mobility decreases the overall efficiency remarkably. Only high external bias (> 10 V) can reduce the recombination losses [Che10]. Also OPDs with layers thicknesses comparable to spin-coated devices exhibit a quite low efficiency.

For comparison, equally structured OPDs were fabricated with the blend layer prepared with toluene instead of DCB. The resulting IV-curves and the EQE are shown in Fig.5.12 and 5.13. The IV-curves exhibit comparable dark and photocurrents to the spin-coated references. The EQE is significantly higher than compared to DCB-sprayed

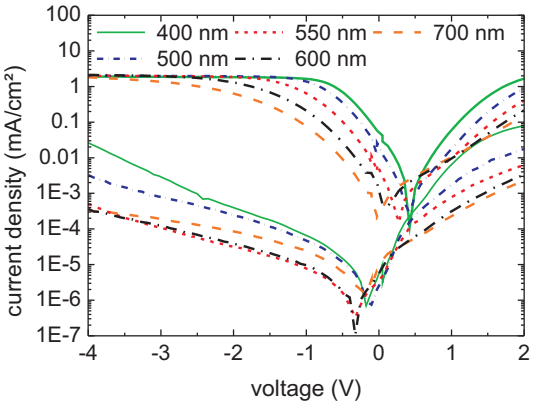

Figure 5.12: The IV-curves of inverted OPDs with a spraycoated blend prepared with Tol, a spin-coated PEDOT:PSS layer and a gold anode.

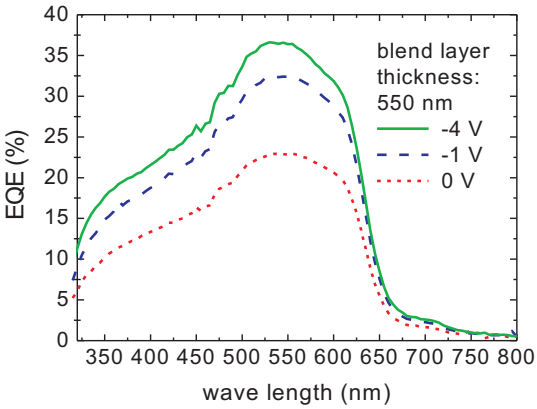

Figure 5.13: The EQE-curve of the device with 550 nm blend layer thickness, at different external applied bias.

OPDs. The maximum EQE which could be reached at -4 V, depending on the layer thickness, is about 35 %. This value is still smaller than for spin-coated samples, but this is partly attributed to the PEDOT:PSS layer which is spin-coated (flat thickness: 170 nm) on top of the blend layer, comprising a roughness between 100-200 nm, which leads also to the formation of a non-uniform, locally thin, PEDOT:PSS layer which can worsen the efficiency, as will be adressed in Fig.5.17 at the end of this section. For replacing the spin-coated PEDOT:PSS layer with a sprayed one, much higher EQEs can be obtained as will be shown in section 5.3.2.

Compared to devices with toluene blends, also the DCB based devices with a sprayed instead of spin-coated PEDOT:PSS do not exhibit higher EQE although the very rough DCB layers should have a bigger impact on the PEDOT:PSS layer non-uniformities than the less rough toluene blends. The reason for the general low efficiency of DCB-devices could be related to a lowered carrier mobility due to a bad interdrop connection. This assumption is supported by the fact the DCB exhibits a significant higher surface tension (35.4 mN/m at 20 °C) compared to toluene (27.9 mN/m at 20 °C) which hinders the spreading of the liquid onto the substrate. This characteristic may also explain the higher layer roughness of DCB-blends compared to blends fabricated with toluene (see Fig.5.9).
Also toluene is not an ideal solvent due to the already mentioned very high material consumption and also due to the fact that the device characteristics are very dependent on the layer thickness. This is observable in Fig.5.12 at the strong decrease of photo-and forward current by increasing the layer thickness from about 550 nm to 700 nm which was not observed for the DCB-devices.

If the assumption is right that a small surface tension is favorable for good interdrop-connection, a two-solvent system should lead to improved results compared to toluene in case it exhibits the so called Marangoni-flow [Fan98] which appears in case two requirements are fulfilled by the two solvents [Gir11]:

- A high and a low boiling point solvent is needed
- The less volatile liquid must exhibit a significantly higher surface tension

In case suitable solvents are mixed, the liquid with high surface tension will cause a higher co-adhesive force on the surrounding liquid than the other component. In case the mixed liquid exhibits phases of the two solvents, the resulting surface tension gradient will cause the liquid to flow away from regions of low surface tension.
The gradient of surface tension can be realized with the difference of the boiling points. On the drop surface, especially on the thin edge near the substrate interface, the concentration of the high boiling point solvent is high due to the evaporation of the volatile component. The resulting surface tension gradient leads to a force which is outwardly directed, resulting in a spread of the liquid with a velocity $v(r)$ parallel to to the substrate according to the formula [Fan98]:

$$v(r) = \frac{d(r)}{2\eta} \cdot \frac{d\sigma}{dr} \tag{5.1}$$

with d the local drop thickness, η the dynamic viscosity depending on the fractions of volatile and non-volatile components and the surface tension gradient $\frac{d\sigma}{dr}$ in parallel to the substrate. An enhanced spreading capability was already reported in [Gir11, Hot09] for a two solvent system consisting of DCB and mesitylene, for organic solar cell fabrication.
Due to the high difference of boiling points and surface tensions, also DCB and toluene are very suitable candidates for a Marangoni liquid. In Fig.5.9 the roughness of a blend sprayed with a mixture of DCB:Tol=1:1 is shown. Compared to the pure DCB film, the roughness of the mixture is significant lower and even slightly better as for a pure toluene film.
In Fig.5.14 and Fig.5.15 the corresponding electro-optical characteristics for typical devices are shown. For the DCB:Tol=1:1 mix the advantages of both solvents are combined. The course of the photocurrent is more stable for increasing the layer thickness as with DCB, and the EQE, with maximum values around 35 %, is as high as with toluene. The material consumption during spraying turned out to be about the same as with pure DCB. These three benefits as well as the low layer roughness make this solvent mixture the most suitable candidate for inverted OPD fabrication.

To finally prove that devices with a spray-deposited blend layer can exhibit the same performance as spin-coated devices, non-inverted OPDs with an ITO-anode were fabricated. The advantage of the non-inverted layer structure is that the spin-coated PEDOT:PSS layer is deposited on the ITO which does not lead to layer non-uniformities

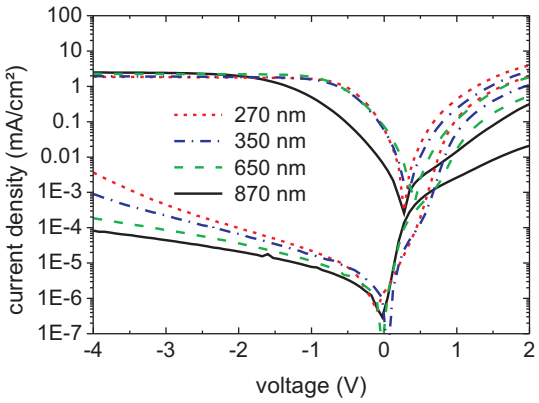

Figure 5.14: The IV-curves of inverted OPDs with a spraycoated blend prepared with DCB:Tol=1:1, a spin-coated PEDOT:PSS layer and a gold anode.

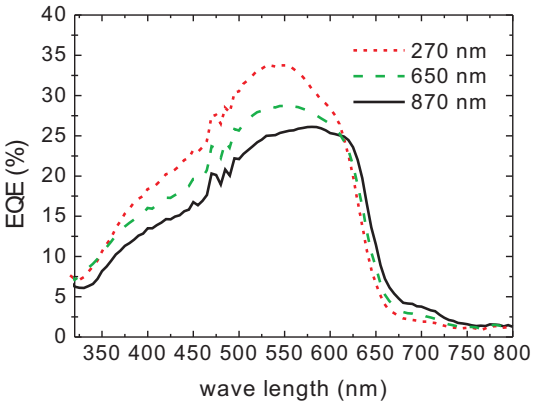

Figure 5.15: The corresponding EQE-curves of the diodes shown in Fig.5.14, measured at -4 V.

as with the spin-deposition on top of the rough sprayed blend in inverted devices. The performance of theses devices is shown in Fig.5.16 and Fig.5.17. The dark cur-

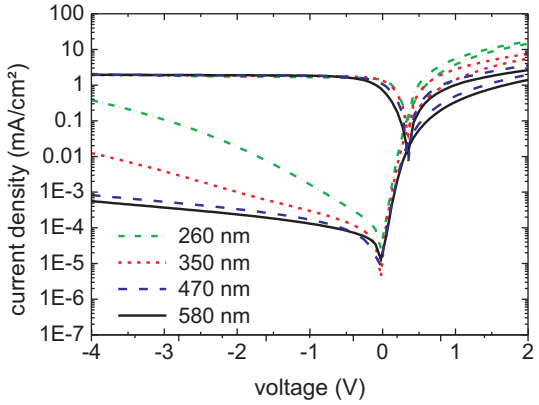

Figure 5.16: The IV-curves of non-inverted OPDs with ITO-anode and a spraycoated blend prepared with DCB:Tol=1:1 and a spraying pressure of 2 bar.

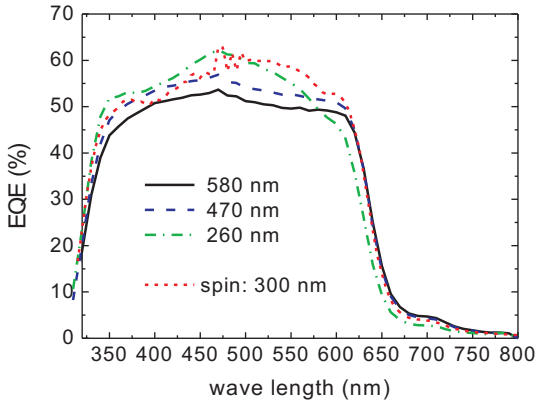

Figure 5.17: The corresponding EQE-curves, measured at -4 V, and as comparison the EQE of a spin-coated reference diode.

rent saturation, as shown in Fig.5.16, appears at about 500 nm layer thickness. The corresponding EQE-curve in Fig.5.17 exhibits a maximum of about 60 %. The completely spin-coated reference OPD with about 300 nm blend layer thickness, exibits a comparable efficiency, which finally underpins the suitability of the spray-coating method.

5.2.2 PEDOT:PSS hole conductor

The commercial aqueous PEDOT:PSS formulations are optimized for spin-coating deposition. For spraying, a further diluting is necessary to avoid a blocking of the spraying head due to high viscosity as well to increase spraying reproducibility (highly concentrated mixtures lead to a strong slope of layer thickness with increasing spraying time). As Girotto et al. showed in [Gir11], a diluting with isopropanol results in a Marangoni flow, but with the spraying setup used in this thesis, the use of the low-boiling point solvent isopropanol (82.5 °C) leads to an enhanced evaporation in the spraying beam giving rise to very low film thicknesses for reasonable spraying times (< 5 min). Hence, PEDOT:PSS dilution with water proved to be more practicable. The spraying parameters for a mixture of 2:1=H_20:PEDOT:PSS can be found in the *experimental details* 7.2.
Regarding fabrication of inverted OPDs, the spraying temperature is critical since it reverses the plasma treatment effect as shown in section 4.1.1. In section 5.1.2 it was described that room-temperature spraying leads probable to the formation of wet layers, but also to the smoothest films. Hence, for devices, an underlayer (consisting of a monolayer of drops) is sprayed at 35 °C and then the temperature is increased to 50 °C. The information about PEDOT-thicknesses in the following sections include this underlayer, also for non-inverted devices. The process proved to be the most reliable one regarding reproducibility and device performance.

5.2.3 Polymer electrode

The spraying of the conductive PEDOT:PSS layer required more optimization than for the hole conductor since a minimum sheet resistance R_{sheet} is necessary for good device performance. For four-point-probe characterization, 1 cm x 1 cm big square-shaped spraying fields, defined with an aluminum mask, were deposited. Larger fields suffer from layer thickness non-uniformity due to the gaussian beam profile as reported in section 5.1.1. Since four-point-probe measurements are only valid for infinitely spread layers, a correction factor of 0.8 (needle spacing s=1.67 mm), as calculated with a table in [Smi58] was multiplied with all measurements.
The handling of the PEDOT:PSS formulation PH1000 turned out to be critical since it tends to massive flocculation inside the spraying head which increases the probability for nozzle blocking. Extensive diluting with water decreases this problem slightly, but increases also the probability of spraying in the wet regime. Increasing heating during the spraying process to overcome the wet regime is critical since the heat budget on the blend inside an inverted device can worsen the performance. This accounts also for the post-annealing to remove water and EG for decreasing R_{sheet}. Finally, a compromise of dilution to 1:1=H_2O:PEDOT:PSS and spraying at 100°C led to good morphological results (for spraying parameters see the *experimental details*).
A major issue with adding water occurred regarding reproducibility. For spraying

subsequent layers with the same spraying parameters, the layer thickness increased compared with the previous sprayed layer. This phenomenon is shown in Fig.5.18 with the change of transmission of the subsequently sprayed layers. Since the origin of this

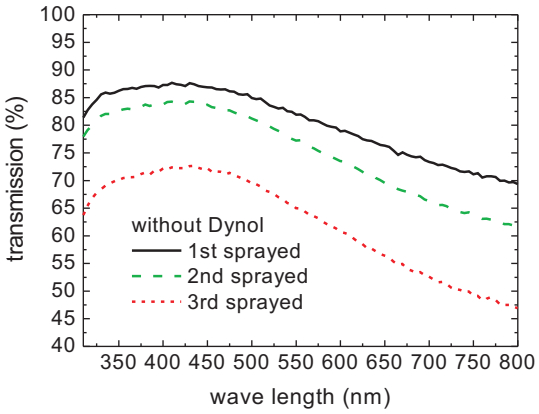

Figure 5.18: The spectral transmission of equally, subsequent sprayed layers prepared with a solution of H_2O:PEDOT:PSS:EG=1:1:0.2.

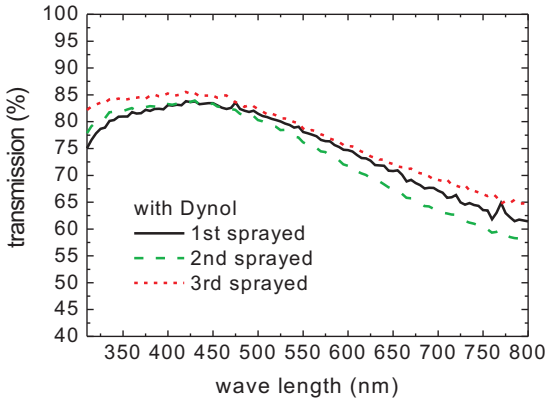

Figure 5.19: In difference to Fig.5.18, 0.3 % Dynol was added to the solution.

effect can be related to a demixing of the solution, resulting in an increased spraying flow rate of the materials with lower viscosity (ethylene glycol: 16.1 mPas, water: 0.894 mPas, PH1000: 50 mPaS), the concentration of the viscous PEDOT:PSS PH1000 increases in the reservoir. To overcome this issue, Dynol 604 was added to the solution to change the wetting ability of the solution which is related to a change of surface tension and dynamic viscosity as well. Dynol was already added to the spin-coating solution to improve the substrate wetting in section 4.3 where it was shown that Dynol does not have an impact on the conductivity.
With 0.3 % Dynol added to the solution, as shown in Fig.5.19, the spraying proved to be stable. The spectral transmission exhibits the same shape as for spin-coated layers, with a spectral maximum around 450 nm.

To obtain a minimum R_{sheet}, the optimal amount of EG in the PEDOT:PSS-water-mix has to be determined. For the spin-coated layers, about 10 % EG is optimal. Mixing a comparable amount EG to the spray solution does not lead to satisfying results as shown in Fig.5.20 on sprayed layers fabricated with a mixing ratio of H_2O:PEDOT:PSS:EG=1:1:0.2. Comparing the results of spin-coated layers in section 4.3 respective Fig.5.20, at 90 % transmission at 450 nm R_{sheet} has doubled. Only a doubling of the EG amount in the solution leads to results comparable to spin-coated layers, as shown in Fig.5.20. Since with spin-coating the maximum layer thickness and hence the minimum sheet resistance is limited, the spraying offers the possibility of deposition of low-resistiv films. The minium value achieved was 35 Ω/sq. at a transmission of about 75 % at 450 nm. A further increase of the amount of EG does

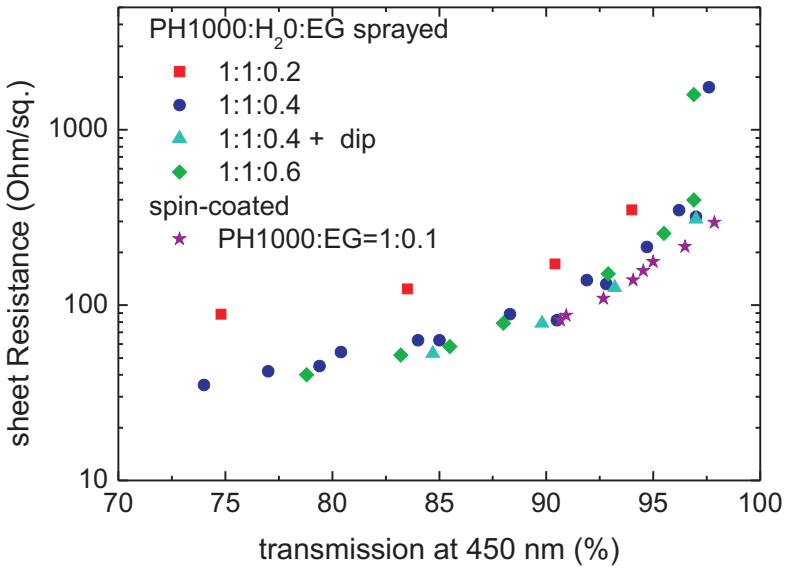

Figure 5.20: The sheet resistance versus the transmission at 450 nm for different contents of EG. The dip in EG, for 5 min, was performed before the post-annealing. The previous spin-coating results are including for comparison.

not improve the film conductivity. The saturation is also valid for films which were additionally dipped in EG, as shown in Fig.5.20.
Varying the post-annealing time, in order to remove water and EG from the film, at 120°C, between 0 and 30 min, does not significantly alter R_{sheet}.
For the device fabrication in the following section, the conductive anode was sprayed using a H_2O:PEDOT:PSS:EG=1:1:0.4 solution with 0.3 % Dynol. The spraying time is adjusted to deposit an about 200 nm thick film with a low roughness of about 40 nm which is related to the use of the wetting agent Dynol. The film exhibits a transmission of about 85 % at 450 nm (comparable to ITO) and $R_{sheet} = 50 - 60\ \Omega$/sq. (about factor 2-3 higher than with ITO).

5.3 Complete sprayed OPDs

In the previous section optimal material mixing ratios were determined as well the influence of spraying parameters on the layer roughness is investigated. This knowledge will be exploited in this section to fabricated OPDs with optimized electro-optical performance. To ease this optimization, firstly non-inverted OPDs were fabricated since their processing is easier as the inverted ones. As w the sprayed inverted OPDs, the sprayed conductive PEDOT:PSS solution will serve as anode instead of ITO.

5.3.1 Non-inverted OPDs

As starting point for optimization of a completely sprayed non-inverted OPD (except the aluminum top electrode) the knowledge of the previous sections is exploited:

- The bottom electrode consists of conductive PEDOT:PSS, prepared as described in section 5.2.3, and resulting in an about 200 nm thick film with 40 nm roughness, 85 % maximum transmission and $R_{sheet} = 50 - 60\ \Omega/\text{sq}$.
- The PEDOT:PSS hole conductor follows, deposited at 50°C to ensure minimum roughness.
- Minimum roughness also accounts for the blend layer sprayed at 2.8 bar pressure. The optimal blend thickness is, as e.g. visible in Fig.5.16, reached for dark current saturation and occurs for about 450-500 nm.
- The aluminum cathode is thermally evaporated as for spin-coated devices and exhibits a thickness of 150 nm.

Firstly, the optimal PEDOT:PSS layer thickness has to be determined. Spin-coated devices exhibit a PEDOT:PSS layer with 170 nm thickness to ensure low dark current and high EQE, but due to the roughness related with the spraying process, a difference is expected.
OPDs with different thick PEDOT:PSS layers were fabricated as well as reference layers on glass to determine the thicknesses via profilometer measurements. In Fig.5.21

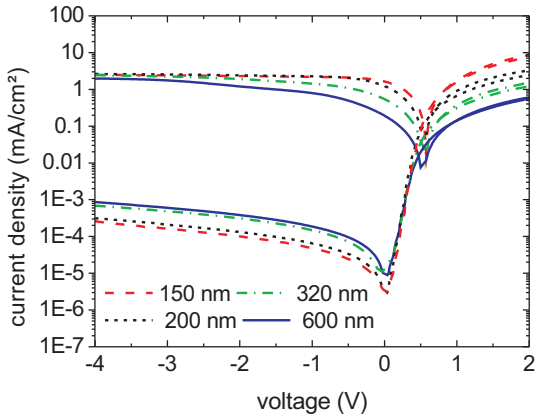

Figure 5.21: The averaged IV-curves of sprayed non-inverted OPDs with differently thick PEDOT:PSS layers.

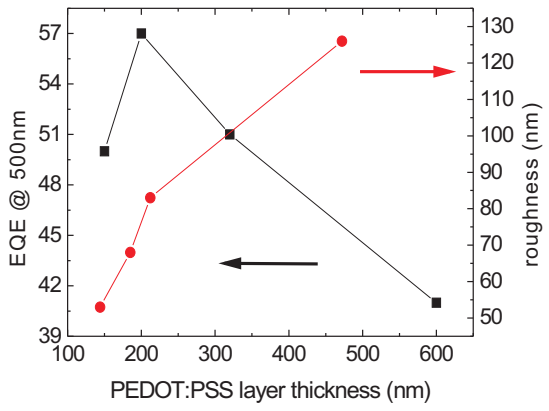

Figure 5.22: The EQE, measured at 500 nm and -4 V external bias, dependent on the PEDOT:PSS layer thickness and the corresponding layer roughness.

it can be seen that an increasing PEDOT:PSS layer thickness is related to an increase of the device serial resistance since the forward current is decreasing. Another consequence, much more critical to the OPD performance, is an increase of the dark

current with increasing PEDOT:PSS thickness. This phenomenon was already observed with spin-coated films [Fri09]. In [Fri09] the increase of the dark current was simultaneously observed with an increase of roughness and explained with a different film drying dynamic due to the low spin-speed and hence PEDOT:PSS morphology. Internal morphology changes are not expected for spray-coating, films deposited at different temperatures exhibit the same effect. A more fundamental explanation is that since the thermal generation and recombination rates in the organic materials are dependent on the number of states available in the respective material, an increase of the bulk material (or layer thickness) and of the interface area (because of the higher roughness) is probable related also to an increased dark current.
In Fig.5.22 the respective maximum EQE-values (averaged for at least 3-4 diodes) are shown as well the roughness of the PEDOT:PSS layers. For decreasing the layer thickness, the EQE increases due to the lowered serial devices resistance. After reaching a maximum value, the EQE drops abruptly. This effect was observed for many devices exhibiting thin PEDOT:PSS layers. The sharp decrease can be attributed to the layer roughness. As shown in Fig.5.22, with decreasing the thickness from 500 nm to about 150 nm, the roughness increases from 1/5 to 1/3 of the thickness. For thin layers, the probability for leakage paths increases which worsens the efficiency.
As conclusion, regarding dark current and EQE, thin PEDOT:PSS layers are preferable. To avoid leakage paths, an optimal PEDOT:PSS layer thickness of around 250-350 nm was chosen for OPD fabrication. A more precise value could not be determined since the spray setup was not reproducible enough. The thickness can be adjusted in a spray process by simply comparing the color of a sprayed test layer with a sprayed color scale with known thicknesses. For more precise determination before device spraying, a profilometer measurement is necessary.

Next, it was investigated if it is possible to optimize the blend layer for obtaining maximum EQE. The spraying pressure has the biggest impact on layer uniformity and was also tested in device fabrication. Since a change of spraying pressure also changes the spraying time needed to reach a certain layer thickness, the impact on layer roughness on device performance can only be rated taking the blend layer thickness into account. The devices were fabricated as described previously. In Fig.5.23 the maximum EQE-values for different spraying pressures and blend layer thicknesses are shown. The corresponding dark currents, not shown here, saturate for pressures from 1 - 2.8 bar at about 450 nm, the 0.5 bar samples exhibit increased dark currents also for higher values due to the high layer roughness, which is shown in Fig.5.8 for all pressures used for Fig.5.23. Interestingly, the spraying pressure respective layer roughness does not have an impact on the EQE. Dependent on the blend layer thickness, the EQE changes approximately linear with the same slope for all pressures. Thus, a further increase of spraying pressure (which is limited by the spray setup) might not be advantageous regarding efficiency.
As shown also in Fig.5.22, the generally observed maximum EQE (for dark current saturation) is around 50-55 %. This is still considerably lower than for spin-coated

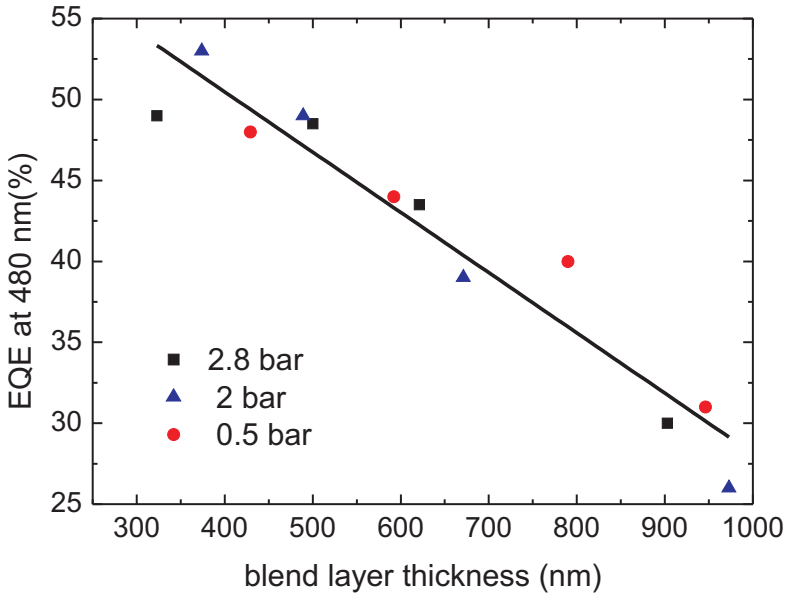

Figure 5.23: The EQEs of OPDs with blend layers sprayed at different spraying pressures, measured at 480 nm and -4 V external bias. The curve is a linear fit of all devices shown in the graph.

devices with conductive PEDOT:SS electrode as reported in section 4.3 and [Bai11a]. There, maximum values around 70 % EQE could be reached.
To identify the sprayed layer which has the biggest impact on the lowered EQE compared to spin-coated OPDs, different devices were fabricated, as shown in Fig.5.24. The conductive polymer electrode was either sprayed or spin-coated and combined with an either sprayed or spin-coated hole conductor. The blend layer was sprayed for all OPDs. The resulting EQEs, averaged over at least three to four OPDs, are particularly interesting around the optimal blend layer thickness of 500 nm. For the completely sprayed device, maximum values of about 55 % can be reached. For replacing the sprayed anode with a spin-coated one (with $R_{sheet} \approx 100\ \Omega$/sq.), the EQE is slightly better. Replacing also the sprayed hole conductor with a spin-coated one, the EQE is about 10 % higher than with the completely sprayed OPD. The maximum value of about 65 % indicates that in spite of the blend sprayed with a high roughness compared with a spin-coated one and the fact that the deposition was performed in air and not inside a glove box, the device is almost as good as a completely spin-coated one (maximum values are around 70 % [Bai11a]).
A factor which can worsen the device performance is the device fabrication in air. To investigate this impact, spin-coated devices were fabricated in a nitrogen glove-box, but stored for half an hour in air after each spin-coating step. No performance differences were observed compared to spin-coated devices which were not exposed to air during their processing.

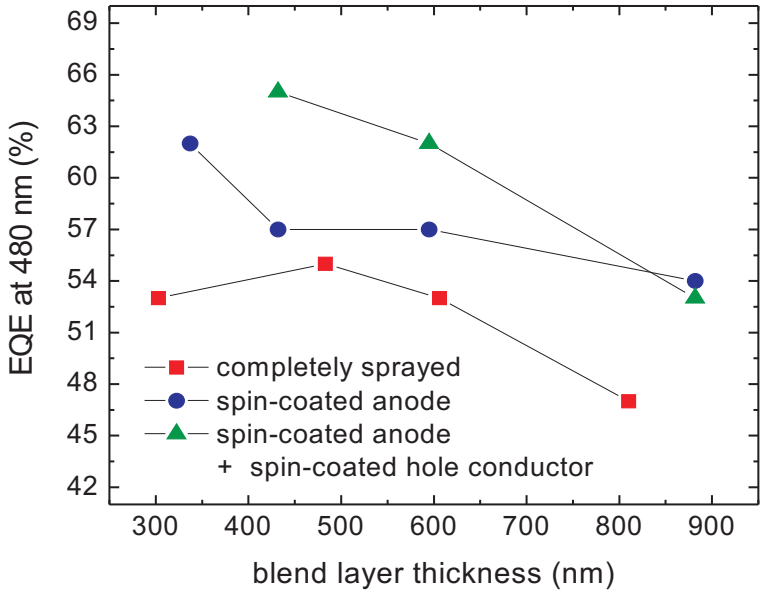

Figure 5.24: The EQEs of different OPDs with spin-or spray-coated layers, measured at 480 nm and -4 V external bias.

Hence, the differences of the performances might be mainly related to the layer non-uniformities which prevent attaining an optimal electro-optical device performance.

5.3.1.1 Dynamic behaviour

The increased layer roughness due to the spray-coating turned out to be crucial for the speed of the photodetector. In Fig.5.25 and Fig.5.26 the impact of the spraying pressure of the blend layer in a completely sprayed non-inverted OPD on the cut-off frequency is displayed. Doubling the pressure, starting at 0.5 bar, results almost also in a doubling of the cut-off frequency, depending on the layer thickness. The layer thickness has a major impact on the cut-off frequency since the dominating carrier transit time $t_{tr} = d^2/\mu V$ [Bai11a] through the layer is increased (with the layer thicknesses d, the carrier mobility μ and the voltage drop V). Since also devices with constant layer thickness, but different spraying pressures, exhibit different cut-off frequencies, the layer roughnesses have also a major impact on the detector speed. In Fig.5.26 the cut-off frequencies are shown dependent on the layer roughnesses which are different for each spraying pressure since the layer thickness is varied. High roughness at constant pressure indicates also a high layer thickness. For the different spraying pressures, the slope is different. For 2.8 bar, the steep slope hypothesizes that a further combined reduction of roughness and layer thickness could enhance the cut-off frequency towards values comparable to spin-coated devices (300-400 kHz, see section 4.1.4 and 4.3.2).

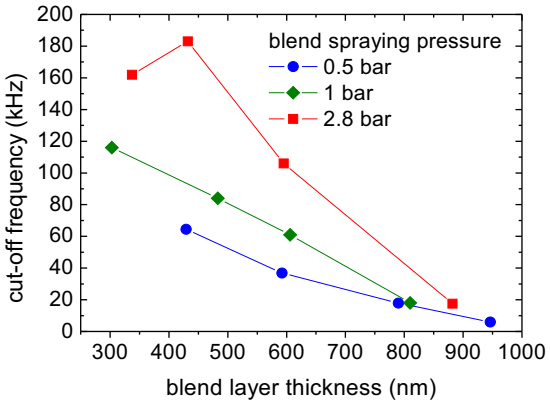

Figure 5.25: The cut-off frequencies of non-inverted, completely sprayed OPDs dependent on the average layer thickness. The data represents dynamic measurements performed on single diodes, fabricated on the same day to avoid fabrication fluctuations.

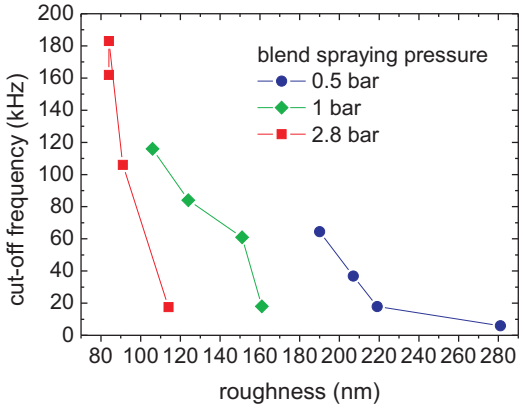

Figure 5.26: The same measurements, but plotted with the layer roughness as x-axis.

The origin of this significant impact of the roughness on the dynamic behavior is not yet understood. Also taking into account that the transit time does not dependent on the averaged layer thickness but has to be considered as $t_{tr} = \left(\frac{\sum d_i^2}{n}\right) \cdot \frac{1}{\mu V}$, with d_i as local layer thickness as measured with a profilometer, the observed behavior can not be explained.

The effect must not be directly related to the physical change of the blend, but can also result from a different electrical interdrop mobility due to the different velocities of drops impinging on each other.

The impact of the roughnesses of the other layers integrated in the device on the detector speed was also investigated. Replacing the sprayed anode with a spin-coated one with similar sheet resistance, the OPD speed is only slightly better. This small effect is attributed to the already smaller sprayed layer roughness of the anode of about 40 nm.

Replacing additionally the hole conductor with a spin-coated one gives a much better cut-off frequency which might be related to the fact that the thickness of the spray-coated layer is about twice as high as for the spin-coated layer (170 nm) and that the sprayed roughness of 100 nm is quite high.

With only the blend layer sprayed, the maximum cut-off frequencies are in the order of spin-coated devices [Bai11a].

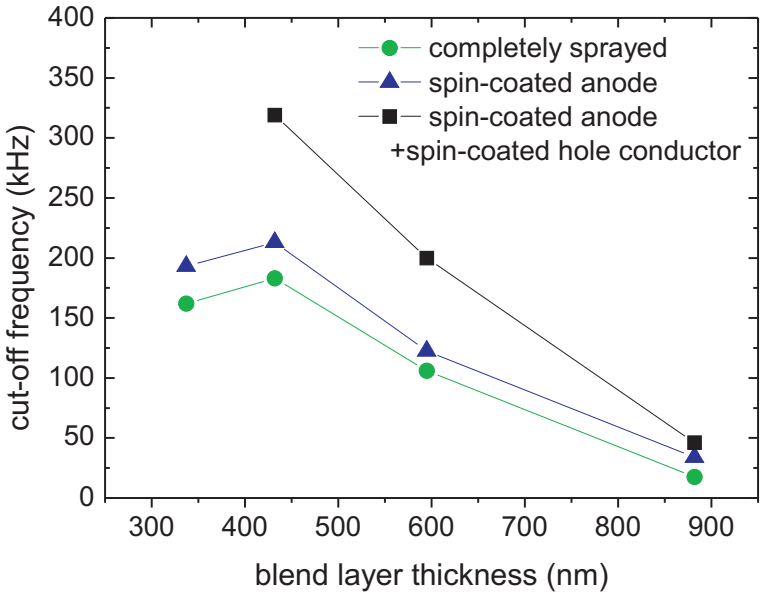

Figure 5.27: The cut-off frequencies of OPDs with spin- and spraycoated PEDOT:PSS layers. The blend layer was sprayed with different thicknesses. The data represent dynamic measurements performed on single diodes, fabricated on the same day to avoid fabrication fluctuations.

5.3.2 Inverted OPDs

For the fabrication of CMOS-compatible OPDs, the inverted process, investigated in chapter 4, and the spray deposition explored in this chapter are combined.
In difference to the non-inverted sprayed devices, for the inversion of the layer sequence, the plasma treatment has to be included which affects the PEDOT:PSS deposition as described in section 5.2.2.
In Fig.5.28 and Fig.5.29 the typical device characteristics of a sprayed inverted OPD with gold anode are shown. Compared to the inverted diode with spin-coated PEDOT:PSS layer as shown in Fig.5.14, the dark currents are even better. The most interesting difference concerns the EQE. Firstly, the voltage dependence of the EQE in forward direction is unexpected since the EQE increases again after reaching a minimum at about -1 V, with a different spectral dependence. This effect can be explained by photo-enhanced injection currents [Szm07], as also visible as offset of the light and dark forward current in Fig.5.28.
Secondly, compared to the maximum EQE of about 35 % in Fig.5.14, for the completely sprayed device values up to 55 % and even 60 % can be reached until the EQE saturates or the device starts to degrade. The EQE is as high as with the non-inverted devices with conductive polymer anode and is not easy understandable since the transmission of a 20 nm thick gold layer, either as flat layer or measured on a rough sprayed PEDOT:PSS layer, does not exceed about 55 %. Since the PEDOT:PSS hole conductor

and the encapsulation absorb and reflect the incoming photons, an EQE of more than 50 % seems unlikely. Also for devices fabricated on the same day, the resulting EQE is about equally high for both depositing gold or the high transparent conductive polymer electrode, although the transmission difference is significant. The low gold transmis-

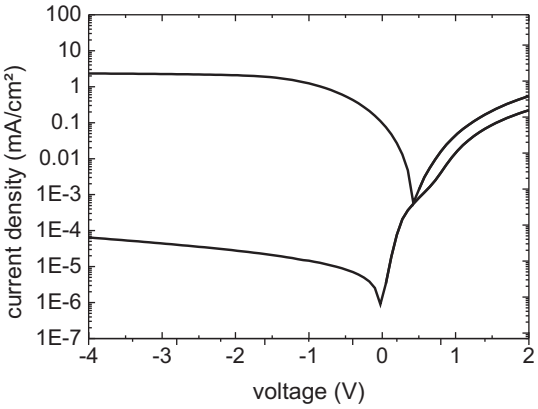

Figure 5.28: The IV-curves of an inverted sprayed OPD with gold anode.

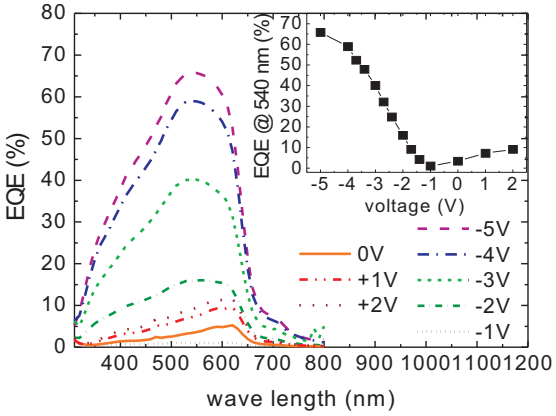

Figure 5.29: The corresponding EQE for different voltages. The inset shows the voltage dependence of the EQE.

sion contradicts the observed high EQE, but since transmission measurements can not be performed on a whole device including the opaque aluminum electrode, additional (electro-)optical effects might explain the high EQE. Since the very thin evaporated gold layer (20 nm) on top of a PEDOT:PSS with a roughness of about 100 nm can not exhibit a uniform film thickness due to shadowing effects during the thermal evaporation, the gold can be considered as a metallic, random periodical structured film. This unintended structuring might exhibit collective electron oscillations known as surface plasmons which can enhance the absorption of light. This effect is already exploited in numerous intents, different general geometries are shown in [Atw10], including e.g. the deposition of silver nanoparticles [Kim08b] [Duc09] and metallic gratings [Min10] for organic solar cells.

To confirm the assumption of plasmonic excitations, full field electromagnetic simulations are required, but they are very difficult to perform due to the random and unknown gold geometry. Although the effect is very interesting for further investigation, the fabricated devices turned out to be particular prone to degradation, either during performing electric measurements or just after a short time scale. This degradation effect is likely due to the non-uniform, partly very thin gold thickness. That a thin gold anode can lead to enhanced device degradation was already reported in section 4.3. The increased degradation of an inverted OPD with gold is shown in Fig.5.30. After two months, the EQE is decreased from about 50 % to about 15 %, independently of the carefulness of encapsulation. In comparison, the EQE of the inverted OPD with a top anode consisting of the conductive PEDOT:PSS decreases typically

to about 30 % on the same time scale. Although also this value is significant worse than for spin-coated devices reported in section 5, it has to mentioned that the whole device (except for the cathode) was fabricated in air which enhances the incorporation of airand especially water to the hygroscopic PEDOT:PSS.
The significant difference between these two kinds of devices prove that the strong degradation in Fig.5.30 must be indeed related to the gold anode. As conclusion, for

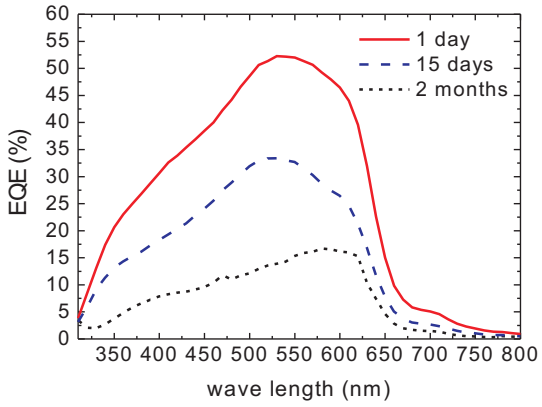

Figure 5.30: Lifetime measurements on an inverted device with gold anode, showing the decrease of the EQE at -4 V (device stored in air).

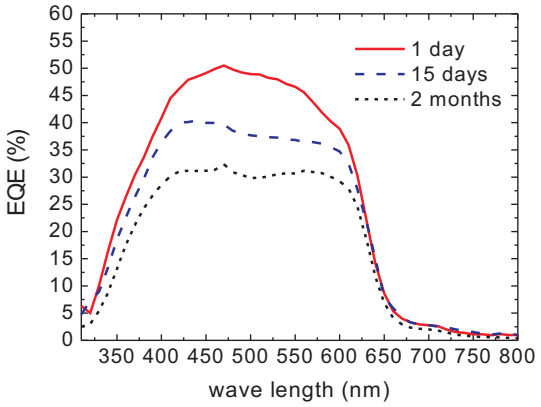

Figure 5.31: Lifetime measurements on an inverted device with polymer anode, showing the decrease of the EQE at -4 V (device stored in air).

the inverted build-up the polymer electrode is the better choice than a gold anode. The low dark currents and similar high EQE as for non-inverted sprayed devices make the inverted OPD suitable for CMOS-integration.

5.3.3 CMOS-dummmy structures

Prior to the fabrication of hybrid CMOS-detectors and along with the fabrication of large scale detectors, the inverted process was transferred to dummy substrates which exhibit a similar surface topography and which were fabricated with materials (silicon substrate with sputtered aluminum pads and SiN-passivation) also used for the CMOS-process. The intended use was to identify problems which could arise during hybrid imager fabrication. The layout of these substrates was already described in section 3.1.2. During the testing, the following issues turned out to be either negligible or gave motivation to certain process changes which were reported in this thesis so far:

- The spin-coating process turned out to be not suitable for the CMOS-dummy substrates. Diodes were fabricated, but exhibit some orders of magnitude increased dark currents which hints to the inhomogeneous deposition on top of the pixels.

- The roughness of the aluminum pads is critical. Whereas the RMS-roughness of thermally evaporated aluminum is less than 10 nm, sputtered aluminum can exhibit a much larger roughness, as measured for the dummies (roughness about 20 nm). In addition, the sputtered layer can exhibit high spikes which can be higher than 100 nm, as observed with the dummy substrates. The consequence is also an increase of the dark current of several orders of magnitude, as shown in Fig.5.33. Hence, for the CMOS-substrates, a sputtering process was deployed which allowed the fabrication of very smooth aluminum layers with roughness below 10 nm.
- The deposition of the organic layers on silicon and SiN-layers was unproblematic since no adhesion problems occurred. Hence, no additional wetting treatments were necessary. The height of the passivation layer, which was increased to a typical value of 2 µm as used for CMOS-chips, turned out not to hinder the polymer deposition with the spray setup.
- The roughness of sprayed organic layers is critical since the small lateral diode sizes, varying from 40 to 70 µm, have a similar dimension than the sprayed drop sizes. In Fig.5.32, the distribution of the dark currents of about 30 diodes of a dummy substrates, fabricated with a non-optimized spraying process, are shown. The variation is more than one order of magnitude. For an average current of 8 pA at -1.5 V, the standard deviation is 3 pA. Hence the fixed-pattern noise (see section 6.2.1) is about 7 pA which corresponds to about 88 % of the signal compared to the optimized spraying process resulting in 50 % shown in section 6.2.1. To improve this aspect, the single organic layers were optimized as described in section 5.1.2 and 5.1.3 to reach the small dark current distribution for the CMOS-detectors as later shown in section 6.2.1.

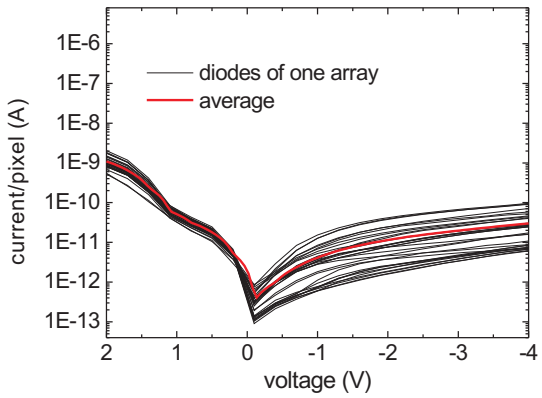

Figure 5.32: The dark IV-curves of about 30 diodes of an array as showed in Fig.3.5. The spray parameters of the blend (1 bar spraying pressure) and PEDOT:PSS (deposited at 100°C) are not optimized.

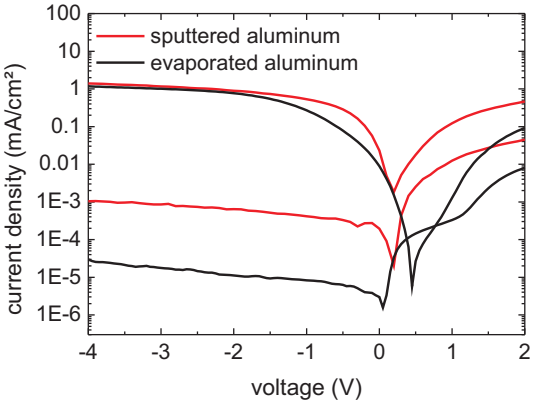

Figure 5.33: Two IV-curves of diodes fabricated on a CMOS-dummy substrate. Once, the aluminum was sputtered with a roughness of about 20 nm and peaks exceeding a height of 100 nm, the other was thermally evaporated with a roughness < 10 nm.

Chapter 6

Realization of a first solution-processable hybrid CMOS-imager

In this chapter, the preliminary work on the inverted OPD as well the spray-deposition will be used to finally fabricate a hybrid detector. Firstly, the inorganic part of the detector, the CMOS-chip will be described as well the particularities arising due to integration of the organic layers. In the following section, the results of the optoelectronic characterization of the hybrid imager will be presented.

6.1 Chip technology

The CMOS-chips used for the hybrid imager were designed at the Bruno-Kessler-foundation in Trento and fabricated in commercial facilities. Since prototype chip fabrication costs are high, the foundry 'austriamicrosystems', offering multi-project wafer fabrication, was chosen as manufacturer. Here, the area of a silicon wafer, processed in standard CMOS 0.35 µm technology, is shared with other projects to keep the costs low but which also results in a small number of available chips (with a small area of 4 mm^2) for the hybrid imager fabrication. The cost for the about 20 chips was about 4000 Euro which is mainly attributed to the manufacture of masks for the different photolithographic steps. Although the costs are high in the prototyping phase, concerning a mass production (> 10000 chips), the cost for a single chip would drop to a few Euros per chip.
As comparison, the prototyping costs for the organic layer spray deposition for 20 chips are about 50 Euro, attributed mainly to the polymeric materials, with almost negligible costs for the production since no vacuum nor high temperatures are involved during the spray deposition.

6.1.1 Layout and architecture

The CMOS-chip was mainly intended to be a test bench for the hybrid technology, to gather information about the most important imager characteristics, but also to allow the acquisition of low-resolution images, as reported in [Bai11b].

The architecture of the chip is shown in Fig.6.1. A charge-integrating amplifier read-

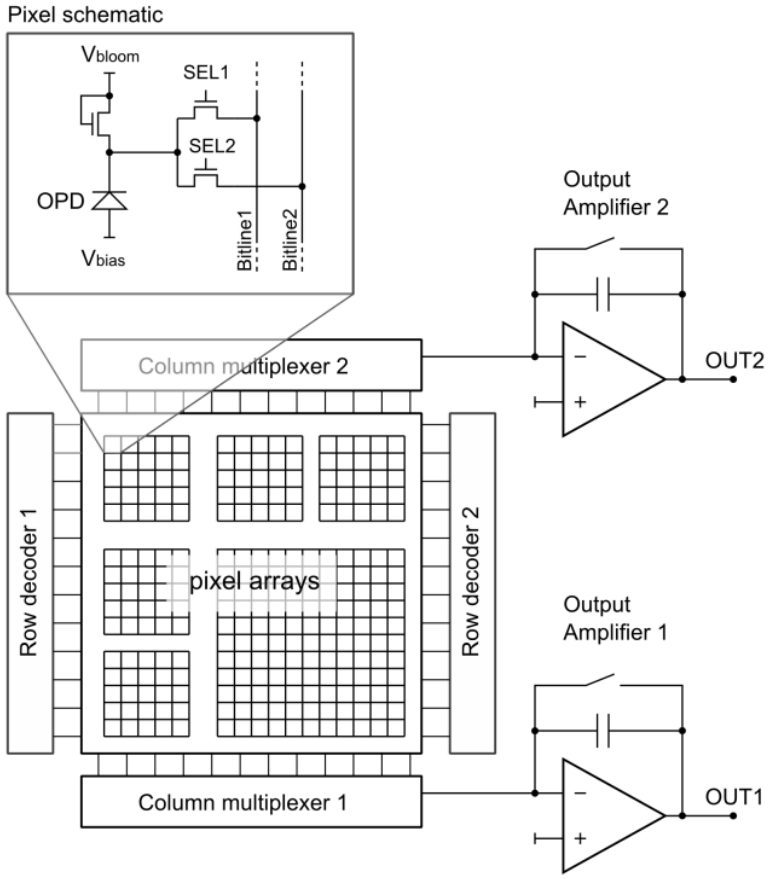

Figure 6.1: The architecture of the CMOS-chip integrated in the hybrid concept.

out channel was chosen to maintain the OPD at a fixed voltage during operation. In order to measure the intrinsic noise of the OPDs and to be able to distinguish photon shot noise from other possible noise contributions, a low-noise charge amplifier was implemented.

Considering the area needed for this amplifier with 100 fF feedback capacitance and to avoid read-out channel non-uniformities, a passive pixel sensor (PPS) configuration was chosen [Den91], meaning that only one amplifier is implemented for the read-out of all pixels, as already addressed in section 2.2. To allow cross talk measurements, which requires to address two pixels simultaneously, a second, identical charge amplifier was also integrated. To connect, respective select the pixels to those amplifiers, two sets of

each a row decoder and a column multiplexer were added to the layout. The wiring between pixels and amplifiers is short due to the small pixel array size, thus keeping the parasitic line capacitances smaller or comparable to the OPD capacitance, thus having a negligible effect on the measured noise characteristics.
The pixels, with different pad sizes (50 µm, 35 µmn and 15 µm) are arranged in different arrays, the largest one with 30x30 pixels is also suitable for acquiring low resolution images. In the hybrid approach, in contrast to a standard CMOS-imager, the whole pixel is covered with a metalization layer so that the full pixel area can be employed for the organic photodetector. The fully CMOS-compatible aluminum layer, used here, has to connect the read-out electronics to the organic photoactive layer, therefore acting also as the bottom electrode of the OPD. Furthermore, each pixel contains two transistor switches which connect the OPD to the two different readout channels. Additionally, also an anti-blooming transistor is integrated to clamp the cathode voltage when the diode is not selected. The purpose for this transistor, which acts like an emergency valve, is to prevent the OPD cathode to go below ground potential due to the presence of high illumination. Without the anti-blooming transistor, the switch transistor would inject electrons into the substrate which could be collected by nearby pixels.
A few pixels based on standard silicon np photodiodes were also included to the chip as references.

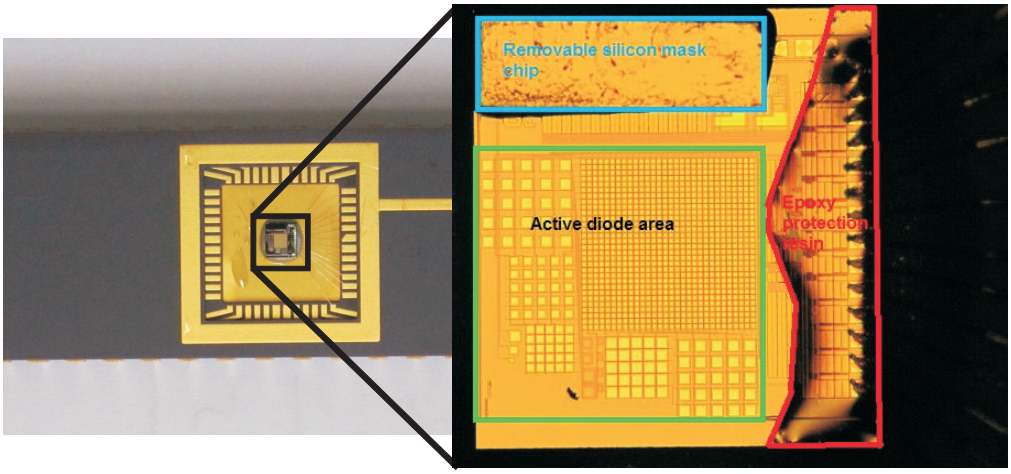

Figure 6.2: The chip inside the chip carrier, the enlargement shows a microscope picture of the different chip parts, including the post-processing steps (silicon chip for protection of the top electrode contacts, PDMS for bonding wire protection).

The layout of the chip with the different arrays and post-processed parts is shown in Fig.6.2. The bonding to a so-called chip carrier, as shown in Fig.6.2, was performed prior to the organic deposition to avoid a damage of the organics later on due to the heat budget of bonding. The purpose of the chip carrier is to ease the handling during

the characterization since it exhibits electronic contacts which can be simply clamped into a read-out-device. Additionally, the carrier is also easier to handle during spray deposition. This is due to the large dimension compared to the chip itself, which is only 2x2 mm^2.
All the bonding pads have been grouped on a single side of the chip to facilitate the protection of them and the bonding wires during spraying. Since they are not electrically isolated, short-circuits between anode and cathode are possible. To shield them electronically as well as to integrate them in a stabilizing matrix, drops of PDMS (polydimethylsiloxane) were applied on top of the wires, as indicated in Fig.6.2.
Another post-processing step concerns the protection of the contacting pads before the PEDOT:PSS top electrode deposition. A small silicon chip was glued to these pads to keep the pads free from photoactive blend and the hole conductor, afterwards it was removed with a tweezer to start the electrode deposition.

6.1.2 Integration of the organic layers

For the spray deposition of the organic layers the optimized process of chapter 5, in which small blend drop sizes were realized (5-10 µm) as well as small layer roughness (≈ 100 nm RMS-roughness), is used. Regarding that the substrate has changed from a large scale glass substrate to a the small CMOS-chip glued into the chip carrier, several process modifications were needed.

Firstly, the whole chip carrier was dipped into ammonium hydroxide, as described

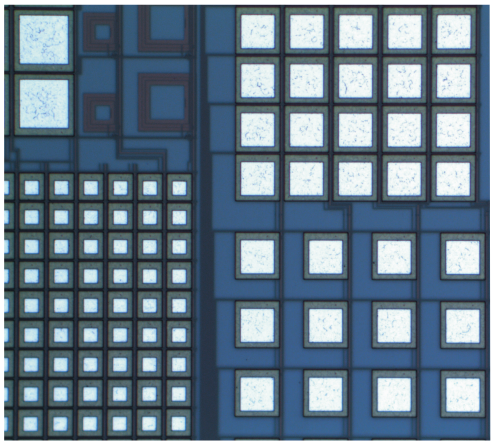

Figure 6.3: Microscopic picture of the chip before organic deposition.

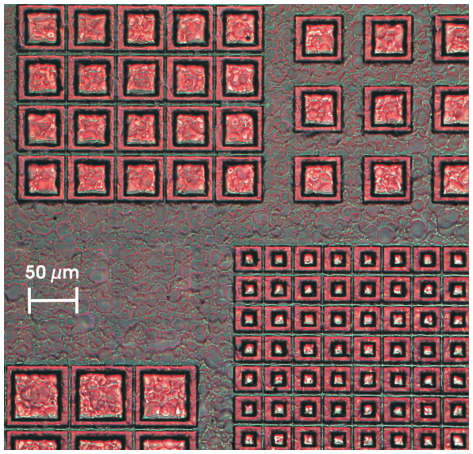

Figure 6.4: Chip after blend spray deposition.

in section 4.2, to remove the native aluminum oxide on top of the metalized pixels. After ultrasonic cleaning in isopropanol, the photoactive layer was sprayed, see Fig.6.4, through a spraying mask on the chip, followed by the plasma treatment (see section 4.1).

It turned out that the microwaves generated to produce the plasma damage the chip due to an antenna coupling. This coupling appears since the microwave length is about 6 cm, whereas the electric contact lines inside the chip carrier are about 3 cm long. Hence, the chip carrier acts like a $\lambda/2$ antenna which produces voltages peaks inside the carrier lines, hence destroying the chip electronics. The only way to prevent this coupling was to introduce a faraday cage of massive copper with only one hole with chip dimensions to allow the plasma to diffuse towards the chip. Additionally, a grounding of all pins of the chip carrier to the faraday cage as well the frame ground of the plasma asher was necessary to totally exclude chip damages.
After plasma treatment, the two PEDOT:PSS layers were sprayed and annealed as described in section 5.3.2. The fabrication process was completed by an encapsulation step (see section 4.5) which enclosed all organic parts to ensure a long-life stability of the hybrid detector.

6.1.3 Signal acquisition

In section 2.2 the basics of the signal read-out of a CMOS-imager are described. As for an APS, also in the hybrid PPS imager charge carriers which are produced in the photodiode are integrated over a certain integration time after pixel reset. The read-out circuitry is schematically shown in Fig.6.5. The voltage V_{ref} resets the photodiode to a certain reverse bias. C_{int} represents normally the internal photodiode capacitance. In a common PPS imager, the charge is integrated during illumination on this photodiode capacitance and shifted afterwards from the diode to the charge amplifier. In this operation concept the bias voltage V_{ref} of the diode is not constant during integration since the photodiode discharge is related to a voltage drop. Instead, since the hybrid pixel characteristics should be investigated dependent on the applied bias, a slightly different concept was chosen: the charge amplifier is directly connected to the photodiode thus the charge integration is performed on the feedback capacitance (C_F=100 fF) of the amplifier while keeping the biasing at a constant value.
In Fig.6.6 the voltage output over time is shown, starting with the pixel reset phase during the closing of the reset switch. During integration, the switch stays opened and the voltage signal is produced in the charge amplifier.
For further signal read-out, the chip is connected over the pins of the chip carrier to a testboard which acts as adapter between the chip and a microcontroller. The used *mbed-controller* has several functions:

- Providing a power supply to the chip (3.3 V).
- Generating digital control signals for the chip. Among the most important ones: the reset signal for the charge amplifier, a reset for the column and row decoder and a clock for scanning the pixels.
- The analog-to-digital conversion.

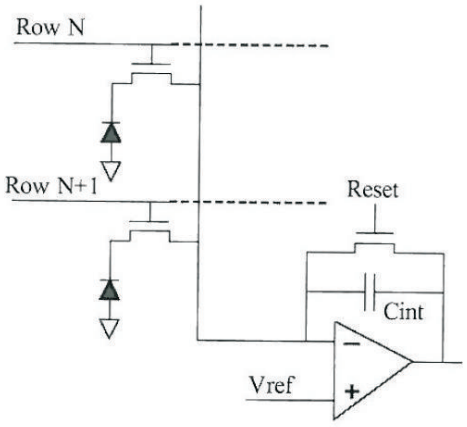

Figure 6.5: The hybrid PPS read-out architecture with a separate charge amplifier for all pixels. (adapted from: [YP04])

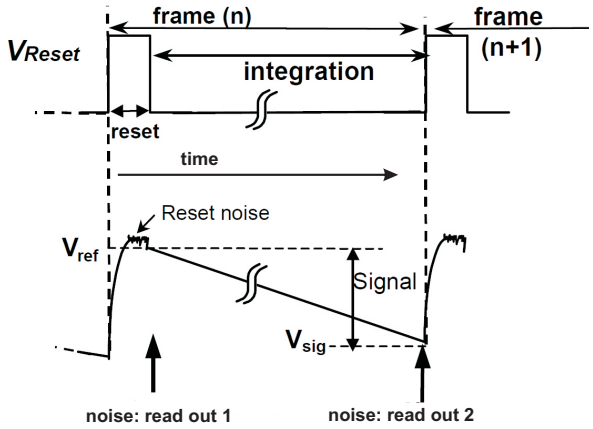

Figure 6.6: Read-out schematic of the hybrid imager (from: [Mag03]). The arrows labeled with 'noise:read out' indicate the moments of noise voltage acquisition as desbribed in section 6.2.2

- Communication with an interface, all data acquisition programs were programmed with *LabView*.

6.2 Performance of the first solution-processable hybrid CMOS-imager

In order to validate the suitability of the hybrid CMOS-imager, optoelectronic measurements on the essential photodiode characteristics were performed and also low-resolution images were taken. Although focusing on the PCBM:P3HT bulk hetereojunction as organic photoactive layer in this section, also the panchromatic detector containing squaraine, see section 4.4, was implemented on the CMOS chips.
The most important photodiode characteristics, which were investigated, are:

- Dark current: Actually, the amount of dark current is not important, but since a high dark signal is also related to an increased amount of temporal noise (shot noise, see section 3.4.4) which can not be electronically compensated, a low dark current is important for a high detectivity.

- EQE: Since the hybrid concept is motivated with an increase of the pixel fill factor up to 100 %, the prototype should exhibit an EQE higher than that of a standard CMOS-imager which is < 30 % [Fos97].

- Detector speed: For conventional imaging application typical frame rates are around 100 frames/s since typical charge integration times and data transfer

times, which are both in the order of milliseconds, limit the speed of the detector. Cut-off frequencies in the order of 1 kHz are hence sufficient.

- Temporal noise: The dark noise voltage determines the ability of the imager to detect small light signals and the light noise voltage sets a fundamental limit to the signal-to-noise ratio and hence to the sensitivity. Both have to kept as low as possible.

- Pixel cross-talk: In the following section, two different fill factors are distinguished: the pixel fill factor which is the photosensitive part of the pixel itself and the overall chip fill factor which accounts for the 'dead' area between two pixels which are separated by pitch width minus the pad length. The pixel fill factor is already increased to 100 % due to the vertical polymer integration, but also the overall fill factor has to be increased as much as possible to increase the number of pixels on the same area. The signal exchange between two adjacent pixels, measured as cross talk, is a quantity to estimate the minimum spacing required between two pixels.

In the following sections, the results of the hybrid imager characterization are summarized as published also in [Bai12].

6.2.1 Performance under dark and illuminated conditions

By integrating the photodiode output charge ΔQ over an integration time Δt_{int}, the dark and photocurrents of the PCBM:P3HT hybrid imager using $I = \Delta Q/\Delta t_{int}$ are obtained. Unlike the large scale photodetectors, the hybrid imager is illuminated with a green LED @ 535 nm which was also used for other measurements requiring illumination. The applied light intensity for all IV-curve measurements was 70 µW/cm^2.
Fig.6.7 shows the IV-curve for a typical pixel with 15 µm pad size for both the absolute current values as well the current density. The rectification ratio for the dark current is as high as for a large scale reference detectors, from -2 V to +2 V the current increases 4 orders of magnitude. Hence, the serial resistance is also comparable to large scale devices with a freshly evaporated aluminum cathode which hints to a good interface quality of the etched chip to the organic layers.

The superior low dark current, which is one order of magnitude lower than for the large scale detector, ranges from about 15 fA/pixel ($7 \cdot 10^{-6}$ mA/cm^2) at -1.5 V to about 50 fA/pixel ($2 \cdot 10^{-5}$ mA/cm^2) at -4 V. The origin of this very low dark current can be related to the down-scaling of the photoactive diode area from 7 mm^2 to areas with about $2.5 \cdot 10^{-3}$ mm^2 size (50 µm pad width) and smaller, which can be related to a considerable reduction of ohmic pathways of the donator/acceptor phase between the electrodes.
The dark current values shown in Fig.6.7 are within the FWHM of the Gaussian distribution of all dark pixel values with 15 µm pad size contained in the 30x30 array. The

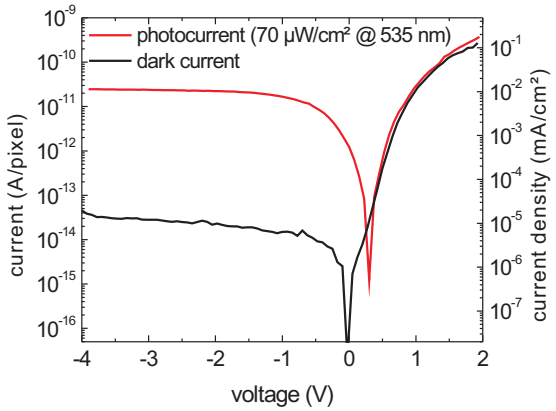

Figure 6.7: Absolute current and current density versus voltage characteristics of a single pixel with 15 µm pad size.

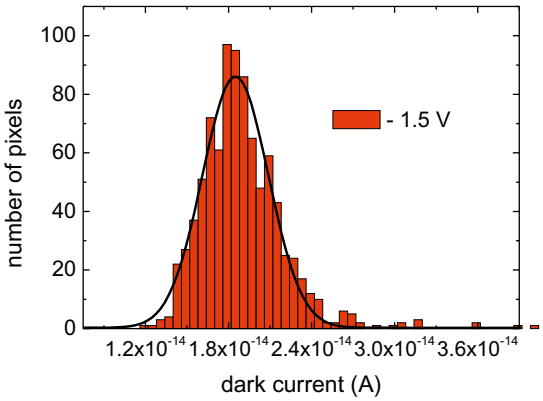

Figure 6.8: The distribution of the dark currents of all pixels (pad size 15 µm) in a 30x30 pixel array fitted assuming a Gaussian distribution.

histogram of the dark current distribution is shown in Fig.6.8 for an applied voltage of -1.5 V. The average dark current of all these pixels is about 20 fA, with a FWHM of 6 fA. This dark current distribution appears as so-called fixed pattern noise (FPN) in the output signal of the hybrid imager. Since a PPS architecture with shared read-out electronics for all pixels was chosen for the hybrid imager, the origin of the FPN is not related to read-out non-uniformities but to the organic layer themselves. Since the spraying introduces a surface roughness of the blend of about 100 nm, the thickness variations are the mean reason for dark current non-uniformities, see section the *supplementary information* in [Bai12]. Since FPN is not a temporal noise source, it can be almost eliminated by on-chip processing. The FPN is not usually expressed as current, but as voltage variation for a typical integration time at video rate, resulting in FPN=1.2 mV for FWHM(I)=6 fA and t_{int} =20 ms. The amount of FPN in the hybrid imager is similarly low as compared to silicon CMOS-imagers [Dec98].

Fundamentally, the performance under illuminated conditions of the hybrid imager is not affected by any electronics contained on the chip. In the PPS layout, the pixels do not contain the read-out amplifier, but also in case of an APS, the output would be the same since the photoactive material is placed on top of the electronics.
The spectral dependent EQE of a typical pixel (15 µm pad size) of the hybrid imager for different applied voltages is shown in Fig.6.9. The spectral maximum of more than 40 %, for bias voltages larger than -1.5 V, can be found around 420 nm, although the EQE stays quite constant in the visible range of the spectrum up to the absorption edge of PCBM:P3HT at around 650 nm and would allow therefore the separation of the three primary colors with additional filters. The average EQE (Fig.6.10) of all pixels in the 30x30 array stays at about 40 % , although single pixels exhibit EQEs

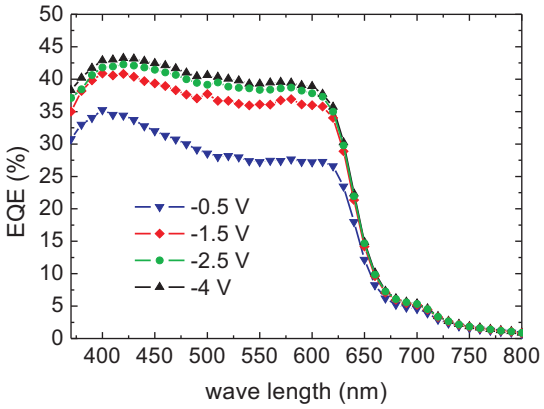

Figure 6.9: A typical spectral EQE for a single pixel with 15 µm pad size is shown for different external applied voltages.

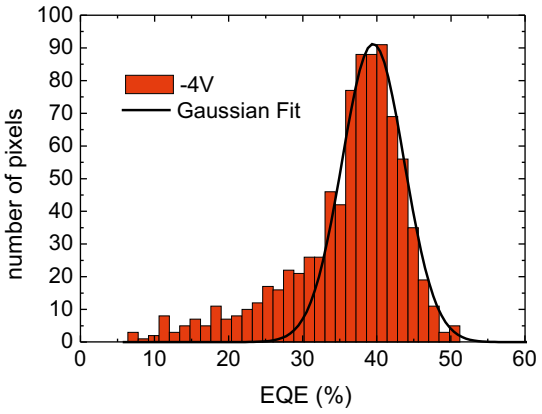

Figure 6.10: The asymmetric distribution of the EQE of all pixels (pad size 15 µm) in a 30x30 pixel array overlaid by a Gaussian fit.

up to 50 % . These values are lower than demonstrated in section 5.3.1 because the average photoactive layer thickness (about 650 nm) in the hybrid imager was chosen to be slightly higher than the optimum of about 500 nm for maximum EQE as investigated in section 5.3.1 to prevent single leaky pixels and to ensure the low uniform dark current in Fig.6.8 in spite of layer thickness fluctuations. Still, the achieved average EQE of the hybrid imager is better than that of most standard front-side illuminated APS imagers, which is usually below 30 % [Fos97, Big06].
Since the roughness of the sprayed PCBM:P3HT layer is about 100 nm, large EQE variations are expected due to the about 5 % decrease of EQE for increasing the photoactive layer thickness by 100 nm, as shown in Fig.5.23. The FWHM of the assumed Gaussian distribution in Fig.6.10, a measure of the photo response non-uniformities (PRNU), is about 9 % EQE. This value is higher compared to conventional silicon imagers but can be still mostly compensated with electronic post-processing [Hos07].

Another important photoresponse measurement, the dynamic behavior, is illustrated in Fig.6.11. The acquisition of response times was performed in a different way than for large scale detectors since for the hybrid imager, the voltage signal itself is a time dependent measurement due to the charge integration. The pixels were illuminated with square-waved light pulses (about 4 mW/cm^2, duty cycle 1 %) and the corresponding photoresponse in Fig.6.11 was extracted from the time-domain charge integration signal with the oscilloscope by calculating the derivative. To reduce the noise due to the differentiation, the integrated output signal was averaged over a large number of acquisitions (> 100) and a low-pass filter with a time constant of 100 ns was applied. Since the OPD rise and fall time had a much larger time constant, this operation caused a negligible distortion in the measured pulse response. For a typical pixel, in Fig.6.11 with a pad size of 50 µm and a reverse bias of -3.5 V (-2 external plus -1.5 V

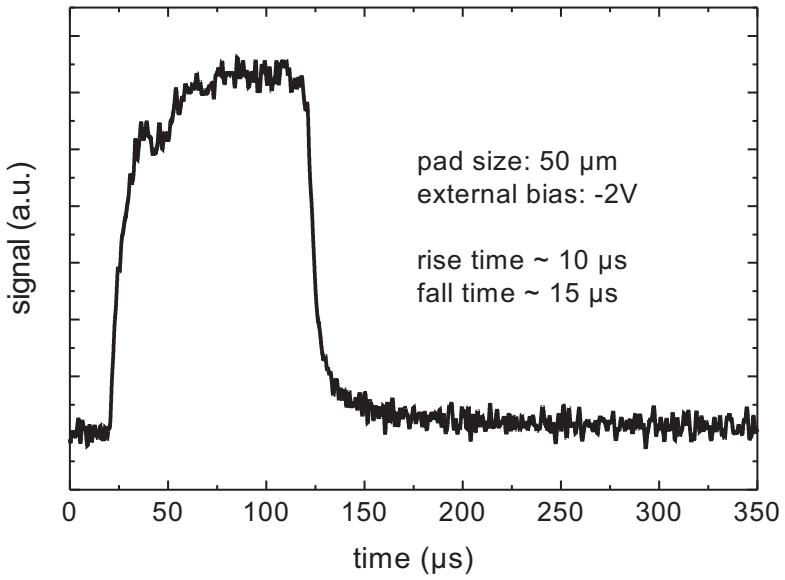

Figure 6.11: The dynamic photoresponse, derived from the charge integration signal. Illumination: square wave pulses, 4 mW/cm^2, duty cycle 1 %.

internal), typical response times are in the order of 10-15 µs. These values correspond to a bandwidth $1/2\pi t$) of about 10-15 kHz which is more than enough for imaging as explained at the beginning of section 6.2.

6.2.2 Temporal noise

The types and origins of temporal noise were already discussed in section 3.4.4. For an imager, a low noise level is of fundamental importance since it determines the operational range. This range can be described by the dynamic range (DR) which quantifies the ability of the sensor to adequately image both high light intensities and dark shadows in a scene. DR is defined as the ratio between the maximum and minimum detectable voltage signal, DR= $20 \cdot log(V_{max}/V_{min})$. With the hybrid imager, the maximum voltage signal due to light illumination which can be read-out is about 2 V which is limited by the amplifier operational range. The minimum signal is related to the residual noise under dark conditions.
For a CMOS-imager, shot noise (see section 3.4.4) is the dominant noise component, although also the chip electronics (amplifier noise, pixel reset noise) contribute to the overall noise level. The shot noise is the root-mean-square (RMS) value of the dark signal following a Poisson distribution, $\sqrt{N}$, with the number of leakage carriers N, due to the discrete and independent motion of carriers over a potential step and is

given by:

$$V_{noise} = \sqrt{N}\frac{e}{C} = \sqrt{\frac{Signal(V) \cdot e}{C}} \tag{6.1}$$

with e the elementary charge and C the charge amplifier feedback capacitance. The root-dependence on the signal implicates that high dark currents should be avoided in order to keep the noise low.
With C=100 fF and depending on the integration time, shot noise voltages below 2 mV (for signal voltages V < 2 V) are expected which are also usual for common CMOS-imagers.
The noise measurements of the hybrid CMOS-imagers were not performed in the frequency domain as commonly employed (with a spectrum analyzer or via fast Fourier transform) due to the charge integration over a specific time, producing a time dependent voltage signal of the chip output. Instead, the measurements were performed in the time domain by acquiring the voltage signal with an oscilloscope (LeCroy wavepro 7200), performing signal filtering and Correlated Double Sampling operations on the digitized output. The term 'Correlated Double Sampling' is a technical expression used to indicate that two samples are acquired after the same reset event. For the noise measurements, many samples were acquired (> 100 acquisitions) and averaged at two different times, after the pixel reset and at the end of the integration time, as indicated in Fig.6.6. The resulting averaged values were then treated as two single samples and their difference was calculated. The output noise was extracted as the standard deviation (RMS value) of the sampled output voltage. Additionally, for every set of parameters, the measurement was repeated for 5-10 times to increase accuracy. The standard deviation of this operation is showed in the following noise graphs (Fig.6.12 and 6.13). In Fig.6.12 noise measurements under dark conditions are shown. They indicate the RMS-noise voltage deviation of a hybrid pixel with 35 µm pad size for different output dark currents (obtained by applying different external bias voltages) and integration times. While for t_{int}=10 ms the noise level stays well below 1 mV, increasing the dark current leads to a noise level increase of about one order of magnitude for t_{int}=1 s. The strong impact of integration time hints to a dominant flicker noise contribution which is proportional to the current I and frequency f: [Mar00]

$$flickernoise \propto \frac{I^{\alpha}}{f^{\beta}} \tag{6.2}$$

Flicker noise is known to be present in many electronic devices, since the origin is related to a slow fluctuation of properties of the materials used in the device. For organic photodiodes, little is known about flicker noise, differently from inorganic MOSFETs [Hun90] and organic thin-film-transistors (OTFTs) [Mar00, Zha10, Kan, Lin10], where flicker noise is observed for the drain current. Here, the two dominant flicker noise sources described are trapping-detrapping of carriers in the channel at the gate oxide (causing a carrier number fluctuation) and bulk scattering (causing a mobility fluc-

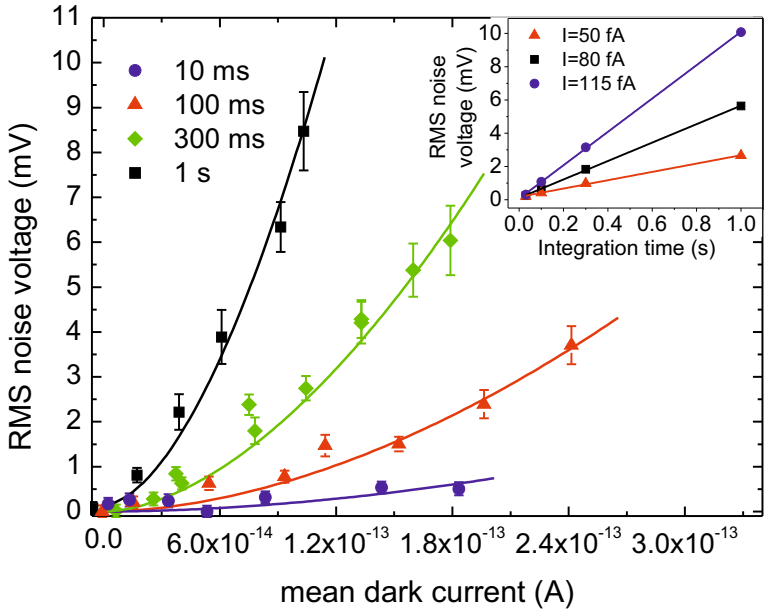

Figure 6.12: Noise under dark condition. The current standard deviation, expressed as noise voltage, versus the dark current which was varied by applying different external voltages. The error bars represent the standard deviation of a set of noise voltage measurements. The fitting was done assuming a quadratic dependence on the dark current. The inset shows the linear increase of the noise voltage with different integration times and constant dark current.

tuation). Recent publications hint to various types of traps within the disordered, amorphous organic semiconductor, like at grain-boundaries of pentacene [Kan, Lin10] not only at the gate oxide. Similar mechanisms could apply for the solution-processable disordered organic photodiodes. The experiment shows a linear dependence of the noise voltage on the integration time in the inset of Fig.6.12, proving that $\beta = 1$, which indicates a uniform distribution of trap energies [Chr68]. The dependence on the dark current, fitted quadratically in Fig.6.12, indicates that $\alpha \rightarrow 2$, hinting to dominant volume trapping instead of a surface nature [Zie88].
Regarding the impact on imaging, the high flicker noise for integration times in the range of 1 s is not detrimental since for most imaging applications integrations times are in the ms range. The dynamic range of the hybrid detectors can be henceforth estimated to about 60 dB, assuming 2 mV as minimum detectable dark signal (for integration times smaller than 100 ms). This value is quite comparable to silicon CMOS-imagers, although it has to be mentioned that the upper range is usually not limited by the photodiode itself but the read-out-electronics.

Since detection of N photons is a random process obeying Poisson statistics, Eq.6.1 accounts for the photon shot noise as well. It presents the fundamental limit in the signal-to-noise ratio as described in section 3.4.4. In Fig.6.13, noise voltage measurements of the hybrid imager performed under varying illumination and with typical

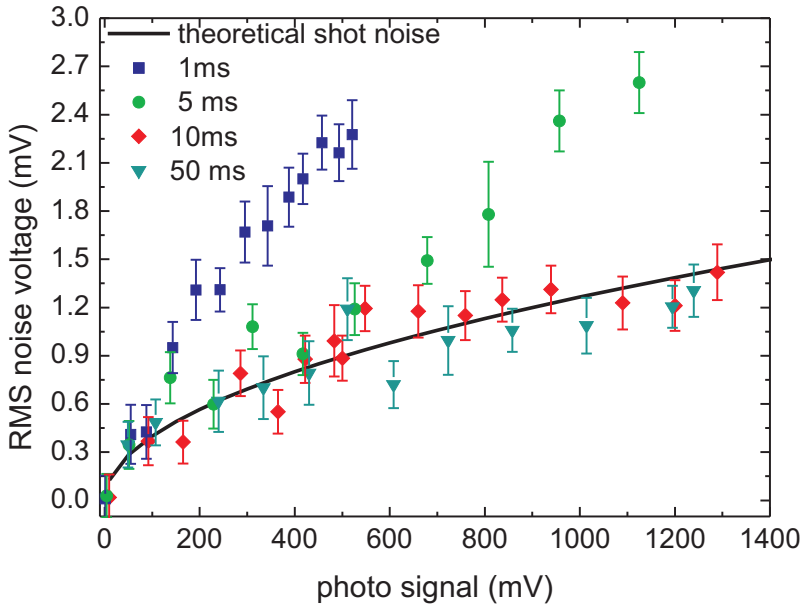

Figure 6.13: Photon noise. The change of the photocurrent and the corresponding voltage signal was achieved by varying the light power of a green LED (535 nm). The external applied bias was kept constant at -1.5 V. The corresponding dark signal was subtracted from the data. The theoretical shot noise is plotted for comparison.

integration times for imaging (1 ms - 50 ms) are shown. In contrast to the dark signal, the results are much closer to the theoretical shot noise, also included in the graph. The reason for that might be related to the presence of the high (photo) currents which saturate all available trap states [Arc13]. Interestingly, for integration times $\geq$ 10 ms the noise voltage matches the photon shot noise. Decreasing the integration time increases slightly the noise level. This can be due to an additional noise component associated with the high current flowing in the device due to illumination. Possibly, the origin of this behavior is related to the space charge accumulation at the blend-PEDOT:PSS interface and a related change of the electric field which was reported in section 4.1 and in [Bai10, Bai11a]. The related electric field dependence of the mobility [Zau07, Mov86] could account for the flicker noise component as well.
Since the photon noise does not significantly deviate from shot noise, a negative impact on the signal-to-noise ratio is not expected. For a detailed understanding of the noise-behavior an in-depth-understanding of all contributing trap states is necessary.

6.2.3 Pixel cross talk

The maximum overall fill factor of the photoactive chip area, the ratio between pixel and interpixel area, is limited by the minimum space between adjacent pixels at which

negligible cross talk is generated. Cross talk quantifies the amount of signal from one pixel collected by a neighboring pixel. To determine this amount, the light of an green LED was focused with an objective on a single pixel (pad size 15 µm pitch 30 µm) and the generated photocurrent as well the signal of a neighboring pixels were read-out simultaneously by the two charge amplifiers. In Fig.6.14 the crosstalk between the pixels, at an applied external bias of -3.5 V, is illustrated, distinguishing between close (vertical plus horizontal) and diagonal neighbors. The signal of the outside pixels is on the dark current level of all other pixels in the array. Including all neighboring pixels, the cross talk is 0.165 % of the illuminated pixel signal (close neighbors: 0.258 %, diagonal neighbors: 0.072 %). By reducing the applied voltage to -1.5 V, the cross talk is slightly increased to 0.182 % (close neighbors: 0.368 % , diagonal neighbors: 0.114 %). These very low values imply that both photocarrier diffusion across the organic layers and the optical cross-talk (in spite of the reflective aluminum cathode) are well suppressed which could be related to the general low mobility of organic bulk-heterojunctions ($1 \cdot 10^{-4}$ $cmV^{-1}s^{-1}$). For a standard silicon imager, the 'dead' space/length between two pixels is usually in the order of only few µm (< 5µm) compared to the pixel distance in the hybrid imager of 15 µm. Hence values cannot be directly compared, especially, since color filters and micro lenses (which can be omitted in the hybrid design) increase the optical cross talk in a CMOS-sensor. Since, as described in section 2.2.1, the absorption length of photons with higher wave lengths (IR) as well the carrier diffusion length in silicon are high, it can be concluded that silicon sensors suffer in general more of cross talk as the low-mobility organic sensors.

6.2.4 Imaging

With the biggest array, containing 30x30 pixels, on the chip, low resolution monochrome images can be acquired. As test objects, simple sketches of different items were used which were illuminated by ambient air. The light was collected by an objective (focal length: 6 mm, focal ratio: 1.2) and focused on the pixel array. The integration time was set to 5 ms. The resulting image, showing a football, can be seen on the upper left side of Fig.6.15. It is quite noisy, mainly due to the large light fixed pattern noise. To compensate the sensitivity inhomogeneities among the pixels, a dark and a gain correction were performed as also used for standard silicon sensors. The final images were corrected by subtracting the dark level of each pixel which was determined by acquisition of an image under dark condition. This operation was followed by multiplication with the gain factor which is defined by the ratio of each pixel raw data signal divided by the corresponding signal obtained by sensing a white sheet of paper under ambient light. These corrected images are also shown in Fig.6.15, the huge difference between raw and corrected image is demonstrated on the image of a football.
After the corrections, only about 5 pixels of the imager remain darker than the surrounding bright background because of high leakage current, meaning that more than 99 % of the pixels are working.

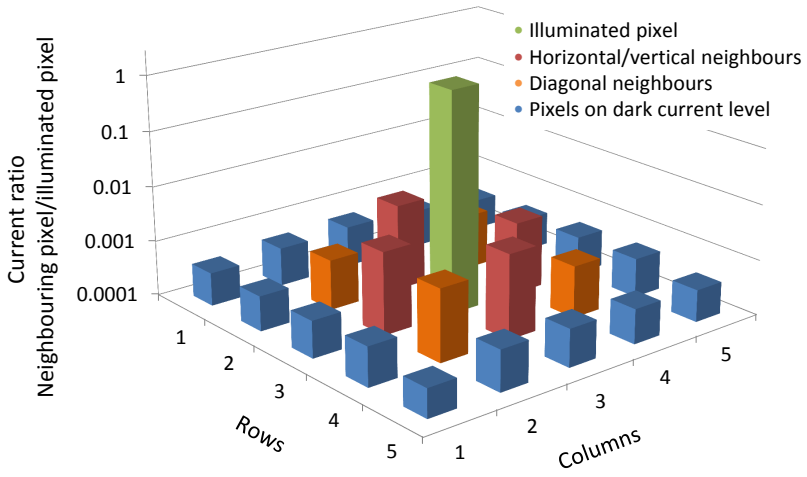

Figure 6.14: Pixel-to-pixel crosstalk. The percentage of photocurrent, created in the central illuminated pixel on a semi-logarithmic scale, which reaches adjacent pixels. The pixel pad size is 15 µm, the pitch 30 µm. The applied external bias is -3.5 V and the light power is about 450 μW/cm^2 (535 nm)

6.2.5 Hybrid imaging with squaraine

One of the major strengths of solution-processable organic electronics, the ease of switching between different organic materials without increasing process complexity, was demonstrated here by adding the dye squaraine (SQ) to the hybrid imager. As already described and investigated in detail in section 4.4, the addition of SQ to the PCBM:P3HT bulk heterojunction leads to the formation of a panchromatic detector sensitive up to about 900 nm. For the hybrid imager, the in section 4.4 optimized PCBM:P3HT:SQ solution, was sprayed on the chip without any change of process parameters or of the imager build-up.
The measured dark currents of the chip proved to be similar to the pure PCBM:P3HT hybrid imager, 26 fA/pixel ($1.2 \cdot 10^{-6}$ mA/cm) at -1.5 V. The EQE, in comparison, showed a different behavior. The SQ part of the EQE-spectrum exhibits values up to about 20 % (similar to the results in section 4.4). In the green region, in which the PCBM:P3HT blend predominantly absorbs, the EQE was increased up to 100 %. This could hint to an increased pixel-to-pixel crosstalk, but the measured values for 15 µm pixels (30 µm pitch), 1.04 % average cross talk between neighbors (close neighbors: 1.70 %, diagonal neighbors: 0.38 %), at an applied voltage of -3.5 V, seem to be too small to explain the results. Especially, since larger pixels (50 µm pad and 100 µm pitch size) exhibit comparably high EQE although the pixel-to-pixel distance is increased by fac-

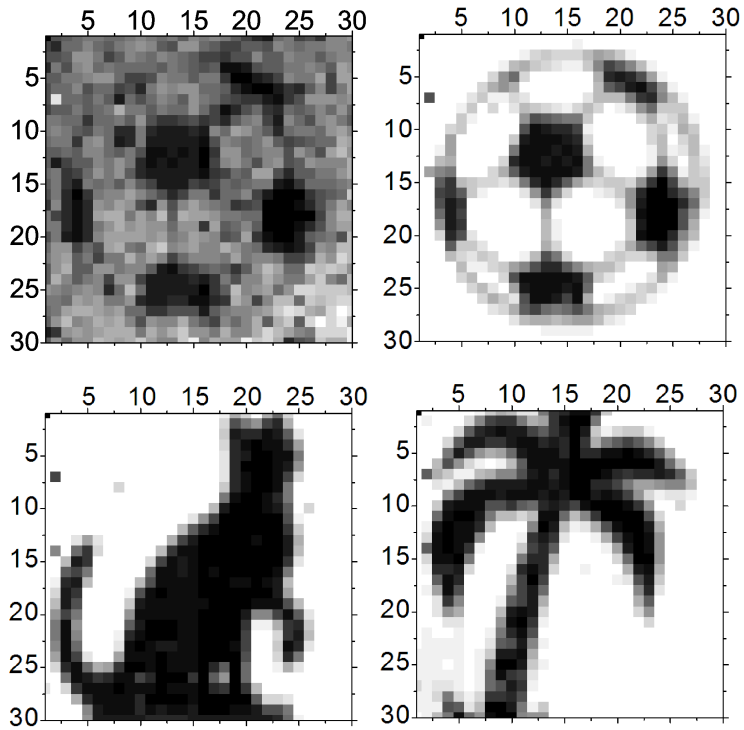

Figure 6.15: Four monochrome images, showing a football, a cat and a palm, are acquired by the 30x30 pixel array under ambient light. The left image of the football is without dark and gain corrections.

tor 3, a more probable reason could be a material-dependent lateral photoresponse due to drifting of photogenerated carriers near the pixel edge to the pixel. Since a common top PEDOT:PSS anode for all pixels is implemented, an extension of the photodiode built-in electric field from the pixel area, defined by the aluminum cathode area, is possible and can contribute to collecting photogenerated carriers. As long as the cross talk remains small, this effect is advantageous for imaging due to the increased light sensitivity.

To validate the hybrid panchromatic sensor, simple images were acquired at two different wave lengths (by illumination with different LEDs) as shown in Fig.6.16. At 535 nm, only the PCBM:P3HT is sensitive to the light, not only for the pure PCBM:P3HT sensor but also for the one containing SQ. At 850 nm, in addition to the squaraine, there can be also a small contribution of the collection of diffusing photocarriers generated in the silicon substrate. Since the pure PCBM:P3HT hybrid imager is almost blind at this wavelength, as shown in Fig.6.16 d), the influence of the silicon can be neglected. Since the images were acquired more than three months after the sensor fabrication, also the good stability against degradation of the device is demonstrated.

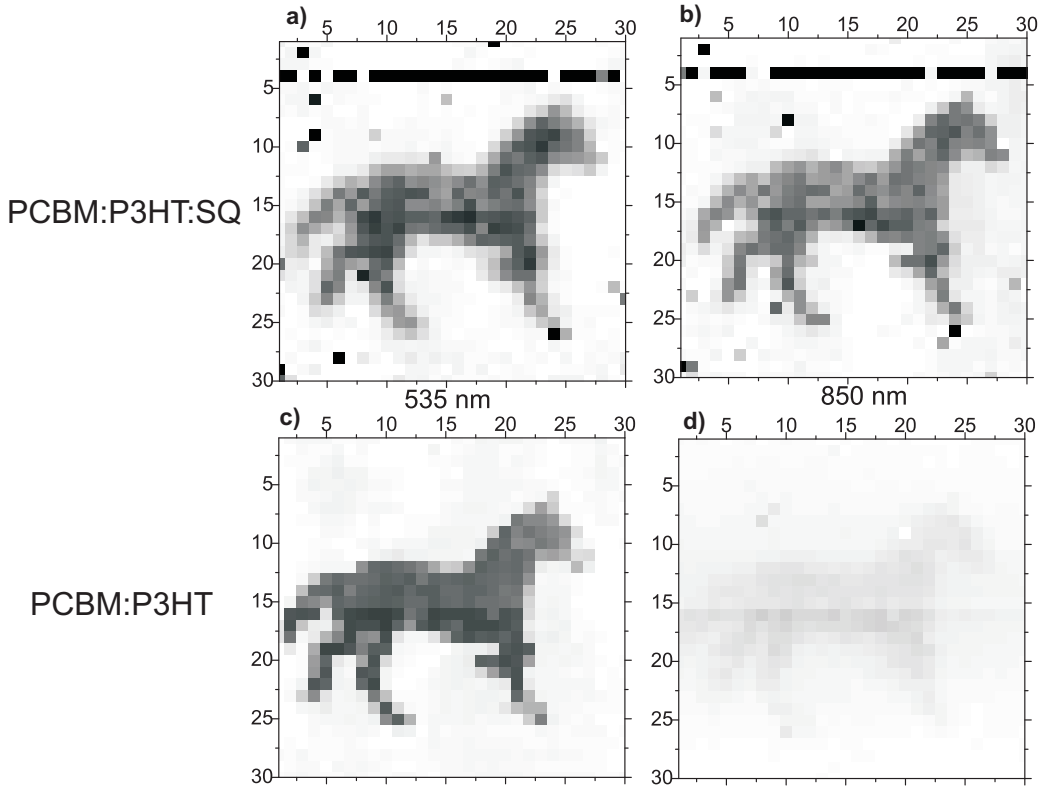

Figure 6.16: Images of at two different wavelengths acquired with two different sensors, one with and one without squaraine.

Chapter 7

Conclusion

7.1 Summary

The aim of this thesis was to develop a hybrid CMOS-imager with solution-processable organic layers. To reach this goal, several issues had to be dealt with. For light detection on top of an opaque substrate, like the CMOS-chip, the state-of-the-art bottom-absorbing organic photodiode was transformed to a top-absorbing device. This was achieved by inverting the layer sequence of the photodiode, starting the fabrication with the deposition of the cathode. To deposit the water-based PEDOT:PSS solution on top of the hydrophobic PCBM:P3HT blend layer, a sensitive oxygen plasma treatment is performed which creates a hydrophilic blend surface without causing damages to the polymer. This surface layer was characterized by surface sensitive characterization methods like AFM, XPS and contact angle measurement to learn about the composition and understand the physical impact on the device performance. Electro-optical device measurements revealed the presence of space-charge limited current with deep traps and proved that the inverted photodiodes do not suffer from reduced performance compared to the non-inverted reference diodes.
In addition to the electro-optical characterization, also the lifetime of the inverted, spin-coated devices was investigated and improved. Stabilities of at least 9 month are observed.
In order to improve the low EQE (45 %) of the inverted diodes due to the use of a semi-transparent gold anode, a novel kind of conductive PEDOT:PSS was investigated regarding the suitability as anode material. The composition of the solution-processable anode was optimized and the trade-off between sheet resistance and transmission was investigated. For an anode exhibiting a sheet resistance of 100 Ω/sq., maximum EQEs over 70 % and dynamic cut-off frequencies above 400 kHz are observed.
The second main challenge which had to be overcome, after attaining the top-absorption, concerned the deposition on highly textured substrates like CMOS-chips. Spray-coating turned out to be a suitable deposition method due to the vertical application. For each

organic layer, an optimal set of spraying parameters was defined to obtain homogeneous layers with low roughness. The roughness turned out to be critical for the performance of small area detectors like the single pixels on a CMOS-chip since the layer thickness non-uniformity on a lateral scale which is comparable to the pixel size leads also to non-uniform EQE and dark current. For the blend layer, the choice of the solvent turned out to be critical for good device performance and layer roughness. As optimal solvent a 1:1 mix of 1,2-dichlorobenzene and toluene was determined, most probable due to the good spreading capability related to Marangoni flow.
For completely sprayed devices (with an evaporated bottom aluminum cathode), maintaining a low dark current of about $1 \cdot 10^{-4}$ mA/cm^2, EQE values of about 55 % could be reached.
Combining finally the inverted fabrication process and the spray deposition on a silicon chip, processed in standard (commercial) CMOS 0.35 µm technology, gave rise to the first solution-processable hybrid CMOS-imager. These passive pixel sensors were fully electro-optically characterized using charge integration on a feedback capacitance for signal read out and a testboard with integrated microcontroller for generating the timing signals and further data processing (digitalization) and transfer (to a *LabView*-interface).
Among the novelties of the hybrid imager are the so far smallest organic photodiodes (containing a sandwich structure), with a pad width of 15 µm, and the most precise cross talk measurements (15 µm distance between illuminated and measured pixel) performed on this kind of diodes. Additionally, due to the chip design containing a low-noise charge amplifier, the first organic photodiode noise measurements were performed which reveal the noise types (flicker and shot noise) as well the amount present in the organic layers.
The performance of the hybrid imager is not only sufficient for imaging application, but turned out to be superior regarding two aspects. Firstly, the measured EQE of up to 50 % is remarkably higher than for typical silicon CMOS-imagers. Secondly, the integration of squaraine as additional donor material in the hybrid imager, proved the ease of switching the material system to reach different spectral sensitivities. This portability of the hybrid concept is indeed the major strength since it offers a cost-effective imaging concept also for wavelength regions beyond the absorption edge of silicon.

7.2 Future work

Although the imager prototype fabricated during this thesis proves the strength of the hybrid concept, for a commercial application two further issues arise. The long term stability of the device performance is crucial for organic photodiodes. Although it was shown in this work that also with a very simple encapsulation a minimum device life time of about one year is feasible, this was not true for the spray-coated devices,

probably because they were fabricated in air. Also for switching the material system from PCBM:P3HT to other polymers, degradation can be a more severe problem. These issues have to be investigated and solved before transferring the hybrid concept to even more expensive prototype imagers with state-of-the-art pixel numbers (several Megapixels).
The other issue concerns the switching of the material system to more interesting wave length regions. Beyond the absorption edge of silicon at about 1.1 µm, no low-cost imagers are available and hence the hybrid imager can unfold its full potential. As mentioned in the introduction, the wave length window spanning from about 1200 nm to 1800 nm is especially interesting for night vision cameras due to the night glow phenomenon. The only limitation is the poor availability of efficient organic polymers in this region. Only [Gon09] reports about a photodetector with high detectivity at NIR wave lengths, but only up to about 1400 nm. The main drawback for the performance related with narrow-band gap semiconductors is the increase of the thermally generated dark current. Another approach for NIR detection with hybrid CMOS-imagers is the mixing of inorganic nanoparticles in an organic matrix. With colloidal quantum dots that exhibit an absorption wave length defined by the quantization energy and hence the dot size, absorption up to wave lengths of about 2 µm is feasible [Rau09, Im11].

Experimental details

Spin-coated photodetectors

Inverted OPDs with 1,2-DCB as solvent

Preparation of the PCBM:P3HT solution

- Mixing PCBM and P3HT with a ratio (per weight) of PCBM:P3HT=0.75:1
- Addition of 1,2-DCB, PCBM:P3HT:DCB=0.75:1:50
- Stirring of the solution overnight at 80°C

Ultrasonic cleaning of the glass substrates

- 10 min with acetone
- 5 min with isopropanol

Thermal evaporation of the aluminum cathode

- Evaporation rate: 10 Å/s
- Layer thickness: 100 nm

Spin-coating of the photoactive PCBM:P3HT

- The blend solution is cooled down to room-temperature
- Filtering of the solution with a teflon membrane with pore size 0.2 µm (PTFE 0.2)
- Spincoating parameters: first step: 600 rpm, ramp 5 s, 90 s; second step: 300 rpm, ramp 5, 60 s
- Annealing of the blend for 5 min at 140°C

Plasma treatment

- parameters: 100 W, 1 min, 0.35 Torr oxygen pressure

Spin-coating of the hole-conductor PEDOT:PSS (Clevios P VP CH 8000 by H.C. Starck)

- Filtering of the PEDOT:PSS solution with a RC (Regenerated Cellulose) membrane with 0.45 µm pore size
- Spin-coating parameters: first step: 2000 rpm, ramp 5 s, 30 s; second step: 300 rpm, ramp 5 s, 20 s
- Annealing of the blend for 10 min at 140°C

Deposition of the top-electrode (gold or conductive PEDOT:PSS)

Thermal evaporation of the gold anode

- Evaporation rate: 0.2 Å/s
- Layer thickness: 20 nm

Spin-coating of the conductive PEDOT:PSS (Clevios PH 1000 by H.C. Starck)

- Preparation of the PEDOT:PSS (PEDOT) solution: Addition of ethylene glycol (EG) and Dynol 604 (by Air products), PEDOT:EG:Dynol=100:10:0.3
- Stirring of the solution at room temperature for 2 h
- Spincoating of the solution: 700 rpm, ramp 5 s, 40 s; second step: 300 rpm, ramp 5 s, 30 s
- Annealing: 10 min for 140°C. The previous annealing step of the underlying hole-conductor is decreased to 5 min.

Encapsulation

- Deposition of the epoxy glue Dymax OP-4-20632 and a glass sheet (0.2 mm thickness) on top
- UV-hardening for 10 min

Inverted OPDs with toluene as solvent

Differences to the 1,2-DCB devices

- Blend preparation: PCBM:P3HT:toluene=1:1:100, annealing at 60°C
- Blend spin-coating: first step: 1000 rpm, ramp 3 s, 20 s; second step: 300 rpm, ramp 5, 30 s

Spray-coated photodetectors

Preparation of the solutions for spraying

- Hole conductor PEDOT:PSS, diluted with water: PEDOT:H_2O=1:2, stirring for 2 h at room temperature
- Blend solution: DCB:Tol:PCBM:P3HT=50:50:0.75:1, stirring overnight at 80°C
- Conductive PEDOT:PSS: PEDOT:H_2O:EG:Dynol=1:1:0.4:0.003, stirring for 2 h at room temperature

Spray-coating parameters

- Blend solution: distance nozzle-substrate: 15 cm, annealing during spraying: 100°C, spraying pressure: 2.8 bar
- Hole-conductor: distance nozzle-substrate: 25 cm, annealing during spraying: 35°C for the first monolayer of drops, then 50°C, spraying pressure: 1 bar
- Conductive PEDOT:PSS: distance nozzle-substrate: 25 cm, annealing during spraying: 120°C, spraying pressure: 1 bar

Differences to spin-coated devices

- No annealing after blend deposition
- Annealing of the hole conductor PEDOT:PSS was performed in air
- Annealing of the conductive PEDOT:PSS: performed partly in air (5 min, 120°C), partly in nitrogen atmosphere (5 min, 140°C)

Bibliography

[Ahn08] S. H. Ahn and L. J. Guo: *High-Speed Roll-to-Roll Nanoimprint Lithography on Flexible Plastic Substrates*, Advanced Materials **20**, 2044 (2008).

[Air05] A. Airoldi, G. Alimonti, M. Amati, A. Andreazza, A. Bulgheroni, M. Caccia, D. Giugni, W. Kucewicz, T. Lari, C. Meroni, F. Ragusa, C. Troncon and G. Vegni: *A chip removal facility for indium bump bonded pixel detectors*, Nuclear Instruments and Methods in Physics Research Section A: Accelerators, Spectrometers, Detectors and Associated Equipment **540**, 259 (2005).

[Arc13] F. Arca, S. F. Tedde, M. Sramek, J. Rauh, P. Lugli and O. Hayden: *Interface Trap States in Organic Photodiodes*, Scientific Reports **3**, 1324 (2013).

[Ark01] V. I. Arkhipov, E. V. Emelianova and G. J. Adriaenssens: *Effective transport energy versus the energy of most probable jumps in disordered hopping systems*, Phys. Rev. B **64**, 125125 (2001).

[Ark02] V. I. Arkhipov, P. Heremans, E. V. Emelianova, G. J. Adriaenssens and H. Bässler: *Weak-field carrier hopping in disordered organic semiconductors: the effects of deep traps and partly filled density-of-states distribution*, Journal of Physics: Condensed Matter **14**, 9899 (2002).

[Atw10] H. A. Atwater and A. Polman: *Plasmonics for improved photovoltaic devices*, Nat Mater **9**, 205 (2010).

[Aud10] J.-N. Audinot, P. Leveque, R. Bechara, N. Leclerc, J. Guillot, H.-N. Migeon, G. Hadziioannou and T. Heiser: *Characterization of P3HT/PCBM bulk heterojunction photovoltaic devices using advanced secondary ion mass spectrometry techniques*, Surface and Interface Analysis **42**, 1010 (2010).

[Bae93] H. Baessler: *Charge Transport in Disordered Organic Photoconductors a Monte Carlo Simulation Study*, physica status solidi (b) **175**, 15 (1993).

[Bai08] D. Baierl: *Diplomarbeit (TU München): Epitaxie und Charakterisierung von GaAs- und InP-basierten InAs-Quantenpunkten mit Emissionswellenlängen bei 1.3 μm und 1.55 μm* (2008).

[Bai10] D. Baierl, B. Fabel, P. Gabos, L. Pancheri, P. Lugli and G. Scarpa: *Solution-processable inverted organic photodetectors using oxygen plasma treatment*, Organic Electronics **11**, 1199 (2010).

[Bai11a] D. Baierl, B. Fabel, P. Lugli and G. Scarpa: *Efficient indium-tin-oxide (ITO) free top-absorbing organic photodetector with highly transparent polymer top electrode*, Organic Electronics **12**, 1669 (2011).

[Bai11b] D. Baierl, M. Schmidt, G. Scarpa, P. Lugli, L. Pancheri, D. Stoppa and G.-F. Dalla Betta: *Towards a hybrid cmos-imager with organic semiconductors as photoactive layer*, in *Ph.D. Research in Microelectronics and Electronics (PRIME), 2011 7th Conference on*, 2011, p. 89–92.

[Bai12] D. Baierl, L. Pancheri, M. Schmidt, D. Stoppa, G.-F. Dalla Betta, G. Scarpa and P. Lugli: *A hybrid CMOS-imager with a solution-processable polymer as photoactive layer*, Nature Communications **3**, 1175 (2012).

[Bar12] M. Bareiss, F. Ante, D. Kälblein, G. Jegert, C. Jirauschek, G. Scarpa, B. Fabel, E. M. Nelson, G. Timp, U. Zschieschang, H. Klauk, W. Porod and P. Lugli: *High-Yield Transfer Printing of Metal-Insulator-Metal Nanodiodes*, ACS Nano **6**, 2853 (2012).

[Bel67] A. Bell: *The Application of Plasmas to Chemical Processing*, M.I.T. Press, Edited by Raymond F. Baddour and Robert S. Timmins, 1967.

[Bev10] L. Beverina and P. Salice: *Squaraine Compounds: Tailored Design and Synthesis towards a Variety of Material Science Applications*, European Journal of Organic Chemistry **2010**, 1207 (2010).

[Big06] M. Bigas, E. Cabruja, J. Forest and J. Salvi: *Review of CMOS image sensors*, Microelectronics Journal **37**, 433 (2006).

[Bin09] M. Binda, T. Agostinelli, M. Caironi, D. Natali, M. Sampietro, L. Beverina, R. Ruffo and F. Silvestri: *Fast and air stable near-infrared organic detector based on squaraine dyes*, Organic Electronics **10**, 1314 (2009).

[Bin11] M. Binda, A. Iacchetti, D. Natali, L. Beverina, M. Sassi and M. Sampietro: *High detectivity squaraine-based near infrared photodetector with nA/cm^2 dark current*, Applied Physics Letters **98**, 073303 (2011).

[Bla09] L. Blankenburg, K. Schultheis, H. Schache, S. Sensfuss and M. Schrödner: *Reel-to-reel wet coating as an efficient up-scaling technique for the production of bulk-heterojunction polymer solar cells*, Solar Energy Materials and Solar Cells **93**, 476 (2009).

[Bra01] C. J. Brabec, A. Cravino, D. Meissner, N. S. Sariciftci, T. Fromherz, M. T. Rispens, L. Sanchez and J. C. Hummelen: *Origin of the Open Circuit Voltage of Plastic Solar Cells*, Advanced Functional Materials **11**, 374 (2001).

[Bro99] T. M. Brown, J. S. Kim, R. H. Friend, F. Cacialli, R. Daik and W. J. Feast: *Built-in field electroabsorption spectroscopy of polymer light-emitting diodes incorporating a doped poly(3,4-ethylene dioxythiophene) hole injection layer*, Applied Physics Letters **75**, 1679 (1999).

[Cai07] M. Caironi, T. Agostinelli, D. Natali, M. Sampietro, R. Cugola, M. Catellani and S. Luzzati: *External quantum efficiency versus charge carriers mobility in polythiophene/methanofullerene based planar photodetectors*, Journal of Applied Physics **102**, 024503 (2007).

[Car09] B. Carter and R. Mancini: *Op ams for everyone*, Texas Instruments, 2009.

[Che10] E.-C. Chen, C.-Y. Chang, J.-T. Shieh, S.-R. Tseng, H.-F. Meng, C.-S. Hsu and S.-F. Horng: *Polymer photodetector with voltage-adjustable photocurrent spectrum*, Applied Physics Letters **96**, 043507 (2010).

[Cho11] F.-P. Chou, G.-Y. Chen, C.-W. Wang, Y.-C. Liu, W.-K. Huang and Y.-M. Hsin: *Silicon Photodiodes in Standard CMOS Technology*, Selected Topics in Quantum Electronics, IEEE Journal of **17**, 730 (2011).

[Chr68] S. Christensson, I. Lundström and C. Svensson: *Low frequency noise in MOS transistors*, Solid-State Electronics **11**, 797 (1968).

[CQ08] M. Campoy-Quiles, T. Ferenczi, T. Agostinelli, P. G. Etchegoin, Y. Kim, T. D. Anthopoulos, P. N. Stavrinou, D. D. C. Bradley and J. Nelson: *Morphology evolution via self-organization and lateral and vertical diffusion in polymer:fullerene solar cell blends*, Nat Mater **7**, 158 (2008).

[Cri03] X. Crispin, S. Marciniak, W. Osikowicz, G. Zotti, A. W. D. van der Gon, F. Louwet, M. Fahlman, L. Groenendaal, F. De Schryver and W. R. Salaneck: *Conductivity, morphology, interfacial chemistry, and stability of poly(3,4-ethylene dioxythiophene)poly(styrene sulfonate): A photoelectron spectroscopy study*, Journal of Polymer Science Part B: Polymer Physics **41**, 2561 (2003).

[Cri06] X. Crispin, F. L. E. Jakobsson, A. Crispin, P. C. M. Grim, P. Andersson, A. Volodin, C. van Haesendonck, M. Van der Auweraer, W. R. Salaneck and M. Berggren: *The Origin of the High Conductivity of Poly(3,4-ethylenedioxythiophene)-Poly(styrenesulfonate) (PEDOT:PSS) Plastic Electrodes*, Chemistry of Materials **18**, 4354 (2006).

[Dec98] S. Decker, D. McGrath, K. Brehmer and C. Sodini: *A 256 times 256 CMOS imaging array with wide dynamic range pixels and column-parallel digital output*, Solid-State Circuits, IEEE Journal of **33**, 2081 (1998).

[Dee97] R. D. Deegan, O. Bakajin, T. F. Dupont, G. Huber, S. R. Nagel and T. A. Witten: *Capillary flow as the cause of ring stains from dried liquid drops*, Nature **389**, 827 (1997).

[Dei09] C. Deibel, T. Strobel and V. Dyakonov: *Origin of the Efficient Polaron-Pair Dissociation in Polymer-Fullerene Blends*, Phys. Rev. Lett. **103**, 036402 (2009).

[Dei10a] C. Deibel, V. Dyakonov and C. Brabec: *Organic Bulk-Heterojunction Solar Cells*, Selected Topics in Quantum Electronics, IEEE Journal of **16**, 1517 (2010).

[Dei10b] C. Deibel, D. Mack, J. Gorenflot, A. Schöll, S. Krause, F. Reinert, D. Rauh and V. Dyakonov: *Energetics of excited states in the conjugated polymer poly(3-hexylthiophene)*, Phys. Rev. B **81**, 085202 (2010).

[Den91] P. B. Denyer, D. S. Renshaw, G. Wang, M. Y. Lu and S. Anderson: *On-chip CMOS sensors for vlsi imaging systems*, in *VLSI*, 1991, 157–166.

[Den05] G. Dennler and N. Sariciftci: *Flexible Conjugated Polymer-Based Plastic Solar Cells: From Basics to Applications*, Proceedings of the IEEE **93**, 1429 (2005).

[Duc09] D. Duche, P. Torchio, L. Escoubas, F. Monestier, J.-J. Simon, F. Flory and G. Mathian: *Improving light absorption in organic solar cells by plasmonic contribution*, Solar Energy Materials and Solar Cells **93**, 1377 (2009).

[ED09] M. El-Desouki, M. Jamal Deen, Q. Fang, L. Liu, F. Tse and D. Armstrong: *CMOS Image Sensors for High Speed Applications*, Sensors **9**, 430 (2009).

[Fan98] X. Fanton and A. M. Cazabat: *Spreading and Instabilities Induced by a Solutal Marangoni Effect*, Langmuir **14**, 2554 (1998).

[Fos97] E. R. Fossum: *CMOS image sensors: electronic camera-on-a-chip*, Electron Devices, IEEE Transactions on **44**, 1689 (1997).

[Fri09] B. Friedel, P. E. Keivanidis, T. J. K. Brenner, A. Abrusci, C. R. McNeill, R. H. Friend and N. C. Greenham: *Effects of Layer Thickness and Annealing of PEDOT:PSS Layers in Organic Photodetectors*, Macromolecules **42**, 6741 (2009).

[Fuj00] I. Fujimori, C. Wang and C. Sodini: *A 256 - 256 CMOS differential passive pixel imager with FPN reduction techniques*, IEEE Journal of Solid State Circuits **35**, pp. 2031 (2000).

[Gil72] W. D. Gill: *Drift mobilities in amorphous charge-transfer complexes of trinitrofluorenone and poly-n-vinylcarbazole*, Journal of Applied Physics **43**, 5033 (1972).

[Gir09] C. Girotto, B. P. Rand, J. Genoe and P. Heremans: *Exploring spray coating as a deposition technique for the fabrication of solution-processed solar cells*, Solar Energy Materials and Solar Cells **93**, 454 (2009).

[Gir11] C. Girotto, D. Moia, B. P. Rand and P. Heremans: *High-Performance Organic Solar Cells with Spray-Coated Hole-Transport and Active Layers*, Advanced Functional Materials **21**, 64 (2011).

[Gla05] M. Glatthaar, M. Niggemann, B. Zimmermann, P. Lewer, M. Riede, A. Hinsch and J. Luther: *Organic solar cells using inverted layer sequence*, Thin Solid Films **491**, 298 (2005).

[Gla07] M. Glatthaar, M. Riede, N. Keegan, K. Sylvester-Hvid, B. Zimmermann, M. Niggemann, A. Hinsch and A. Gombert: *Efficiency limiting factors of organic bulk heterojunction solar cells identified by electrical impedance spectroscopy*, Solar Energy Materials and Solar Cells **91**, 390 , selected Papers from the European Conference on Hybrid and Organic Solar Cells-ECHOS'06 (2007).

[Gon09] X. Gong, M. Tong, Y. Xia, W. Cai, J. S. Moon, Y. Cao, G. Yu, C.-L. Shieh, B. Nilsson and A. J. Heeger: *High-Detectivity Polymer Photodetectors with Spectral Response from 300 nm to 1450 nm*, Science **325**, 1665 (2009).

[Gro12] R. Gross: *Solid State Physics I + II*, 2012, oldenbourg Verlag Munich.

[Gu95] J. Gu, M. D. Bullwinkel and G. A. Campbell: *Spin Coating on Substrate with Topography*, Journal of The Electrochemical Society **142**, 907 (1995).

[Gun07] S. Gunes, H. Neugebauer and N. S. Sariciftci: *Conjugated Polymer-Based Organic Solar Cells*, Chemical Reviews **107**, 1324 (2007).

[Had95] R. C. Haddon, A. S. Perel, R. C. Morris, T. T. M. Palstra, A. F. Hebard and R. M. Fleming: *C_{60} thin film transistors*, Applied Physics Letters **67**, 121 (1995).

[ham] *Photodiode technical guide*, http://sales.hamamatsu.com/assets/html/ssd/si-photodiode/index.htm, accessed: 06/15/2012.

[Hau08] S. K. Hau, H.-L. Yip, O. Acton, N. S. Baek, H. Ma and A. K.-Y. Jen: *Interfacial modification to improve inverted polymer solar cells*, J. Mater. Chem. **18**, (2008).

[Hau09] S. K. Hau, H.-L. Yip, J. Zou and A. K.-Y. Jen: *Indium tin oxide-free semi-transparent inverted polymer solar cells using conducting polymer as both bottom and top electrodes*, Organic Electronics **10**, 1401 (2009).

[Hos07] K. Hoshino, F. Nielsen and T. Nishimura: *Noise Reduction in CMOS Image Sensors for High Quality Imaging: The Autocorrelation Function Filter on Burst Image Sequences*, ICGST-GVIP Journal **7**, 17 (2007).

[Hot07] C. Hoth, S. Choulis, P. Schilinsky and C. Brabec: *High Photovoltaic Performance of Inkjet Printed Polymer:Fullerene Blends*, Advanced Materials **19**, 3973 (2007).

[Hot09] C. N. Hoth, R. Steim, P. Schilinsky, S. A. Choulis, S. F. Tedde, O. Hayden and C. J. Brabec: *Topographical and morphological aspects of spray coated organic photovoltaics*, Organic Electronics **10**, 587 (2009).

[Hsi09] Y.-S. Hsiao, C.-P. Chen, C.-H. Chao and W.-T. Whang: *All-solution-processed inverted polymer solar cells on granular surface-nickelized polyimide*, Organic Electronics **10**, 551 (2009).

[Hun90] K. K. Hung, P. K. Ko, C. Hu and Y. C. Cheng: *A unified model for the flicker noise in metal-oxide-semiconductor field-effect transistors*, Electron Devices, IEEE Transactions on **37**, 654 (1990).

[Hur97] J. E. D. Hurwitz, P. B. Denyer, D. J. Baxter and G. Townsend: *800-thousand-pixel color CMOS sensor for consumer still cameras*, Proc. SPIE: Solid State Sensor Arrays: Development and Applications **3019**, 115 (1997).

[Hwa08] I.-W. Hwang, D. Moses and A. J. Heeger: *Photoinduced Carrier Generation in P3HT/PCBM Bulk Heterojunction Materials*, The Journal of Physical Chemistry C **112**, 4350 (2008).

[Iid97] Y. Iida, E. Oba, K. Mabuchi, N. Nakamura and H. Miura: *A 1/4-inch 330 K square pixel progressive scan CMOS active pixel image sensor*, Solid-State Circuits, IEEE Journal of **32**, 2042 (1997).

[Im11] S. H. Im, H. jung Kim and S. I. Seok: *Near-infrared responsive PbS-sensitized photovoltaic photodetectors fabricated by the spin-assisted successive ionic layer adsorption and reaction method*, Nanotechnology **22**, 395502 (2011).

[Jai01] S. C. Jain, W. Geens, A. Mehra, V. Kumar, T. Aernouts, J. Poortmans, R. Mertens and M. Willander: *Injection- and space charge limited-currents in doped conducting organic materials*, Journal of Applied Physics **89**, 3804 (2001).

[Jas72] J. J. Jasper: *The Surface Tension of Pure Liquid Compounds*, Journal of Physical and Chemical Reference Data **1**, 841 (1972).

[Jor08] M. Jorgensen, K. Norrman and F. C. Krebs: *Stability/degradation of polymer solar cells*, Solar Energy Materials and Solar Cells **92**, 686 (2008).

[Kan] H. Kang, L. Jagannathan and V. Subramanian: *Measurement, analysis, and modeling of flicker noise in pentacene thin film transistors*, Applied Physics Letters **99**, 062106.

[Ker95] M. Kertesz: *Structure and Electronic Structure of Low-Band-Gap Ladder Polymers*, Macromolecules **28**, 1475 (1995).

[Kim06] Y. Kim, S. Cook, S. M. Tuladhar, S. A. Choulis, J. Nelson, J. R. Durrant, D. D. C. Bradley, M. Giles, I. McCulloch, C.-S. Ha and M. Ree: *A strong*

regioregularity effect in self-organizing conjugated polymer films and high-efficiency polythiophene:fullerene solar cells, Nat Mater **5**, 197 (2006).

[Kim08a] J. Kim, D.-Y. Khang, J.-H. Kim and H. H. Lee: *The surface engineering of top electrode in inverted polymer bulk-heterojunction solar cells*, Applied Physics Letters **92**, 133307 (2008).

[Kim08b] S.-S. Kim, S.-I. Na, J. Jo, D.-Y. Kim and Y.-C. Nah: *Plasmon enhanced performance of organic solar cells using electrodeposited Ag nanoparticles*, Applied Physics Letters **93**, 073307 (2008).

[Kim11] Y. H. Kim, C. Sachse, M. L. Machala, C. May, L. Müller-Meskamp and K. Leo: *Highly Conductive PEDOT:PSS Electrode with Optimized and Thermal Post-Treatment for ITO-Free Organic Solar Cells*, Advanced Functional Materials **21**, 1076 (2011).

[Kir05] S. Kirchmeyer and K. Reuter: *Scientific importance, properties and growing applications of poly(3,4-ethylenedioxythiophene)*, J. Mater. Chem. **15** (2005).

[Kre03] F. C. Krebs, S. V. Hoffmann and M. Jorgensen: *Orientation effects in self-organized, highly conducting regioregular poly(3-hexylthiophene) determined by vacuum ultraviolet spectroscopy*, Synthetic Metals **138**, 471 (2003).

[Kre07] F. C. Krebs and K. Norrman: *Analysis of the failure mechanism for a stable organic photovoltaic during 10 000 h testing*, Progress in Photovoltaics: Research and Applications **15**, 697 (2007).

[Kre09] F. C. Krebs: *All solution roll-to-roll processed polymer solar cells free from indium-tin-oxide and vacuum coating steps*, Organic Electronics **10**, 761 (2009).

[Kum09] A. Kumar, S. Sista and Y. Yang: *Dipole induced anomalous S-shape I-V curves in polymer solar cells*, Journal of Applied Physics **105**, 094512 (2009).

[Lee04] C. Lee, A. Uddin, X. Hu and T. Anderssonb: *Study of Alq3 thermal evaporation rate effects on the OLED*, Materials Science and Engineering: B **112**, 14 (2004).

[Lee11] S. Lee, K. Lee, J. Park, H. Han, Y. Park, T. Jung, Y. Jang, B. Kim, Y. Kim, S. Hamami, U. Hizi, M. Bahar, C. Moon, J. Ahn, D. Lee, H. Goto and Y.-T. Lee: *A 1/2.33-inch 14.6M 1.4 μm-Pixel Backside-Illuminated CMOS Image Sensor with Floating Diffusion Boosting*, 2011 IEEE International Solid-State Circuits Conference (2011).

[Li97] F. Li, H. Tang, J. Anderegg and J. Shinar: *Fabrication and electroluminescence of double-layered organic light-emitting diodes with the Al_2O_3/Al cathode*, Applied Physics Letters **70**, 1233 (1997).

[Li07] G. Li, V. Shrotriya, Y. Yao, J. Huang and Y. Yang: *Manipulating regioregular poly(3-hexylthiophene) : [6,6]-phenyl-C61-butyric acid methyl ester blends-route towards high efficiency polymer solar cells*, J. Mater. Chem. **17**, 3126 (2007).

[Lim08] Y.-F. Lim, S. Lee, D. J. Herman, M. T. Lloyd, J. E. Anthony and G. G. Malliaras: *Spray-deposited poly(3,4-ethylenedioxythiophene):poly(styrenesulfonate) top electrode for organic solar cells*, Applied Physics Letters **93**, 193301 (2008).

[Lim11] Y. Lim, Y.-S. Park, Y. Kang, D. Y. Jang, J. H. Kim, J.-J. Kim, A. Sellinger and D. Y. Yoon: *Hole Injection/Transport Materials Derived from Heck and Sol-Gel Chemistry for Application in Solution-Processed Organic Electronic Devices*, Journal of the American Chemical Society **133**, 1375 (2011).

[Lin10] K. Lin, S. Bin Dolmanan, C. Vijila, C. Soo Jin, H. Ye Hua and M. Ting: *Investigation of the Device Degradation Mechanism in Pentacene-Based Thin-Film Transistors Using Low-Frequency-Noise Spectroscopy*, Electron Devices, IEEE Transactions on **57**, 385 (2010).

[Lis93] M. Liston and L. Martinu: J. Adhesion Sci. Technol. **7**, 1091 (1993).

[Lop91] G. P. Lopez, D. G. Castner and B. D. Ratner: *XPS O 1s binding energies for polymers containing hydroxyl, ether, ketone and ester groups*, Surface and Interface Analysis **17**, 267 (1991).

[Lu08] F.-H. Lu, H.-D. Tsai and Y.-C. Chieh: *Plasma oxidation of Al thin films on Si substrates*, Thin Solid Films **516**, 1871 (2008).

[Lue04] L. Lueer, H.-J. Egelhaaf, D. Oelkrug, G. Cerullo, G. Lanzani, B.-H. Huisman and D. de Leeuw: *Oxygen-induced quenching of photoexcited states in polythiophene films*, Organic Electronics **5**, 83, current Trends in Crystalline Organic Semiconductors: Growth Modelling and Fundamental Properties (2004).

[Lul99] T. Lule, B. Schneider and M. Böhm: *Design and fabrication of a high-dynamic-range image sensor in TFA-technology*, Solid-State Circuits, IEEE Journal of **34**, 704 (1999).

[Lul00] T. Lule, S. Benthien, H. Keller, F. Mutze, P. Rieve, K. Seibel, M. Sommer and M. Böhm: *Sensitivity of CMOS based imagers and scaling perspectives*, Electron Devices, IEEE Transactions on **47**, 2110 (2000).

[Lun07] C. Lungenschmied, G. Dennler, H. Neugebauer, S. N. Sariciftci, M. Glatthaar, T. Meyer and A. Meyer: *Flexible, long-lived, large-area, organic solar cells*, Solar Energy Materials and Solar Cells **91**, 379 (2007).

[Luo10] Y. Luo, J. Remillard and D. Hoetzer: *Pedestrian detection in near-infrared night vision system*, 2010, 51–58.

[Mag03] P. Magnan: *Detection of visible photons in CCD and CMOS: A comparative view*, Nuclear Instruments and Methods in Physics Research Section A: Accelerators, Spectrometers, Detectors and Associated Equipment **504**, 199 , proceedings of the 3rd International Conference on New Developments in Photodetection (2003).

[Man07] M. M. Mandoc, B. de Boer, G. Paasch and P. W. M. Blom: *Trap-limited electron transport in disordered semiconducting polymers*, Phys. Rev. B **75**, 193202 (2007).

[Mar00] S. Martin, A. Dodabalapur, Z. Bao, B. Crone, H. E. Katz, W. Li, A. Passner and J. A. Rogers: *Flicker noise properties of organic thin-film transistors*, Journal of Applied Physics **87**, 3381 (2000).

[Mau10] R. Mauer, M. Kastler and F. Laquai: *The Impact of Polymer Regioregularity on Charge Transport and Efficiency of P3HT:PCBM Photovoltaic Devices*, Advanced Functional Materials **20**, 2085 (2010).

[Mic77] H. B. Michaelson: *The work function of the elements and its periodicity*, Journal of Applied Physics **48**, 4729 (1977).

[Mih04] V. D. Mihailetchi, L. J. A. Koster, J. C. Hummelen and P. W. M. Blom: *Photocurrent Generation in Polymer-Fullerene Bulk Heterojunctions*, Phys. Rev. Lett. **93**, 216601 (2004).

[Mil60] A. Miller and E. Abrahams: *Impurity Conduction at Low Concentrations*, Phys. Rev. **120**, 745 (1960).

[Min10] C. Min, J. Li, G. Veronis, J.-Y. Lee, S. Fan and P. Peumans: *Enhancement of optical absorption in thin-film organic solar cells through the excitation of plasmonic modes in metallic gratings*, Applied Physics Letters **96**, 133302 (2010).

[Mis12] A. Mishra and P. Bäuerle: *Small Molecule Organic Semiconductors on the Move: Promises for Future Solar Energy Technology*, Angewandte Chemie International Edition **51**, 2020 (2012).

[Mon09] J. M. Montero, J. Bisquert, G. Garcia-Belmonte, E. M. Barea and H. J. Bolink: *Trap-limited mobility in space-charge limited current in organic layers*, Organic Electronics **10**, 305 (2009).

[Mon11] J. M. Montero and J. Bisquert: *Trap origin of field-dependent mobility of the carrier transport in organic layers*, Solid-State Electronics **55**, 1 (2011).

[Mor11] C. Mortimer: *Chemie: Basiswissen der Chemie*, Georg Thieme Verlag, 2011.

[Mou06] A. J. Moule, J. B. Bonekamp and K. Meerholz: *The effect of active layer thickness and composition on the performance of bulk-heterojunction solar cells*, Journal of Applied Physics **100**, 094503 (2006).

[Mov86] B. Movaghar, M. Grünewald, B. Ries, H. Bassler and D. Würtz: *Diffusion and relaxation of energy in disordered organic and inorganic materials*, Physical Review B **33**, 5545 (1986).

[Mul01] H. van Mullekom, J. Vekemans, E. Havinga and E. Meijer: *Developments in the chemistry and band gap engineering of donor-acceptor substituted conjugated polymers*, Materials Science and Engineering: R: Reports **32**, 1 (2001).

[Na08] S.-I. Na, S.-S. Kim, J. Jo and D.-Y. Kim: *Efficient and Flexible ITO-Free Organic Solar Cells Using Highly Conductive Polymer Anodes*, Advanced Materials **20**, 4061 (2008).

[Na09] S.-I. Na, G. Wang, S.-S. Kim, T.-W. Kim, S.-H. Oh, B.-K. Yu, T. Lee and D.-Y. Kim: *Evolution of nanomorphology and anisotropic conductivity in solvent-modified PEDOT:PSS films for polymeric anodes of polymer solar cells*, J. Mater. Chem. **19** (2009).

[Na10] S.-I. Na, B.-K. Yu, S.-S. Kim, D. Vak, T.-S. Kim, J.-S. Yeo and D.-Y. Kim: *Fully spray-coated ITO-free organic solar cells for low-cost power generation*, Solar Energy Materials and Solar Cells **94**, 1333, national Conference on the Emerging Trends in the Photovoltaic Energy and Utilization (2010).

[Ons38] L. Onsager: *Initial Recombination of Ions*, Phys. Rev. **54**, 554 (1938).

[Ouy05] J. Ouyang, C.-W. Chu, F.-C. Chen, Q. Xu and Y. Yang: *High-Conductivity Poly(3,4-ethylenedioxythiophene):Poly(styrene sulfonate) Film and Its Application in Polymer Optoelectronic Devices*, Advanced Functional Materials **15**, 203 (2005).

[Pai05] B. Pain: *Fabrication and Initial Results for a Back-Illuminated Monolithic APS in a Mixed SOI/Bulk CMOS technology*, Proc. 2005 IEEE Workshop on CCD and Advanced Image Sensors , 102 (2005).

[Pan00] S. S. Pandey, W. Takashima, S. Nagamatsu, T. Endo, M. Rikukawa and K. Kaneto: *Regioregularity vs Regiorandomness: Effect on Photocarrier Transport in Poly(3-hexylthiophene)*, Japanese Journal of Applied Physics **39**, L94 (2000).

[Par09] S. H. Park, A. Roy, S. Beaupre, S. Cho, N. Coates, J. S. Moon, D. Moses, M. Leclerc, K. Lee and A. J. Heeger: *Bulk heterojunction solar cells with internal quantum efficiency approaching 1003*, 297 (2009).

[Pei55] R. E. Peierls: *Quantum Theory of Solids*, University Press, Oxford, 1955.

[Pun07] M. Punke, S. Valouch, S. W. Kettlitz, N. Christ, C. Gartner, M. Gerken and U. Lemmer: *Dynamic characterization of organic bulk heterojunction photodetectors*, Applied Physics Letters **91**, 071118 (2007).

[Ram06] B. Ramachandhran, H. G. A. Huizing and R. Coehoorn: *Charge transport in metal/semiconductor/metal devices based on organic semiconductors with an exponential density of states*, Phys. Rev. B **73**, 233306 (2006).

[Ram08] M. Ramuz, L. Buergi, C. Winnewisser and P. Seitz: *High sensitivity organic photodiodes with low dark currents and increased lifetimes*, Organic Electronics **9**, 369 (2008).

[Rau04] T. Rauch, D. Henseler, P. Schilinsky, C. Waldauf, J. Hauch and C. Brabec: *Performance of bulk-heterojunction organic photodetectors*, in *Nanotechnology, 2004. 4th IEEE Conference on*, 2004, 632 – 634.

[Rau09] T. Rauch, M. Böberl, S. F. Tedde, J. Fürst, M. V. Kovalenko, G. Hesser, U. Lemmer, W. Heiss and O. Hayden: *Near-infrared imaging with quantum-dot-sensitized organic photodiodes*, Nat Photon **3**, 332 (2009).

[Res12] T. M. Research: *Organic electronics market - global industry analysis, market size, share, growth and forecast 2012 - 2018*, http://www.transparencymarketresearch.com/global-organic-electronics-market.htm, accessed: 05/15/2012 (2012).

[Rob75] J. K. Roberge: *Operational amplifiers: Theory and Practise*, J. Wiley & sons, New York, 1975.

[Ron07] J. Roncali: *Molecular Engineering of the Band Gap of π-Conjugated Systems: Facing Technological Applications*, Macromolecular Rapid Communications **28**, 1761 (2007).

[Sal98] U. Salzner, J. Lagowski, P. Pickup and R. Poirier: *Comparison of geometries and electronic structures of polyacetylene, polyborole, polycyclopentadiene, polypyrrole, polyfuran, polysilole, polyphosphole, polythiophene, polyselenophene and polytellurophene*, Synthetic Metals **96**, 177 (1998).

[Sch98] B. Schneider, P. Rieve and M. Böhm: *Image sensors in TFA (thin film on ASIC) technology*, Handbook on Computer Vision and Applications (Academic, Boston) **1**, 237 (1998).

[Sch02] R. Schmechel: *Gaussian disorder model for high carrier densities: Theoretical aspects and application to experiments*, Phys. Rev. B **66**, 235206 (2002).

[Sch04] P. Schilinsky, C. Waldauf, J. Hauch and C. J. Brabec: *Polymer photovoltaic detectors: progress and recent developments*, Thin Solid Films **451-452**, 105, proceedings of Symposium D on Thin Film and Nano-Structured Materials for Photovoltaics, of the E-MRS 2003 Spring Conference (2004).

[Sch09] H. Schmidt, H. Flugge, T. Winkler, T. Bulow, T. Riedl and W. Kowalsky: *Efficient semitransparent inverted organic solar cells with indium tin oxide top electrode*, Applied Physics Letters **94**, 243302 (2009).

[Shi09] R. Shinar and J. Shinar: *Organic electronics in sensors and biotechnology*, McGraw-Hill biophotonics, McGraw-Hill, 2009.

[Shr06] V. Shrotriya, G. Li, Y. Yao, C.-W. Chu and Y. Yang: *Transition metal oxides as the buffer layer for polymer photovoltaic cells*, Applied Physics Letters **88**, 073508 (2006).

[Sil08] F. Silvestri, M. D. Irwin, L. Beverina, A. Facchetti, G. A. Pagani and T. J. Marks: *Efficient Squaraine-Based Solution Processable Bulk-Heterojunction Solar Cells*, Journal of the American Chemical Society **130**, 17640 (2008).

[Smi58] F. M. Smits: *Measurement of sheet resistivities with the four-point probes*, Bell System Technical Journal **34**, 711 (1958).

[Sol08] D. Soltman and V. Subramanian: *Inkjet-Printed Line Morphologies and Temperature Control of the Coffee Ring Effect*, Langmuir **24**, 2224, pMID: 18197714 (2008).

[Spa78] H.-J. Spangenberg: *Plasmachemie. Prozesse der chemischen Stoffwandlung unter Plasma-Bedingungen. Von H. Drost; Akademie-Verlag, Berlin 1978*, Zeitschrift für Chemie **20**, 235 (1978).

[SR00] L. Stolz Roman, O. Inganaes, T. Granlund, T. Nyberg, M. Svensson, M. R. Andersson and J. C. Hummelen: *Trapping Light in Polymer Photodiodes with Soft Embossed Gratings*, Advanced Materials **12**, 189 (2000).

[Sto02] D. Stoppa: *Review of CMOS image sensors*, PhD thesis, University of Trento (2002).

[Sun11] Z. Sun, D. Liu, S. Stafstrom and Z. An: *Scattering process between polaron and exciton in conjugated polymers*, The Journal of Chemical Physics **134**, 044906 (2011).

[Sus11] G. Susanna, L. Salamandra, T. M. Brown, A. D. Carlo, F. Brunetti and A. Reale: *Airbrush spray-coating of polymer bulk-heterojunction solar cells*, Solar Energy Materials and Solar Cells **95**, 1775 (2011).

[Sze69] S. M. Sze: *The Physics of Semiconductor Devices*, J. Wiley & sons, New York, 1969.

[Sze94] S. M. Sze: *Semiconductor sensors*, J. Wiley & sons, New York, 1994.

[Szm07] J. Szmytkowski: *The photocurrent quantum efficiency dependence on the applied voltage in organic solar cells*, Semiconductor Science and Technology **22**, 1329 (2007).

[Ted07] S. F. Tedde, E. Zaus, D. Henseler, J. Fürst and P. Lugli: *Active Pixel Concept Combined With Organic Photodiode for Imaging Devices*, Electron Device Letters, IEEE **28**, 893 (2007).

[Ted09] S. F. Tedde, J. Kern, T. Sterzl, J. Fürst, P. Lugli and O. Hayden: *Fully Spray Coated Organic Photodiodes*, Nano Letters **9**, 980 (2009).

[Tob04] Tobias and Nyberg: *An alternative method to build organic photodiodes*, Synthetic Metals **140**, 281 (2004).

[Van06] P. Vanlaeke, A. Swinnen, I. Haeldermans, G. Vanhoyland, T. Aernouts, D. Cheyns, C. Deibel, J. DHaen, P. Heremans, J. Poortmans and J. Manca: *P3HT/PCBM bulk heterojunction solar cells: Relation between morphology and electro-optical characteristics*, Solar Energy Materials and Solar Cells **90**, 2150 (2006).

[Vit72] M. l. Vitsia: *Research and development technical report ecom-702 atmospheric optical environment* (1972).

[Vog06] M. Vogel, S. Doka, C. Breyer, M. C. Lux-Steiner and K. Fostiropoulos: *On the function of a bathocuproine buffer layer in organic photovoltaic cells*, Applied Physics Letters **89**, 163501 (2006).

[Wal48] R. Walker and H. Wallman: *Vacuum-Tube Amplifiers*, McGraw-Hill, New York, 1948.

[Wal06] C. Waldauf, M. Morana, P. Denk, P. Schilinsky, K. Coakley, S. A. Choulis and C. J. Brabec: *Highly efficient inverted organic photovoltaics using solution based titanium oxide as electron selective contact*, Applied Physics Letters **89**, 233517 (2006).

[Wan05] T. Wang, Y. Qi, J. Xu, X. Hu and P. Chen: *Effects of poly(ethylene glycol) on electrical conductivity of poly(3,4-ethylenedioxythiophene):poly(styrenesulfonic acid) film*, Applied Surface Science **250**, 188 (2005).

[Wei10] G. Wei, S. Wang, K. Renshaw, M. E. Thompson and S. R. Forrest: *Solution-Processed Squaraine Bulk Heterojunction Photovoltaic Cells*, ACS Nano **4**, 1927 (2010).

[Xue04] J. Xue and S. R. Forrest: *Carrier transport in multilayer organic photodetectors: I. Effects of layer structure on dark current and photoresponse*, Journal of Applied Physics **95**, 1859 (2004).

[Yao08] Y. Yao, J. Hou, Z. Xu, G. Li and Y. Yang: *Effects of Solvent Mixtures on the Nanoscale Phase Separation in Polymer Solar Cells*, Advanced Functional Materials **18**, 1783 (2008).

[YP04] O. Yadid-Pecht and R. Etienne-Cummings: *CMOS Imagers: from Phototransduction to Image Processing*, Cluwer Academic Publishers, 2004.

[YTF00] C.-S. P. Yang-Tung Fan and C.-Y. Chu: *Advanced microlens and color filter process technology for the high-efficiency CMOS and CCD image sensors*, in *Proc. SPIE 4115*, 2000, pp. 263.

[Zau07] E. S. Zaus, S. Tedde, J. Fürst, D. Henseler and G. H. Dohler: *Dynamic and steady state current response to light excitation of multilayered organic photodiodes*, Journal of Applied Physics **101**, 044501 (2007).

[Zen10] L. Zeng, C. W. Tang and S. H. Chen: *Effects of active layer thickness and thermal annealing on polythiophene: Fullerene bulk heterojunction photovoltaic devices*, Applied Physics Letters **97**, 053305 (2010).

[Zha10] J. Zhang, I. Meric, K. L. Shepard and I. Kymissis: *Doping and Illumination Dependence of 1/f Noise in Pentacene Thin-Film Transistors*, Electron Device Letters, IEEE **31**, 1050 (2010).

[Zho08] Y. Zhou, F. Zhang, K. Tvingstedt, S. Barrau, F. Li, W. Tian and O. Inganas: *Investigation on polymer anode design for flexible polymer solar cells*, Applied Physics Letters **92**, 233308 (2008).

[Zho11] C. Zhong, C. Duan, F. Huang, H. Wu and Y. Cao: *Materials and Devices toward Fully Solution Processable Organic Light-Emitting Diodes*, Chemistry of Materials **23**, 326 (2011).

[Zie88] A. van der Ziel: *Unified presentation of 1/f noise in electron devices: fundamental 1/f noise sources*, Proceedings of the IEEE **76**, 233 (1988).

[Zim07] B. Zimmermann, M. Glatthaar, M. Niggemann, M. Riede, A. Hinsch and A. Gombert: *ITO-free wrap through organic solar cells. A module concept for cost-efficient reel-to-reel production*, Solar Energy Materials and Solar Cells **91**, 374 , selected Papers from the European Conference on Hybrid and Organic Solar Cells - ECHOS '06 (2007).

[Zim08] B. Zimmermann: *Inversion of the layer sequence in organic solar cells - physical and technological aspects*, Dissertation, Albert-Ludwigs-Universität Freiburg im Breisgau, 2008.

Publications

Journal publications (peer-reviewed)

- Daniela Baierl, Lucio Pancheri, Morten Schmidt, Gian-Franco Dalla Betta, David Stoppa, Giuseppe Scarpa, Paolo Lugli: *A hybrid CMOS-imager with a solution-processable polymer as photoactive layer*, Nature Communications 3, 1175 (2012)
- Daniela Baierl, Bernhard Fabel, Paolo Lugli, Giuseppe Scarpa: *Efficient indium-tin-oxide (ITO) free top-absorbing organic photodetector with highly transparent polymer top electrode*, Organic Electronics 12, 1669-1673 (2011)
- Daniela Baierl, Bernhard Fabel, Paolo Gabos, Lucio Pancheri, Paolo Lugli, Giuseppe Scarpa: *Solution-processable inverted organic photodetectors using oxygen plasma treatment*, Organic Electronics 11, 1199-1206 (2010)

Conferences & proceedings

- Daniela Baierl, Morten Schmidt, Giuseppe Scarpa, Paolo Lugli, Lucio Pancheri, David Stoppa, Gian-Franco Dalla Betta: *Towards a hybrid CMOS-imager with organic semiconductors as photoactive layer*, 7th Conference on Ph.D. Research in Microelectronics and Electronics - PRIME 2011, 3-7 July 2011, Madonna di Campiglio (Italy), pg.89-92
- Daniela Baierl, Alaa Abdellah, Bernhard Fabel, Giuseppe Scarpa, Paolo Lugli, Paolo Gabos, Gian-Franco Dalla Betta, Lucio Pancheri, David Stoppa: *Organic semiconductors as photoactive material on hybrid CMOS-imagers*, Nanoelectronic Devices for Defense & Security Conference, 28 September - 2 October 2009, Fort Lauderdale, Florida (USA)

Danksagung

Diese Doktorarbeit wurde zwischen 2008 und 2012 am Lehrstuhl für Nanoelektronik (Technische Universität München) unter Anleitung von Prof. Paolo Lugli in Kooperation mit der Bruno-Kessler-Stiftung (fondazione Bruno Kessler) und der Universität Trento durchgeführt.

Zum Gelingen dieser Arbeit haben viele Personen beigetragen, insbesondere geht mein Dank an:

Prof. Dr. Paolo Lugli für die Möglichkeit an seinem Lehrstuhl an einem spannenden Projekt arbeiten zu dürfen. Besonders hervorzuheben ist, dass er mir viele Freiräume für die Verwirklichung des Projekts gelassen hat und mich immer unterstützt und gefördert hat.

Dr. habil. Giuseppe Scarpa für die Hilfe bei der Durchführung meiner Doktorarbeit, besonders für seine guten Ideen und die administrative Unterstützung.

Den Kooperationspartnern in Trento, die das Layout der CMOS-Chips entworfen haben und ihre Labore für die Vermessung der hybriden Sensoren zur Verfügung gestellt haben. Besonders danke ich Lucio Pancheri, der mir unermüdlich mikroelektronische Fragen erklärt hat und durch seine Fachexpertise wesentlich zur Entwicklung und Verständnis der Prototypen beigetragen hat. Ich danke auch David Stoppa und Prof. Gian-Franco Dalla Betta, die dieses Projekt überhaupt ermöglicht haben und mir immer schnell und unkompliziert geholfen haben. Danke auch an die Doktoranden am FBK, die mein Leben bereichert haben durch die Einführung in die trentinische Gastronomie und die wunderbaren alpinen Landschaften.

Lucia Weik und Rita von Grafenstein für die tolle organisatorische Unterstützung und die Ratschläge.

Ein großes Dankeschön an Rosi Heilmann und Bernhard Fabel, die nicht nur für den Zusammenhalt der Labore sorgten, sondern auch des gesamten experimentellen Teils des Lehrstuhls.

Allen meinen Studenten für das Beitragen zum Gelingen des Projekts. Besonders Morten Schmidt für die großartige und klaglose Unterstützung bei der Herstellung der Sensoren.

Allen weiteren Kollegen, die mir entweder auf fachlicher oder sozialer (Dach)Ebene geholfen haben. Besonders Mario Bareiß, Omar Fakhr, Christian Jirauschek, Tobias Häberle und Alexandra Münzer.

Vielen (TUM-)Kollegen für ihre Unterstützung: Werner Kraus für die Benutzung des Plasma-Ashers. Linda Mora und Ralf Meyer, die auch schon während der Diplomarbeit für mich da waren. Herrn Hilgers für die engagierte Arbeit in der Werkstatt. Matthias Sachsenhauser und Sebastian Schöll für die XPS-Vermessungen. Prof. Marco Sampietro für die Bereitstellung von Squaraine. Tobias Rauch und Sandro Tedde (Siemens Erlangen) für die Expertise in der Herstellung und Charakterisierung von organischen Photodioden.

Meinem Vater für die Unterstützung während des Studiums. Und für den unermüdlichen Druck mit “Wann hab ich denn jetzt endlich eine Frau Doktor als Tochter?”.